Novel radiation-activated Photodynamic Therapy (radioPDT) Theranostic Nanoparticle for Treatment of Deep-seated Tumors

by

Deepak Karthesh Dinakaran

A thesis submitted in partial fulfillment of the requirements for the degree of

Doctor of Philosophy

in

Cancer Sciences

Department of Oncology
University of Alberta

ABSTRACT

Radiotherapy is used in the treatment of 50% of all cancer patients. It has evolved into a high precision therapy in cancer care. Radiotherapy's main limitation is the damage incurred on normal tissue. Advances in modern radiotherapy allowed for improved precision in delivery and optimizes its Therapeutic Index (TI). Advances in precision are still pursued, but diminishing returns exist with little additional benefit seen with further precision. Photodynamic therapy (PDT) has evolved in clinical use over the last 30 years. It produces anti-tumor cytotoxicity with limited normal tissue damage. PDT's dependence on activating light has limited its impact on clinical care in oncology. Attempts to combine radiotherapy's deep penetration and precise targeting with PDT's superior TI has led to radiation-induced PDT (radioPDT), which uses scintillators to activate PDT with radiation using Forster Resonant Energy Transfer (FRET). Contemporary radioPDT agents have been limited by biocompatibility, toxicity, practicality, or lack of evaluation in a clinically relevant setting such as in hypoxia. This thesis explores the development of a novel radioPDT nanoparticle consisting of $LaF_3:Ce^{3+}$ nanoscintillator co-encapsulated with PPIX into a PEG-PLGA nanocarrier system. The nanoparticle exhibited a high safety profile, ease of synthesis and scalability, exceptional *in vivo* compatibility and delivery, superior therapeutic effect to radiation alone *in vitro* and *in vivo*, and utility as a CT contrast agent with theranostic potential. The nanoparticle exhibits negligible toxicity in inactive form, but once activated with radiotherapy it converts X-ray energy and molecular oxygen into cytotoxic singlet oxygen. This yields impressive anti-tumor cytotoxicity in normoxic and hypoxic conditions with partial oxygen-dependence characteristics and favourable treatment of potentially deep-seated tumors.

PREFACE

This thesis is the original work of myself, under the supervision of Dr. Ronald B. Moore, and supported through collaborations with the research groups of Dr. John D. Lewis (Department of Oncology) and Dr. Ravin Narain (Department of Chemical and Materials Engineering) in the University of Alberta. Contributions from members of the research groups are as described below.

A portion of Chapter 1 is in submission for academic publication in the manuscript: Deepak Dinakaran, David Murray, Ronald Moore; "Photodynamic Therapy (PDT) for Deep Seated Tumors: Review of Recent Advances and Future Combinations with Radiotherapy", where I am the primary and corresponding author, with Dr. Murray and Dr. Moore acting as senior and supervisory authors, as well as contributing to manuscript edits.

A portion of Chapter 2 is in submission for academic publication in the manuscript: Deepak Dinakaran, Jayeeta Sengupta, Desmond Pink, Arun Raturi, Hua Chen, Nawaid Usmani, Piyush Kumar, John D. Lewis, Ravin Narain, Ronald Moore; "PEG-PLGA Nanospheres Loaded with Nanoscintillators and Photosensitizers for Radiation-Activated Photodynamic Therapy (RadioPDT)". I conceived the experimental design and performed the experiments, data analysis and writing of the manuscript. Dr. Jayeeta Sengupta assisted with data collection, analysis and manuscript writing. Dr. Pink and Dr. Raturi assisted with experimental design and analysis. Dr. Hua Chen assisted with data collection. Dr. Usmani assisted with conception of the experimental design. Dr. Kumar assisted with experimental design and analysis. Dr. Lewis, Dr. Narain and Dr. Moore acted as supervisory authors and

assisted in the conception of the experimental design. All authors contributed to manuscript edits. Animal experiments were conducted under the animal ethics protocol AUP0000053 "Design of new treatment for prostate cancer" registered in the University of Alberta (Edmonton, Canada).

A portion of Chapter 3 is being submitted for academic publication in the manuscript: Deepak Dinakaran, Hua Chen, Brad Warkentin, Hans-Sonke Jans, Melinda Wuest, David Murray, Nawaid Usmani, Ravin Narain, John D. Lewis, Ronald Moore; "Increased Therapeutic Effect of Radiation in Combination with Novel Radiation-activated Photodynamic Therapy (radioPDT) Nanoparticles for Treating Hypoxic Tumors". I conceived the experimental design and performed the experiments, data analysis and writing of the manuscript. Dr. Chen assisted with data collection. Dr. Warkentin and Dr. Jans assisted in data analysis. Dr. Wuest assisted with data collection. Dr. Murray, Dr. Usmani, Dr. Narain, Dr. Lewis and Dr. Moore are supervisory authors that contributed to conception of the experimental design. All authors contributed to manuscript edits. Animal experiments were conducted under the animal ethics protocol AC17233 "Novel X-Ray Activated Nanotheranostics agent for Photodynamic Therapy of Deep seated Tumors" registered in the Cross Cancer Institute (Edmonton, Canada).

A portion of Chapter 4 is being submitted for academic publication in the manuscript: Deepak Dinakaran, Hans-Sonke Jans, Melinda Wuest, Hua Chen, David Murray, Nawaid Usmani, Ravin Narain, Frank Wuest, John D Lewis, Ronald Moore; "CT imaging and Biodistribution of Novel Radiation-activated Photodynamic Therapy (radioPDT)

Theranostic Nanoparticles in Flank Tumor Mice Model". I conceived the experimental design and performed the experiments, data analysis and writing of the manuscript. Dr. Jans assisted with data collection and analysis. Dr. M. Wuest assisted with data collection. Dr. Chen assisted in data collection. Dr. Murray, Dr. Usmani, Dr. Narain, Dr. F. Wuest, Dr. Lewis and Dr. Moore are supervisory authors. All authors contributed to manuscript edits. Animal experiments were conducted under the animal ethics protocol AC17233 "Novel X-Ray Activated Nanotheranostics agent for Photodynamic Therapy of Deep seated Tumors" registered in the Cross Cancer Institute (Edmonton, Canada).

ACKNOWLEDGEMENT

My journey to become a physician has showed me that where I truly belong is as a clinical scientist, and this necessitated my pursuit of graduate studies. To this end, I came to the University of Alberta with the intent of pursuing a PhD during my medical residency, specifically in radiation-activated Photodynamic Therapy (radioPDT). This was an unconventional approach as a student, and this is why I am deeply grateful for my supervisor, Dr. Ronald B. Moore, in taking such a risk with me as a new graduate student bringing in a new, unproven, and in some ways counterintuitive research concept into his lab. Dr. Moore's uncanny insight into key scientific questions, combined with his willingness to let me lead my own project, and his belief in my abilities as an independent thinker were what ultimately lead me to succeed beyond my highest expectations. I am also grateful for Dr. John D. Lewis, who acted as a mentor and co-supervisor and taught me not just about scientific methodology but also about translational sciences, and the challenges to overcome to carry research from bench to bedside.

I would also like to thank my committee members, who came together to provide me with supervision for my thesis and act as collaborators in this novel project. Dr. Nawaid Usmani has been a source of support, encouragement and guidance since I was a medical student, and he continues to be a strong mentor for me. Dr. Piyush Kumar and Dr. David Murray have provided me with their strong insights into radiobiology and hypoxia, and they have been an important resource for me to bounce ideas and write strong manuscripts and grant proposals. Dr. Ravin Narain's guidance, advice and strong insight into nanoparticle design and biomedical applications were instrumental in my successful development of the novel nanoparticle in this

thesis. The combined expertise of my supervisory committee were instrumental in my accomplishments as a graduate student.

Outside of my committee, there still remains two important mentors that have each contributed greatly to my journey as a graduate student. Dr. John R. Mackey has truly become a role model for me for his seamless ability to connect disparate ideas and concepts into a cohesive picture, thereby solving difficult problems in completely novel ways. I have modeled his way of thinking in my approach to solving problems and approaching research questions. John Walker has been gracious enough to mentor me in successful translational clinical trial design and execution, and his support has led me to meet many great leaders in oncology worldwide. These are life-changing opportunities that I never thought would happen for me. Both Drs. Mackey and Walker continue to support me in achieving my career and life goals, and for that I cannot thank them enough. My residency supervisors, Dr. Brock J. Debenham, Dr. David L. Bigam, and Dr. Sean McMurtry have also been important in their support in my research pursuits and I thank them for giving me the opportunity to achieve my career goals.

Several important members of the three labs I worked in for my thesis have also been critical to my success. Dr. Hua Chen has been a companion in the lab, a great source of knowledge, an ardent teacher of proper lab and scientific techniques, and a great support in completing my experiments particularly in the times I had to balance research experiments with clinical needs. Drs. Arun Raturi and Desmond Pink continued to be a wealth of knowledge and experience that provided me the much needed insight in crucial moments. Dr. Katia Carmine-Simmen, Mrs. Deborah Sosnowski, and Mr. Douglas W. Brown for their technical help and friendship that made my research work that much more enjoyable. Dr. Jayeeta Sengupta was also an important

contributor in the course of her post-doctoral studentship in assisting in synthesizing and characterizing the novel nanoparticle.

Finally, I am very thankful to have my wife Dr. Charlene N. Dinakaran in my life. I could not have asked for a more understanding and loving partner, and I am blessed to have a wife that is such a talented physician in her own right but is so supportive in helping me achieve my life goals. My father and mother have also sacrificed greatly in bringing me and my sister to Canada for a better life, and my drive to make a meaningful contribution in medicine stems from the work ethic I have seen in my parents, and also in my desire to maximize on the opportunities they have given me. My family's support in this endeavour was integral to my successful completion of my thesis.

This research was supported by the Canadian Urological Association (CUA), Canadian Uro-Oncology Group (CUOG) Astellas Research Grant Program awarded to me, and funded by Astellas Pharma Canada, Inc. and jointly established by Astellas Pharma Canada, Inc., CUOG, and the CUA. Dr. Lewis holds the Frank and Carla Sojonky Chair in Prostate Cancer Research funded by the Alberta Cancer Foundation. Dr. Moore holds the Mr. Lube Chair in Uro-Oncology. My salary support was provided by the University of Alberta's Clinician Investigator Program funded by Alberta Health Services. A portion of my stipend was also funded by the Cathy and Harold Roozen Scholarship.

Table of Contents

Abbreviations

2PE	2 Photon Excitation
5-ALA	5-Aminolevulinic Acid
ADR	Adjusted Dose Rate
AMP	Adenosine Monophosphate
ANOVA	Analysis of Variance
AP-1	Activator Protein 1
APC	Antigen Presenting Cell
ATP	Adenosine Triphosphate
CAM	Chorioallantoic Membrane
CHA	Canada Health Agency
CFU	Colony Forming Units
cGAS	Cyclic GMP-AMP Synthase
CBCT	Cone Beam Computed Tomography
CT	Computed Tomography
CTL	Cytotoxic T-lymphocyte
CTLA-4	Cytotoxic T-Lymphocyte Associated Protein 4
DAMPs	Damage-associated molecular patterns
DAPI	4′,6-diamidino-2-phenylindole
DC	Dendritic Cell
DCM	Dichloromethane
GAMP	Guanosine and Adenosine Monophosphate
GMP	Guanosine Monophosphate
DMEM	Dulbecco's Modified Eagle Medium
DNA	Deoxyribonucleic Acid
FBS	Fetal Bovine Serum
FRET	Forster Resonant Energy Transfer
FDA	Food and Drug Agency
FDG	Fluorodeoxyglucose
FGF	Fibroblast Growth Factor
FLT	Fluorothymidine
FMISO	Fluoromisonidazole
FSC-A	Forward-scattered light-area
FSC-H	Forward-scattered light-height
FSD	Focus-to-Skin Distance
GM-CSF	Granulocyte-macrophage colony-stimulating factor
Gy	Gray
HER2	Human Epidermal Growth Factor Receptor 2
HIF-1	Hypoxia Inducible Factor – 1
HIFU	High Frequency Ultrasound
HMGB1	High mobility group box 1
HSP	Heat Shock Protein
HU	Hounsfield Unit
IAZA	Iodoazomycin arabinoside
ICD	Immunogenic Cell Death

IFN	Interferon
IL	Interleukin
IV	Intravenous
IT	Intratumoral
IMRT	Intensity Modulated Radiation Therapy
KeV	Kilo-Electron Volt
KV	Kilovolt
LET	Linear Energy Transfer
LINAC	Linear Accelerator
LNP	Lipid Nanoparticle
LQ	Linear-Quadratic
MBq	Mega-Becquerel
MDSC	Myeloid-derived suppressor cell
MeV	Mega-Electron Volt
MHC	Major histocompatibility complex
MPS	Mononuclear Phagocyte System
MRI	Magnetic resonance imaging
MV	Megavolt
NCCN	National Comprehensive Cancer Network
NFkB	Nuclear Factor kappa B
NIR	Near-infrared
NK	Natural killer cell
NSC	Nanoscintillator
NSG	NOD SCID gamma (NOD.Cg-Prkdcscid Il2rgtm1Wjl/SzJ)
NTA	Nano-Tracking Analysis
NTCP	Normal Tissue Complication Probability
NP	Nanoparticle
OS	Overall Survival
PAMPs	Pathogen-associated molecular patterns
PEG	Polyethylene Glycol
PET	Positron Emission Tomography
PBS	Phosphate-buffered saline
PC3	Human Prostate Cancer cell line
PD-1	Programmed cell Death protein 1
PD-L1	Programmed Death-ligand 1
PDT	Photodynamic Therapy
PI	Propidium Iodide
PI3K	Phosphatidylinositol-4,5-bisphosphate 3-kinase
PL	Photoluminescence
PLGA	poly(lactic-co-glycolic acid)
PPIX	Protoporphyrin IX
PPM	Parts Per Million
PS	Photosensitizer
PSA	Prostate-specific antigen
PTV	Planning Target Volume
PVA	Poly-vinyl Alcohol

radioPDT	Radiation-activated Photodynamic Therapy
RFA	Radiofrequency Ablation
RLR	Retinoic Acid-inducible Gene-I-like receptors
ROI	Region of Interest
ROS	Reactive Oxygen Species
RES	Reticuloendothelial System
RNA	Ribonucleic Acid
RPMI	Roswell Park Memorial Institute medium
SARRP	Small Animal Radiation Research Platform
SBRT	Stereotactic Body Radiation Therapy
SDT	Sonographic photodynamic Therapy
SOSG	Singlet Oxygen Sensor Green
SSC-A	Side-scattered light-area
SRS	Stereotactic Radiosurgery
STING	Stimulator of Interferon Genes
SUV	Standardized Uptake Value
T	Tesla
TCR	T-cell Receptor
TCP	Tumor Control Probability
TEM	Transmission Electron Microscope
TGF	Tumor Growth Factor
TLRs	Toll-like Receptors
TNF	Tumor Necrosis Factor
UCNP	Upconverting Nanoparticle
UV	Ultraviolet
Vis	Visible
XRD	X-ray Diffraction

CHAPTER – 1

GENERAL INTRODUCTION

1.1 Strategies for Cancer Therapy

Cancer is a multi-factorial disease that continuously challenges attempts to advance treatment. Its prevalence and burden in the Canadian population continues to grow, with 1 in 2 Canadians expected to develop cancer in their life time and 1 in 4 Canadians are expected to die from the disease (1). Since 2010, cancer has surpassed heart disease as the number one killer of Canadians, which highlights the need for effective cancer prevention and management strategies (1). This need for treatment is being addressed from many different angles, with several advances seen in the fields of radiotherapy, surgery, chemotherapy, targeted biologic agents, and radionuclide based treatments (2). The field of cancer therapy is becoming increasingly crowded with therapeutic options that promise to deliver higher therapeutic efficacy with less toxicity.

1.1.1 The Advent of Radiotherapy

The main therapeutic options of surgery, radiotherapy, and chemotherapy can all be effective at curing the disease, but the main limiting factor is the morbidity and mortality risk that these treatments confer. All three have brought forth major paradigm changes in how cancer therapy is approached and there was initial optimism in the early 20th century in curing the disease with these therapies alone (3). This enthusiasm was tempered with realization that with cancer therapy the efficacy must always be balanced with the toxicity, in a concept known as Therapeutic Index (TI). Radiotherapy in particular has been a modality that has seen rapid evolution since the discovery of X-rays in 1895 (3). Within 15 years of that discovery, the first radiotherapy device was introduced to treat skin cancers (4). The results of these early radiotherapy treatments were accompanied by major toxicities and limited oncologic benefit. This resulted in a low TI. Years of further research

have led to insights gained into the mechanisms of radiobiology on death and cell survival and how this can be manipulated through total dose and fractionation (5). This has led to significant advances in optimizing the TI of radiotherapy. Treating skin malignancies is now possible with good efficacy and limited toxicity to the surrounding normal skin tissue.

1.1.2 Overview of Cancer Radiobiology

The main mechanism of cytotoxicity for ionizing high energy beams on living cells is mediated by damage to the nuclear deoxyribonucleic acid (DNA). The type of ionizing energy used to deliver radiotherapy can consist of electromagnetic particles such as photons; subatomic particles such as electrons, protons, or neutrons; or other charged heavy ions. Their ability to transfer energy to the living tissue is defined as the Linear Energy Transfer (LET). Different forms of ionizing energy have higher and lower LET, depending on their interaction with body tissue. Charged particles such as protons, electrons, and heavy ions can directly ionize molecules within cells, whereas neutral particles such as photons and neutrons rely on indirect ionization via interaction with the atoms to produce charged electrons particles (6). Depending on the type of particle and its energy, the LET value typically used in treatment of cancers can range from 0.3 keV/μm for 250 kVp orthovoltage X-rays to 12 keV/μm for 14 MeV neutron beam therapy (6). The effectiveness of different modalities of radiotherapy is standardized as a function of LET in a ratio known as Relative Biological Effectiveness (RBE). The amount of radiation energy deposited is defined most commonly in units of Gray (Gy), where 1 Gy = 1 Joule/kilogram.

The effect of the radiotherapy beam on cells depends on the phase of cell cycle. Cells are generally most radiosensitive in the mitotic and premitotic phases (M and G_2, respectively)

of the cell cycle, while they are most radioresistant in G_1 and S phase (7). The radiation dose needed to kill a cell in the radioresistant phases of the cell cycle are typically close to 10 Gy, whereas radiation doses of 2 Gy are sufficient to kill cells in the radiosensitive phases (7). In general, cancerous cells are more proliferative than normal tissue cells, which means they statistically spend more time in the more radiosensitive phases of the cell cycle. This confers some level of preferential toxicity on cancerous tissue versus normal tissue.

The charged particles that directly or indirectly results from the radiation beam primarily affect the cell by damaging DNA by causing breaks in the DNA structure **(Figure 1.1)**. This can be through direct ionization and breakage of the phosphodiester backbone, or through the creation of free radical species that inflict the same damage (8). The most common free radical formed is hydroxy radicals from ionizing water, due to its abundance in cell, but also through ionizing molecular oxygen into oxyradicals. Radiation modalities with LET values that are similar to photons generate about two thirds of the DNA damage via indirect free radical species generation, and one third comes from direct DNA damage (6).

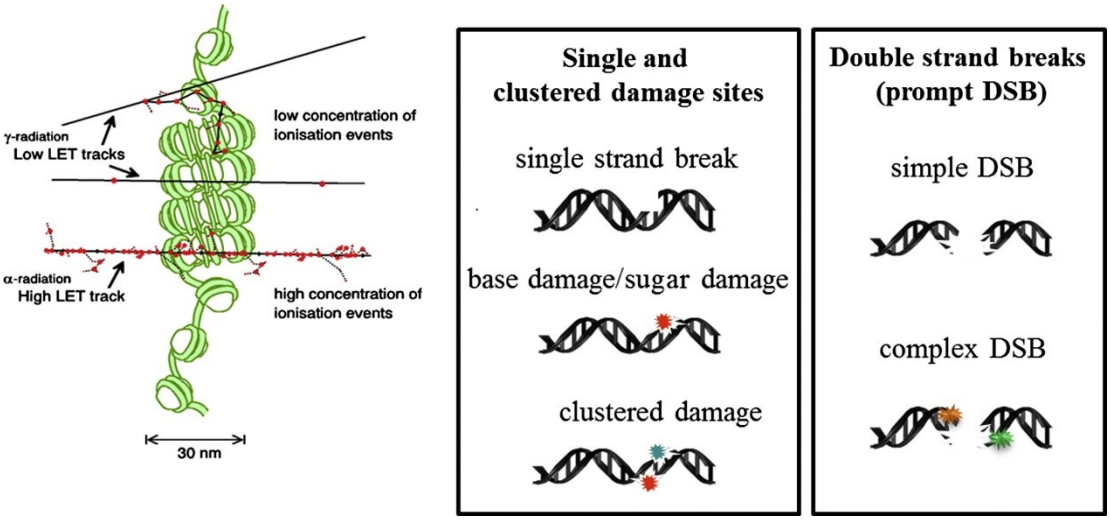

Figure 1.1: Differences in energy deposition and ionization events from low LET and high LET radiation beams (**left**), which lead to single strand (**middle**) or double strand (**right**) phosphodiester breaks in the DNA structure. The two low LET tracks (**left**) are demonstrating direct ionization events in the bottom track versus indirect ionization events in the top track. Image adapted from Lomax *et al.*, 2013 (8).

The resultant effect of the DNA damage depends on the LET, dose rate, total dose, and fractionation. Additional factors such as availability of molecular oxygen to promote indirect DNA damage, presence of free radical scavengers (radioprotectors) and radiation damage enhancing agents (radiosensitizers), and the cell cycle effects also impact the effect of radiation on the cell's survival. The probability of cell survival can be modeled with cell survival assays, which led to the development of the concepts of Tumor Control Probability (TCP) and Normal Tissue Complication Probability (NTCP). Optimizing the previously-mentioned factors can help produce a higher TCP to lower NTCP, and increase the TI (6).

The cell survival characteristics with radiotherapy have been mathematically modeled in the Linear-Quadratic (LQ) equation, with a constant of α for the linear component and β for the quadratic component of cell response (6). This incorporates both the deterministic and stochastic effects of radiotherapy, respectively, on cells depending on radiation dose used. All tissue types have some component of linear and quadratic effects. The LQ model varies with the type of tissue, as some tissues have a predominance to either more linear or quadratic effect and represent the inherent radiosensitivity of the target tissue. For rapidly responding tissue, there is a greater component of linear effects and early cell death, whereas for late responding tissues the have a greater quadratic component and experience cell death much later **(Figure 1.2)**. A given body tissue's response characteristic to radiotherapy can be captured in the α/ β ratio, which has allowed for therapeutic effect and toxicity modeling. These insights into radiobiology have underpinned the effort of clinical trials to use dose and fractionation methods to optimize cancer-specific killing while minimizing long-term normal tissue complications and has significantly contributed to the utility of contemporary radiotherapy (9).

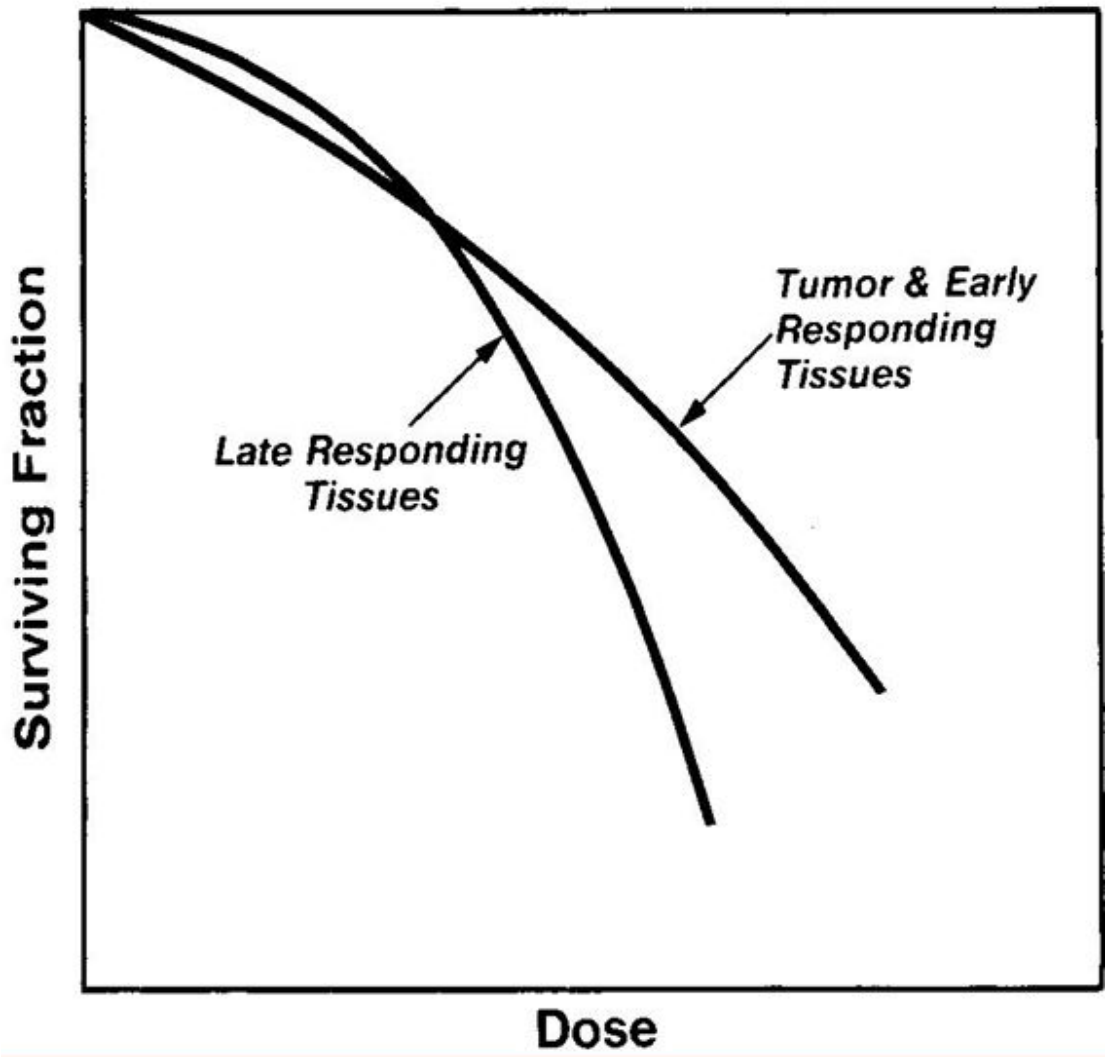

Figure 1.2: Linear-quadratic curve of early and late responding tissues in response to radiation dose.

1.1.1 Overview of Radiation Physics

The majority of radiation therapy for cancer uses photon beam systems. In the energy levels typically used for radiotherapy (100 kV to 18 MV), the major mechanisms that govern how photons interact with atoms in the body can be broken down into photoelectric effect, Compton effect, and pair-production (**Figure 1.3)** (6). The photoelectric effect is the dominant interaction for photons in the lower energy range, whereby the photon interacts with an orbiting electron, transfers all its energy before disappearing, and ejects the electron from the atom. This interaction is strongly influenced by the atomic number (Z) of the atom and is greatly enhanced with high Z matter (10). The photoelectric effect is primarily important for diagnostic X-ray scans but is also involved with dose deposition with orthovoltage machines. The Compton effect occurs in higher energy ranges, where typical MV range radiotherapy equipment is used, and involves interacting and ejecting the valence electron and deflection of the incident photon at a different scattering angle at a lower energy. Compton effect is directly dependent on electron density, but not Z-dependent, and is the most common interaction in soft tissues with clinical radiotherapy machines. The pair production effect occurs at a minimum energy of 1.022 MeV and starts to become a significant mechanism of interaction at the higher end range of clinical MV irradiators (10). At these energies the incident photon interacts directly with the nucleus, disappears, and produces a pair of electron with opposite charges (negative electron and positron) with equal energy (11).

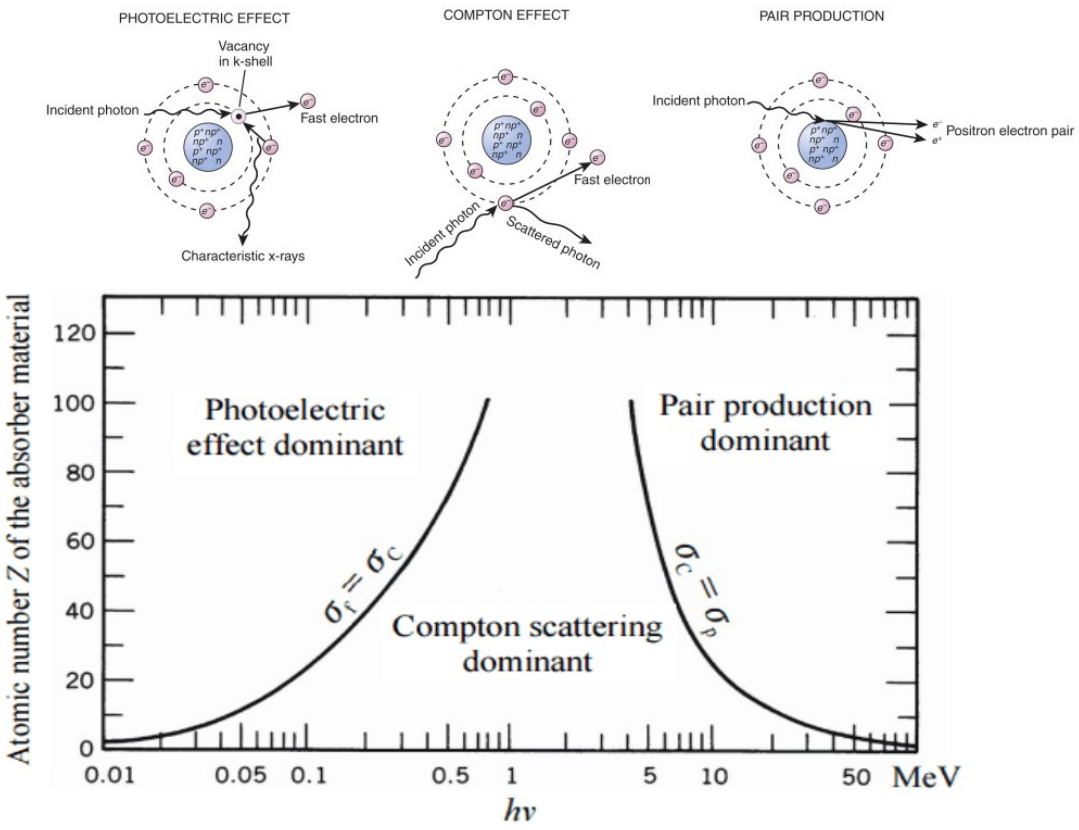

Figure 1.3: Types of interaction with atoms of body tissue as a function of incident photon (*hv*) energy. Image adapted from Hall *et al.*, 2010 (11) and Choppin *et al.*, 2002 (10).

Insights into how radiation at different energy levels interact with body tissues has allowed for major advances in diagnostic and therapeutic radiation use. It led to the second major improvement in radiotherapy, which was with the advent of high energy X-rays, particularly in the Megavolt (MV) range. This allowed better penetrance of treatment X-rays into the body, decreasing toxicity to more superficial structures such as the skin, and the ability to non-invasively manage tumors deep in the body (3). This is particularly relevant for oncology since the majority of all cancer diagnoses arise from deep-seated disease within the body. The most commonly diagnosed cancers in Canada include lung, breast, colorectal, and prostate cancer (12). The ability to treat malignancies deep within the body allows radiotherapy to be used in a curative or palliative setting for all of these malignancies with acceptable morbidity, which has led contemporary radiotherapy to become widespread in cancer care. It is now employed in the care of over 50% of all diagnosed cancer patients for curative and palliative indications (3).

1.1.2 Evolution of Modern Radiotherapy

Further advances in precision radiotherapy have refined its TI to a much higher level. Multiple advances in radiation medical physics have increased the ability to monitor, calculate, deliver, and provide quality assurance for radiotherapy systems (13-16). The ability to standardize therapy has allowed major advances in refining the dose, fractionation, and delivery techniques in the setting of clinical trials to make further gains in TI. The employment of Image-Guided Radiotherapy (IGRT), conformal radiotherapy techniques, computer-aided Intensity Modulated Radiotherapy (IMRT), and Stereotactic Radiosurgery (SRS) and Stereotactic Body Radiotherapy (SBRT) have continued to evolve

radiotherapy into the 21st century in delivering greater efficacy with less toxicity (17, 18). These advances have allowed radiotherapy to be used in new contexts, such as for the treatment of limited metastatic (oligometastatic) disease for curative intent, which is starting to redefine contemporary understanding of what is a curable stage of cancer (19-21). With the benefit in advances in radiobiology, radiation physics, and technology; radiation oncologists continue to push the boundaries of treating malignancies anywhere in the body with greater effectiveness.

Despite these major advances, the main limitation of radiotherapy remains the same: the toxicity to normal organs. The side-effects of radiotherapy, particularly the permanent and sometimes highly morbid or life-limiting long-term side effects, have posed major challenges to this strategy of cancer therapy. These side effects are particularly prevalent in deep-seated tumors, where inevitably, a significant volume of normal tissue is irradiated in order to adequately treat the target volume of malignancy. The damage and impact of these side effects have been realized particularly in the 1980s and onwards, which has led to the decreased use of radiotherapy in settings such as pediatric malignancies and hematologic malignancies, where chemotherapy has become more prevalent (22, 23). Even with the employment of the latest radiotherapy techniques, deep-seated malignancies such as prostate cancer still have up to 20% incidence rate of significant long-term toxicities (24). Furthermore, the benefits of higher precision radiotherapy may be reaching a point of diminishing returns, as radiation techniques are rapidly closing in on the last few millimeters of target volume uncertainty, and rising concerns of positive margins similar to surgery. Radiation equipment such as the Gamma Knife (Elekta, Stockholm, Sweden) can already employ zero-millimeter (0 mm) planning target volumes (PTV) due to the near-

absolute precision with which it can be employed to deliver radiation to deep-seated intracranial structures (25). Yet even still, significant toxicities such as unintended damage and death to nearby brain tissue (radionecrosis) can occur at a rate of 5 to 10% – leading to significant and debilitating patient morbidity (26). This highlights the need for a new direction of evolution for radiotherapy to evolve other than with higher precision equipment and techniques, in order to continue to make significant progress in managing current and future indications for radiotherapy in cancer care.

1.2 Radiosensitizers to Augment the Efficacy of Radiotherapy

Previous attempts at building on radiotherapy and augmenting its TI has been done mainly by combining radiotherapy with systemic agents, in the context of radiosensitizers. Research into radiosensitizers dates back to the 1970s, and was an early attempt at using insights into cancer biology and radiobiology to augment the efficacy of radiotherapy without increased radiation dose (27). The broad categories of radiosensitizers include: oxygen mimetics hypoxia-targeted compounds, radiation synergistic cytotoxic drugs and radiation dose-enhancing agents (28). The use of chemotherapeutics alongside radiotherapy has been shown to provide additive effect in multiple tumor groups (29). This added therapeutic efficacy, however, comes at a cost of toxicities from both chemotherapy and radiotherapy simultaneously (chemoradiation). For chemotherapy in particular, the issues of myelosuppression and risk of serious infections are difficult to mitigate, and patient comorbidities may make them unfit or unable to tolerate chemoradiation (30). The overall benefit often tends to be modest as well, such as in head and neck cancers where the 5 year OS benefit is only about 5% in many chemoradiation trials (31). Therefore,

alternative radiosensitizers are an attractive idea, especially if their effect could be tailored specifically towards synergizing and mitigating the problem of radioresistant tissue without adding additional toxicity. The general principle of these agents is to address a disadvantageous situation for radiotherapy effect, such as hypoxia, and/or enhance the DNA damage and cellular death mechanisms induced by radiotherapy.

1.2.1 Hypoxia-targeted Radiosensitizers

One of the earliest radiosensitizer strategies evolved once the importance of oxygen on radiobiology was understood. Oxygen can have a strong effect on the radiosensitivity of cells, particularly with low-LET radiotherapy (32). Certain cancer histologies such as gliomas of the brain and squamous cell carcinomas of the cervix and head and neck have also demonstrated significant radioresistance mediated through hypoxia (33, 34). This has been further explored clinically, where studies have found that tumors in patients often harbor regions of hypoxia (28, 35, 36). These areas of hypoxia often appear to be related to poor vascular supply, which in turn confer radioresistance partly through oxygen enhancement effect from DNA damage fixation, but also from the induction of cell survival mechanisms via upregulation of Hypoxia Inducible Factor – 1 (HIF-1) (37, 38). Advances in hypoxia detection have brought about immunohistochemical stains such as pimonidozole and carbon anhydrase IX to investigate regions of relative chronic and acute hypoxia and chronic hypoxia, respectively (39). This was followed by *in vivo* diagnostic nuclear medicine scans to investigate hypoxia using radiotracers such as [123I]-iodoazomycin arabinoside (IAZA) and [18F]-fluoromisonidazole (FMISO) in preclinical and clinical models (34, 40, 41). Through these detection and imaging techniques, the

problem of tumor hypoxia and its negative effects on radiotherapy have been more fully appreciated. Using these imaging techniques along with modern IMRT, hypoxic-adaptive radiotherapy techniques are being trialed in order to increase therapeutic effect to these hypoxic regions (42).

Another approach is to artificially replace the activity of oxygen in these hypoxic tissues, using oxygen mimetic agents. These are oxidative agents that can act as a substitute to oxygen in DNA damage fixation, and prevents its repair by reductants such as thiols (28). Oxygen mimetics are commonly nitro-containing compounds, such as misonidazole, nimorazole and tirapazamine (28, 35). These agents accumulate within hypoxic tissue by being selectively reduced in hypoxic cells and becoming trapped within them by undergoing electron reduction and binding to biomolecules. They have demonstrated significant radiosensitizing effect *in vitro* with rodent models also demonstrating radiosensitizing capability, but human studies were not able to deliver a high TI due to the drug's long half-life and consequent high toxicity to normal tissues (35, 43). The bioreductive alkylating effect of these oxygen mimetic drugs have also shown beneficial enhancement in Photodynamic Therapy (PDT) as well, by taking advantage of the rapid induction of a local hypoxic environment caused by PDT (44, 45). Perhaps due to the dose reductions necessitated by the high toxicity profile, oxygen mimetics such as tirapazamine failed to show greater therapeutic effect in a phase III trial setting (46). Oxygen mimetics are still under investigation in under clinical investigation, but the enthusiasm for them within radiation oncology has greatly diminished after the initial failed trials, high toxicity concerns and modest expected benefit (47, 48).

1.3 Promise of New Cancer Management Strategies

Several new targeted biologic agents promise to address the tumor directly or indirectly via modulation of the immune system and vascular system and have been predicted to be game-changers for cancer therapy (49). The optimism around these drug therapies went as far as to question if there was still a role for traditional therapies such as radiation, surgery, and even conventional chemotherapy (2). The results of clinical trials have demonstrated some of these agents to deliver on their promises but many others have not (50-53). In comparison, there has been a resurgence in aggressive local therapies such as radical resections, lymphadenectomies, and stereotactic radiotherapy for loco-regional disease (54-60). Even in the metastatic setting, surgical metastatectomies and stereotactic radiotherapy have demonstrated a clear role via significant progression-free and overall survival (OS) benefits (60-62). These benefits exist even with more advanced targeted drug therapies and perhaps even synergize with drugs such as immunotherapy agents for better overall cancer treatment (63, 64).

The main challenge that currently still remains is in limiting the toxicities of these aggressive local therapies. The mainstays of intensification of local therapies remain through surgery and/or radiation. Surgical oncology has made significant advances in the past few decades via improved surgical technique and with minimally invasive surgeries (65-67). Further advances are expected to come through robotic assisted minimally invasive surgeries but despite many years of use, this has yet to manifest into a clear clinical benefit (68). Other factors that limit more aggressive surgical management include patients with significant comorbidities, advanced age, disease-related decline in performance status, or long-term side effects from previous cancer therapies.

As mentioned previously, radiotherapy has made great advances in achieving local dose escalation without undue toxicities, mainly through the use of advanced technologies. High precision radiotherapy technologies have existed for some time in machines such as: Gamma Knife, Cyber Knife, Tomotherapy, Linear Accelerators (LINACs) with motion-tracking and cones or high definition multi-leaf collimators. The addition of inverse planning-based IMRT, and more recently real-time imaging with MRI, have also significantly advanced the field. These technologies allowed radiation oncologists to use high precision ablative-intent radiotherapy techniques that can rival surgical treatments with much less toxicity (69). This has proven useful in managing primary disease as well as limited burden oligometastases (60). The clinical implementation of these technologies has hit its stride in this decade of radiation oncology but its future growth may be limited by the ability for technological advancements to provide better treatment. We are rapidly approaching the era of 0mm PTVs in intracranial and extracranial sites of disease but the clinical benefit of this compared to a standard 5 mm PTV may not provide as significant a leap as 2D planning versus IMRT. New modalities such as ultra-high dose rate FLASH radiotherapy may provide some additional benefit in maximizing tumor treatment effect while minimizing toxicity (70). Further refinements in radiation dose, fractionation, and indication will continue to advance the field, but without newer modalities of safe dose-escalation radiation oncologists may eventually reach the limits of conventional radiotherapy in treating patients.

Other modalities to locally treat cancers have also been developed with the intent of raising the TI and deliver higher efficacy with lower toxicity. Techniques such as Radiofrequency Ablation (RFA), High-Intensity Focused Ultrasound (HIFU), endovascular embolization,

thermal therapy, and cryotherapy have been used clinically in an attempt to improve local oncologic treatments (71-73). These techniques have met with varying degrees of success, and some have carved out new niches in cancer therapy, but none have ultimately been transformative to the field of cancer therapeutics. Their limitations, such as the invasiveness of the procedure, the lack of tumor specificity, and damage to surrounding normal tissue have limited their appeal in treating a wide range of tumors.

1.4 The Role of Photodynamic Therapy in Cancer Care

One form of local therapy that has demonstrated high anti-tumor activity with low toxicity is PDT. This modality has existed for over 50 years in a preclinical setting and has been implemented since the 1980s in a clinical setting, with regulatory approval in the 1990s (74). It was once thought to be the next paradigm shift in local cancer therapy (75). Indeed, it has become common place in the treatment of superficial cancers, and endoscopically accessible tumors (76). PDT has even proven to be an effective local therapy to tumors refractory to radiotherapy (77). However, it has failed to gain greater acceptance in the field of cancer therapy mainly due to its inability to address most deep-seated cancers, which is mainly a result of its dependence on red and infrared spectrum light with limited tissue penetrance. The most common cancers, such as lung, prostate, breast, and gastrointestinal are mainly deep-seated disease that are not readily amenable to access with a light source to effect PDT (78). This limitation may be changing as preclinical and early clinical studies for PDT in deep seated tumors are evolving, which may allow PDT to effectively manage tumors anywhere in the body. One such direction of evolution may eventually involve an overlap with the field of radiation oncology, whereby the precise

targeting technology employed by radiation oncology today may provide the excitation energy needed to effect PDT.

1.4.1 PDT Mechanism

PDT uses a two-step activation process to induce cytotoxic tissue damage. The PDT system uses visible light to provide the activating energy for a Photosensitizing drug (PS), which in turn generates reactive oxygen species (ROS) for therapeutic effect (79). These two components are individually nontoxic and have no therapeutic effect. The most common clinically used PS are porphyrin ring-based molecules that were first discovered in the 1960s (80). These molecules are analogous to endogenous porphyrin ring structures that are precursors in the heme-biosynthetic pathway (81). The key structure to the currently used PS is the tetrapyrrole backbone that is also found in chlorins and phthalocyanines. The most commonly used light sources are either lamp-based systems for skin malignancies or solid-state laser based systems (82). The wavelength used generally is in the 600nm to 850nm to allow for some penetrance into body tissues (<1 cm) and still provide enough excitation energy. Other energy forms that have been used to effect PDT include infrared (2 photon excitation) and ultrasound stimulation (sonoluminescence) (83, 84). A schematic example of the PDT process is shown in **Figure 1.4**.

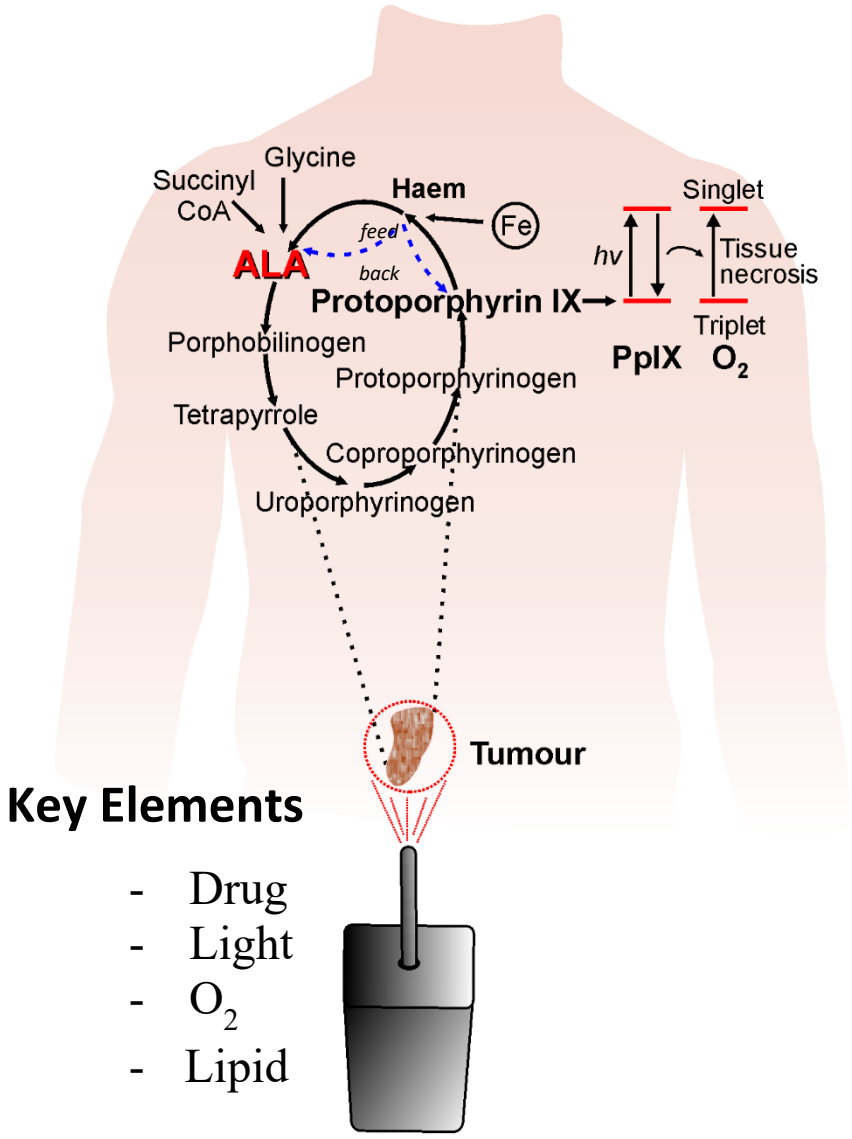

Figure 1.4: A schematic example of a porphyrin derived PS Aminolevulinic Acid (ALA) that is converted protoporphyrin IX from the heme biosynthetic pathway being used along with laser light activation to induce PDT in treating malignancies. Image adapted from Kennedy *et al.*, 1990 (85).

Once the ground state photosensitizer (^{1}PS (S_0)) is excited by visible light, it enters an excited singlet state (^{1}PS* (S_1)) capable of creating free-radical species. The excited singlet state of the PS ($^1PS^*$ (S_1)) can return to the ground state either via non-radiative internal conversion or fluorescence emission, or it can undergo intersystem crossing to an unstable triplet state ($^3PS^*$ (T_1)), as shown in **Figure 1.5** (80). The PS in this excited triplet state can decay back to the singlet ground state (^{1}PS (S_0)) either via the emission of a phosphorescent photon or non-radiative intersystem crossing or it can react with a suitable molecular substrate via a Type I or Type II mechanism. In the Type I reaction the ^{3}PS* (T_1) directly reacts with substrates such as lipid membranes, macromolecules, or water to form free radical species (80). The Type II reaction refers to the triplet ^{3}PS* (T_1) transferring energy to molecular oxygen (which exists as a triplet in its ground state) to form the highly reactive species, singlet oxygen ($^1O_2$). Both types of reaction occur on a time scale of nanoseconds, which limits the range of migration of these excited species in body tissues (mainly to cellular organelles) and restricts the biological effects to a highly localized region. This confers a high degree of control over PDT, which helps direct its activity only at the target while limiting off-target damage. Of the two types of reaction, Type II has been determined to be the more clinically significant process leading to radical species that will induce tissue (organelle) damage (86). This means that PDT's clinical effect is largely dependent on $^1O_2$ generation, which in turn is limited by available molecular oxygen in the local tumor environment.

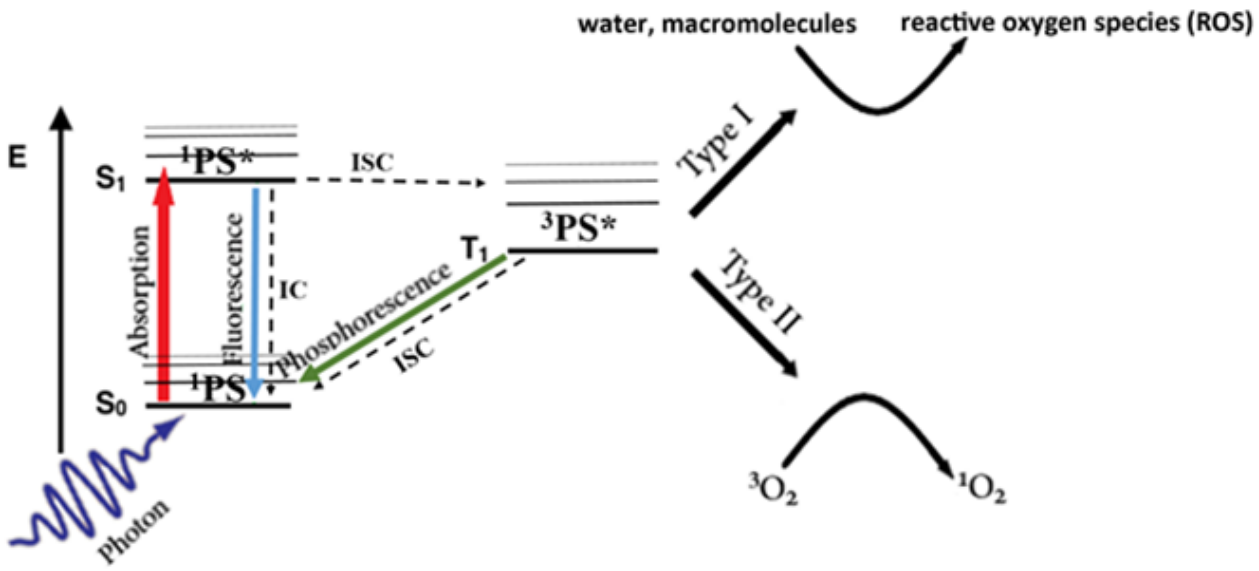

Figure 1.5: Principles of the mechanism of PDT illustrated with a simplified Jablonski diagram. Photon energy from a light source is used to excite a photosensitizer (PS) from its ground state (^{1}PS (S_0)) to (^{1}PS* (S_1)). This unstable excited singlet state can return to the ground state via internal conversion (IC) or fluorescence (blue) or it can undergo inter-system crossing (ISC) to the triplet state (^{3}PS* (T_1)). The triplet state is also relatively unstable and can go back to the ground state (S_0) via phosphorescence (green) or ISC or it can undergo a Type I reaction with water or macromolecules such as lipids to create hydroxyl radicals and macromolecule radical species. The triplet state can also react with molecular oxygen ($^3O_2$) to form an excited singlet oxygen species ($^1O_2$). The $^1O_2$ is the predominant species responsible for reacting with nearby cellular structures to inflict cytotoxicity. Radiative transitions are shown as colored arrows and non-radiative transitions as black/dashed arrows.

1.4.2 PDT's Effect on Biological Tissue

The net effect on the target tissues is oxidative stress, which manifests in three different processes at the level of cellular, tumor, and immune system effects. In the cancer cell, the $^1O_2$ reacts with macromolecules, particularly lipids, which causes plasma membrane damage, disruption of lysosymes, mitochondrial and endoplasmic reticulum damage, and induces cellular stress pathways which eventually lead to cell death with a predominance towards apoptosis and necrosis (86). These dying cells can also release cytokine signals to promote cell death in nearby cells that are not directly affected by the PDT's oxyradical species. In the tumor, PDT is known to cause significant vascular damage, particularly to the endothelial cells, which leads to vascular collapse and ensuing infarction within the tumor (87). Lastly, an important contributor in PDT's success in clinical therapy is its immune priming abilities. This effect was seen early on in preclinical murine studies, with PDT's ability to generate durable cures in immune-competent animals (88).

1.4.3 PDT and Radiotherapy Interaction with the Immune System

PDT's activity in damaging plasma membranes elicits a strong pro-inflammatory signalling response and results in a robust innate immune response leading to Immunogenic Cell Death (ICD). The rapid anti-tumor innate immune response also potentiates an adaptive response for long-term control. The oxidative stress causes vascular injury induced tumor ischemia, as well as strong direct cytotoxicity via lipid membrane disruption, cell death, and cytoplasmic content spillage that act as damage associated molecular patterns (DAMPs). These processes activate multiple signaling pathways such as DAMP-mediated Toll-like receptors (TLRs) and retinoic acid-inducible gene-I-like

receptors (RLRs) on dendritic cells, Heat Shock Protein (HSP) pathways, Nuclear Factor kappa B (NFκB), Tumor Necrosis Factor alpha (TNFα), and Activator Protein 1 (AP-1). DAMPs also activate $CD8^+$ cytotoxic T lymphocytes through similar mechanisms to radiotherapy, leading to multiple proinflammatory interleukins, chemokines, interferons, and Macrophage Inflammatory Proteins (MIP). In turn, the innate and adaptive immune response activate T lymphocytes, macrophages, Natural Killer (NK) cells, and neutrophil infiltration to directly kill tumor cells and produce further proinflammatory activity, immune cell activating mediators, and complement cascade activation (89, 90). Hence, an acute and powerful inflammatory response is induced by PDT. The strong induction of an early and long-term immune response has led PDT to demonstrate abscopal response in preclinical and clinical studies (41, 79, 87, 91-95).

Radiation has also been under investigation as a potentiator of immunotherapy drugs, particularly in the scenario of poor response to immune checkpoint inhibition (96-99). The main proposed mechanisms are via DAMPs in the microenvironment that lead to proinflammatory cytokines such as interleukin-1β (IL-1β) and Transforming Growth Factor β (TGF-β), fibroblast growth factor (FGF), and TNFα. In addition, cytosolic DNA ingested by dendritic cells from radiation-damaged tumor cells produce cyclic Guanine monophosphate (cGMP) and Adenosine Monphosphate (cAMP) via cGMP-AMP synthase (cGAS) and induces Stimulator of Interferon Genes (STING) to transcribe type I interferon (IFN). ICD dampening simultaneously exists through TGF-β and IL-10 mediated regulatory T lymphocytes (T_{reg}) and Myeloid-derived Supressor Cells (MDSC) activation, which act to suppress Cytotoxic T Lymphocyte (CTL) activity (100). These competing ICD promoting and dampening pathways with radiotherapy can lead to a spectrum of

responses such as tumor elimination, equilibrium, dormancy, or escape. In practice, the clinical response to radiotherapy with immunotherapy has not been conclusively positive nor with a large magnitude of improvement (101-103).

Some of the immune-priming mechanisms are shared with radiotherapy and PDT, but key differences do exist. Both have the potential of generating abscopal effects in isolation via systemic spread of T and B lymphocytes sensitized to tumor neoantigens. Both rely on DAMP-mediated Antigen-Presenting Cell (APC) activity leading to recruitment and activation of effector T lymphocytes (T_{eff}), and both cause chemokine and chemotaxic release to promote T lymphocyte infiltration, proliferation and hence inflammation (63, 89, 104). One of the key differences with PDT is it has a much larger component of innate immune response causing high degree of tumor inflammation, which tips the balance of immune-priming and immune-dampening more towards the former. ROS damage to tumor cells favours necrosis and a high load of DAMPs from the cytosol being directly spilled into the environment. This induces strong cytokine/chemokine activation for the innate immune response and produces many neoantigens for the adaptive immune response. Radiotherapy's cytotoxicity is primarily mediated by DNA damage and the cell death from this, along with DAMP presentation and cGAS-STING activation, does not produce as profound an innate immune response and inflammation (90, 105). In addition, radiation can have direct inhibitory effect on the infiltrating immune cells. This is evident in inflammation and necrosis seen in clinical PDT versus radiotherapy (105). Hence, PDT offers advantages in synergizing with immunotherapy over radiotherapy.

The time course for cellular effects of PDT is also more rapid than conventional and hypofractionated radiotherapy. Within the first 3 days, cell death often reaches its peak-

often with over 80% of the tumor cells experiencing cell death. This level of response cannot be attributed to direct cytotoxic damage alone, since the range of activity for PDT is limited. The domino effect of PDT's damage on some cells induces widespread cell death produced by the previously mentioned cell signalling factors of the damaged cells, indirect vascular damage and infarction, and immune effects (86). Normal tissue is more resistant than tumoral cells to damage from these indirect effects, which along with selective cancer cell retention of the PS is partly what confers a high degree of cancer cell selectivity to PDT (86). These indirect effects are similar to the mechanisms employed by spatially fractionated radiotherapy techniques, although the latter has major logistical challenges for implementation and is still susceptible to radio-resistance mechanisms and long-term dose related toxicity (106). Of note, a key differentiator of PDT from radiation is the toxicity profile. The short-term toxicities mainly relate to relatively minor photosensitivity issues, depending on the PS used, but in contrast to radiotherapy PDT has no long-term toxicity concerns.

1.4.4 Review of Use in Clinical Cancer Care

PDT's first use for clinical cancer therapy started with Porfimer sodium (Photofrin) in 1993 when it gained Food and Drug Administration (FDA) and Canadian Health Agency (CHA) approval for use in bladder cancer (74, 107, 108). Several other PS followed for clinical approval. Since the approval of these agents for clinical use, there have been several case reports and clinical trials exploring the use of PDT for localized cancer therapy. To date at least 49 clinical trials have been conducted with PDT, the large majority of them being positive studies (109). Several more PDT studies are also on-going. These trials have

ranged from PDT monotherapy to combined therapy with PDT and radiation, surgery, chemotherapy, and more recently targeted drug therapy such as checkpoint inhibitors. PDT's indications range from the initial bladder cancer, to skin, lung, pancreas, head and neck, esophagus, anal canal, brain tumors, breast, cervical, and prostate. Trials have ranged from Phase I to Phase III studies, some with more than 200 patients treated. PDT's indications range from primary cure of disease to treating symptomatic metastases. Drug delivery methods have ranged from topical application on skin malignancies, to intravenous administration, intra-arterial embolization (110), and nanocarrier-mediated targeted drug delivery systems (111). Light delivery systems have ranged from natural sunlight to laser-based endoscopic or interstitial approaches (112, 113).

Clinical examples of PDT include skin malignancies, which are often treated remarkably effectively with PDT, with very minimal damage and long-term cosmetic effect on the normal skin (114). Similar types of high therapeutic effect with very minimal damage is seen across multiple other malignancies as well. This high TI is rarely seen in other local therapies such as radiation. This has led to the use of PDT in radiation-refractory cases, such as for salvaging esophageal, head and neck, and other types of cancers previously treated with definitive chemoradiation (115-117). The use of PDT in these settings has demonstrated encouragingly high complete response rates in disease resistant to conventional therapy (118-120). Despite this, the limitations of PDT, particularly in treating deep-seated tumors, has limited its clinical utility.

Currently, PDT is not considered standard of care for any known cancer setting. The National Comprehensive Cancer Network (NCCN) currently recommends considering PDT in basal cell carcinoma and cutaneous squamous cell carcinoma only when the disease

is low-risk, superficial, and where surgery and radiotherapy is contraindicated (121, 122). There are mentions in other settings such as for mesothelioma, where its use in combination with surgery is considered experimental (123). A summary of the recommended use of PDT per NCCN guidelines is presented in **Table 1.1**. In comparison, other local therapies such as RFA were developed around the same time period of PDT, but have risen to front-line standard-of-care use in cancer treatments to a much greater extent (124). Despite some important advantages of PDT, it seems it has failed to gain widespread adoption that was initially predicted. This again is mainly due to the key limitation of treating deep-seated tumors within the body.

Table 1.1 NCCN recommendations for the use of PDT in standard of care settings across malignancies.

CANCER SITE	RECOMMENDED INDICATION	PDT TYPE	LEVEL OF EVIDENCE
Cutaneous basal cell carcinoma	Low-risk, superficial disease when surgery/radiotherapy not feasible	5-ALA/Photofrin with 570 nm to 670 nm light source	Phase III randomized data against cryotherapy (125)
Cutaneous squamous cell carcinoma	Precancerous lesions (Bowen's disease, diffuse actinic keratosis)	Topical 5-ALA or methyl aminolevulinate (MAL) with red or green light source	Phase III randomized trial against cryotherapy (126)
Bladder	Diagnosis only	5-ALA with blue light to detect fluorescence	Meta-analysis(127)
Mesothelioma	Alternative adjuvant therapy, not recommended over radiotherapy	Intravenous Photofrin with intracavitary 630nm laser	Phase I/II series in conjunction with IMRT (128, 129)
Central nervous system	Diagnosis only – intraoperative surgical adjunct	5-ALA with blue light to detect fluorescence	Phase III randomized trial against white-light microsurgery (130)
Non-small cell / small cell lung	Alternative palliative modality for malignant endobronchial obstruction or hemoptysis	Photofrin or chlorin PS with 630 nm laser	Phase II single arm study (131)
Prostate	None, warrants further study	Padeliporfin with interstitial 753 nm laser	Phase III randomized trial against active surveillance in low-risk disease (132)

1.4.5 The Challenges of PDT in Deep-Seated Tumors

The limitation of PDT in treating deep-seated tumors was identified as one of its greatest weaknesses from the start. The two-step activation consists of a biochemical method of localization of the PS to the site of disease and the spatial localization of the activating light to the target. This has allowed PDT to be highly effective in treating cancers while sparing normal tissue. Using advances in the understanding of the pharmacokinetics and mechanisms of distribution of PS in the body, the second generation PS are designed for disease selectivity by targeting up-regulated pathways in cancerous cells (80). If the tumor is easily accessible to light irradiation, the accumulated PS can selectively be activated in the target area of intended therapeutic effect with remarkable precision. This application is especially evident in the theranostic application of photodynamic diagnosis (PDD), such as for observing bladder cancer (133).

Once tumors start to become less accessible and more deep-seated, delivering the activating light to the target becomes a major challenge. One issue is the limited depth penetrance of the typical red wavelengths of light used by PDT, which clinically limits the treatment effect to 0.5 cm, or less depending on the tissue. The effect of light propagation through different body tissue also complicates the delivery of activating energy. Even within the same tissue type, enough heterogeneity exists with differential light absorption and scattering properties to significantly complicate light delivery. This results in light irradiance inhomogeneities that are difficult to account for and to produce accurate light dosimetry modeling (74, 134, 135). Furthermore, the light delivery protocol, including fluence rate, constant versus pulsed light delivery, and total time for treatment also can significantly affect the clinical outcomes (74, 136). The impact on clinical effect with light

delivery is also additionally complicated in deep-seated tumors by tumoral hypoxia. With high light fluence for activation, it is possible for PDT to easily deplete the tumors oxygen quite rapidly and ultimately limit its overall effectiveness (41, 137, 138). In addition to depleting the oxygen substrate, high fluence rates can also cause PS inactivation and limits its effectiveness in a process called photobleaching (139, 140). Thus, attempting to use PDT for deep-seated tumors starts to produce many difficulties primarily with controlling light delivery. Attempts at light dosimetry modeling and fractionation techniques have been undertaken (**Figure 1.6**), but to date, no universally accepted or practiced PDT dosimetry standard has resulted from these efforts.

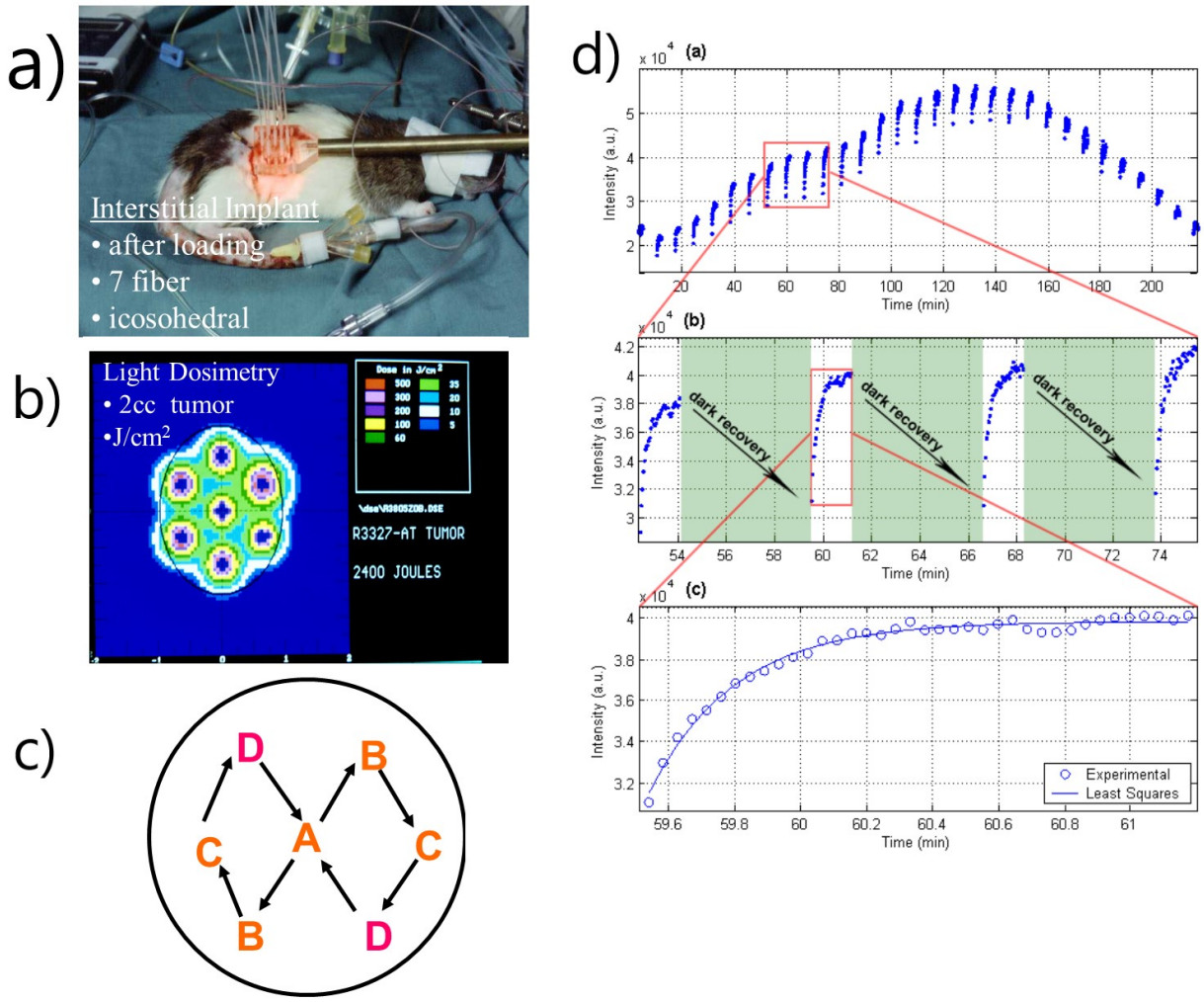

Figure 1.6: Methods of interstitial light delivery combined with spatial and temporal fractionation for optimal PDT effect. A Dunning R3327 rat prostate cancer model implanted with light catheters in a standardized icosahedral catheter layout (a). This layout was adopted for ease of light dosimetry calculation and geometric expansion to larger tumors (b). The catheters were pulsed in a specific geometric pattern (c) to allow fractionated therapy (d), reoxygenation of the tissues, and higher therapeutic yield. Image adapted from Xiao *et al.*, 2007 (136).

Initial attempts at solving the issue of light delivery focused on catheter-based fiber optic delivery into target tissues. The primary approach for this is via interstitial light catheters inserted into the tumor. These light catheters attempt to homogeneously diffuse light from a laser source directly into the target tissue (141). This method of PDT has been employed clinically in cancer sites such as prostate, pancreas, head and neck, brain, and various sites of metastases.

Clinical trials in these tumor groups have met with varying levels of success in phase I, II and III settings. Azzouzi *et al.* have developed padaleporfin (Tookad™, Steba Biotech, New York, USA) along with transperineal interstitial light catheter implants analogous to prostate brachytherapy setups. They were able to demonstrate significantly improved progression-free survival with minimal toxicity over active surveillance in low-risk prostate cancer, which is particularly significant since traditional surgery and radiotherapy have struggled to demonstrate benefit in low-risk disease (132, 142-145). Interstitial PDT with *meta*-tetra(hydroxyphenyl)chlorine (mTHPC) (Foscan®, Biolitec Pharaceuticals Ltd. Dublin, Ireland) has also been successfully employed as salvage therapy in a phase I/II trial of head and neck cancers that recurred after chemoradiation (146). A 20% complete response rate was achieved along with significant disease response in almost all patients and some long-term survivors. Of note, no significant toxicities were encountered in most patients, but two patients did experience significant morbidity in terms of carotid rupture within 2 weeks of PDT due to disease invasion into the carotid and rapid response post-treatment (146). Another phase I/II trial with verteporfin (Visudyne™, Valeant Pharmaceuticals, Bridgwater, USA) and MRI-guided interstitial light catheters in unresectable pancreatic cancer was also able to generate positive results via tumor response

and necrosis and improved OS (147). The challenge in this study was in predicting the diameter of necrosis created at the catheter tip, which was not repeatably energy-dependent and appeared to depend on tissue heterogeneities in light propagation. The investigators were ultimately limited to creating a 12mm diameter of necrosis at the catheter tip, which limited the ability to perform PDT to the whole site of disease. For treatment of metastatic disease, PDT can prove effective for local control and symptom relief from a metastasis. For example, a phase I trial for pathologic vertebral compression fractures showed PDT was safe, feasible, and produced significant pain relief when it was done alongside kyphoplasty. This was done using the vertebroplasty needles to delivery light to the site of disease following intravenous PS administration (148). This technique had the advantage of not causing any short or long-term effects on the spinal cord, which would generally be the concern had the kyphoplasty procedure been consolidated with the usual palliative radiotherapy or SBRT.

Despite successful implementation of PDT to deep-seated cancers via interstitial light delivery, the challenge still remains in accurately predicting light dosimetry in body tissues, which is significantly more susceptible to tissue heterogeneity than radiation dosimetry (149). One strategy is to use interstitial light sensing catheters to monitor the distribution and fluence of light or the fluorescence from the activated PS itself (150-152). Doing this can provide feedback on calculated dosimetry and real-time adjustment of light delivery to optimize standardization and therapeutic effect, but it introduces another level of complexity and invasiveness to the PDT workflow. Furthermore, there is no standardized method that is universally accepted on PDT light dosimetry, with each PDT group usually developing their own method, often with assumptions made on light dosimetry in the target

tissues (153). This lack of light dosimetry standardization ultimately undermines the widespread adoption of interstitial PDT, despite some promising clinical results.

1.4.6 Addressing Light Penetrance for PDT

1.4.6.1 Advances in PS Chemistry

A strategy to augment PDT's effectiveness in deep seated tumors is to focus on development of new PS. Although porphyrin derivatives are the most widely used PDT agents, these represent an earlier generation of PS that have lower quantum yields (0.5-0.6) of $^1O_2$. This translates into low efficiency in converting light to oxyradical species, and an inability to effect PDT at depth due to inadequate light penetrance (154, 155). Newer generation PS such as chlorins, bacteriochlorines, phthalocyanine, and hypocrellin based agents are significantly more efficient than porphyrin structures at generating $^1O_2$ per photon absorbed, with quantum yields approaching 0.9 or greater (154, 155). Some are also optimized for light absorbance at longer wavelengths approaching 800nm, which allows the use of deeper penetrating light to 1 cm (156). Hence, even in low levels of photon fluence resulting from increased tissue depths from light source, these PS can still result in significant singlet oxygen yield and sufficient cytotoxicity, especially with 2 photon excitation (2PE) and upconversion strategies. Several other agents have also been proposed for use as a PS, but the major classes of PS that have been used or are considered for clinical trials in human patients are limited to the ones discussed above. **Figure 1.7** demonstrates their chemical structures. They all share a common porphyrin ring derivative-based structure, which allows the PDT electron intersystem crossing mechanism to occur.

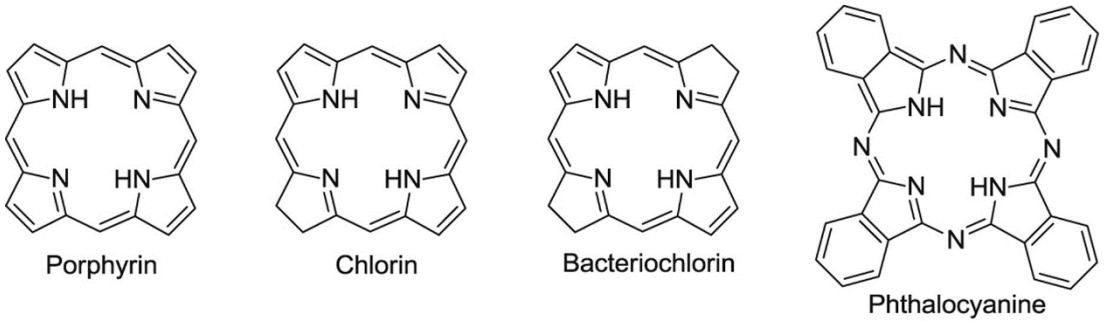

Figure 1.7: Chemical structures of major PS compound classes considered for use in clinical application.

These agents come with newer potential issues, however, in terms of their phototoxicity profiles *in vivo* and in humans (157). The pharmacokinetics of these agents can be slow to be taken up by the tumor, there can be unintended distribution into normal body tissues, and potentially low clearance from the body after treatment. While these PS are designed to be nontoxic in dark conditions, they are often also activated by visible light, particularly by sunlight, which means patients must follow special precautions to avoid skin and retinal burns. The incidence of unintended phototoxicity can reach as high as 40% if the patient is exposed to sunlight even for a few minutes (158). With slower clearing PS, this can leave patients susceptible to light toxicity for weeks (159). To limit this issue of uptake and clearance rates, a subclass of PS agents has been developed which are vascular-targeted. The advantage of these agents is they can be administered minutes prior to therapy, maintain a high concentration in blood and vasculature with low uptake into body tissues, and are cleared from the body within hours (160). Vascular-targeted PDT PS such as padeliporfin and verteporfin have even been used clinically with good success (132, 147). These agents do, however, sacrifice direct cytotoxic damage and immune-priming mechanisms in the tumor to focus more exclusively on the vascular effects of PDT for efficacy. Another method to limit this unintended photoxicity and increase the tumor-specific effect is to use nanotechnology to encapsulate PS into a nanoparticle. These are considered third generation PS. By optimizing the nanoparticles for pharmacokinetics and drug release characteristics, the PS's contact and absorption into cells of normal tissue can be limited, which also limits toxicity (161, 162).

1.4.6.2 Advances in PDT Light Delivery Systems

Further basic science studies on proposed PS agents include those capable of activation by Near-Infrared (NIR) light, 2PE, or ultrasound activation instead of traditional light activation, which is summarized in **Table 1.2**. For NIR light-based PDT, the use of longer wavelengths (700 nm to 1000 nm) can confer increased tissue penetrance, theoretically, as high as 5 cm due to less absorbance and scatter (163). Several PS have been developed that are capable of NIR PDT (164-168). The main challenge with this technique is thermal loading that can occur with light wavelengths approaching infrared, which may cause hyperthermic damage to normal tissue (169). This is particularly important in NIR PDT since the longer wavelength photons often lead to lower quantum yields of singlet oxygen, which requires higher energy inputs (up to 40 W/cm^2) of light to compensate (170). Furthermore, the accuracy of irradiating with NIR light at depth also becomes a challenge as longer wavelength causes increased divergence and the spot size to greatly increase with the inverse square of distance from the light source (163). The issues of accuracy and thermal loading can be improved with two-photon PDT, where the PS is excited when it absorbs photons of two different wavelengths of NIR light. This has the advantage of spreading the thermal loading of each incident light beam and allows for better spatial localization at the intersection of the two light beams (80, 171). Similarly, upconverting nanoparticles operate by converting infrared light into visible light for activation of a traditional PS. These have also encountered difficulties with energy input needed and the side effect of thermal heating, with energy inputs approaching 10 W/cm^2 (172). However, this heating could be advantageous at the site of disease as prior studies have shown additive effects to conventional PDT (173, 174). An alternative PS activating strategy to

light energy is to use sound energy from ultrasound systems similar to HIFU, in a process termed Sono-Photodynamic Therapy (SDT). This is a relatively new technology with some demonstrated clinical benefit in small patient trials. The ultimate safety and efficacy of SDT compared to PDT is currently still under exploration (175). Furthermore, similar to HIFU, SDT still may have issues with tissue density and heterogeneity and difficulty effectively treating tumors deeper than 3 cm without more invasive techniques (176).

Table 1.2 Summary of deep-penetrating PDT activation modalities.

MODALITY	PS	DEPTH OF TISSUE PENETRANCE	DISADVANTAGES	STAGE OF DEVELOPMENT
NIR	Modified second and third generation	Up to 5 cm	Tissue heating, high energy input, decreased spatial precision	Preclinical studies
Two-photon	Nanoparticle-based	Up to 5 cm	Tissue heating over wider area	*In vitro* / *in vivo* studies
Upconverting nanoparticle	Nanoparticle-based	Up to 5 cm	Tissue heating	*In vitro* / *early in vivo*
SDT	Modified chlorin-based	Up to 3 cm	Off target effects from high intensity ultrasound	*In vitro* / *early in vivo*

1.5 Potential Role for Radiotherapy in PDT

PDT is a treatment technique familiar in radiation oncology (177-181). Its advantages can be considered complimentary to the use of radiotherapy, particularly with treating superficial disease or radioresistant disease. Transferable knowledge and understanding of electromagnetic and particle radiation dosimetry, as well as support from physicists, place radiation oncologists in a good position to take a lead in advancing this technology. Light dosimetry, photon fluence, and pulsing frequency are analogous to radiation dosimetry, radiation dose, and fractionation, respectively. As mentioned previously, these parameters are not only important for ensuring adequate PS activation and PDT effect, but also to prevent unnecessarily high photon fluence that can deplete oxygen or cause photobleaching, which can also negatively impact PDT. Beyond the parallels in technique for PDT and radiotherapy, there are emerging roles for PDT to potentially advance the field of radiation oncology.

1.5.1 Potential Synergism with Biological Effects of Radiotherapy and PDT

The use of PDT with radiotherapy in treating challenging disease cases has demonstrated advantages in this combined approach. Radiation's primary method of treating malignancies is by inducing significant DNA damage to cause cell death (182). PDT's mechanism of killing cells is mainly through oxyradical species mediating damage of extra-nuclear cell structures vascular effects, and immune effects as previously described. These are complementary mechanisms of action that may lead to an effective synergism between the two treatment modalities, without greatly increasing toxicity. The majority of preclinical studies have demonstrated at least additive effects of radiotherapy and PDT

(183-185). Some have even demonstrated possible synergy, with *in vitro* models of MCF-7 breast cancer cell lines treated with radiation and PDT showing decreased cell viability to a much greater extent than either treatment modality alone, even when treatment doses were de-escalated for both modalities (186). Similar results were obtained with other PS agents as well (187, 188). This potential synergistic effect was also seen by Nakano *et al.* in treating recurrent Bowen's disease with PDT and electron radiotherapy, where complete response rates of 80-100% was achieved with no additional toxicity (189). Similar highly positive results with combination radiotherapy and PDT have also seen in studies with endobronchial tumors, sarcomas, and esophageal cancers (190-192). These results present combination radiotherapy with PDT as a potential therapeutic strategy for increased disease control with minimal added toxicity.

1.5.2 Use of Radiotherapy to Activate PDT

1.5.2.1 Methods of Radiation-activated PDT (radioPDT)

Another evolving strategy is to directly combine radiotherapy with PDT, using a process of radiation-activated PDT (radioPDT). This process uses the X-rays delivered by radiotherapy as the activating energy for the PS, which allows PDT to occur in deep-seated tumors without the previously mentioned challenges with light delivery. The potential for X-rays to effect PDT noninvasively for deep seated tumors was first shown by Chen *et al.* (94). Luminescence in scintillating nanoparticles (nanoscintillators or NSC) was induced with X-rays (scintillation) and via fluorescence resonance energy transfer (FRET) it produced visible light locally to excited a PS for PDT effect (91, 94). Zou *et al.* (2014) reported a nanocomposite system of Ce^{3+} doped lanthanum (III) fluoride ($LaF_3:Ce^{3+}$) and

the photosensitizer PPIX that can be activated by X-rays to induce oxidative stress, mitochondrial damage, and DNA fragmentation in cancer cells to kill them (93). Using scintillating nanoparticles as an interstitial light source for photodynamic activation was successfully demonstrated in prostate cancer cells *in vitro* (93). Further, there are reports of using a CeF_3 nanoparticle (NP) conjugated with the photosensitizer verteporfin and quantifying $^1O_2$ yield that demonstrated cancer cell-kill upon irradiation with X-rays (193). Proof of concept *in vivo* studies have also shown promise for therapeutic efficacy in mouse solid tumor models (21). Similar results were obtained by multiple other groups as well (91, 94). Further studies have evolved multiple iterations of radioPDT nanoparticles aimed at increasing therapeutic yield, optimizing the physical characteristics, and targeting specific cellular structures (91, 93, 95, 194, 195). The field has quickly grown in the past 10 years with multiple groups now developing radioPDT agents. If successfully translated to a clinical setting, radioPDT may provide the holy grail for both radiotherapy and PDT: it combines the much deeper penetrance, precise targeting (radiation and drug) and dosimetry of modern radiotherapy, with the superior tumor control capability and low toxicity of PDT.

1.5.2.2 Challenges with radioPDT

Before successful translation to clinical practice, radioPDT still has several challenges to overcome. One challenge is in increasing the efficiency of the radioPDT system. Early radioPDT agents used NSC and PS with low quantum yields for visible light photons and $^1O_2$, respectively (94). The FRET efficiency is also important to optimize, as losses in FRET conversion lowers the available energy converted from X-rays to visible light for

PDT effect (195). Many of the proposed radioPDT agents are made from novel designs and foreign elements that have challenges in terms of biocompatibility, *in vivo* toxicity, and pharmacokinetics that need to be addressed before translational studies can be considered. Another important question to address is the oxygen dependence that both modalities share. In a sequential treatment approach, as done in the previously mentioned combined radiation and PDT studies, there is an opportunity for re-oxygenation to occur. In a radioPDT approach, where the radiation effect and PDT effect are occurring concurrently, the opportunity for oxygen competition and consequent limitation of treatment effect exists. The level of oxygen dependence for cytotoxicity in PDT and radiation can be quantitatively compared by modeling the impact of gradients of oxygen limitation on therapeutic effect (**Figure 1.8**). The overall magnitude of dependence can be quantitatively compared by examining the oxygen concentration at which the 50% of the impact on therapeutic effect is generated, or otherwise known as the half maximal rate ($1/2K_{max}$). PDT's $1/2K_{max}$ is estimated to occur at an oxygen concentration of 1% (196). In comparison, the oxygen enhancement ratio of radiation's $1/2K_{max}$ is also reported to be around 3% to 4% (**Figure 1.8)** (197). This is comparable to many deep-seated tumors which have average oxygen concentration levels of well under 4% (198). ***Due to this potential for hypoxia-induced deleterious effect on therapeutic yield, understanding radioPDT's performance under hypoxic conditions is crucial to pursing this approach in a clinical setting.***

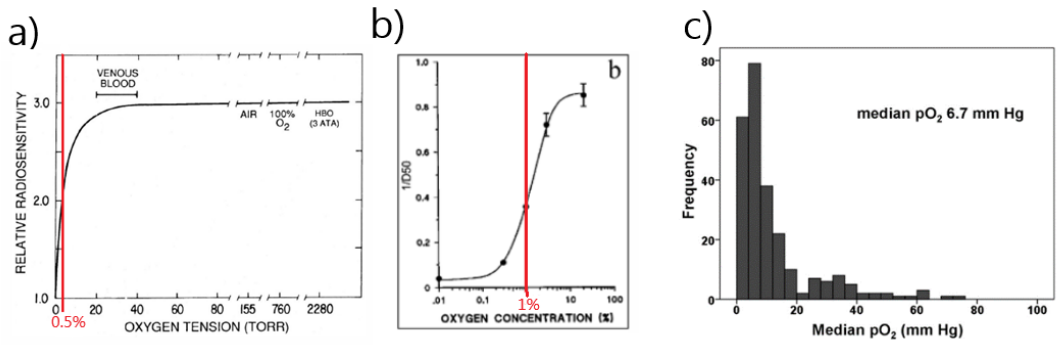

Figure 1.8: Comparison of the $1/2K_{max}$ of radiotherapy (a) and PDT (b) with respect to oxygen level. Distribution of oxygen levels in patients with prostate cancer is shown in (c). Images adapted from Rockwell *et al.*, 2009 (199), Moore *et al.*, 2007 (196), and Milosevic *et al.*, 2012 (198), respectively.

To date, minimal data exists on the effect of hypoxia on radioPDT. Other groups have demonstrated the ability to synthesize non-oxygen dependent inorganic PS that rely more on the Type I reaction pathway to function as a radioPDT agent to mitigate hypoxic effects (200). These *in vitro* results have been backed up with *in vivo* results that demonstrated radioPDT's ability to work in physiologic tumor environments including hypoxia (201-203). While more investigations are needed into the effectiveness of radioPDT in hypoxic conditions, early results seem to suggest this may be a limitation that can be mitigated.

1.6 Utility of Nanoparticles in IGRT

Another step that may facilitate radioPDT's translation into clinical care is the ability to use it as a therapeutic and diagnostic (theranostic) agent. The field of theranostics has been under development for many years, with many theranostic agents focusing on systems for nuclear medicine imaging (204). The introduction of theranostic radioPDT agents may hold some value in external beam radiotherapy as well, particularly with the advent of IGRT. Some proposed PDT nanoparticles have a diagnostic capability under Computed Tomography (CT) or Magnetic Resonance Imaging (MRI) (205-210). This offers potential applications in IGRT if the nanoparticles can be visualized and tracked with onboard CT imagers or MRI imaging built into a LINAC machines or other radiotherapy machines. The nanoparticles could be tracked with the imagers to ensure adequate tumor uptake and compensate for variations in pharmacokinetics, or it could aid the IGRT software to track the physiologic movement of tumors based on enhancement from the nanoparticles. For radioPDT, if the amount of nanoparticles in the tumor can be detected and quantified, this, in combination with radiation dosimetry data, can allow the calculation of the therapeutic yield from radioPDT. Ultimately, this can allow for better standardization of therapeutic

effect and more personalized therapy by reducing variability between pharmacokinetics of different patients or even the same patient over successive fractions and improving the quality of IGRT as well as overall therapeutic effect.

1.7 Development of Nanoparticles in Cancer Therapy

Advancement in the field of nanotechnology has opened new approaches for cancer therapy. Nanomedicines show great promise in terms of multi-functionality, targeted delivery, improved release profile, pharmacodynamics and mitigated toxicity (211). NPs are generally defined as particles sized from 1 nm to 1000 nm, and are generally designed to be injected into the body for clinical benefit (212). The first use of NP clinically in cancer therapy was liposomal based systems such as liposomal doxorubicin (Doxil®, Pfizer, New York, USA), which achieved FDA approval in 1995 (212). The main focus of interest for early nanoparticles such as Doxil® was to increase cancer specificity of chemotherapeutic drugs while minimizing toxicity. In the 2000s and onwards, however, NPs were increasingly used in other forms of cancer therapeutics such as radiosensitizers, thermal therapy and photodynamic therapy (28, 213). Another field of research that also started to develop for cancer nanomedicine was for improved diagnostic capability (214). As an extension of the developments in diagnostics and therapeutics, a new direction of "Nanotheranostics" combines therapy and diagnosis into a single NP platform (215, 216). All of these strategies have the potential to treat and diagnose cancer disease simultaneously at macroscopic, cellular and molecular levels.

1.7.1 General Categories of Nanoparticles for Cancer Treatment/Diagnosis

NP compositions can be quite innovative and varied. They broadly fall into the categories of lipid-based, polymer-based, viral-based, inorganic, and protein/polymer conjugates. Lipid-based NPs (LNPs) are one of the most mature cancer nanomedicines, and include subcategories of: solid and nanostructured LNPs that are composed of an admixture of lipids and drug in a spherical shape, liposomes being a more sophisticated systems with an outer lipid bilayer encapsulating drug, and vesicles being composed of a monolayer lipid envelope (217, 218). The advantage of LNPs is their biocompatibility in the body; their ability to conjugate to proteins, DNA, ribonucleic acid (RNA), and macromolecules for targeting or therapeutic effect; ability to fuse to the plasma or nuclear membranes to release its contents; and their long history of preclinical and clinical research (217). LNPs hold some disadvantages in terms of their relatively more complicated synthesis techniques, difficulty standardizing NP size and drug loading within the same batch, as well as batch to batch, and difficulty loading inorganic or highly charged payloads (212, 218).

Polymeric NPs use synthetic polymers to design a wide range of NPs with multiple properties. Some polymeric NPs are meant to emulate the properties of LNPs, such as Poly (lactic-co-glycolic acid) (PLGA) polymers that can self-assemble into liposomal and vesicle-like structures (218). Others can be far more sophisticated such as polymeric nanogels that can respond to environmental stimuli of pH, temperature, light, and many other possible factors (219, 220). Because of the wide range of possible constructs, polymeric NPs can vary greatly in complexity of synthesis (218). They are, however, highly tunable in their characteristics, which allows a high degree of flexibility in the

payload they can be loaded with and remarkable control over their pharmacokinetics and drug release profile (218).

Viral-based NPs refers to the use of specially modified viruses that are capable of expressing specific proteins for targeting or therapeutic effect (212). These NP are elegant in their use of a virus' natural pathogenicity and biocompatibility along with cell-specific recognition and cytotoxicity to produce therapeutic effect (221). Viral NPs do carry disadvantages in terms of their ability to mutate over successive generations, potential for biosafety concerns with off-target effects and thus far suboptimal clinical response in clinical trials (222, 223).

Inorganic NPs, such as gold, copper, and carbon nanotube based systems, focus on providing diagnostic qualities or as a therapeutic system in response to optical or ionizing irradiation (212). Their therapeutic effect is often exerted through thermal heating or, in the case of ionizing radiation, through a dose-enhancement effect mediated through the production of Auger electrons and transfer of energy to ROS (28). Other mechanisms of action can also include paramagnetic effects for MRI diagnostic attributes, and X-ray attenuation for CT imaging enhancement properties (221). Inorganic NPs can also act be conjugated to organic molecules such as proteins, small molecules, DNA/RNA, and other macromolecules. This allows them to have enhanced targeting capability or complementary biological activity with accompanying drugs (28). One such application is in radioPDT agents, where inorganic compounds such as NSC can absorb ionizing energy and fluoresce it at a longer, visible wavelength to excite drugs such as PS for PDT (see **Section 1.5.2**). Inorganic NP tend to be highly stable and offer unique properties that may not be achievable by organic-based NPs, but they can also less biocompatible *in vivo* and

often cannot exert direct therapeutic effects on cancer without activation or a accompanying drug (28).

The other possible category of NP is a hybrid form of NP that are composed of conjugates of organic macromolecules and/or polymers and inorganic NPs. These can include antibody-drug conjugates that can target epitopes on cancerous cells to deliver drugs directly (212). Another conjugate system-based NP includes PS conjugated to phospholipids to make a selectively activated NP that is inactive (through self-quenching) when in NP form, but becomes activated when broken down inside the target cell to deliver cancer-selective PDT effect (224). Another conjugate system is the use of cowpea mosaic virus (CPMV) conjugated to PEG and EGFL7, a marker of neovascularization, in order to identify and track tumor angiogenesis (225). Through combinations of different entities into novel NP designs, a variety of attributes can be produced including multiple different attributes within the same NP.

1.7.2 Advantages of Nanoparticle-based Therapies

The use of a NP-based cancer therapy system can afford multiple advantages, from reduced toxicity and increased feasibility in human use to increased cancer-specific therapeutic effect and less off-target effects. The exact benefits derived depend significantly on the construct of the NP system and its specific attributes. NPs offer a high degree of flexibility and the ability to “mix-and-match” different attributes together, particularly in a modular-based NP system (212). Despite the variation, some shared common attributes exist in cancer NPs.

Most NP systems are designed to enhance tumor-targeting to deliver a higher therapeutic effect while decreasing off-target toxicity. The principle mechanism employed is through the Enhanced Permeability and Retention (EPR) effect (226). This is a passive targeting system that takes advantage of the difference in vascular architecture between normal tissue and cancerous tissue. One of the hallmarks of cancer is its induction of angiogenesis in order to form neovasculature and support the tumor's continued growth (227). This neovasculature tends to be aberrant with larger pores compared to normal tissue vasculature. This allows tumor neovasculature to allow entities as large as NPs to freely pass from the blood vessel into the tumor interstitum, whereas normal tissue vasculature would prevent this due to its smaller pore size (228). Thus, with a NP of an optimum size, the tumor can be targeted preferentially and deliver a higher proportion of the payload to it versus to normal tissue. Mathematical modeling, correlated with empirically studies, have determined that the ideal size for tumor-targeting via EPR effect is approximately 100 nm (229).

Beyond size alone, other factors can help NPs target tumors preferentially; such as the addition of surface aptamers that can actively bind to target ligands, and by evading immune-mediated clearance thereby increasing vascular circulation time (228). Active targeting via aptamers are particularly effective in smaller NPs (<50 nm), which tend to have biodistribution profiles similar to proteins (229). Larger NPs closer to 100 nm tend to have biodistribution profiles dominated by EPR effect, with little additional benefit seen with active targeting. Further targeting benefits can be gained by decreasing its immunogenicity via surface coating. Molecules such as PEG and other organic compounds can decrease the rate of NP detection by the reticuloendothelial system (RES), otherwise

known as the mononuclear phagocytic system (MPS) (230). This evasion of the immune system augments the *in vivo* circulation time, which can allow more time for the NP to accumulate in the tumor via EPR rather than be cleared by the MPS typically in the liver and spleen (231).

NP systems are also advantageous because they can stabilize drugs that are otherwise incompatible with physiologic conditions needed to have therapeutic effect on the cancer. Drugs such as paclitaxel are poorly water-soluble and unstable in physiologic media, which requires formulations in media such as Cremaphor to become a deliverable drug (232). The formulation however, is known to cause significant side effects and even anaphylactic reactions in patients, which limits its clinical utility (232). These issues have been successfully mitigated with nanomedicine, where paclitaxel can be loaded into an albumin-based NP (Abraxane®, Celgene, Summit, NJ, USA) that confers much less toxicity with the same or better efficacy (233, 234).

Using NP systems for delivery of therapeutic effect also opens up different strategies for drug delivery. The traditional delivery method of intravenous (IV) is the most commonly used for NP agents, but other strategies can also be employed. Intratumoral injections (IT) have been successfully used to deliver large doses directly to the tumor to augment the effect of radiotherapy (235). Similarly, NP systems can be selectively administered to target tissues via intra-arterial approaches that have demonstrated a high degree of selectivity for the organ of interest in preclinical and clinical studies (110, 236).

Hence, with the use of nanomedicine a therapeutic agent can be developed that can simultaneously solve issues of biocompatibility, drug stability, tumor selectivity, and normal tissue toxicity. NPs also allow for multimodal agents that can simultaneously

perform two different tasks, such as providing therapy and diagnostic capability – a nanotheranostic agent. NP-based therapeutic strategies make complicated processes such as radioPDT much more feasible in practical application.

1.8 Summary of Current Role of PDT in Deep-Seated Tumors and Radiotherapy

PDT is a treatment modality that offers great benefits to the field of oncology, but over the last 30 years it has not significantly changed standard of care as it was expected to. Several preclinical and clinical studies have demonstrated its ability to locally treat tumors with rapid response and long-term control, limited short-term toxicity, and virtually no long-term toxicity. It has even shown potential for improving therapeutic benefit in situations where surgery and radiation struggle to, such as in low-risk prostate cancer. Its main mechanisms involve direct cancer cell cytotoxicity from oxyradicals, but clinically much of the therapeutic gain from PDT comes from cell-signaling, vascular infarction, and immune response. This has contributed to a favorable TI for PDT. ***The main limitation of PDT is its inability to treat deep-seated tumors effectively, which stems from challenges with light delivery and dosimetry to deep-seated regions of the body.*** This is likely why PDT has thus far failed to deliver on the initial optimism of its contribution to oncology.

Modern advances in light delivery techniques, dosimetry modeling, and PS development has increased PDT's capabilities in treating deep-seated tumors. Advanced interstitial approaches and the use of interstitial catheters are showing promising results in clinical trials. PDT has also demonstrated effectiveness in treating radiotherapy refractory disease, such as in esophageal and head and neck tumors. Tissue light dosimetry modeling along with light monitoring systems have also demonstrated benefit in assisting in treating deep-

seated structures with PDT. The use of these techniques in PDT may benefit from the expertise posed in radiation oncology, as they are analogous to the challenges and solutions to radiation dosimetry.

The field of radiation oncology could, in turn, benefit from PDT's ability to treat radioresistant diseases. PDT's mechanism of action focuses more exclusively on oxidative damage to the cell membrane and organelles, along with the indirect cytotoxicity from cell-signaling, vascular, and immune effects. In contrast, radiotherapy's main mechanism of action is through DNA damage. Given that the target structures of damage for PDT and radiotherapy are in part different, the opportunity for complementary activity exists. This has been seen to be at least additive if not synergistic, which has also been seen in clinical response to combine radiotherapy and PDT. The other major benefit to radiotherapy with PDT is that there is very limited additional toxicity, which makes it far more appealing than traditional radiosensitizing oxygen mimetic bioreductive drugs. Some of these drugs were even applied to PDT, with the bioreductive agents showing additive effects with PDT and the ability to monitor PDT response (41, 237, 238). Despite these efforts, these bioreductive agents have not been implemented widely in radiotherapy or PDT.

The ultimate benefit from PDT may be finally realized with the direct combination of the two. The advanced ability of radiotherapy techniques to target any lesion in the body can be combined with PDT's biological effectiveness by using the X-ray energy to excite the PS. This process, called radioPDT, may finally unlock the true potential of PDT. It can also significantly advance the field of radiation oncology by providing greater therapeutic effect to even radioresistant tumors, without additional significant toxicity. However, enthusiasm for the radioPDT approach must be tempered until key issues of the combined modality is

addressed. ***Current nanoparticles capable of radioPDT are usually of quite exotic designs and are not readily applicable in a clinical setting due to challenges with biocompatibility, safety, tumor-targeting, and clearance questions that still need to be addressed.***

1.9 Project Summary and Rationale

This thesis demonstrates that the use of nanotechnology, with a novel NSC to advance radioPDT as a new paradigm in cancer therapy. Radiotherapy has evolved significantly over the last century with many major innovations that have contributed to treating cancers more safely and effectively. The current state-of-the-art radiotherapy systems can deliver radiation precisely anywhere in the body using computer-aided control of dose distribution and effective intensity modulating strategies in steering dose around critical structures. The ease and reliability with which deep-seated tumors can be locally and non-invasively treated by radiotherapy is unmatched. However, even with newer and more sophisticated radiation delivery techniques under development, radiotherapy still has major limitations in terms of long-term morbidity and radioresistant cancers. These limitations are innate to the mechanism of action of radiotherapy itself. Despite multiple innovations over 100 years of cancer care, radiotherapy is still predominantly dependent on DNA damage mechanisms to treat cancer. Several radioresistance mechanisms have been identified to limit its effectiveness (239-242). Radiosensitizers and advanced dose-escalation technology have mitigated but not solved the issue of radioresistance and have unfortunately increased radiotherapy toxicity (243, 244).

In contrast, PDT is a treatment system with very low long-term toxicity profiles and very high efficacy even in tumors refractory to surgery, chemotherapy, and/or radiotherapy. In the emerging era of immunotherapy, PDT may also be one of the most potent forms of local therapy to potentiate an immune response. PDT's main clinical limitation is the lack of ability to easily treat deep-seated tumors, due to the difficulty with delivering activating light to the target and the lack of ability to standardize light delivery. The complementary strengths and weaknesses of these two modalities makes the combination of the two a rationale treatment modality to further explore for effective cancer therapy.

By shifting the mechanism from purely DNA damage to a combination of DNA damage and PDT's cell and organelle membrane damage, vascular damage, and immune-priming effects, radioPDT may hold the key to greatly increasing the effect of radiotherapy without increasing its toxicity. Here, I report the development and efficacy of a novel radioPDT nanoparticle (NP) that incorporates a $LaF_3:Ce^{3+}$ NSC and PPIX PS into a PEG-PLGA nanosphere as a nanotheranostic cancer agent. This radioPDT NP was designed to be highly biocompatible with good biodistribution and toxicity characteristics, while delivering high anti-tumoral effect when activated. Furthermore, the use of high Z compounds in the design allow it to be reliably detected and tracked *in vivo* by CT, and aid in IGRT. The radioPDT NP showed reliable synthesis and scalability of production, high stability characteristics in storage and biological conditions, negligible *in vitro* and *in vivo* toxicity profile, and good biodistribution characteristics. When activated with radiotherapy, the radioPDT NPs were able to significantly increase the anti-cancer cytotoxic yield in normoxic and various hypoxic *in vitro* conditions, which correlated with increased singlet oxygen yield from radioPDT effect. *In vivo,* the radioPDT NP was able

to be used in combination with IGRT to induce significant tumor regressions and disease control in NSG mice flank tumor models xenografted with PC3 human prostate cancer. This resulted in no detectable active disease in the treated tumor and significantly prolonged median survival of mice over radiotherapy alone. Finally, the radioPDT NP's utility as a diagnostic agent was demonstrated via serial CT scans of PC3 xenograft mice models, in which the distribution of the NP over time was tracked over time based on CT enhancement and correlated with post-mortem mass spectrometry measurements in the tumor and normal organs. The diagnostic qualities of the radioPDT NP also aided in tumor identification for radiation targeting and planning techniques in the delivery of IGRT.

In summary, this thesis demonstrates the characteristics, safety and anti-tumor efficacy of a novel theranostic radioPDT NP in prostate cancer models. The significantly better efficacy, with negligible additional toxicity over radiotherapy alone can allow the field of radiation oncology to pursue further dose escalation strategies, better treat radioresistant tumors, better target disease with IGRT, and lower the need for high doses of ionizing radiation and the concomitant normal tissue toxicity it confers. This can provide a new paradigm of advancement in radiation oncology to continue to pursue higher cure rates with less side effects in localized disease and continue to redefine the role of radiotherapy in therapy-resistant and metastatic disease.

CHAPTER – 2

SYNTHESIS, CHARACTERIZATION, AND BIOCOMPATABILITY OF PEG-PLGA NANOSPEHERES LOADED WITH NANOSCINTILLATORS AND PHOTOSENSITIZERS FOR RADIATION-ACTIVATED PHOTODYNAMIC THERAPY (RadioPDT)

CONTRIBUTIONS

The research I present here required a multidisciplinary team approach. I conceived the nanoparticle paradigm of the project, designed and performed the experiments that led to all the data presented, unless otherwise stated, and contributed significantly in writing the majority of the manuscript for publication as described in the **Preface**. Dr. Jayeeta Sengupta contributed by optimizing the drug delivery system, and performed the experiments that led to the data presented in Table 2.2, Figure 2.8, 2.9, 2.10, 2.11, 2.14, 2.15, 2.16, 2.17, 2.18, 2.19ii, and contributed significantly in writing of the manuscript. Dr. Desmond Pink and Dr. Arun Raturi provided analysis and interpretation. Dr. Hua Chen assisted in data collection. Dr. Xuejun Sun assisted in TEM analysis. Douglas Brown assisted in the animal studies. Dr. Piyush Kumar assisted in the design and interpretation of experiments. Dr. Nawaid Usmani participated in project conception. Dr. Ronald Moore, Dr. John D. Lewis and Dr. Ravin Narain assisted in conception, design, interpretation of data, and supervision of the project. Dr. Ronald Moore assisted in conception and is the primary supervisor of the project. Patent protection is filed for the drug design and purpose (patent# WO/2019/241891).

2.1 Introduction

Advancement in the field of nanotechnology has opened new approaches for cancer therapy. Nanomedicines show great promise in terms of multi-functionality, targeted delivery, improved release profile, pharmacodynamics, and mitigated toxicity (211). "Nanotheranostics" combines therapy and diagnosis into a single nanoparticle platform. It has the potential to treat and diagnose cancer disease simultaneously at the macroscopic, cellular and molecular levels (215, 216).

The unmet promises of nanomedicine in the last 10+ years highlight the challenges in establishing a new paradigm to supersede current standard of care, even with initially promising results (245). The difficulty lies in balancing drug delivery, toxicity, efficacy, and practicality. To successfully deliver on the promise of a new paradigm, a NP should ideally demonstrate superiority in all aspects of cancer therapy (246).

Nanoparticles have also been applied to creating a radioPDT system, where a process was developed using scintillating luminescent NPs in combination with the photosensitizer (94). The NSC utilizes X-ray irradiation to produce a local light source for activating the photosensitizer that enables the production of $^1O_2$. This method of locally generating light for PDT eliminates the limitations of an external light source for activation, and may augment the effectiveness of radiotherapy (94). Many studies have since built around this concept. In 2014 Zou *et al.* reported a nanocomposite system of Ce^{3+} doped lanthanum (III) fluoride (LaF_3:Ce^{3+}) and the photosensitizer PPIX that can be activated by X-rays to induce oxidative stress, mitochondrial damage, and DNA fragmentation in cancer cells to kill them (93). As further evidence of the concept, these scintillating nanoparticles have been used as an in-situ light source for photodynamic activation in prostate cancer cells *in vitro* (93).

Further, there are reports of using CeF_3 NPs conjugated with the photosensitizer verteporfin and quantifying $^1O_2$ yield that demonstrated cancer cell-kill upon irradiation with X-rays (193). Proof of concept *in vivo* studies have also shown promise for therapeutic efficacy in mouse solid tumor models (21).

The concept of using scintillating NSCs to activate a photosensitizer by X-ray excitation therefore has the potential to provide an effective and less toxic system to treat deep-seated tumors, such as prostate cancer. The low α/β ratio radiobiology of prostate cancer lends itself to high doses and dose rates, but clinically the irradiation of the prostate must be balanced with the radiation damage incurred on the rectum, bladder, and urethra. Previous clinical trials have demonstrated radiation dose escalation confers higher levels of local tumor control, but at the cost of higher toxicities (247). The main reason for this is that it is still challenging to deliver increased doses to the prostate without toxicity occuring to surrounding organs, despite advanced precision radiotherapy techniques. One of the important limitations of the NPs currently presented in the literature are their biocompatibility problems and feasibility in using them as clinical agents. These are important limitations that need to be addressed before radioPDT can be advanced further in medical therapy. Herein, I report the synthesis and full characterization of a highly biocompatible radioPDT capable theranostic NP using poly(ethylene glycol) methyl ether-*block*-poly(lactide-*co*-glycolide) (PEG-PLGA) nanospheres with $LaF_3:Ce^{3+}$ nanoscintillators (NSC) and PPIX photosensitizer for radioPDT of prostate cancer and other deep-seated tumors.

2.2 Materials and Methods

2.2.1 Poly(ethylene glycol) methyl ether-block-poly(lactide-co-glycolide) Nanospheres Loaded with Nanoscintillators and PPIX - Preparation, Encapsulation, & Characterization

2.2.1.1 Nanoscintillator Synthesis

The NSC were synthesized using the following protocol: the reagents lanthanum(III) nitrate hydrate ($La[NO_3]_3 \cdot xH_2O$, 99.9%), cerium(III) nitrate hexahydrate ($Ce[NO_3]_3 \cdot 6H_2O$, 99.9%), ammonium fluoride (NH_4F, 99.9%), were purchased from Sigma-Aldrich (MO, USA). All the commercially available reagents were used as is, without any further purification. Standard wet chemistry methods, with some modifications were followed to synthesize the nanoscintillators (94). Cerium was doped at 10% due to the expected optimal scintillation profile (248). 4.5 mmol $La(NO_3)_3$ and 0.5 mmol $Ce(NO_3)_3$ in dry powder form was dissolved in 21 mL ultrapure Milli-Q water and was stirred thoroughly at room temperature (21 °C) for 30 minutes until fully dissolved. This solution was then heated with constant stirring over an oil bath maintained at 100 ºC. Atmospheric oxygen was flushed from the flask using compressed pure nitrogen gas for 15 minutes under 5 psi of positive pressure, and then the reaction flask was sealed. This prevents the formation of undesired lanthanide oxides instead of the desired lanthanide fluoride products. Another solution of 15 mmol NH_4F dry powder dissolved in 5 mL Milli-Q water was prepared similarly with stirring at room temperature for 30 minutes. The NH_4F solution was added dropwise using a 3-neck flask under nitrogen protection, while maintaining 100ºC and vigorously stirred. The solution immediately appeared cloudy and

a colloidal suspension was formed. Once the addition was complete, the reaction mixture was stirred under 100ºC and nitrogen protection for another 2 hours. The resultant translucent suspension was centrifuged at 100,000 g for 15 minutes, at which point a translucent pellet was formed. The supernatant was decanted, the pellet resuspended in Milli-Q water, and sonicated for 15 minutes. The centrifugation and resuspension process were repeated twice more for a total of three washes. This removed any excess reagents from the final suspension of NSC. The suspension was stored in water at 21ºC in a stock concentration of 30 mg/mL.

An alternate synthesis method was followed to alter the crystal lattice structure of the synthesized NSC. The reaction process differed from the one listed above in the use of anhydrous methanol as the reaction medium, a reaction temperature of 70ºC, different compounds of lanthanides and fluorides, and adding the lanthanides to an excess of fluoride solution. The solution was also scaled up with proportional amounts of media and reagents used. The reagents for the alternate synthesis method are lanthanum(III) chloride ($LaCl_3$, 99.9%), cerium(III) chloride ($CeCl_3 \cdot 6H_2O$, 99.9%), and ammonium fluoride (NH_4F, 99.9%), were purchased from Sigma-Aldrich (MO, USA). The synthesis was done as follows: 45 mmol $LaCl_3$ and 5 mmol $CeCl_3$ in dry powder form was dissolved in 24 mL anhydrous methanol and was stirred thoroughly at room temperature (21°C) for 30 minutes until fully dissolved. Another solution of 100 mmol NH_4F dry powder dissolved in 180 mL anhydrous methanol was prepared similarly with stirring at room temperature for 30 minutes. The NH_4F solution was then heated with constant stirring over an oil bath maintained at 70ºC in a three-neck flask. Atmospheric oxygen was flushed from the flask using continuous flow pure nitrogen gas under 5 psi of positive pressure from a Schlenk

line, with the exhaust flowed through a reflux column cooled by tap water and vented through a water trap (**Figure 2.1**). This step prevented the formation of undesired lanthanide oxides instead of the lanthanide fluoride products and prevents a potential explosion hazard with the compressed methanol vapor. The lanthanide solution was added dropwise using a 3-neck flask under nitrogen protection, while maintaining 70º C and vigorously stirred. The solution immediately appeared cloudy and a colloidal suspension was formed. Once the addition was complete, the reaction mixture was stirred under 70º C and nitrogen protection for another 2 hours. The resultant translucent suspension was centrifuged at 100,000 g for 15 minutes, at which point a translucent pellet was formed. The supernatant was decanted, the pellet resuspended in Milli-Q water, and sonicated for 15 minutes. The centrifugation and resuspension process were repeated twice more for a total of three washes and stored in a concentration of 30 mg/mL at room temperature. Each batch underwent quality assurance by Transmission Electron Microscopy (TEM) analysis and UV-Vis characterization. Certain batches were also submitted for X-ray diffraction (XRD) analysis for crystal structure.

Figure 2.1 Synthesis setup for anhydrously synthesized $LaF_3:Ce^{3+}$ NSC.

2.2.1.2 Lab-Scale Production of NPs using Nanoprecipitation Method

For making PEG-PLGA encapsulated NSC and PPIX variants, a nanoprecipitation method was used for the formation of the particles (249). PPIX and Poly(ethylene glycol) methyl ether-block-poly(lactide-co-glycolide) (PEG-PLGA, average M_n 5,000 for PEG and M_n 7,000 for PLGA) were purchased from Sigma Aldrich (US).

Initial NP synthesis attempts used a double emulsion technique similar to Zou *et al.* (2014) with modification (93). Dichloromethane (DCM) was substituted for Dimethyl sulfoxide (DMSO) as the organic phase solvent to allow better suspension of PEG-PLGA. Synthesis consisted of 10 mg PEG-PLGA suspended in 1 mL DCM and bath sonication for 15 minutes, followed by the addition of 0.1 mL Milli-Q water with 2% polyvinyl alcohol (average molecular weight of 31,000) and bath sonication for 15 minutes to form an organic/aqueous emulsion. The solution was added dropwise to 20 mL Milli-Q water stirring vigorously at a rate of approximately 1 mL per minute with a syringe and 18-gauge unfiltered needle. This produced unfavourable aggregation and high polydispersity (see results) even with the omission of polyvinyl alcohol. PPIX was added to the organic phase and NSC was added to the aqueous phase for the organic/aqueous emulsion process in an attempt to encapsulate the NSC and PS into the PEG-PLGA (see **Section 2.3.1**). The final iteration of the NP synthesis technique used acetonitrile as the organic solvent since it stably suspended NSC, PEG-PLGA and PPIX, and the synthesis method was changed to a single emulsion nanoprecipitation process as detailed below.

Protoporphyrin IX (1 mg per 1 mL acetonitrile), NSC ($LaF_3:Ce^{3+}$, 1.5 mg per 1 mL acetonitrile) and PEG-PLGA (10 mg per 1 mL acetonitrile) were dissolved in 1 mL of acetonitrile in the synthesis of radioPDT NP. Three alternate NP conditions were also

synthesized as control: PEG-PLGA NP consisting of only PEG-PLGA suspended in acetonitrile to form empty nanospheres, NSC NP consisting of PEG-PLGA and NSC suspended in acetonitrile to form NSC loaded nanospheres, and PPIX NP consisting of PEG-PLGA and PPIX suspended in acetonitrile to form PPIX loaded nanospheres. The acetonitrile/polymer/drug solution was incubated at room temperature on a Belly Dancer Shaker® (IBI Scientific, Dubuque, USA) at its highest speed setting for 1 hour in the dark. Next, the NSC-drug-polymer organic mixture was added dropwise at a rate of approximately 1 mL per minute with a syringe and 18-gauge unfiltered needle under dark conditions to 20 mL Milli-Q water being stirred vigorously. The ratio of solvent to water was 1:20. The solution was left in an open container in a fume hood for 8 hours at 21 ºC with continuous stirring. The formed NP solution was collected, and the excess organic solvent was removed by vacuum evaporation using a rotovap system under 140 mmHg vacuum pressure and 40 ºC water bath for 30 minutes. The NPs were then washed by centrifugation (50,000 g) for 15 minutes at 21 °C three times, where the supernatant was removed, and the pellet was re-suspended in Milli-Q water.

Quality assurance was performed on every synthesized batch via UV-Vis measurements looking for signatures of PEG-PLGA, NSC, and PPIX after the wash procedures and dynamic light scattering (DLS) analysis by Nanosight® LM10-HS NTA system (Nanosight Ltd., UK) was performed to characterize NP diameter, concentration of the raw synthesis product, and the supernatant solution from each wash step. Additionally, sample batches were verified by TEM.

2.2.1.3 Scaled-up Production of the Nanoprecipitation Method

Using the optimized nanoprecipitation method and varying the ratio and amount of the compounds, nanoprecipitation was scaled up. This method has been previously well characterized and optimized by others (249). Both 15 mg of NSC stock solution (30 mg/mL LaF_3:Ce^{3+} in water) and 2.5 mg protoporphyrin IX (from a stock solution of 5 mg/mL in acetonitrile) was dissolved along with PEG-PLGA (100 mg dissolved in 10 mL acetonitrile) and incubated for 1 hour in the dark. Then the NSC-drug-polymer organic mixture was added dropwise to 100 mL Milli-Q water, under moderate stirring, using a peristaltic pump at a rate of 1 mL per minute. The ratio of solvent to water was 1:20. The solution was left under continuous stirring condition for 8 hours at 21°C. The excess organic solvent was removed by vacuum evaporation, followed by washing the NPs by centrifugation (50,000 g) for 15 minutes at 21 °C for 3 times and re-suspending in Milli-Q distilled water.

A further scaled up procedure of 200 mg PEG-PLGA, 30 mg NSC (freeze dried solid), and 5 mg PPIX dissolved in 20 mL acetonitrile was used for synthesis for *in vivo* experiments.

2.2.1.4 Tangential Flow Filtration (TFF) and Particle Recovery

For large volume synthesis of NPs, Tangential Flow Filtration (TFF) was used for particle purification and recovery. The nanoparticle suspension was purified at 1.0 bar Transmembrane Pressure (TMP) on a TFF system (ÄKTA flux tangential flow filtration system, General Electric Healthcare, USA). The NP suspension was circulated through the TFF system using a pump back to a reservoir until it concentrated to a volume of 50 mL and then followed by additional washes by adding Milli-Q water into the reservoir to allow

efficient removal of free PPIX and free NSC. The process of purification started with 50mL of the NP suspension diluted 10 times to 500 mL by adding Milli-Q water. The filtrate was collected and again pumped back to the system for the second wash by diluting the particles with Milli-Q water. A final volume of 50 mL was collected at the end of the last run. During the whole purification process by TFF, the initial and final NP suspensions were collected to measure particle recovery before and after wash by TFF. The particle recovery was determined using Nanosight NTA (Nanosight Ltd., UK).

2.2.1.5 Dynamic Light Scattering (DLS) Analysis and Zeta-Potential

Immediately before use, the radioPDT NPs were dissolved in water to measure the diameter, size distribution and zeta potential by dynamic light scattering (DLS) using Brookhaven Zetasizer (Brookhaven, US). To attain the recommended attenuator settings of 7-9, the NPs were diluted for the DLS measurement.

The size, concentration and distribution of the NPs were also determined using a Nanosight LM10-HS NTA system (Nanosight Ltd., UK).

2.2.1.6 Encapsulation Efficacy

NPs were dispersed in water, and the unbound drug was removed via centrifugation. UV-Vis absorbance Using Nanodrop^{TM} 2000 (ThermoFisher, US) spectrophotometer was used for measuring the entrapment efficiency of the unbound drug in the supernatant. To calculate the entrapment efficiency of the PPIX dye in the NPs, the amount of dye in the supernatant after each step of centrifugation during the synthesis of the NPs was quantified. A standard curve was plotted using standard concentrations of dye dissolved in acetonitrile.

The spectrophotometric quantification was done by measuring the absorbance at 407 nm. The percentage of encapsulated dye was calculated using:

%Entrapment = [1- (free dye concentration/ Initial dye concentration)] x 100

2.2.1.7 Transmission Electron Microscopy

From the NP sample,10 µL was added on a 300-mesh copper grid coated with carbon and were allowed to adhere for 1 minute. The excess sample was removed and a drop of 1% (w/v) uranyl acetate was placed on the grids to negative stain the NPs. The excess negative stain was removed, and the grids air-dried. The morphology and the elemental mapping (Oxygen, Nitrogen, and Lanthanum) of the NPs was observed with a transmission electron microscope (TEM) JEM-2100 HRTEM (JEOL, Japan) under an operating voltage of 200 kV, using Gatan GIF Tridium energy imaging filter and tomography in bright field mode.

2.2.1.8 UV-Vis Spectroscopy

The UV-Vis absorbance spectra of the radioPDT NPs was used to characterize the absorbance spectra of the radioPDT NP for the purposes of measuring drug loading. This was measured using a Nanodrop ^{TM} 2000 (ThermoFisher, US) spectrophotometer. For this, the NPs were dissolved in water and 1 µL of solution was placed on the stage. Measurements were taken at an excitation wavelength (λ_{ex}) of 407 nm.

2.2.1.9 Size Exclusion Chromatography

Verification of drug loading into the PEG-PLGA NP was done using Size Exclusion Chromatography. Seperating the synthesized NP suspension by size can very the UV-Vis

absorbance signal actually reflects drug that is associated with the NP rather than in free solution. The synthesized radioPDT NP were concentrated to a concentration of $1x10^7$ particles/mL via measurement of stock concentration by Nanosight NTA, centrifugation at 50,000 g followed by resuspension in water of the appropriate volume to achieve desired concentrations. The final NP concentration was once again checked by Nanosight and the UV-Vis spectra was compared to stock NP. A gel column was setup using a 10 mL syringe with a small amount of cotton inserted into the tip, and filled with 10 g of Sephadex G-15 (GE Life Sciences, Pittsburgh, USA) obtained from Sigma-Aldrich. The Sephadex gel was setup in a column by adding the 10 g of powder and adding up to 50 mL of Milli-Q water added dropwise. The radioPDT NP suspension was added carefully on top of the gel so as to not disturb the boundary layer. 1-2 mL of MilliQ water was carefully added dropwise to the top of the column and the solution was allowed to run through the gel by gravity. The eluate was collected at the bottom in 0.5 mL aliquots at a time.

The eluate was measured for UV-Vis signal on a Nanodrop 2000, specifically for absorbance at 220 nm and 400 nm to correspond to the aborbance signature of NSC and PPIX, respectively. The secondary absorbance peak of 220 nm for NSC was used instead of the primary peak at 195 nm to avoid signal interference from the Sephadex gel.

2.2.1.10 Fluorescence Emission Spectroscopy

Fluorescence spectroscopy to assess for Fluorescence Resonant Energy Transfer (FRET) was performed using a Perkin-Elmer LS-55 spectrofluorometer (Freemont, CA, US). Measurements were done at a 1 nm spectral resolution for emission. Slit width and gain were calibrated on a set of NPs standardized by UV-Vis absorbance and with a

concentration of 5×10^9 particles/mL before acquisition. An excitation wavelength of 205 nm was used to correspond with excitation peak of NSC, and far outside the range of PPIX. Emission scan was done from 400-800 nm to correspond with the emission wavelength ranges of PPIX, and outside the range of NSC emission. RadioPDT NPs emission spectra under these conditions was compared to PPIX only and NSC NP only.

2.2.1.11 X-ray Diffraction Analysis

X-ray diffraction (XRD) study to characterize the NSC crystal structure was carried out by the University of Alberta Faculty of Environmental Earth Sciences Laboratory (Edmonton, AB, Canada). The stock solution of NSC was lyophilized to powder form. Using a Rigaku Geigerflex Powder X-ray diffractometer (Rigaku, Japan), the powder sample was irradiated, and X-ray diffraction angles were measured before being analysed on JADE 9.1 software (Materials Data, Livermore, CA, USA) using International Center for Diffraction Data and Inorganic Crystal Structure databases.

2.2.1.12 NSC Scintillation Photoluminescence Emission

To capture the Photoluminescence (PL) spectra of the NSC under X-ray irradiation, an Ocean optics USB 4000 spectrometer (Largo, FL, USA) with a 10 µm slit width, 600-line grating, and 200 nm to 850 nm detection range was used. This was coupled with a Thorlabs (Newton, NJ, USA) 30 m long custom 600 µm multimode fibre compatible with UV-NIR range wavelengths. A custom opaque phantom was created with phantom-grade acrylic block, a white plastic cuvette holder that was machined by the Cross Cancer Institute (Edmonton, AB, Canada) machine shop (**Figure 2.2a**). Radiation delivery was done at the

Cross Cancer Institute using a clinical orthovoltage irradiator (Xstrahl, Camberley, Surrey, UK) at 300 KVp energy at a dose rate of 300 Monitor Units (MU) per minute using a 30 cm focus-to-skin distance (FSD) applicator and dose was calculated for appropriate stand-off distance, backscatter, and depth penetration (**Figure 2.2d**). The fiber optic cable was run from the radiation control panel through a conduit into the radiation vault and into the cuvette holding NSC freeze-dried powder or in concentrations ranging from 30 mg/mL to 400 mg/mL. The experiment was repeated with an Ocean optics QEPro high performance spectrometer provided as a demo by the company. All spectroscopy data was collected as the average of 10 second capture windows with 10 repeats. Analysis was done by first taking the average baseline measurement spectra and subtracting it from the spectra during irradiation using Matlab generated spectral analysis code (Mathworks, Natick, USA).

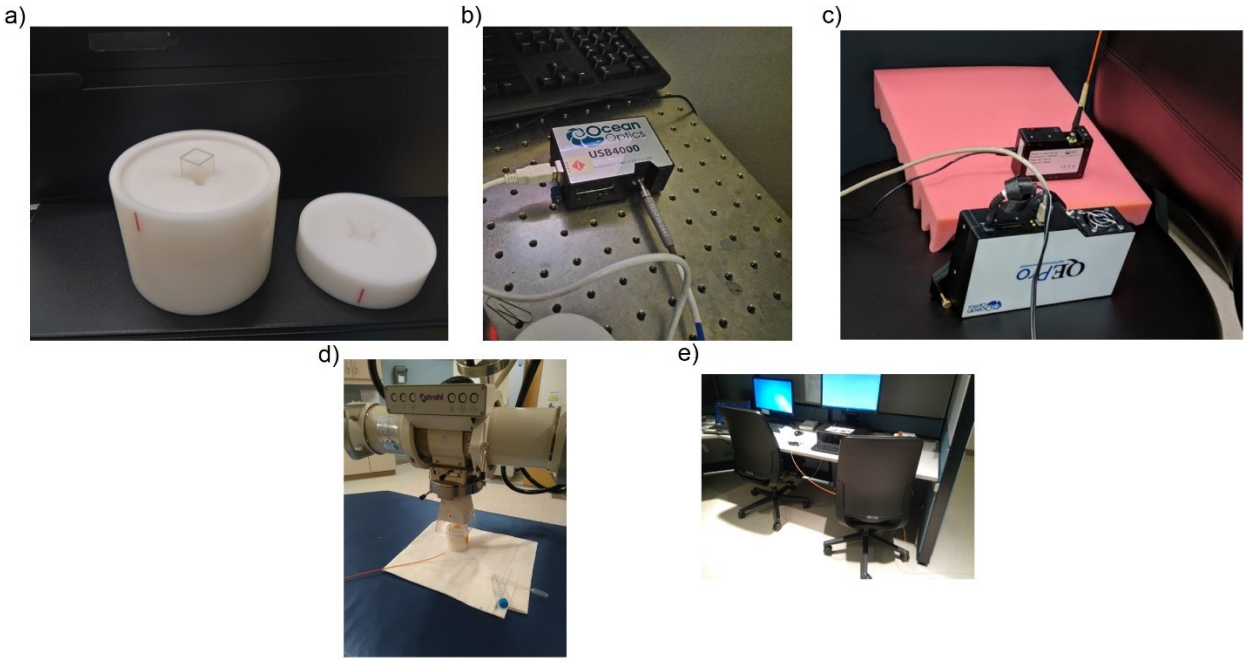

Figure 2.2: Experimental setup of the scintillation measurement experiment. The phantom used to contain the sample measured is shown in (**a**). The Ocean optics USB 4000 (**b**) and

QEPro (**c**) spectrometers were located outside the radiation vault near the control panel (**e**). The phantom setup under the irradiator is shown in (**d**) with the orange line being the multimode fiber optic cable going to the spectrometer via a conduit.

2.2.2 Stability study of PEG-PLGA NP, NSC NP, and radioPDT NP in different media

A stock solution of each NP variant (PEG-PLGA NP, NSC NP, radioPDT NP) was synthesized as described in Experimental **Section 2.2.1**. Next, NPs were added to 50% (v/v) of Milli-Q water and PBS (pH 7.4) and the solution was divided into two sets. One set was kept at 21 °C and the other set was kept at physiologic 37 °C for 48 hours. The particles were measured for size using DLS at different time points. Similarly, NPs were added to 50% (v/v) of 10% FBS supplemented DMEM, serum and plasma for 24 hours. For calculation of PPIX release, an aliquot of the NPs was collected at pre-determined time points and measured by UV-Vis (Nanodrop 2000, ThermoFisher Inc, USA) and Nanosight (NanoSight LM10 NTA, AZoNano, Manchester, UK) to determine the amount of released PPIX and NP size. NPs were centrifuged at 35,000 g for 15 mins at 25 °C and the supernatant was collected and analyzed with a spectrophotometer at an absorbance wavelength of 400 nm to calculate the released PPIX percentage.

2.2.2.1 Stability of NP Solution

The NPs were suspended in Milli-Q water to form a stock solution and stored at 4 °C for up to 6 weeks. Every week the NP size distribution was calculated using DLS. In order to determine the amount of released PPIX, the NPs were centrifuged for 15 mins and the supernatant was analyzed in UV-Vis spectrophotometer to determine the amount of released PPIX.

2.2.3 Cellular Uptake of NP

2.2.3.1 Cell Culture

PC3 cells were grown in Dulbecco's modified Eagle's Medium (ThermoFisher Scientific, Logan, USA) supplemented with 10% FBS and 1% antibiotics. Cultures were incubated at 37°C and 5% CO_2 environment. The cells were passaged regularly after reaching 80% confluence.

2.2.3.2 Cellular Uptake

For studying the cellular uptake of the NPs, radioPDT NP were tagged with TT1 phthalocyanine fluorescent dye (obtained from Dr. Tomas Torres, Department of Organic Chemistry, Universidad Autonoma de Madrid, Spain) by incorporating it into the organic phase of the nanoprecipitation procedure. This was done because previous attempts using only the PPIX as a fluorescence agent failed to produce appreciable results due to the low quantum yield of fluorescence for PPIX (250). TT1 allowed the NPs to be seen under confocal fluorescent microscopy for the cellular uptake study. The cultured PC3 cells (80% confluent) were trypsinized with 0.25% trypsin with EDTA and then re-plated in 6 well tissue culture plates (15×10^3 cells/well) covered with a coverslip. After the cells adhered to the coverslip, the cell media was removed. The NP treatments consisted of each well receiving $1x10^8$ NP/well of empty PEG PLGA NP, NSC NP, radioPDT NP and radioPDT+TT1 dye NP or control. The NPs were added along with media and incubated for 24 hours at standard conditions. Simultaneously, an untreated group of cells were also exposed to similar conditions as a control group. After 24 hours, the media was removed and rinsed twice with PBS. A staining stock solution was prepared beforehand using 5 mL

PBS, 40 µL of Wheat Germ agglutinin (WGA) at a concentration of 5 µg/mL and 1.6 µL of Hoechst 33342 nuclear stain (Sigma Aldrich, St. Louis, MO, USA), at a concentration of 2 µg/mL. 400 µL of the staining stock solution was then added and the contents incubated for 10 minutes, after which, the cells were fixed using 4% paraformaldehyde and 10% sucrose in PBS for 15 minutes. The solution was aspirated and the attached cells washed twice with PBS. The coverslips were mounted face down on slides using ProLong Gold (Invitrogen, ThermoFisher Scientific, Waltham, MA, US) mounting media and then sealed with a coverslip to the slides for 24 hours before being imaged. Imaging was performed by Spinning disc Confocal microscope (Carl Zeiss, US) fixed with an upright epifluorescence microscope (647 nm solid state laser excitation, emission filter of HQ700/50m – bandpass filter centered at 700 nm with a 50 nm bandwidth) with a motorized Z stage controlled by Velocity software (Improvision, US). A series of images were obtained by capturing 3D image stacks from top to bottom of the cell of interest.

2.2.4 Cellular Toxicity Assay

Toxicity study was performed using the radioPDT NP and its control variants of empty PEG-PLGA NP, NSC NP, PPIX, and NSC-only. The loaded drug concentration in the NP was standardized using UV-Vis absorbance. Dosing was done at a highest dose of 1×10^{12} NP/mL and serial dilutions by 50% dilutions down to 6.25×10^{10} NPs/mL. PC3, DU145 and GM38 cells grown to 80% confluency in DMEM media with 10% FBS were plated at 10,000 cells per well in a 96 well plate and left to adhere overnight. The cells were then exposed to the nanoparticles for 48 hours before the media was exchanged. After 48 hours, MTT colorimetric endpoint assay was performed by measuring optical density at 520 nm

against control conditions using a FLUOstar Omega microplate reader (BMG Labtech, Germany). Cell viability was calculated as a percentage ratio of optical density of treated conditions to control untreated cells subtracted from empty well optical density. All experimental conditions were analyzed in triplicates.

2.2.5 *In vivo* Acute Toxicity Study

Serial dose escalation of radioPDT NP in mice was performed using C57bl/6 immunocompetent black mice after institutional ethics approval (AUP0000053). The mice were aged 6 to 8 weeks and housed as per institutional protocol at the University of Alberta for immunocompetent rodents. The radioPDT NP was concentrated via ultracentrifugation at 100,000 g for 30 minutes and resuspended in PBS. A 100 μL bolus was drawn into a 24-gauge single use injection syringe. A mouse restraint apparatus was used to secure the animal, as the dose was injected via the tail vein. The animal was then monitored every 12 hours via a scoring sheet for changes in behaviour such as decreased activity, degree of socialization with littermates, pain, unkempt fur, or mottling of the skin. Additionally, the animal's weight was taken pre-injection, 24 hours post injection, and 48 hours post-injection. Each dose was tested on a minimum of 2 mice. If no toxicity was observed, the dose was doubled for the next group. If mild toxicity was observed, the dose was increased by 50%. If significant toxicity was observed, the dose was decreased by 25%. The dose escalation study continued until major toxicity was encountered, or the experiment was unfeasible to continue.

The mice were euthanized after 48 hours via cervical dislocation under inhaled isoflurane anesthetic. Post-mortem analysis was carried out with gross pathologic analysis of the

internal organs. Following this, the lungs, heart, liver, spleen, and kidneys were harvested for histopathologic analysis via paraffin embedding, sectioning, mounting on standard glass slides, and staining with hematoxylin and eosin by the University of Alberta HistoCore facility (Edmonton, AB, Canada). The slides were further analysed using a Nikon two-photon confocal microscope with an excitation laser of 405 nm and emission filter of 646 nm. Images were captured using a Hamamatsu 512x512 EMCCD camera (Hamamatsu Inc., Japan) and a 20x Zeiss microscopy objective was used for image acquisition.

2.2.6 Data Analysis

All calculations and statistical analysis were performed using Microsoft Excel 2016 (Microsoft, U.S). The graphs were plotted using Python software foundation version 3.6.2 and GraphPad Prism 6 (San Diego, CA, USA). Statistical significance for comparison of NP size, and comparison of standardized mice weight was done with analysis of variance (ANOVA) comparing multiple groups and Tukey's multiple comparison test.

2.3 Results and Discussion

2.3.1 PEG-PLGA-loaded $LaF_3:Ce^{3+}$ nanoscintillators and PPIX nanospheres: Synthesis, encapsulation & characterization.

To induce effective radioPDT, an efficient and stable nanoscintillator (NSC) is necessary to produce the interstitial light from X-rays. For this purpose, $LaF_3:Ce^{3+}$ NSC were prepared using a modified wet chemistry technique in aqueous media (248, 251). Cerium (III) was doped at 10%.

The resulting nanocrystals were determined to be between 10-50 nm in size as determined by transmission electron microscopy (TEM) (**Figure 2.3a-b**). UV-Visible and fluorescence spectroscopy demonstrated the absorbance with a peak of 195nm with several minor peaks of 205 nm, 214 nm, 234 nm and 247 nm, which are in line with previously reported values (**Figure 2.3c**) (252, 253). The fluorescence characteristics of the NSC were also observed, with the peak at 305 nm with a significant luminescence extending to just under 450 nm (**Figure 2.3d**). This appears to have reasonable overlap with the PPIX absorption spectrum, reported at 350 nm to 450 nm (254), which indicates the potential for fluorescent resonant energy transfer (FRET) from NSC to PPIX. The crystals demonstrate a size of 10 to 50nm, and morphology consistent with a hexagonal crystal structure (**Figure 2.4**). Some aggregation develops during sample dehydration, but the samples were well dispersed in aqueous media. Fluorescence signal of the NSC correspond to literature values of the compound (255, 256).

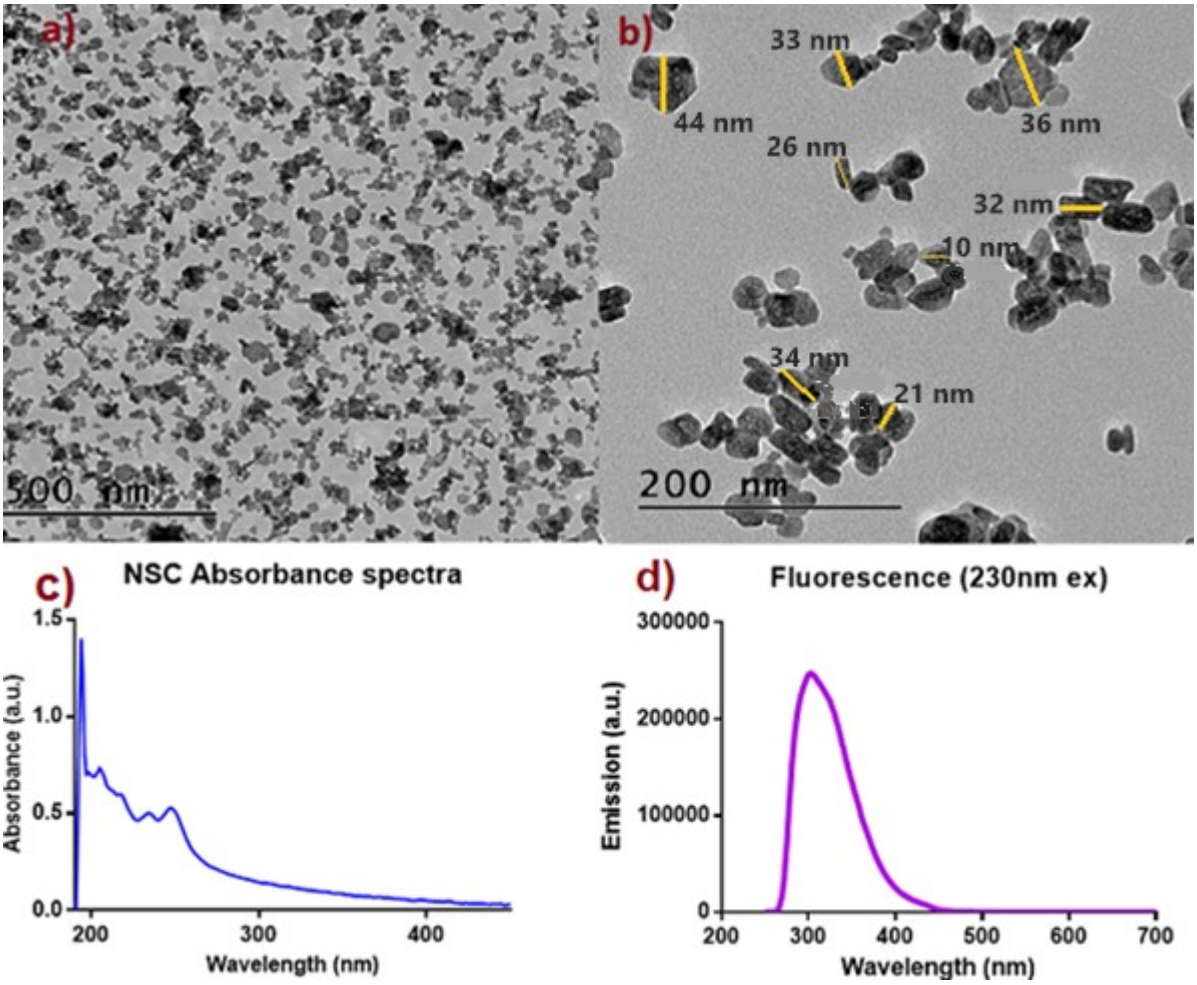

Figure 2.3. a) 10% Ce-doped LaF_3 NSC crystals imaged with TEM. **b)** Close-up view of the NSC with sample length and width size measurements are shown. **c)** UV-Vis absorbance and **d)** Fluorescence signal of the nanoscintillators is shown, with peak at 310 nm and significant fluorescence intensity until just under 450 nm.

X-ray diffraction (XRD) study on the nanoscintillators (NSC) was carried out by the University of Alberta Faculty of Environmental Earth Sciences (Edmonton, AB, Canada). The stock solution of nanoscintillators was lyophilized to powder form. Using a Rigaku Geigerflex Powder diffractometer (Japan), the powder sample was irradiated, and X-ray diffraction angles were measured before being analysed on JADE 9.1 software (Materials Data, US) using ICDD and ICSD databases. Results of the analysis are shown in **Figure 2.4**.

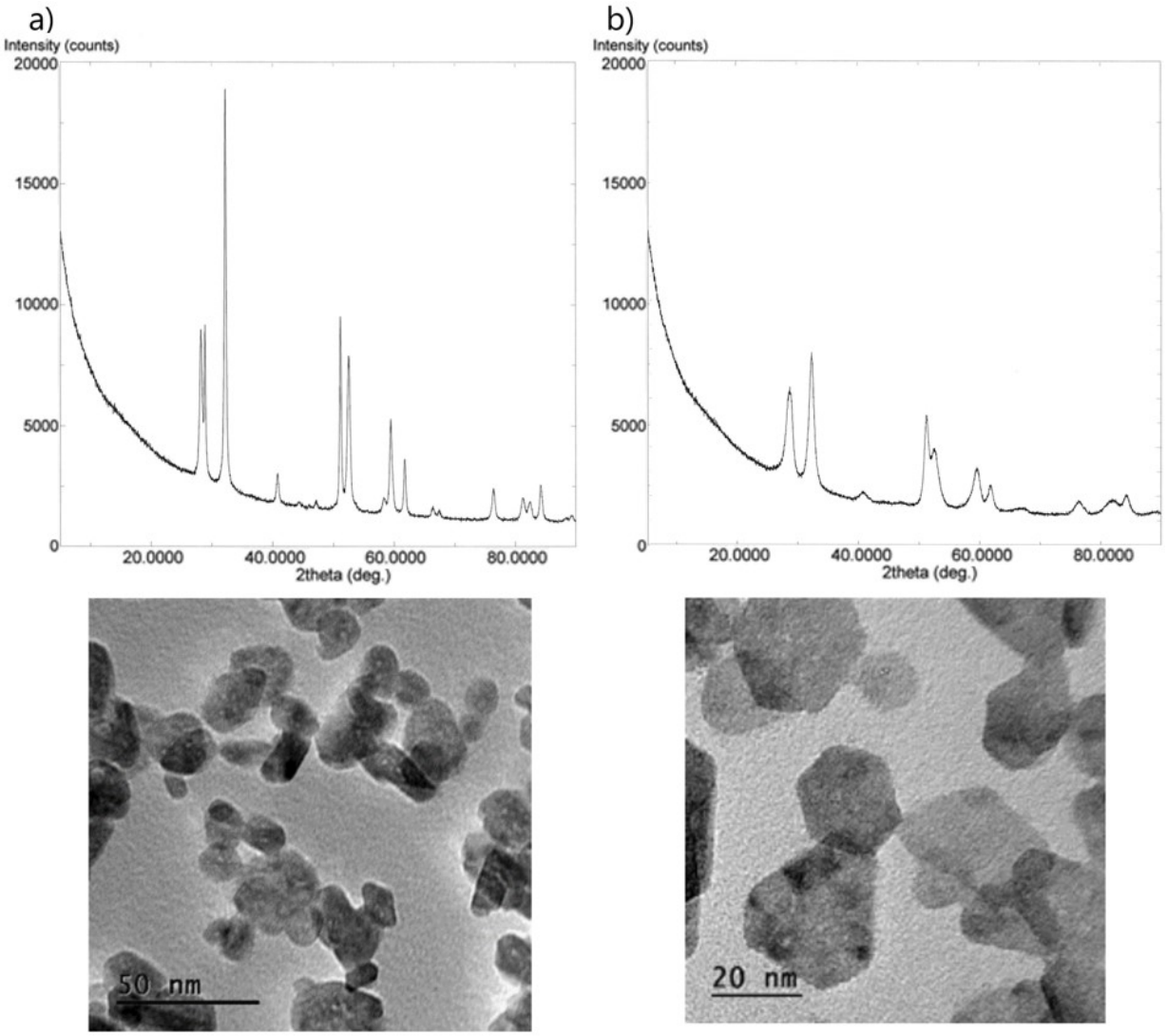

Figure 2.4 Top: X-ray diffraction (XRD) spectra of 10% Ce^{3+} doped LaF_3 synthesized under aqueous conditions **(a)** and anhydrous conditions **(b)**. The peak positions correspond well to database values of hexagonal crystal structure for LaF_3 based compounds. **Bottom**: corresponding TEM images demonstrating the crystal morphology is shown.

The produced crystal structure was verified to be pure crystalline form with a uniform crystal structure in long hexagonal form, as denoted by the sharp peaks (**Figure 2.4a**). The attained results also closely resemble literature published crystal structure analysis (251). The second iteration of the NSC synthesized under anhydrous conditions with methanol produced a slightly different crystal structure, as demonstrated by the different peak intensities on XRD and different NSC morphology on TEM (**Figure 2.4b)**. The crystal structure appeared to align with reference values of a short hexagonal crystal. **Table 2.1** compares the dimensional values between the two crystal structures. The different crystal structures also performed differently for absorbance and fluorescence spectra (**Figure 2.5**), with the short hexagonal structure showing a shift towards 400 nm emission wavelength with a higher relative fluorescence peak. This is more ideal for FRET transfer to PPIX, given its 403 nm excitation peak. The improvement in fluorescence performance is speculated to be due to the well known effects a crystal lattice structure plays and NSC size (note the larger volume for the short hexagonal NSC in **Table 2.1**) on the fluorescence performance of heavy metal fluorides (257). These changes in fluorescence are not always easy to predict prospectively given the complex interplay between the La and Ce content, and the lattice structure.

Table 2.1 Comparison of crystal structure physical characteristics between aqueous and organic phase synthesized $LaF_3:Ce^{3+}$ NSC.

	Dimensions (Å)			Angle (°)			Volume (Å^3)	Density (g/cm^3)
	X	Y	Z	X	Y	Z		
Aqueous Phase NSC	*4.148*	*4.148*	*7.354*	*90*	*90*	*120*	*109.58*	*5.937*
Organic Phase NSC	*7.185*	*7.185*	*7.354*	*90*	*90*	*120*	*328.65*	*5.939*

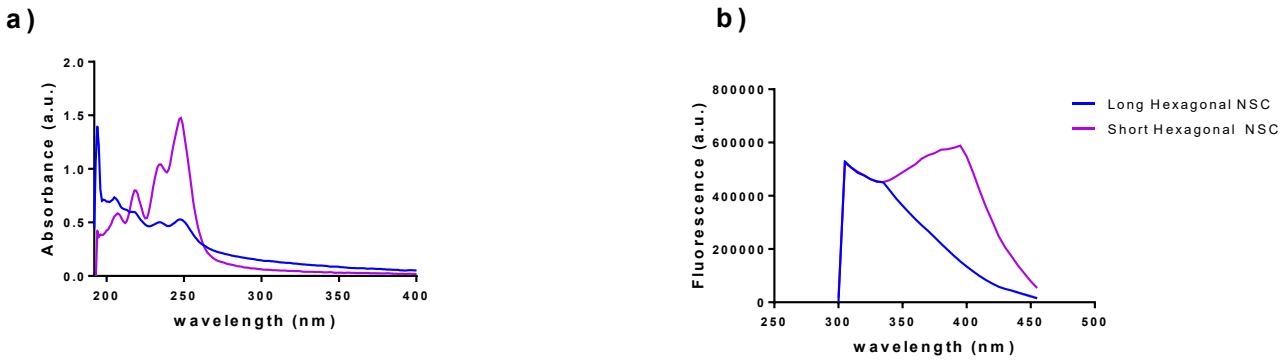

Figure 2.5 Comparison of the absorbance **(a)** and emission **(b)** spectra of the short and long hexagonal crystal structures.

The photoluminescence (PL) emission from the NSC under irradiation was captured with the Ocean Optics USB4000 (**Figure 2.6a**) and QEPro (**Figure 2.6bc**) spectrometers in conditions where the cuvette was not filled (blank), filled with water, or filled with NSC solution. The USB4000 was not able to detect a difference in PL between when the radiation beam was off and on and generated no signal (**Figure 2.6a**). The QEPro was able to detect a difference and generated a signal, but this was not a reproducible signal with successive experiments. The difference between the two crystal structures was not discernable with measurements from the QEPro. Therefore, the scintillation PL of the NSC under irradiation was not established in our setup. This likely due to the low photon yield of LaF_3 and CeF_3 having lower yields of 2200 photons/MeV and 4000 photons/MeV, respectively (248, 258). This level of PL usually would need a photomultiplier tube in order to detect. The PL peak from the previous studies was at 340 nm. The scintillation PL spectra generally aligns well with the fluorescence spectra, due to a similar process of transitions in electron orbitals releasing photons of discreet energy and wavelengths (259).

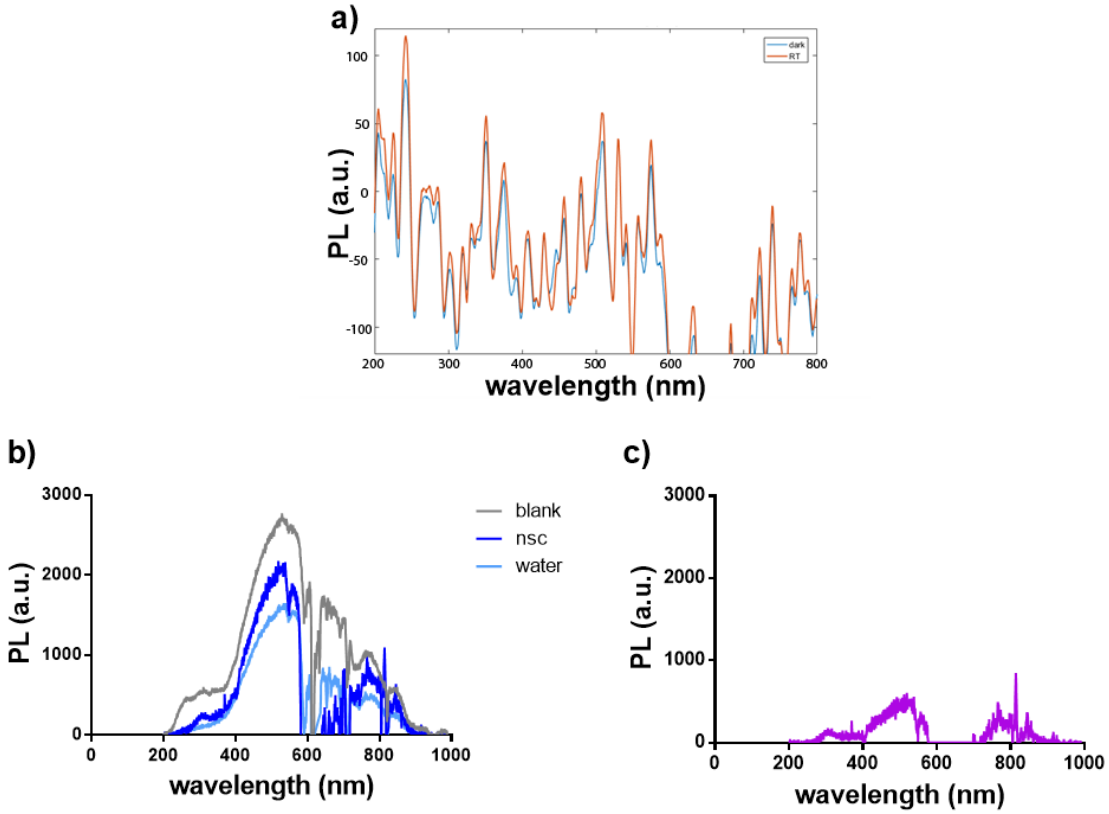

Figure 2.6: PL emission from the NSC under radiation. **a)** Shows the PL of NSC in baseline and irradiated conditions acquired via an Ocean Optics USB 4000 spectrometer. **b)** shows PL under irradiation of blank (no media), water and water containing NSC. **c)** shows subtracted spectra of NSC from baseline water media from **b)**.

The synthesized NSC and commercially purchased PPIX (Sigma-Aldrich, St. Louis, MO, USA) were then loaded into PEG-PLGA nanospheres (NP). Initial attempts as described in **section 2.2.1.2** involved the use of a double emulsion process along with DCM with polyvinyl alcohol. This demonstrated severe aggregation issues with the NP, likely due to the sticky PEG block polymer interacting with polyvinyl alcohol (**Figure 2.7a**). The omission of polyvinyl alcohol still resulted in a relatively large sized PEG-PLGA NP at approximately 200 nm (the target size was 100 nm) with high polydispersity, and unconvincing images of encapsulation (**Figure 2.7bc**). This was thought to be due to the double emulsion product separating the PEG-PLGA polymers from the payload to be encapsulated in separate organic and aqueous phases. Without an opportunity to come into close contact, the encapsulation efficiency was poor and larger NP from the pockets of emulsion were formed and displayed large size variations likely dependent on the homogeneity of emulsion, when dropped into aqueous phase. Switching to single emulsion technique with acetonitrile produced more homogenous particles and demonstrated reliable nanospheric encapsulation as detailed below.

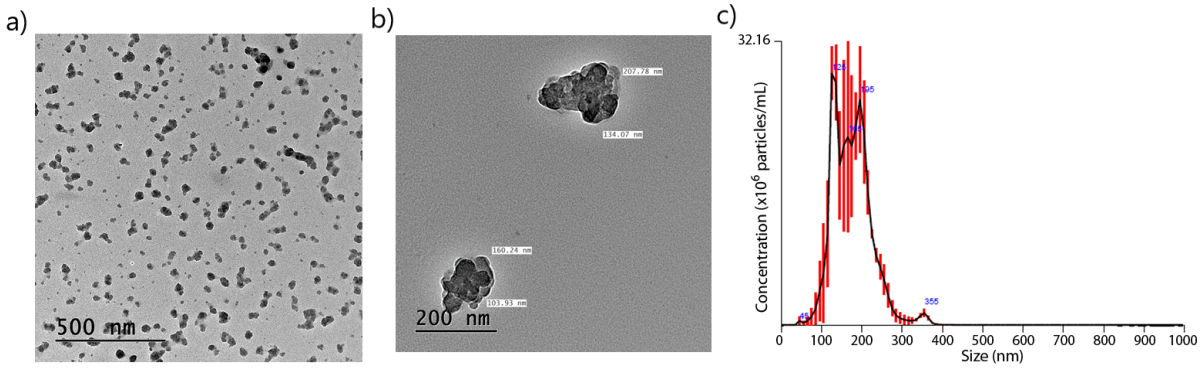

Figure 2.7: TEM of double emulsion process with DCM and water with PVA **a)** and without PVA **b)** are shown for PEG-PLGA+NSC nanospheres. The size and distribution of **b)** is shown in **c)** using Nansight NTA.

Empty PEG-PLGA NP, NSC-encapsulated PEG-PLGA NP (NSC NP) and NSC with PPIX-encapsulated PEG-PLGA NP (radioPDT NP) were prepared by single emulsion nanoprecipitation method with a few modifications (249). The nanosphere synthesis and encapsulation followed the principles of nanoprecipitation, where hydrophobic polymers and payload (the agents to be encapsulated) miscible in an organic solvent are added to an excess of aqueous phase media. In the aqueous phase, the polymer and payload are supersaturated, which causes the payload to act as a nucleus for the polymer to condense and precipitate around (260). This causes the formation of reproducible NPs with encapsulated payload. Once the organic phase was added to the aqueous phase, the organic solvent was evaporated away at 40° C to obtain the nanoparticle suspension in a stable aqueous-only medium. Excess reagents were removed by ultracentrifugation at 50,000 g to form a pellet of NPs, which was re-suspended in fresh aqueous medium. Dynamic Light Scattering (DLS) and TEM measurements (**Figure 2.8, top and bottom panel**) confirmed that the majority of empty PEG PLGA NP, NSC NP, and radioPDT NP were in the 90-120 nm size range, which is close to the target NP size of 100 nm. This size was chosen because it is reported to be the ideal size for delivery via tumor vasculature *in vivo*, due to preferential pharmacokinetics of distribution and preferential accumulation in the tumor by EPR effect (226).

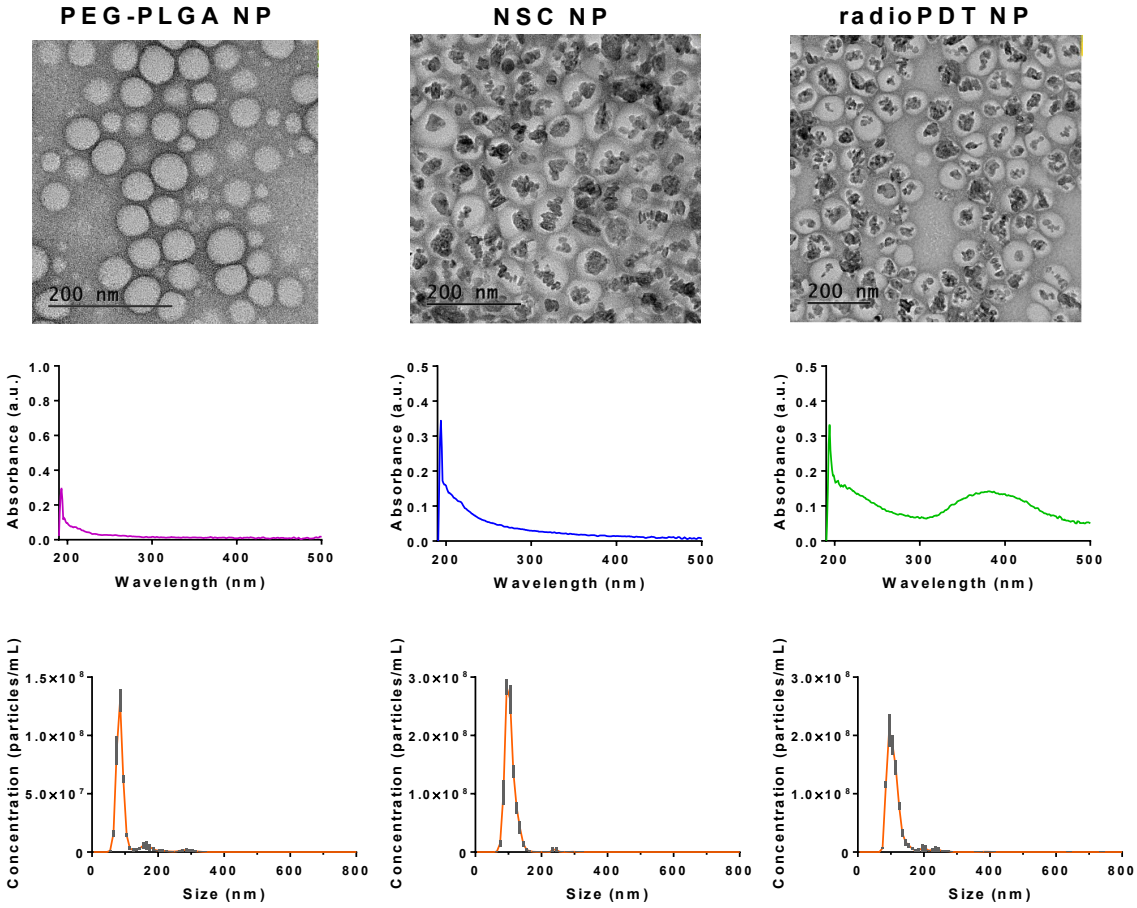

Figure 2.8: TEM images showing shape and size distribution of PEG-PLGA NP when unloaded **(top-left)**, loaded with NSC **(top-middle)**, and loaded with NSC and photosensitizer **(top-right)**. The corresponding UV-Vis spectrum for each condition is shown **(middle panel)**, as well as the concentration as a function of size via Dynamic light scattering (DLS) **(bottom panel)**. The mean size by DLS for each variant is 75, 95 and 125 nm, respectively, with a polydispersity index of < 0.3 (**Table 2.2)**.

The UV-Vis absorbance signal for NSC NP and radioPDT NP show the presence of NSC absorbance and NSC with PPIX absorbance, respectively, in relation to PEG-PLGA NP alone (**Figure 2.8, middle panel**). **Table 2.2** demonstrates the measured zeta potential ranged from -15 to -30 mV, indicating relatively good stability in aqueous media and in physiologic conditions, and a low chance of binding and early clearance by immune cells (261). The polydispersity index was <0.3 in all conditions, which indicates a narrow distribution in size of synthesized NPs for a NP of this construct, and aids in predictability of distribution *in vivo*. The physical characteristics of the NPs were maintained even when the synthesis procedure was scaled up to produce larger batches.

Table 2.2 Zeta potential and polydispersity measurements of the unloaded PEG-PLGA NP, NSC NP and radioPDT NP. The zeta potential ranged from -18.22 to -26.3 mV from fully loaded to unloaded, and the polydispersity index remained < 0.3 in all conditions.

	Zeta potential (mV)	Mean Diameter (nm)	Polydispersity index
PEG-PLGA NP	*-26.30 ± 1.88*	*75*	*0.19 ± 0.32*
NSC NP	*-19.23 ± 1.25*	*95*	*0.14 ± 0.10*
radioPDT NP	*-18.22 ± 0.66*	*125*	*0.27 ± 0.26*

Particle loss during purification procedures is of concern, hence Tangential Flow Filtration (TFF) was used for particle purification and washing when scaling-up NP production. This method has been successful in purification of similar nanoparticles for biomedical uses, without altering their size or characteristics (262-264). This allowed quick and efficient large volume filtration to be done.

Initially, the NPs were produced on a small scale (10 mg per batch), and therefore scaling-up of the NP production was necessary for *in vivo* studies. The scaled-up PEG-PLGA NP, NSC NP, and radioPDT NP were produced at 20-fold higher quantity, which yielded approximately 200 mg of NP for each variant. The scaled-up NPs were approximately 80-120 nm in size, which are quite similar with the NPs produced in small scale (**Figure 2.9**). In the scaled-up production, the nanoparticles were washed after synthesis using Tangential Flow Filtration (TFF), which further improved reproducibility, speed, and efficiency of the production procedure.

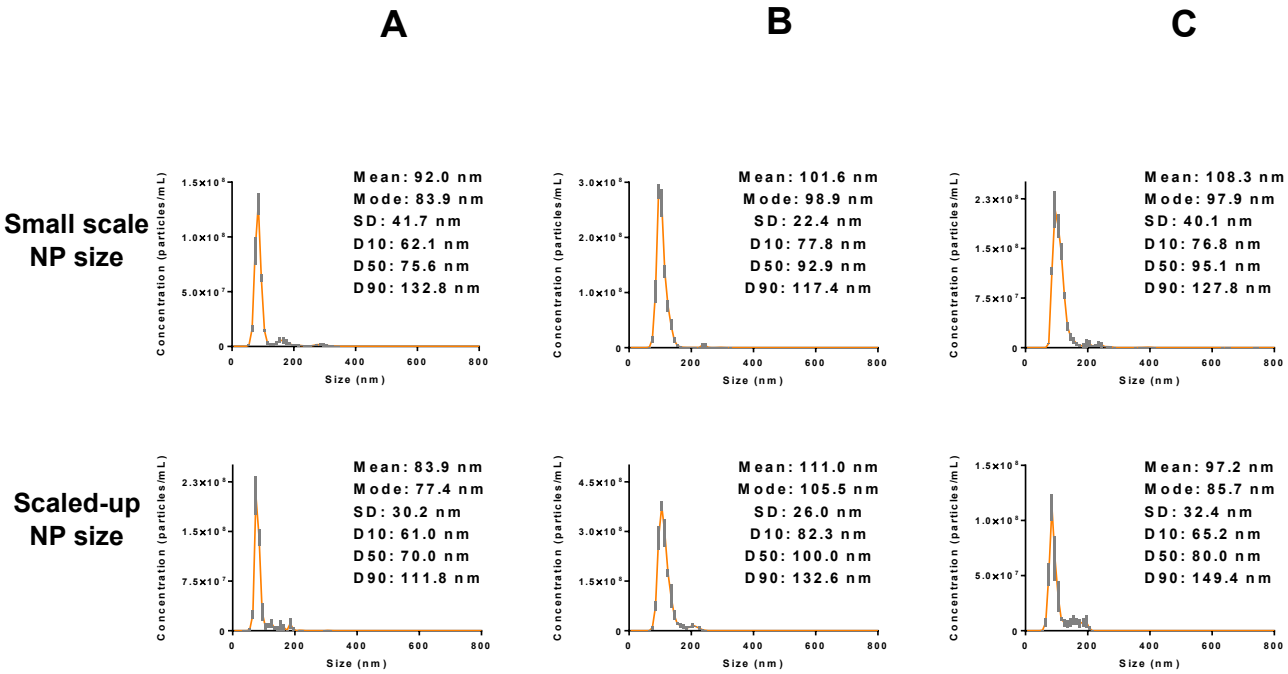

Figure 2.9: Particle size measurement and statistics by Nanosight NTA for smaller scale and scaled-up NP. **A:** Empty PEG-PLGA NP. **B:** NSC NP. **C:** radioPDT NP.

Figure 2.10 shows Nanosight measurement of the particles before and after treatment with TFF. The concentration results demonstrate there is minimal loss of NPs during purification. The particles also retained their average size before and after TFF treatment, and size distribution improved as contaminants were washed away. The volume of synthesized nanoparticles that were able to be purified using TFF were between 100 to 600 mL, which greatly aids in standardizing *in vitro* and *in vivo* experiments by using the same batch of nanoparticles for multiple subsets of an experiment.

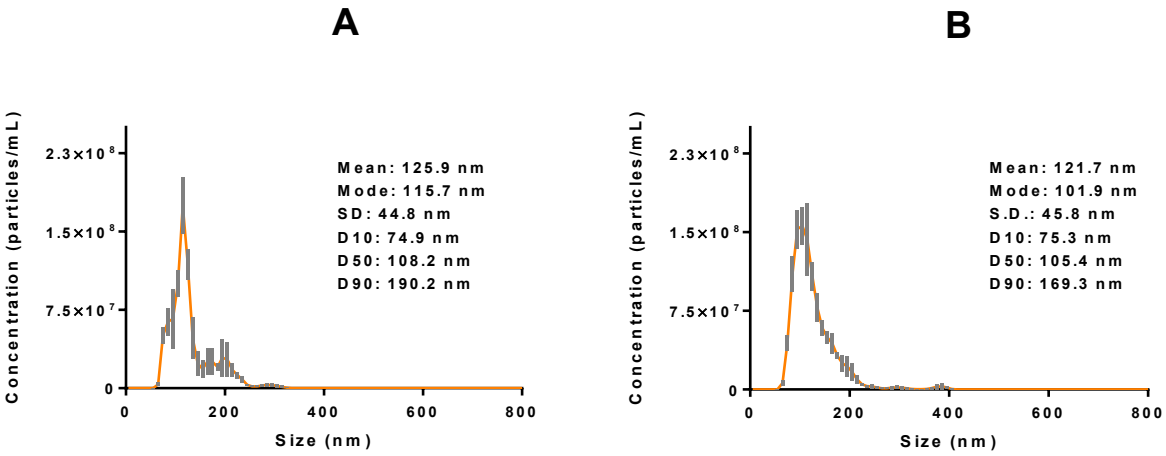

Figure 2.10: Particle size and concentration measurement of radioPDT NP by Nanosight NTA. **A**: NP before washing with TFF. **B**: NP after TFF.

The size of the radioPDT NPs were larger than empty PEG-PLGA NP, which might be due to insertion of hydrophobic PPIX and NSC making the amphiphilic copolymer form a well bonded structure. The encapsulation efficiency calculated showed a high PPIX entrapment of more than 90% of the drug into the radioPDT NPs.

In this size range, the NP are subjected to EPR effect, whereby the NP preferentially accumulate in tumors (226). Through the secretion of growth factors such as vascular endothelial growth factor (VGEF) and others, tumors recruit rapid neovascularization to increase vascular perfusion and support their nutrient needs for rapid growth (265). The tumor vasculature differs from normal tissue vasculature in that it is aberrant, disorganized, with regions of slow and reversed blood flow, and contains compromised endothelial tight junctions that let particles as large as 600 nm pass through to the interstitial tissue (266). Depending on the tissue type, normal vasculature's endothelial tight junctions prevent NP of sizes over 30 nm from extravasating in significant amounts. Tumors also experience poor lymphatic drainage, which prevents rapid clearance of the extravasated particles (267). The dynamic interplay between NP accumulation and clearance rate and NP circulation time allows NP in the size range of 30 nm to 100 nm in size to preferentially extravasate through tumor vasculature over normal tissue vasculature (266).

The NP size, polydispersity and zeta potential compare favourably against previously reported nanocarrier delivery systems for optimal cellular uptake (268). These properties also reportedly confer *in vivo* targeted delivery capabilities via EPR effect (226), which refers to using the high tumor vascular permeability and poor lymphatic drainage to passively accumulate NP of specific size and physical characteristics. The use of a

PEGylated NP also reduces clearance rate by the MPS (230) and augments the *in vivo* circulation time (231), allowing it an extended time for accumulation in a tumor via EPR effect. Therefore, the use of a PEGylated polymer and optimal NP size make our NP construct unique amongst inorganic scintillator and photosensitizer-based nanoparticle systems (269) with potentially enhanced *in vivo* performance. Using the same physical characteristics as we have demonstrated, analogous polymeric NP constructs have been successfully used to deliver cancer chemotherapeutics, such as BIND-014, in Phase II clinical trials by multiple cancer research groups (270, 271).

The shape and localization of the NSC within the NP was confirmed with TEM (**Figure 2.8, top panel**) revealing well defined core-shell structure for the empty PEG-PLGA NP, NSC NP, and radioPDT NP. The particles were well dispersed and homogeneously distributed. The TEM images clearly demonstrated the localization and entrapment of NSC within the core of the nanospheres for the NSC NP, and radioPDT NP. The size of the nanospheres was found to be around 50-70 nm for PEG-PLGA NP, 70-80 nm for NSC NP, and 80-100 nm for radioPDT NP. These NP sizes are in a range, close to the ideal, for bestowing EPR effect in tumors (272, 273).

Elemental mapping of the samples (**Figure 2.11**) was carried out to confirm the entrapment of NSC and PPIX within the PEG-PLGA nanospheres. Empty PEG-PLGA NP showed no signal of lanthanum or nitrogen, confirming the absence of $LaF_3:Ce^{3+}$ NSC or PPIX. For NSC NP, there was a strong lanthanum signal indicating the presence of $LaF_3:Ce^{3+}$ NSC but no nitrogen due to absence of PPIX. Similarly, for radioPDT NP there was a strong lanthanum signal indicating the presence of $LaF_3:Ce^{3+}$ NSC and some increase in nitrogen

due to presence of PPIX. A weak oxygen signal was observed in all three NP conditions, which corresponds to the oxygen present in PEG-PLGA; weak signal coming from the uranyl acetate stain that was used for negative staining of these samples was also seen. The results of elemental mapping confirmed encapsulation with the NSC and the PPIX into the PEG-PLGA NP.

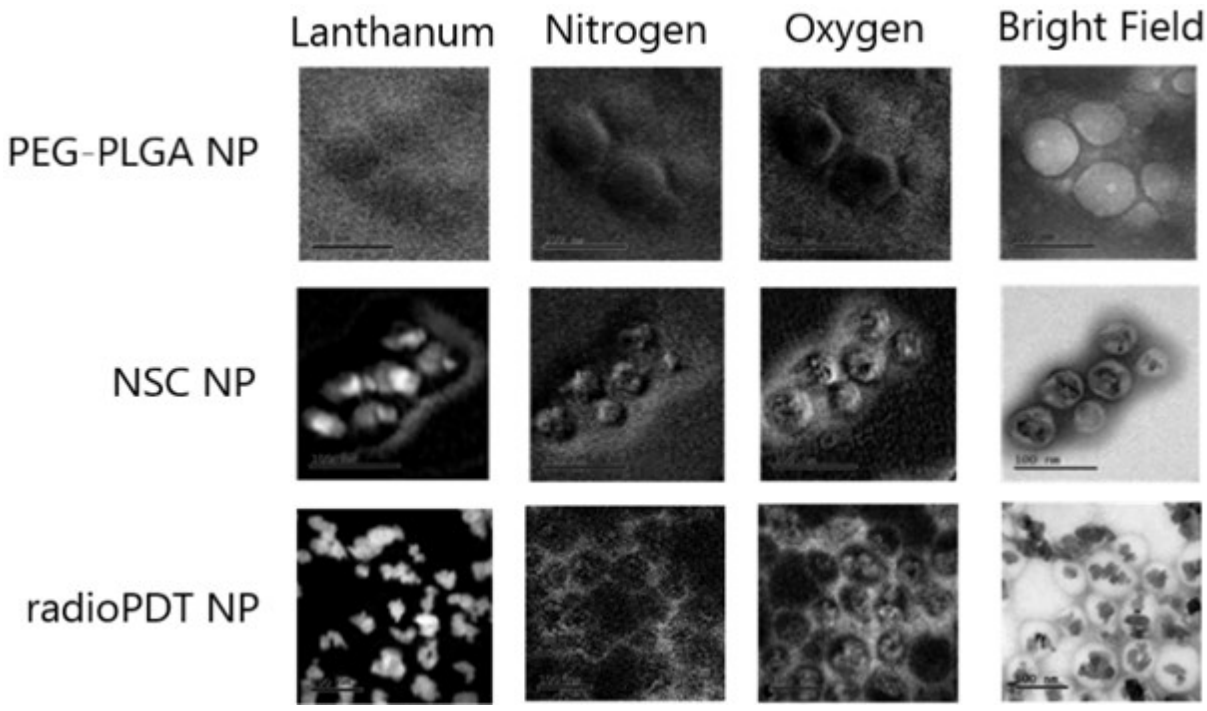

Figure 2.11: High resolution TEM (HRTEM) images and elemental mapping of the various NP conditions. PEG-PLGA NP **(top row)** with no lanthanum and nitrogen signal. NSC encapsulated PEG-PLGA NP (NSC NP, **middle row**) shows strong lanthanum signal from NSC, and no nitrogen signal. PPIX with NSC encapsulated PEG-PLGA NP (radioPDT NP, **bottom row**) shows strong lanthanum signal from NSC and nitrogen signal from PPIX.

Further evidence of encapsulation was demonstrated via size exclusion chromatography. The radioPDT NP was concentrated to 1 x 10^7 particles/mL and 1 mL of this solution was loaded into a Sephedex G-15 gel column (**Figure 2.12**). Twenty millilitres of ultrapure water was added drop-wise to run the radioPDT NP through the column, with the UV-Vis spectra of the eluent measured every 0.5 mL, measuring for absorbance at 400 nm (representing PPIX) and 220 nm (representing NSC). The experiment was also run with 1 mL of 100 μM of PPIX (equivalent concentration of PPIX in the NPs). A sharp, detectable rise in both 400 nm and 220 nm was noted at 1.5 mL consistently, and quickly fell to undetectable levels by 2.5 mL of elution. No peak was detectable for the PPIX only solution, but a constant low level of 400 nm signal was noted. This indicates that the PPIX and NSC were clearing discretely at a certain size range and simultaneously. This is likely due to the two agents being at least associated, if not encapsulated, by the PEG-PLGA nanospheres. It also indicates the NPs have a relatively homogenous size distribution since they are eluted between 1.0 mL and 2.5 mL with a narrow and sharp peak.

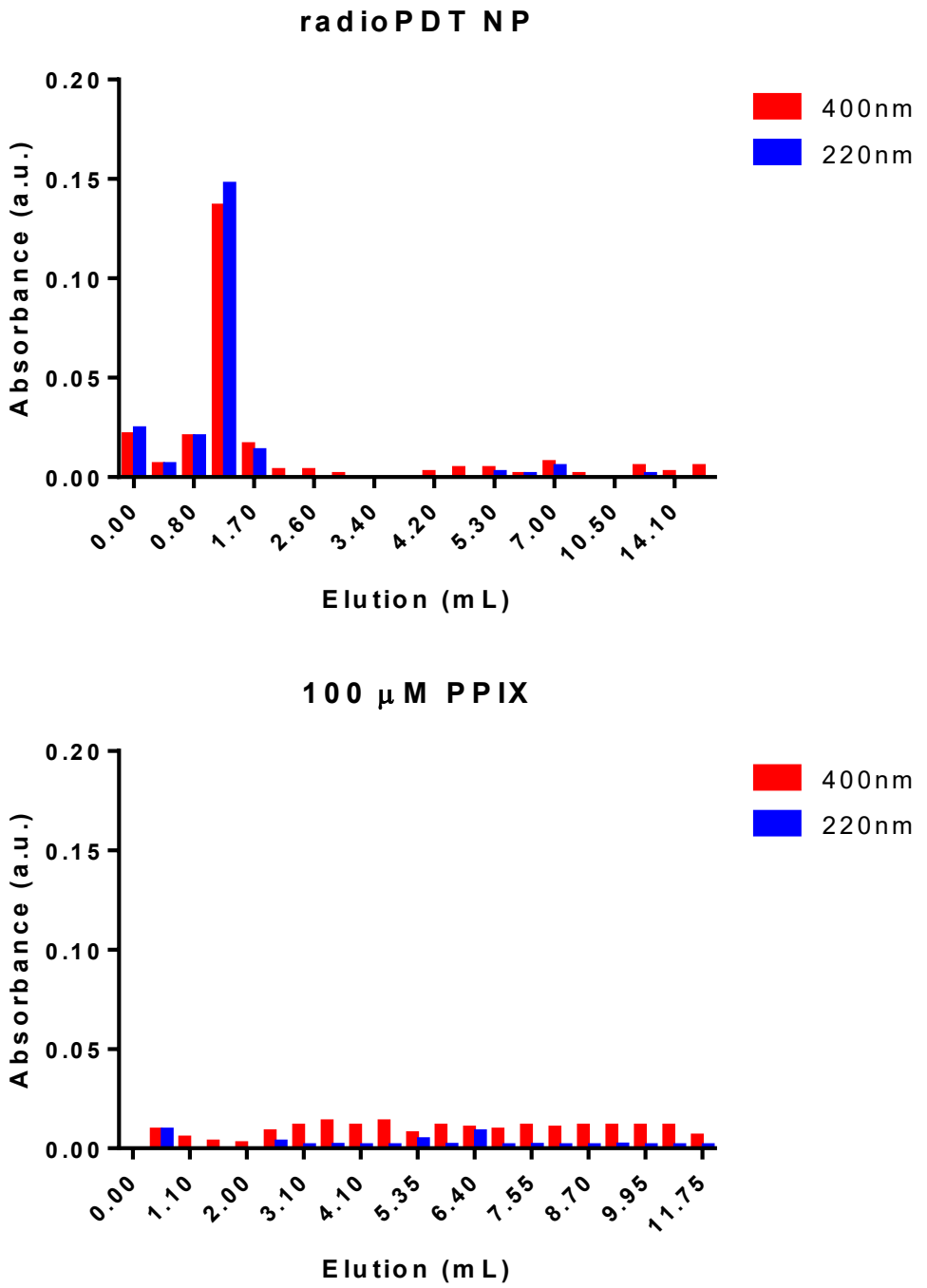

Figure 2.12: Size exclusion chromatography in a gel column of the radioPDT NP (**top**) and comparable PPIX solution (**bottom**) demonstrating UV-Vis absorbance at 400 nm and 220 nm.

Energy transfer within the radioPDT NP via FRET appeared feasible based on emission spectra of NSC (**Figure 2.3d and 2.5b**) and absorption spectra of PPIX. This was demonstrated using fluorescence spectroscopy (**Figure 2.13**). The excitation wavelength used was 205 nm: a secondary absorption peak of the NSC (seen in **Figure 2.3c**), and far shorter wavelength than the Soret band of PPIX (403 nm). The control conditions of NSC NP and PPIX drug failed to produce PPIX's emission peak at 620 nm (254). The complete radioPDT NP loaded with NSC and PPIX demonstrated the emission peak of PPIX (**Figure 2.24**). This is a result of transfer of the incident 205 nm excitation laser to the NSC, and energy from the NSC's fluorescence being absorbed by the PPIX and causing secondary fluorescence of the PPIX via FRET energy transfer.

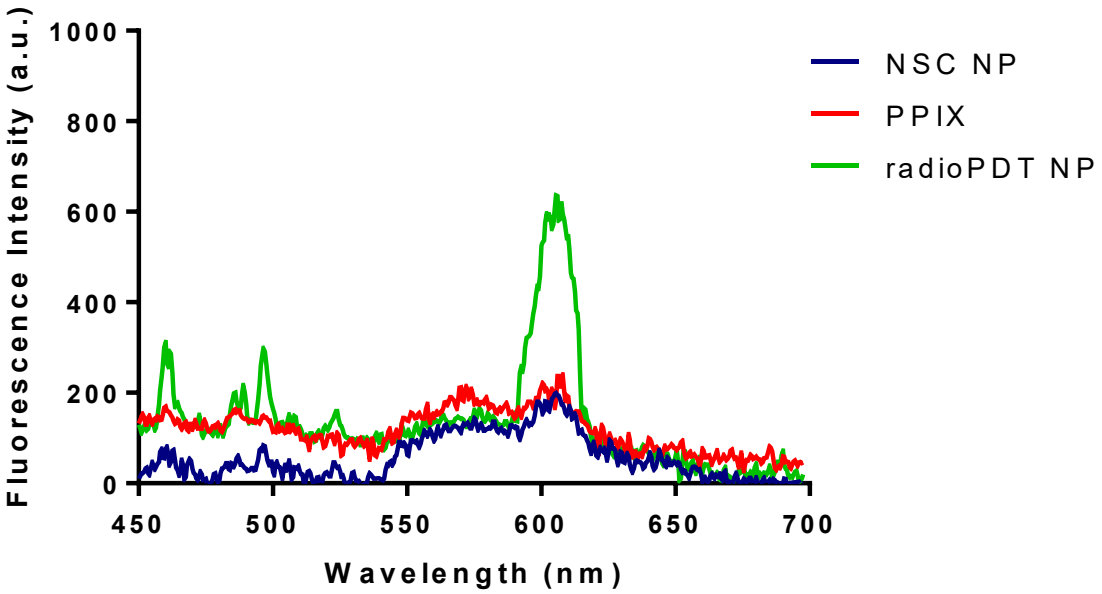

Figure 2.13: Fluorescence spectroscopy with 205 nm excitation. Spectra of NSC NP when excited close to the absorbance maxima of NSC (203 nm). A fluorescence peak at 620 nm (PPIX emission maxima) is apparent only in the functional radioPDT NP with both NSC and PPIX encapsulated. PPIX absorbance maximum (403 nm) is not within range of the excitation energy of 205 nm, and thus the 620 nm emission peak is not seen without the NSC component.

2.3.2 Stability in Physiologic Conditions (PBS, DMEM, FBS, and Human Plasma at 21°C and 37°C)

Determining stability in different media is an important parameter for nanoparticle development, since it is crucial for allowing the interaction of NPs when it is under physiological condition. Under storage conditions of distilled water at 4 °C, the NPs maintained their integrity in terms of size and retention of encapsulated agents for 4 weeks. For assessment of stability in diagnostic and therapeutic scenarios, all the particles (PEG-PLGA NP, NSC NP, and radioPDT NP) were tested in distilled water and phosphate-buffered saline (PBS) at pH 7.4 at both 21 °C and 37 °C (**Figure 2.14**) for 48 hours. In these aqueous media, the NPs appeared to be stable by size for at least 24 hours and started to significantly increase in size at 48 hours. Note, the increased initial size of radioPDT NP was due to a batch-to-batch variation in NP synthesis but produced the same results and trend in size over time. Repeat tests did not show an influence of the initial starting size on the stability of the NP.

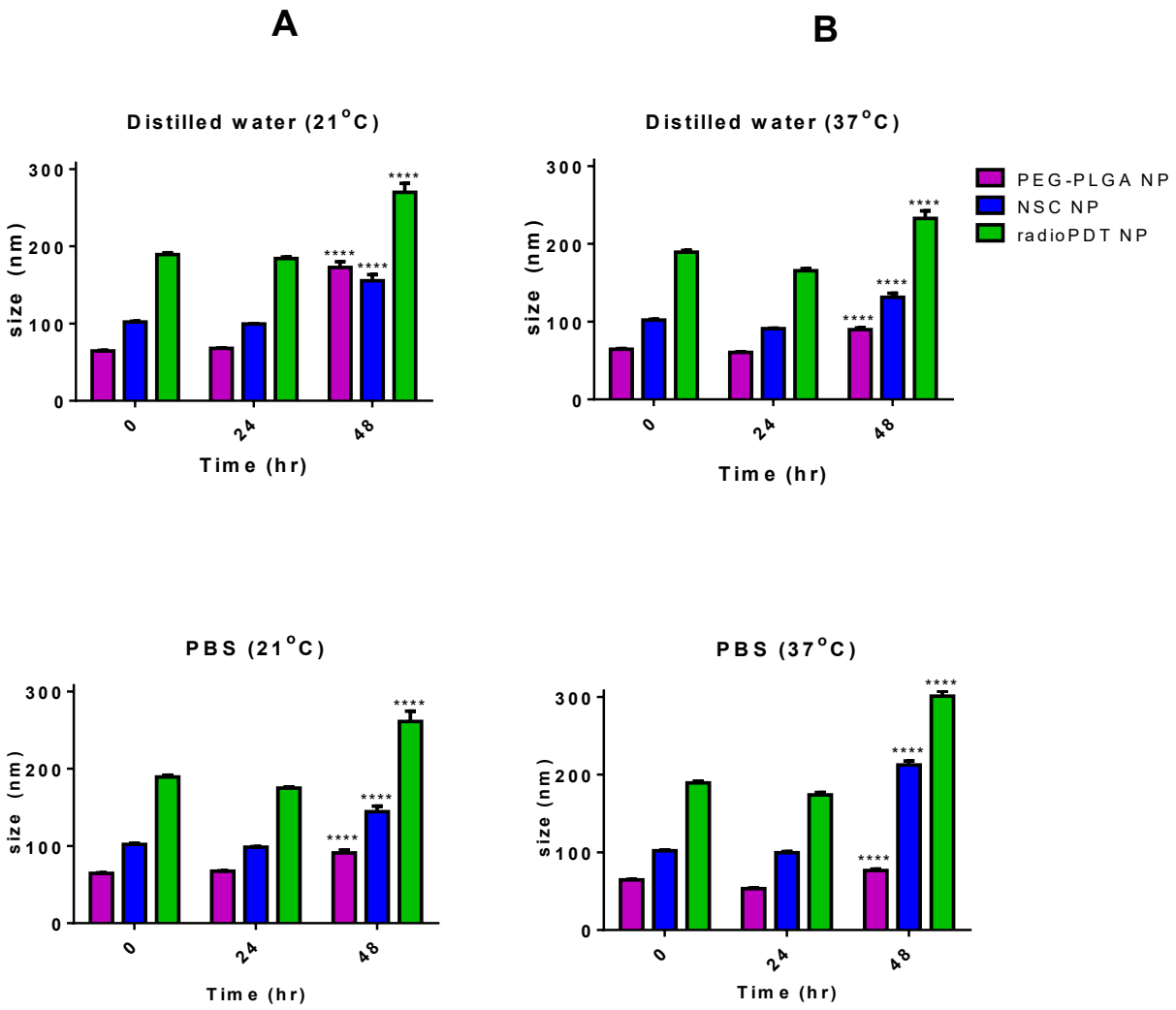

Figure 2.14: Average nanoparticle size of PEG-PLGA NP, NSC NP, and radioPDT NSC NP is shown in distilled water (**top panel**) and in Phosphate-Buffered Saline (PBS, **bottom panel**) at pH=7.4. Stability is shown at 21 ºC (**A**) and 37 ºC (**B**) over time periods of 0, 24, and 48 hours. Size of NP was measured using Nanosight NTA® (Nanosight Ltd., Malvern, UK), and change is size was compared to baseline (0 hour). ****p<0.0001

The stability of the NPs in more physiologic conditions, including media containing typical protein products found in the human circulatory system, was assessed using human blood-derived plasma and serum. Stability was assessed by monitoring for changes in size using Nanosight NTA® (Nanosight Ltd., Malvern, UK). It was noted that the NP immediately increased significantly in size to about 200 nm within 6 minutes. The native media also measured about 200 nm at baseline, which may be representative of the size of protein and its aggregates, such as albumin (274). Alternatively, the NP size may have changed after addition to media because of protein interaction with the NP outershell and formation of a protein corona (274). The radioPDT NPs were stable with no significant change in size until 24 hours in plasma, and serum, after which the particle size significantly increased in plasma and was trending towards a significant increase in serum (**Figure 2.15**). This was also reflected in the Control media-only condition, which can indicate aggregation of the protein and macromolecules within the media. The alternative explaination for the NP change may include the protein corona causing aggregation or possible osmotic swelling (274).

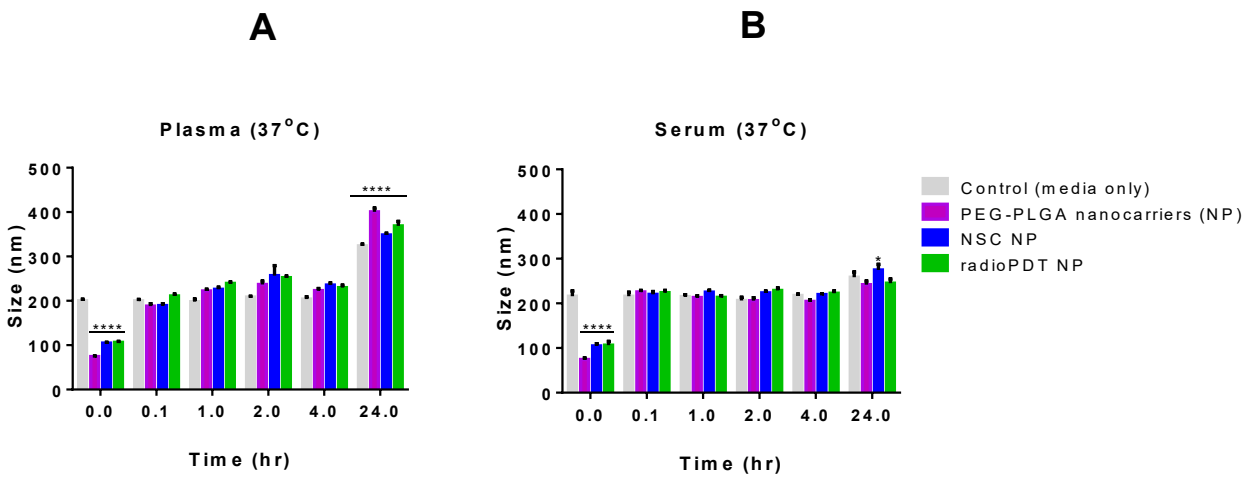

Figure 2.15: Particle size of PEG-PLGA NP, NSC NP, and radioPDT NP measured by Nanosight NTA® for 24 hours at 37 °C in **A**) in human plasma and **B**) in human serum. The baseline (0 hour) NP size were measured prior to addition of the media, whereas the baseline (0 hour) Control was the native media alone. The NP conditions were significantly smaller than Control at baseline but was not significantly different between 0.1 to 4 hours. There was no appreciable size change between 0.1 to 4 hours in Control or NP conditions as well. At 24 hours, Control and all NP conditions significantly increased in size (compared to 0.1 to 4 hours) for plasma. The size of Control and NP conditions were trending towards an increase in size at 24 hours for serum media, but was only significant for NSC NP. *$p<0.05$, ****$p<0.0001$

Characterizing the nanoparticle (NP) stability in cell media conditions was important to determine treatment times and performance for *in vitro* experiments. NP size was used as an indicator of nanoparticle stability at different time points. The cell media used was Dubelcco's Modified Eagle's Medium (DMEM) cell medium supplemented with 10% Fetal Bovine Serum (FBS). From **Figure 2.16**, it is evident that the NPs are stable up to 8 hours with minor size changes, after which point there was a significant increase in size of the particles. This is likely due to degradation and aggregation of the particles.

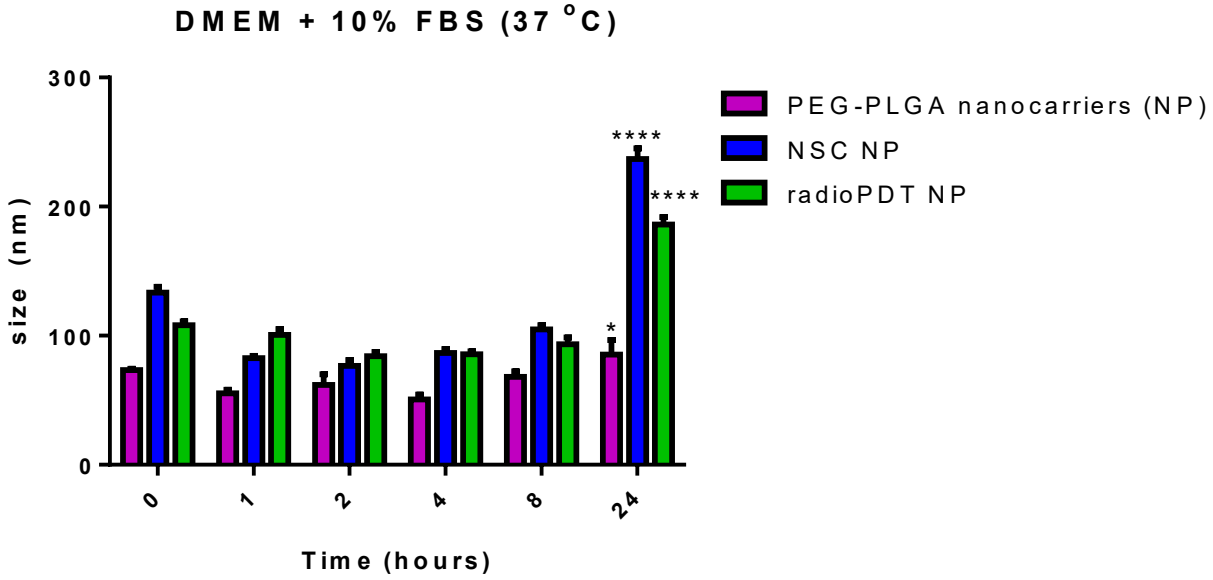

Figure 2.16: Average nanoparticle size of PEG-PLGA NP, NSC NP, and radioPDT NP in DMEM+10% FBS from 0 hour to 24 hours at 37 °C. Changes in size of the NPs were monitored with Nanosight NTA® (Nanosight Ltd., Malvern, UK). Changes in size were assessed against the baseline (0 hour) size. ****p<0.0001

To determine the rate of PPIX release from the NP in a physiological environment, which play a crucial role to predict *in vitro* and *in vivo* behaviour, the radioPDT NPs were incubated in PBS for 72 hours at room temperature and 37 °C. To check the PPIX release in serum conditions, the radioPDT NPs were incubated for 24 hours at 37 °C in DMEM supplemented with 10% FBS.

An initial burst release of around 4% of PPIX was observed after 1 hour of incubation. The release kinetics for radioPDT NP in PBS indicated good stability, with only approximately 10% release at 24 hours (**Figure 2.17**). In contrast, the release of PPIX in 10% FBS supplemented DMEM at 37°C was stable for up to 8 hours with 10% release (**Figure 2.17**). The abrupt release of the PPIX initially can be due to the release of molecules loosely attached to the NP surface. The PPIX molecules maintained in the PEG-PLGA inner core matrix showed a slower release up to 24 hours in PBS medium. In contrast, in DMEM with 10% FBS medium the radioPDT NPs were stable for up to 8 hours, after which the NPs started to break down and showed burst release characteristics. The increased rate of release in DMEM may be due to PPIX's higher solubility in this medium compared to pure aqueous media due to the presence of FBS. The changes in PPIX release and measured NP size in PBS and in serum conditions may also indicate that some molecules present in serum, such as hormones, enzymes, and/or proteins, are replacing the loaded PPIX and triggering their dissociation from the NP into the medium.

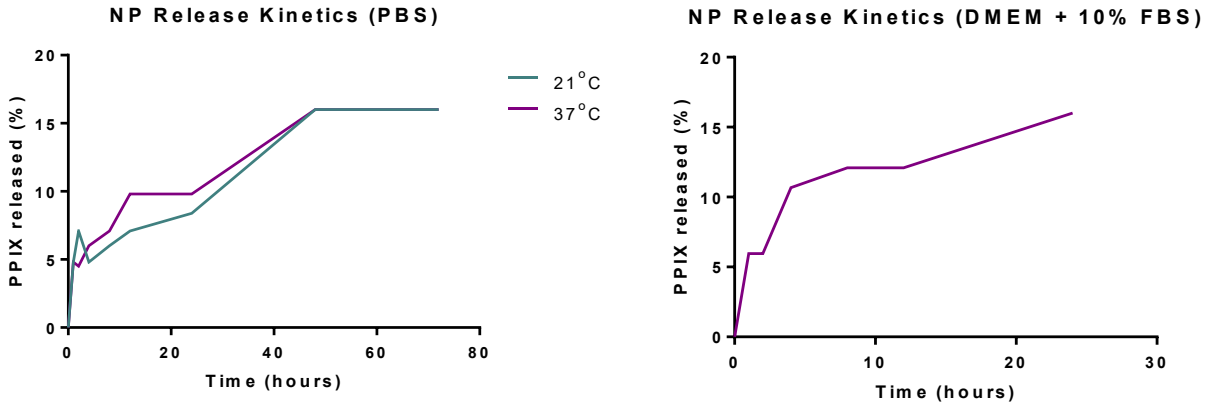

Figure 2.17: Time-dependent release profile of PPIX (measured by UV-Vis absorbance at 400 nm against standardized values) from radioPDT NPs in PBS (**left**) medium at 21°C and 37 °C for 72 hours. The release kinetics in cell media of 10% FBS supplemented DMEM medium at 21 °C over 24 hours is shown on the **right**.

A long-term stability study observed the shelf-life of radioPDT NP in ultrapure Milli-Q water solution. Stability was assessed by particle size and PPIX release. The radioPDT NP was stored in Milli-Q grade water at 4 °C. The radioPDT NP solution showed no release of the PPIX and no significant change in the PDI or size for up to 4 weeks, after which point a more rapid release was observed. Therefore, the radioPDT NPs were found to be stable for 4 weeks at 4 °C before NP disintegration and aggregation occurs (**Figure 2.18**).

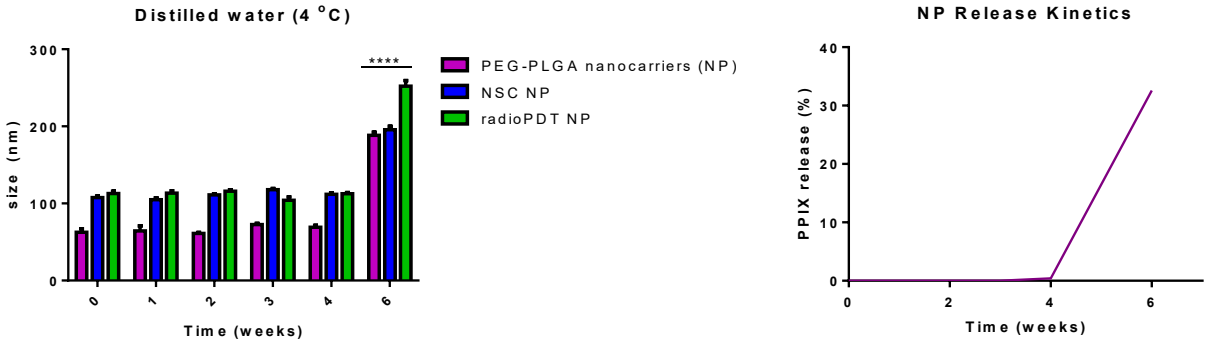

Figure 2.18: Stability and Release study of radioPDT NP over 6 weeks in distilled water at 4 °C, as demonstrated by size as measured by Nanosight NTA® (Nanosight Ltd., Malvern, UK) (**left**) and percentage of loaded PPIX released as measured by UV-Vis absorbance at 400 nm (**right**). NP size changes were assessed by comparing against baseline (0 hour) measurements for the respective NP. ****$p<0.0001$

These results show our various NP constructs have a high degree of stability for up to 24 hours. The long duration of stability can prevent early burst-release and rapid accumulation in vital organs, such as the liver (275). NP stability is also important for the pharmacokinetic distribution since particles in this size range tend to peak in tumor uptake relative to other tissues within the first 24 hours (276).

2.3.3 Nanoparticle Toxicity, Uptake and Confocal Imaging *in vitro*

The safety profile of the radioPDT NP and its constituent parts was assessed *in vitro* with MTT colorimetric proliferation-assay. Cells treated with serial dose escalations for 48 hours did not reveal any significant cytotoxicity over baseline conditions in PC3 and DU145 human prostate cancer cell lines as well as GM38 human skin fibroblast cell lines (**Figure 2.19(i)**).

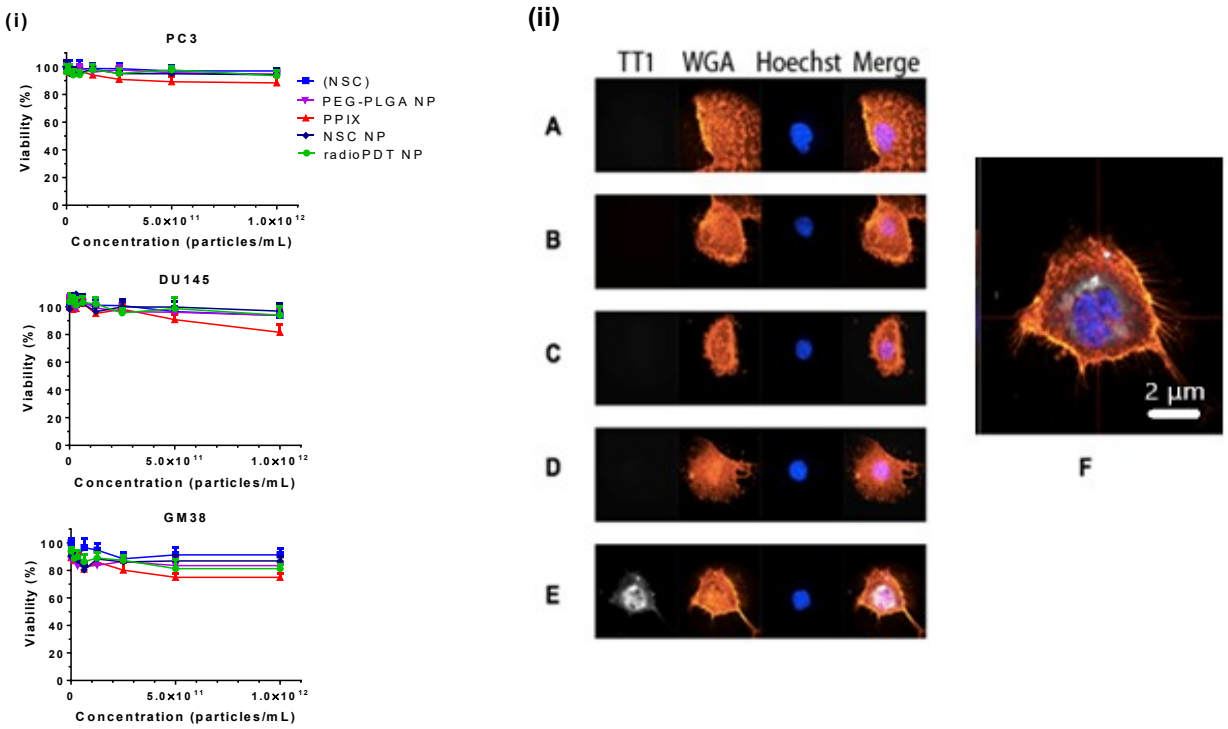

Figure 2.19: (**i**): *in vitro* cytotoxicity of radioPDT NP and its constituents are shown in prostate cancer lines PC3 (**top**) and DU145 (**middle**), and skin fibroblast line GM38 (**bottom**). Viability was assessed using MTT colorimetric assay after treating cells with concentrations up to $1x10^{12}$ NP/mL (or equivalent constituent dose) for 48 hours. (**ii**): Cellular uptake and localization study in PC3 cells. Images were taken after 24 hours, after incubation with (**A**) PC3 untreated cells (**B**) PEG-PLGA NP treated PC3 cells ($1x10^{8}$ NP/mL) (**C**) NSC NP treated PC3 cells ($1x10^{8}$ NP/mL) (**D**) radioPDT NP treated PC3 cells ($1x10^{8}$ NP/mL) (**E**) radioPDT NP with TT1 fluorescent dye (used as a tag for confocal fluorescence microscopy) NP treated PC3 cells ($1x10^{8}$ NP/mL) (**F**) Z-stack of radioPDT+dye NP treated PC3 cells (10^{8} NP/mL) (**right panel**). Images demonstrate the NP with TT1 dye are internalized by the cells into the cytoplasm.

The cellular uptake and localization of the radioPDT NP were visualized within PC3 cells, the intended initial target cells for the radioPDT treatment, by fluorescent confocal microscopy for up to 24 hours of incubation (**Figure 2.19, right panel**). The radioPDT NPs were tagged with TT-1 fluorescent dye. The z-stack image confirmed that the NPs were localised intracellularly after 24 hours of incubation. The location of fluorescent signal from the dye in the NPs indicated that they were taken inside the cell and were not on the surface of the cell.

2.3.4 *In vivo* Acute Toxicity Assays

Acute *in vivo* toxicity of the radioPDT NP was determined using serial dose escalation experiments in immune-competent C57bl/6 mice model. RadioPDT NPs were administered intravenous (IV) via the tail vein. After each dose, the mice were monitored for weight or behavioural changes for 48 hours prior to euthanization for histopathology analysis. The starting dose was $7.5x10^{12}$ NP/mL (50 mg/kg) and, if no significant weight or behavioural changes were observed, the dose was serially doubled to a maximum final dose of 1000 mg/kg. A dose beyond 1000 mg/kg was not pursued due to difficulty in keeping the radioPDT NP suspended in solution for injection. No observable change in behaviour the mice nor significant weight loss was measured after administration of the NPs at any dosage concentration (**Figure 2.20**, **right panel**). On histopathologic analysis, no evidence of toxicity was seen on gross pathology, and microscopy revealed no signs of acute toxicity in the lung, liver, spleen, or kidney (**Figure 2.20, left panel**). Confocal fluorescent microscopy was used to examine PPIX photosensitizer (400 nm excitation, >600 nm emission) uptake in the organs of mice receiving the two highest NP-injected

doses. Of the organs examined, the spleen showed the highest intensity of signal, followed by the liver, and lungs (**Figure 2.20, middle panel**). No signal was seen in the kidneys, which is consistent with MPS clearance of the NPs. Fluorescence was observed to be mostly around the vessels, with discrete points of signal that appeared to be trailing away from the regional vessel tissue area. This was thought to represent uptake and clearance of the NP by macrophages that migrated away and again consistent with NP clearance through the MPS. Diminished fluorescent activity was seen in the lower NP dose groups and no fluorescence was observed in the control mice (**Figure 2.21**).

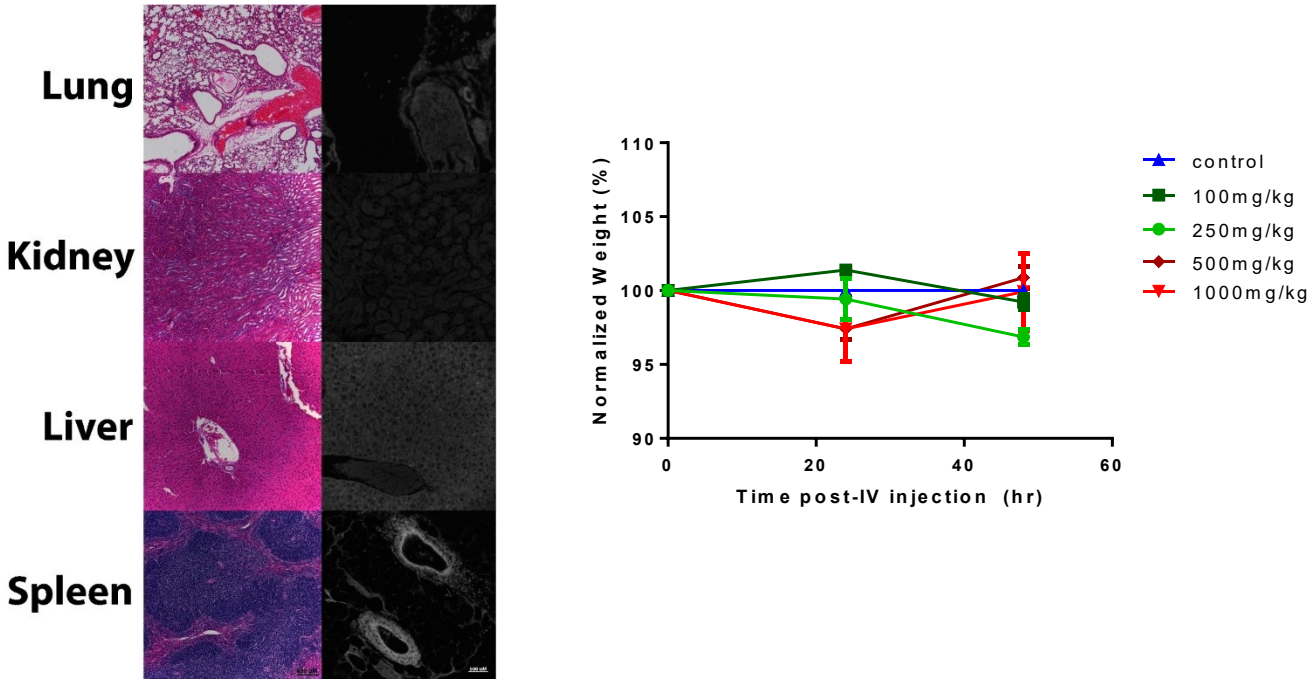

Figure 2.20: On the **left**, hematoxylin and eosin stain of organ histology of mice administered with the highest dose (1000 mg/kg) is shown on the **left**, and fluorescent confocal imaging of NP accumulation (using PPIX fluorescence signal, white) from the same dosage group, is shown in the **middle panel**. C57bl/6 mice weight shown as a surrogate of toxicity in control group and the four highest dose NP groups on the **right**

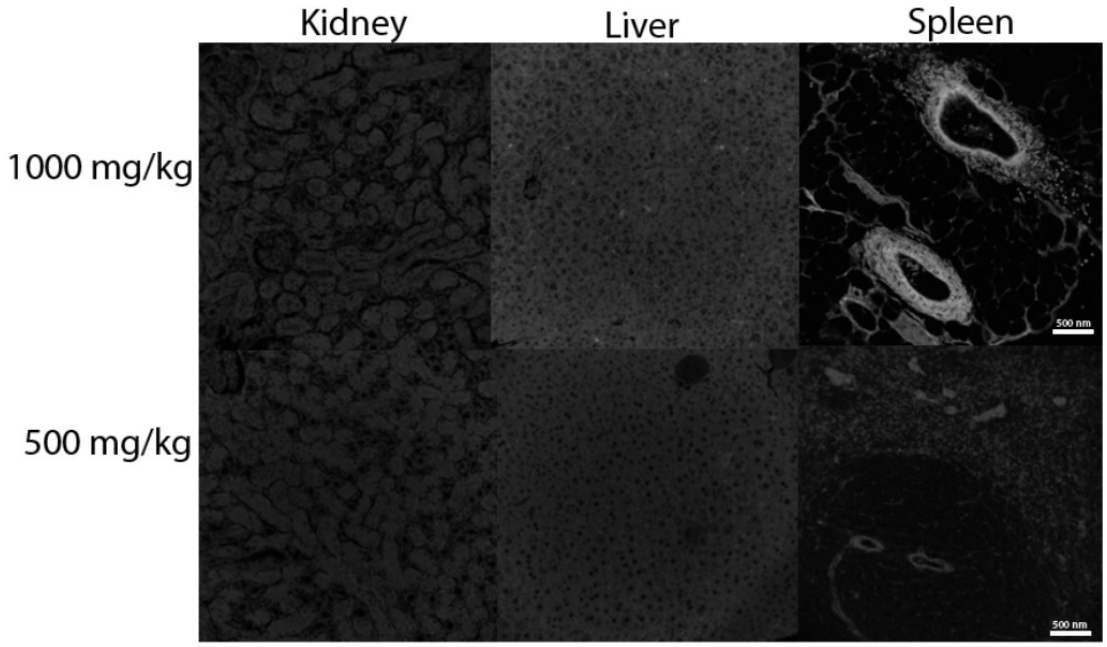

Figure 2.21: Organ fluorescence comparison on confocal imaging of mice injected with 1000 mg/kg and 500 mg/kg of radioPDT NP after 48 hours. More white=higher fluorescence signal. Kidney (**left**) did not show any visible difference between the two dose levels but liver (**middle**) and spleen (**right**) displayed appreciably greater fluorescence signal.

The *in vivo* toxicity profile is very low for the fully active anti-cancer NPs. The toxicity profile is most comparable to inactive PEGylated drug delivery vehicle only (277). This allows for flexibility in dosing and raises the potential TI for our radioPDT NP.

2.4 Summary of Synthesis, Characterization and Toxicity Studies

We successfully developed a novel luminescent NP system for radiation-activated photodynamic therapy (radioPDT) nanoparticle-based system. This potential theranostic tool combines the spatial penetration and localization of radiotherapy with the tumor-killing efficacy of photodynamic therapy. This can lead to potentially superior treatment of deep-seated tumors. Our unique system is comprised of three key components: nanoscintillators for luminescence under X-ray radiation, protoporphyrin IX as photosensitizers for PDT effect, and biodegradable PEG-PLGA nanospheres as carriers.

NSC of a homogenous size was synthesized using a wet chemistry technique under a nitrogen-protected environment. The use of a drop-wise synthesis produced small NP in the size range of 10 nm to 30 nm with relatively homogenous morphology and size distribution. The use of aqueous versus organic medium to synthesize the NSC, as well as different synthesis temperatures, allowed control over the crystalline lattice of the NSC, and allowed control over its luminescence spectra and magnitude. Through iterations in the synthesis process, a single emulsion nanodrop technique was arrived at as the best method of encapsulating the NSC and commercially bought PPIX into a PEG-PLGA nanocarrier, which was verified through TEM with bright field and elemental analysis, size exclusion chromatography, DLS, and UV-Vis absorbance spectroscopy. The synthesis procedure was easily scalable to large batch productions to allow *in vivo* studies with multiple animals while maintaining the same physical characteristics.

The NP was found to be highly stable in biological conditions for up to 24 hours, with no significant change in size or release of payload. It produced no discernable toxicity *in vitro* across multiple human cell lines. The radioPDT NPs were able to accumulate within the cytosol of PC3 prostate cancer cells. *In vivo* acute toxicity dose escalation study did not reach a dose limiting toxicity, and the study was terminated at 1000 mg/kg due mainly to difficulty suspending the NP in solution at such high concentrations. Biodistribution analysis via post-mortem organ examination under fluorescence confocal microscopy revealed accumulation and clearance of the NP mainly in the liver and spleen after 48 hours, which is consistent with clearance by the MPS system.

This novel radioPDT system was designed to meet the biomedical requirements for clinical utility and allows simultaneous targeting and therapy of cancer. The NPs showed high loading capacity, high stability, scalability, and biocompatibility as a cancer therapeutic agent. *In vivo* studies demonstrated uptake of the NPs in major organs but with no signs of toxicity as confirmed by physiological markers of animal health and histopathologic analysis.

Though other radioPDT systems have been developed and described (244, 278, 279), our radioPDT NP system uniquely balances toxicity and efficacy, making it suitable for clinical translation. The characteristics demonstrated here make it an ideal radioPDT system to carry forward into development and further experimentation for treating deep-seated tumors.

CHAPTER – 3

RADIATION-ACTIVATED PHOTODYNAMIC THERAPY (radioPDT) NANOPARTICLES IN TREATING HYPOXIC CANCERS *IN VITRO* AND DEEP-SEATED TUMORS *IN VIVO*

CONTRIBUTIONS

This research project was conducted in a multidisciplinary fashion due to required diverse skill sets. I conceived the nanoparticle and treatment paradigm, designed and performed the experiments, and prepared the manuscript for publication as described in the **Preface**. Dr. Hua Chen assisted in performing the *in vitro* experiments. Dr. Brad Warkentin assisted in radiation dosimetry calculations and delivery. Dr. Hans-Sonke Jans assisted in analysis of radiation dose-enhancement from the NP. Dr. Nawaid Usmani and Dr. David Murray assisted in rationale for radiation dose used and delivery method. Dr. Melinda Wuest assisted in PET imaging of mice. Dan McGinn assisted with the Small Animal Radiation Research Platform (SARRP) for irradiation of the animal models. Dr. Hua Chen assisted in data collection. Curtis Osinchuk and Lance Spiridon (Cross Cancer Institute Machine Shop) designed and produced the hypoxia chamber with my input. Dr. Aja Reiger assisted in planning the live/dead flow cytometry assay. Dr. Ravin Narain, Dr. John D. Lewis, and Dr. Ronald Moore provided guidance in experimental design, data interpretation, and manuscript preparation.

3.1 Introduction

RT is an important modality in cancer management along with surgical and drug therapies, and has been crucial in improving cancer survival rates in Canada (280, 281). RT is highly effective and is used to treat approximately 50% of cancer patients during their disease course and is used in 40% of curative treatments (282). Mechanistically, ionizing rays damage genetic material, which causes cells to undergo apoptosis, necrosis, senescence, or autophagy (283). Modern RT has evolved with sophisticated cell survival modeling with the linear-quadratic model, customized dose and fractionation schemes, and newer technology that can deliver highly focused doses of radiotherapy as reviewed above (284). However, toxicity remains the main limitation of RT. This is especially concerning for deep seated tumors, where significant radiation dose and consequent toxicity to surrounding normal tissues is inevitable. For example, prostate cancer's deep-seated nature leads to 20% of men experiencing significant RT related toxicity such as bowel, urinary, and/or sexual dysfunction (285, 286).

Despite the toxicity conferred by prostate radiotherapy, dose-escalation still confers further disease control benefit. Multiple dose-escalation studies have been pursued which show benefit to higher radiation doses (287). In terms of conventional fractionation, the current standard of 78 Gy in 39 fractions to treat high risk prostate cancer appears to be the limit mainly due a sharp rise in long-term toxicity (288). Studies that have pursued further dose escalation to as high as 86.5 Gy continue to show significant disease control benefit at the cost of significantly increased risk of toxicity (289-291). Similarly, dose escalation with brachytherapy boost after external beam in high-tier intermediate and high risk prostate

cancer has also demonstrated superior disease free survival to standard of care 78 Gy external beam radiotherapy in a Phase III trial, but has received limited adoption in standard clinical practice due to significantly increased serious long-term toxicity risk (292-294). Emerging evidence for SBRT of the prostate has also demonstrated the potential for good disease control but at the risk of greater radiation-induced toxicities (295). Similar evidence for lack of sufficient TI to warrant dose escalation in radiotherapy exist in other cancer sites (296-300). Newer radiation technologies offer the potential for more precise radiotherapy, but precision beyond current standard of care techniques has not yet manifested into more effective or safer treatment. Therefore, there is a need for novel methods of augmenting radiotherapy's TI.

Contemporary radiosensitizers are either biologic agents to augment radiation efficacy or radiation dose enhancers that increase dose deposition at the target. The utility of chemotherapeutic agents as radiosensitizers have been established for many years, and routinely provides a modest benefit, typically with 5 to 10% disease-free or survival benefit, at the expense of significantly increased toxicity (301-305). Newer epidermal growth factor receptor (EGFR) targeted radiosensitizers potentially offer the same therapeutic gain for less toxicity, but have been failing to demonstrate better survival benefit (306). Multiple biologic radiosensitizers have been advanced to augment radiotherapy, but despite decades of development their toxicity concerns limit adoption into standard practice in radiotherapy (307). Conversely, high Z nanoparticles like gold NPs that aim to increase local radiation dose have been relatively safe to use in a clinical setting but have not shown significant therapeutic effect (308, 309). To effectively augment radiotherapy for treatment of cancer, it seems an agent with practically negligible off-target

toxicity with significantly increased therapeutic efficacy needs to be developed in order to achieve a sufficiently high TI and gain traction in clinical use.

Here, I describe the use of a novel radioPDT NP with negligible toxicity in its inactive form, but once activated by radiotherapy it can significantly increase anti-tumor therapeutic effect. This was assessed by the ability to generate singlet oxygen via the radioPDT effect with the activating energy from radiation beams and significantly increasing tumor cell cytotoxicity in normoxic and hypoxic conditions. The effect of radiation and NP dose-dependency was evaluated, particularly for susceptibility to hypoxia in severe hypoxic conditions at low NP and radiotherapy doses. *In vivo* studies with immunodeficient mice xenografted with PC3 tumors was assessed for response to radioPDT treatment over radiation alone, via tracking tumor growth after treatment and survival differences over radiotherapy alone. These experiments were used to investigate the potential of our radioPDT NP (patent# WO/2019/241891) in augmenting the therapeutic effect of radiotherapy without increasing toxicity.

3.2 Materials and Methods

3.2.1 Cell lines and culture

A stock of human PC3 prostate cancer cell line obtained from Dr. R.B. Moore (University of Alberta) was grown in four passages and frozen in liquid nitrogen storage. All experiments were performed on cells cultured from within three passages from this stock batch. Cell cultures were maintained with RPMI 1640 medium supplemented with 10% fetal bovine serum (FBS) with 2 mM L-glutamine, 100 U/mL penicillin, 100 U/mL

streptomycin. Cells were cultured in incubators at 37 °C with 5% CO_2 content and 100% humidity. Cells were grown to 50% to 80% confluency before use in experimentation.

3.2.2 Design of a Hypoxia Chamber

A hypoxia chamber with predictable radiation dosimetry, light dosimetry, ease of transport/handling to the radiation vault and lab experimentation areas, and the ability to test multiple conditions needed to be developed for this study. In consultation with the Cross Cancer Institute (Edmonton, AB, Canada) machine shop, a radiotherapy phantom-grade clear acrylic air-tight chamber was developed with Stevens (Brampton, ON, Canada) 3-way high flow stop cocks to control airflow through two ports (inflow and outflow) and custom milled mounting surface for Corning® (Corning, NY, USA) or equivalent brand 96 well plate with no airgap to the bottom of the plate surface (**Figure 3.1**). The clear acrylic was verified to be transparent to 400 to 800 nm light via a spectrometer and light meter. The walls and floor of the hypoxia chamber were painted with matte black paint to avoid ambient light scatter. A port was bored into the side of the hypoxia chamber to fit a O_2 gas sensor (Vernier Software & Technology, Beaverton, OR, USA) sealed with two rubber O-rings. An acrylic lid with a silicon gasket and thumb screws was then affixed on top to form an air-tight seal.

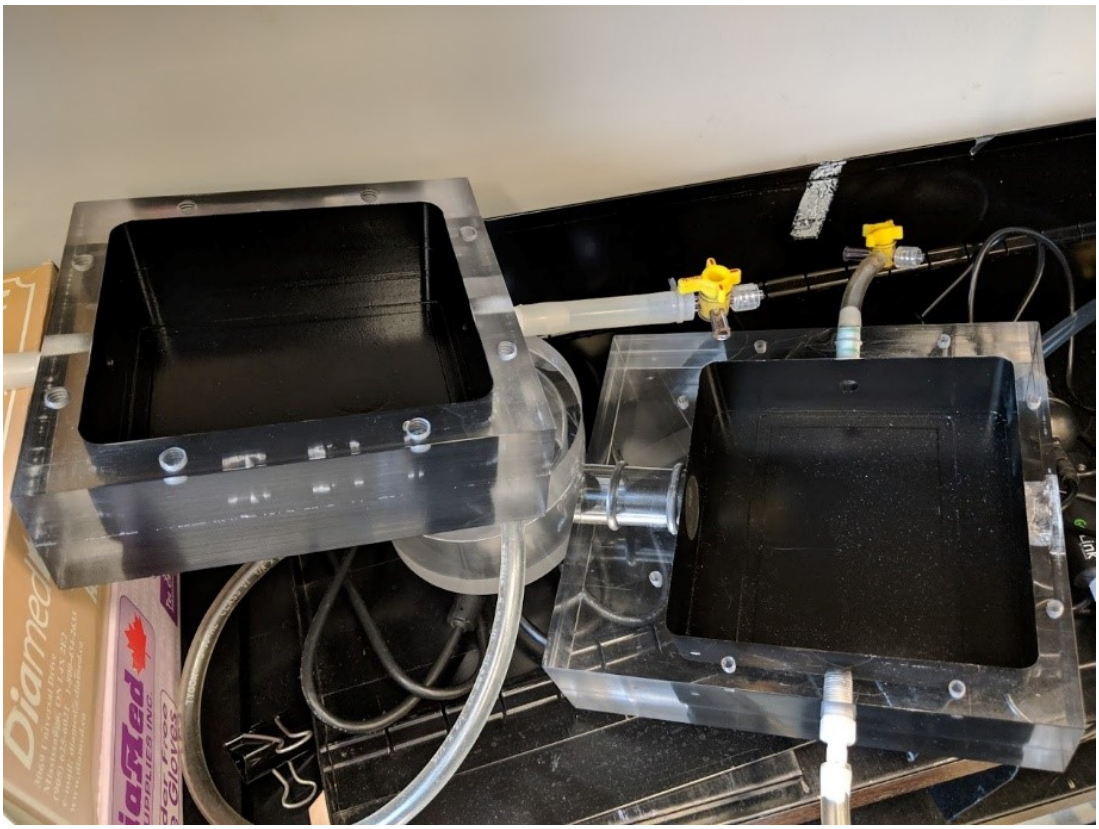

Figure 3.1: Hypoxia chambers developed to produce hypoxic atmospheric conditions for experimentation. The first version (**left**) included a O_2 gas sensor port directly into the side of the chamber, whereas the second version (**right**) moved the O_2 gas sensor to a separate chamber (seen below the chamber on the ***left***) mounted serially in line with the exhaust port of the hypoxia chamber.

The two air flow ports were connected to compressed gas source of N_2 and room air. The inflow port was connected to a pure compressed nitrogen source and compressed room air source 3-way stop cock. The incoming air was humidifed by a water chamber and regulators were used to control airflow pressures to balance the gas mixture. An outflow port was run through a water trap to prevent backflow (**Figure 3.2**). An oxygen gas probe (Vernier Software and Technology, Beaverton, OR, USA) connected to a laptop was used to monitor the chamber's ambient oxygenation and the desired oxygen concentration was reached by balancing inflow gas mixtures via the previously mentioned pressure regulators. Cells plated in a 96 well plate were placed into the chamber and sealed with the lid. Once steady state oxygen concentration was measured by the O_2 probe, the flow was maintained for 15 minutes to equilibrate with the cell media before the stopcocks were used to fully seal the chamber. The chambers were validated to hold a prescribed hypoxic condition for at least 24 hours by submerging the sealed chamber into water and assessing for leakage of water into the chamber or air observed to be escaping from the chamber. Additionally, the chamber was purged with pure N_2 gas and leakage of atmospheric oxygen back into the chamber was measured using the oxygen probe.

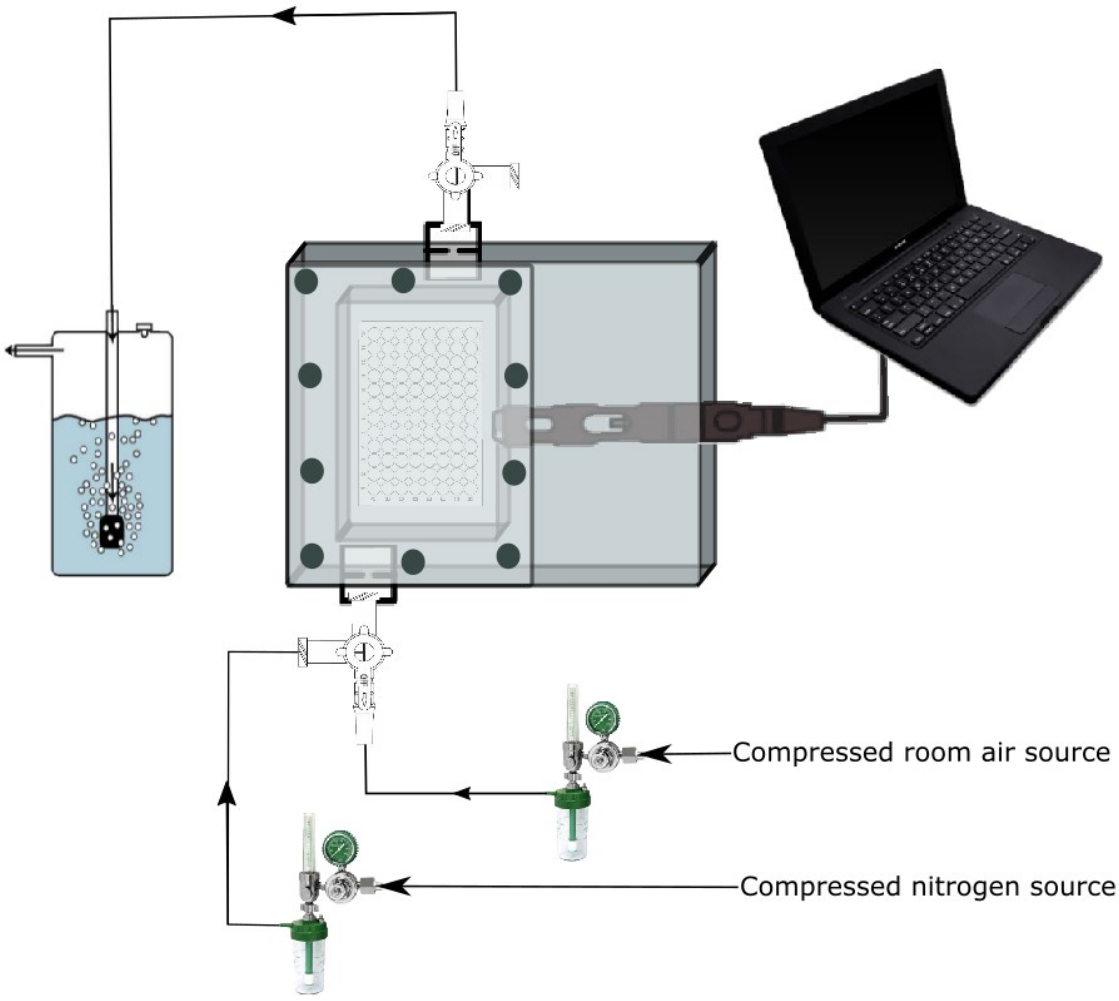

Figure 3.2: Schematic diagram of setup of the hypoxia chamber. Objects in the image are not to scale.

After the oxygen level in the chamber was allowed to equilibrate with the media in the wells, the cells were treated with irradiation from a light source or X-ray source. As the effect of oxygen availability on PDT is relevant during the active PDT process, and PDT consumes oxygen on the sub-microsecond time scale, prolonged periods of hypoxia were not needed to assess hypoxia's impact on radioPDT. Therefore, immediately after the treatment was complete, the chamber was unsealed to prevent confounding effects of long-term hypoxia (310-312).

3.2.3 Validation of novel radioPDT NP against light only PDT

The light PDT experiments were carried out with a monochromatic 20 Watt LED black flood light (HouLight, China) 402 nm light source (the Soret band of the PPIX PS for maximum excitation) that was measured for uniform illumination and wavelength fidelity with an Ocean optics (Largo, FL, USA) USB 4000 spectrophotometer and a Thorlabs (Newton, NJ, USA) PM100D light meter (**Figure 3.3**).

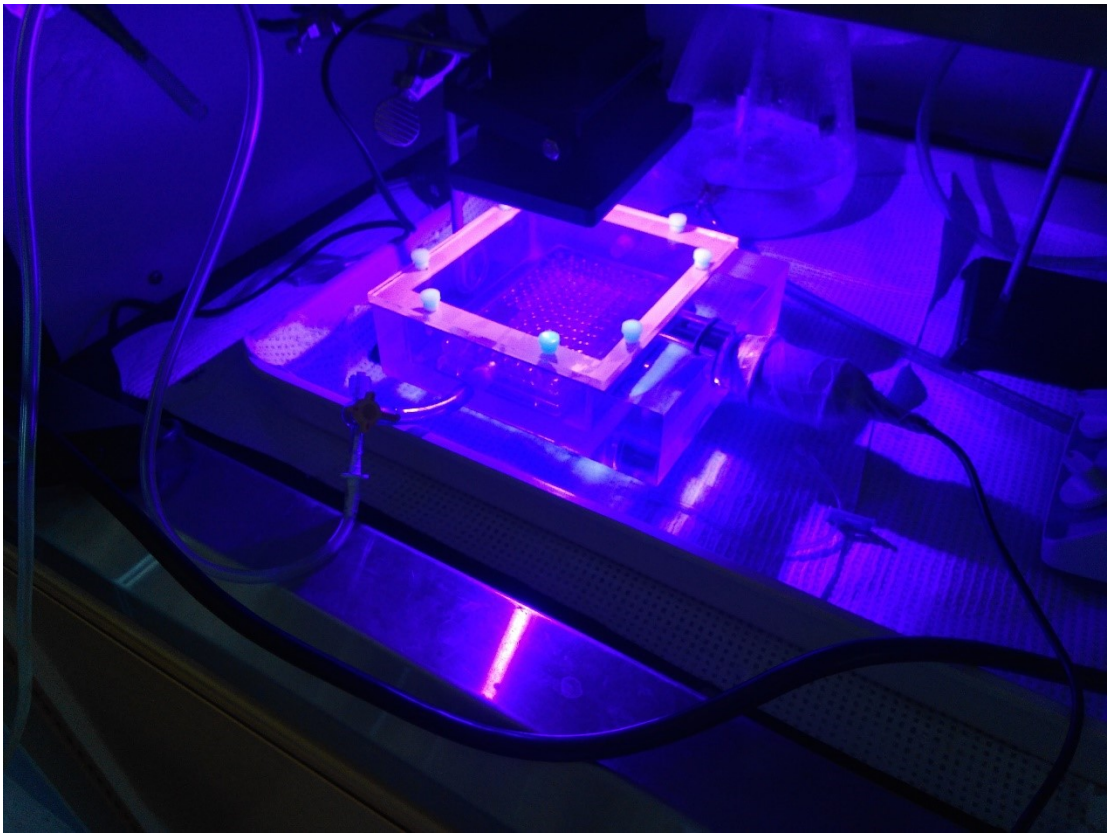

Figure 3.3: Experimental setup for light PDT. The 403 nm LED UV lamp (HouLight, China) has a standoff distance from the bottom of the wells such that inhomogeneity in light irradiation was reduced to less than 10% from the maximum on center. The oxygen probe was mounted directly into the chamber and sealed with two rubber O-rings. A gas inlet port and outlet port allowed custom gas mixtures of room air and pure N_2 to be introduced to form the desired hypoxic conditions.

At a standoff distance of 4 cm from the bottom of the cell culture wells (where the cells exist in a monolayer), the light intensity was measured using a light meter to quantify light irradiation dose, and homogeneity was measured at <10% difference from center of the field to field-edge.

Cells were plated into 96 well plates at a cell density of 5,000 cells per well with 100 μL media and left to grow overnight. A standardized batch of NSC, radioPDT NP, and 50 μM PPIX was synthesized as described in **Section 2.2.1.2** and assessed for NP concentration and payload content via DLS by Nanosight NTA and UV-Vis absorbance by Nanodrop™ 2000, respectively. The NP concentrations were prepared into treatment aliquots in cell culture media solution on the day of experiment. Dosing was done at a highest dose of 1×10^{12} NP/mL and serial dilutions by 50% dilutions down to 6.25×10^{10} NPs/mL for the radioPDT NP, 50 μM to 3.12 μM for PPIX, and 15 mg/mL to 0.9 mg/mL for NSC.

Cytotoxicity with activated NP under 10 J/cm^2 (dose rate = 21.1 W/cm^2) light activation and radiation activation was measured using Alamar blue assay. The radioPDT NP, NSC, and PPIX were used to treat PC3 cells in a 96 well plate 4 hours prior to light activation and left overnight until media was exchanged on the next day. Alamar blue dye (10% v/v) was added 72 hours post-treatment, and the fluorescence was measured with a FLUOstar Omega plate reader with excitation wavelength of 485 nm and emission wavelength of 520 nm. Cell viability was calculated as a ratio percentage of the treated cell's fluorescence versus control cells. Experiment was done at 20% oxygen (room air) and 1% oxygen conditions. All experimental conditions were analyzed in triplicate.

3.2.4 Radiotherapy Delivery *in vitro*

Radiation experiments were carried out in accordance to Xstrahl's (Camberley, Surrey, UK) standard operating procedure, with the radiation dose correctly calculated in collaboration with the Department of Medical Physics (Cross Cancer Institute). **Figure 3.4** shows the experimental setup in use. The Xstrahl 300 orthovoltage machine (Camberley, Surrey, UK) was used with machine's applicator N (10 cm x 15 cm, 50 cm^2 FSD), 300 KVp filter, a standoff distance of 2.5 cm to the meniscus of the media in the 96 well plate, depth of penetration of 1 cm to the bottom of the well, and back-scatter factor of 0 cm since the acrylic of the chamber is isodense to the cell media with no air gap. The MU to deliver per desired radiation dose was calculated as follows:

Dose rate (MU/minute) = Adjusted dose rate (ADR) x Percent Depth Dose (PDD) x standoff

Where PDD is the percent of radiation dose deposited at the reference point of the bottom of the wells, where the cells would be adhered to in a monolayer.

MU = Dose / Dose rate

ADR was obtained for the specific energy and applicator from the standardized values provided by Medical Physics' calibration and quality assurance measurements (Cross Cancer Institute, Edmonton, AB, Canada).

Figure 3.4. Experimental setup of *in vitro* irradiation conditions using an Xstrahl 300 clinical irradiator (Camberley, Surrey, UK) and an in-house developed hypoxia chamber.

3.2.5 Singlet Oxygen Yield Studies of radioPDT NP in Normoxic and Hypoxic Conditions

Singlet oxygen yield was measured using a commercially available probe kit: Singlet Oxygen Sensor Green (SOSG, Invitrogen, ThermoFisher Scientific, Waltham, MA, US). 100 µL of control (1x PBS), NSC NP, PPIX NP, and radioPDT NP in PBS were plated into a white 96 well fluorescence plate (Corning®, Corning, NY, USA) at a concentration of $5x10^{11}$ NP/mL. SOSG probe was prepared by dissolving the dry powder in 330 µL of anhydrous methanol to make 500 µM SOSG. The SOSG solution was then added to PBS (pH 7.4) to make 20 µM concentration of SOSG. 100 µL of the SOSG probe was added to each well to make a final concentration of 10 µM. The experimental setup was verified using conditions described and documented previously (193). Briefly, a 5 µM PPIX and dilutions of SOSG probe of 15 µM, 10 µM, 5 µM and 2.5 µM were irradiated with a 690 nm (a commonly used Q band absorption wavelength of PPIX) diode laser (Optical Fiber Systems Inc., New Ipswich, NH, USA) in standardized NP concentration and irradiation was used to select the SOSG concentration that gave the best signal to noise ratio.

Under dark conditions, the well was irradiated using the experimental method described in **Section 3.2.4**. The predetermined amounts of PPIX in PBS buffered solution was exposed to varying fluence of light with the gain in SOSG probe fluorescence measured as a surrogate for $^1O_2$ yield. The SOSG fluorescence was measured using a FLUOstar Omega plate reader (BMG Labtech, Ortenberg, Germany) with an excitation wavelength of 485 nm and emission wavelength of 520 nm. Measurements were taken immediately prior to and after treatment with radiation.

The experiment was repeated for different radiation doses at 2, 4, 6 and 8 Gy, in oxygen conditions ranging from 20%, 10%, 5% and 1%. All measurements were done in triplicate

and repeated at least three times. Analysis of singlet oxygen yield was done by comparing baseline SOSG fluorescence with post-treatment fluorescence reading. The resulting gain in SOSG signal was expressed as a ratio of post-treatment/pre-treatment value per well.

3.2.6 *In vitro* Cytotoxicity under Normoxic and Hypoxic Conditions for Radiotherapy Alone, radioPDT, NSC NP, PPIX NP, and PEG-PLGA NP

3.2.6.1 Colorimetric Assay and Clonogenic Assay Cytotoxicity Studies

Cytotoxicity experiment with radiation activation of the NP was carried out similar to **Section 3.2.3**. Experiments were done at doses ranging from control (0 Gy) to 8 Gy of radiation at oxygen concentrations ranging from 1% to 20%. These findings were correlated with sample colony forming assays performed with the assistance of Dr. Baht. The starting plating density was determined by irradiating different cell densities ranging from 250 cells/well to 50 cells/well in radiation doses of 0, 2, 4, 6 and 8 Gy in 24 well plates. The cells were initially irradiated in 96 well plates at radiation doses of 0, 2, 4, 6 and 8 Gy in the hypoxia chamber at oxygen levels of 1%, 5%, 10%, and 20% in duplicates. **Figure 3.5** shows the different conditions tested for cytotoxicity.

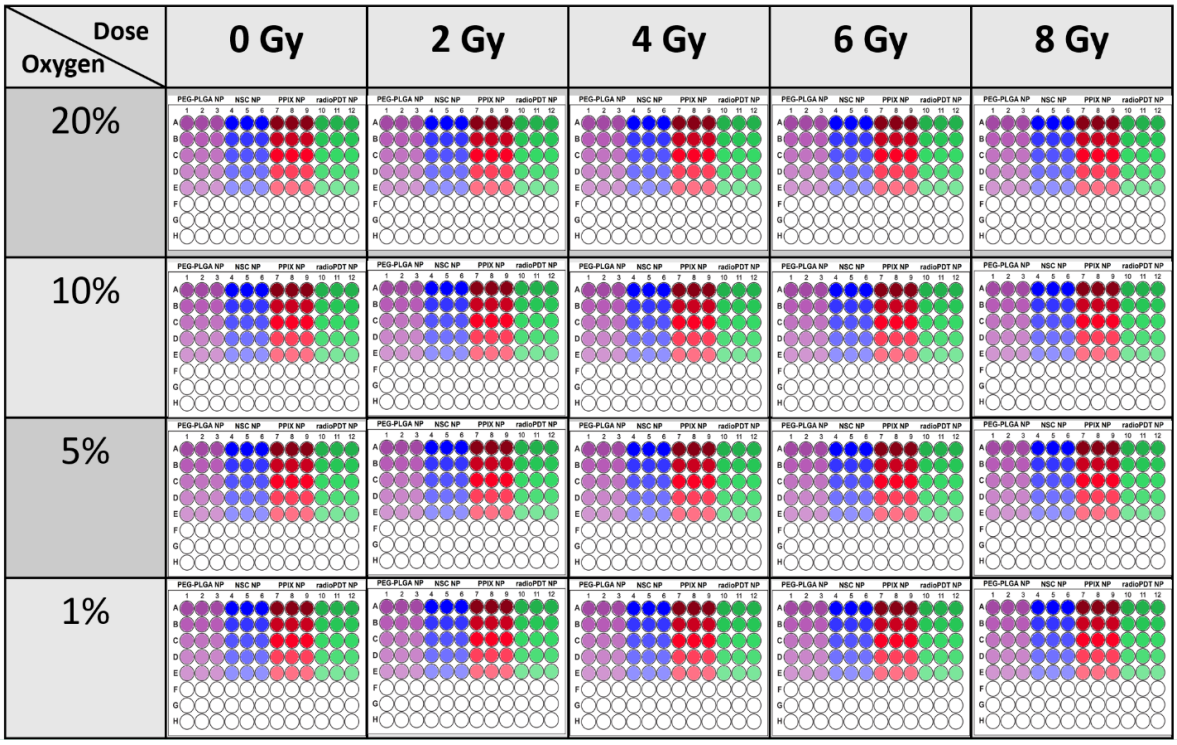

Figure 3.5: Permutations of cytotoxicity assay assessing at different radiation doses, oxygen levels, NP types, and 5 NP concentrations ranging from $1x10^9$ NP/mL to $6.25x10^{10}$ NP/mL. **Purple**: PEG-PLGA NP; **Blue**: NSC NP; **Red**: PPIX NP; **Green**: radioPDT NP.

Each plate contained 4 replicates of each NP treatment condition. After irradiation, the cells were incubated overnight and one replicate from each NP treatment condition was trypsinized and plated at the appropriate density as determined above into a 24 well plate. The plates were incubated for three weeks with cell media changed three times per week before being stained by crystal violet and the colonies formed counted.

3.2.6.2 Live/Dead Flow Cytometry Assay

Further cytotoxicity analysis was assessed by live/dead flow cytometry assay (313-317). The assay was first calibrated with propidium iodide (PI) and 4',6-diamidino-2-phenylindole (DAPI) stains. The rationale of this assay is that PI and DAPI are fluorescent stains that are ineffective at passing through live cell membranes in viable cells. In late apoptotic and dead cells, the cell membrane loses integrity and allows these stains to pass through. PI is a DNA intercalator that increases in fluorescence after binding to the DNA structure found in cell nuclei (318). DAPI binds to the minor groove of adenine-thymine rich segments of DNA and also becomes more fluorescent (317). Both are effective dyes at staining dead and dying cells and are amenable for use in evaluation and quantification of dead cells by live/dead flow cytometry. The calibration assay was done with PC3 cells plated in triplicates in 5 plates. The plates were irradiated at a dose level of 0, 2, 4, 6 and 8 Gy. Then the cells were grown for another 72 hours in the plate with the media was exchanged with phenol red-free RPMI as to not interfere with the flow cytometry reading. The cells were transferred to a nonadherent 96 well plate with the same media to preserve the dead cells in suspension. The DAPI stain was added at a final concentration of 1 μg/mL within 1 hour of the plate being analyzed, and the PI stain at a final concentration of 2

μg/mL was added ideally within 20 minutes of being read.

An LSR-Fortessa X-20 cell analyzer and BD FacsDiva™ software (BD Biosciences, San Jose, USA) with an automated plate reader attachment was used to perform flow cytometry. The DAPI signal was excited using a 488 nm excitation laser and the PI signal was excited using a 633 nm laser. Forward and side scatter was measured. Analysis was done using FlowJo© v10.4 (BD Life Sciences, San Jose, USA). The cells were gated on the forward and side scatter acquisition to include the population of PC3 cells as well as dead cells or fragments of dead cells. From there, the control (unirradiated) plates were gated for fluorescence versus forward scatter of the live/dead marker to show between 0% to 1% dead cells. This same gating was used for all other irradiated cells from the same oxygen concentration to determine additional cell death beyond the control condition. The dead cell population was expressed as percentage of the total cell population in the well. The live/dead flow cytometry assay was calibrated using cells irradiated at 0, 4 and 8 Gy doses.

Cytotoxicity of the radioPDT NP under control and irradiated conditions was assessed as described in the first paragraph of **Section 3.2.6.1** except with the use of the live/dead flow cytometry assay instead of colorimetric and clonogenic assays.

3.2.7 *In vivo* Comparison of the Effect of radioPDT NP with a 4-arm Study Investigating Control, radioPDT NP, Radiotherapy, and Combination radioPDT with Radiotherapy

3.2.7.1 PC3 Prostate Cancer Xenograft Mice Flank Tumor Mice Model

Male NOD-*scid* IL2Rgamma^{null} (NSG) mice were obtained from Dr. L.Postovit (University of Alberta) breeding colony located on campus. Mice were obtained between

4 to 6 weeks old and transferred to the Cross Cancer Institute animal vivarium with an institutionally defined quarantine period. The mice were lightly anesthetized with 2-4% inhaled isoflurane gas and injected subcutaneously into the flank with 100 µL PBS containing 3,000,000 PC3 prostate cancer cells grown to 80% confluency in cell culture. The tumors were grown to a size of 500 mm^3 as measured by calipers with the formula: Volume=L*W*H*π/6. The typical time to reach this size was 6 weeks post-injection. After reaching the target tumor size, experiments were started, and the tumor volume was tracked every 2 to 3 days. The mice were tracked for behavioural changes, weight loss of greater than 10%, fur loss, skin ulceration, and infection. Maximum allowable tumor size per protocol was 1200 mm^3. If the maximum tumor size was reached or the animal displayed significant signs of suffering, the animal was euthanized. Post-mortem analysis consisted of necropsy and harvesting of heart, lungs, liver, spleen, kidneys, tumor, left quadriceps muscle, and any visible tumor metastases.

3.2.7.2 In vivo Treatment with NP

The mice lightly anesthetized 2-4% inhaled isoflurane gas and were treated with radioPDT NP at dose of 400 mg/kg via IT injection of NP suspended in 50 µL PBS injection. Multiple (>10) injections were done per IT injection starting from the center and fanning out radially. The mice were left to recover overnight before experiments were conducted the next day. A parallel control group was injected with 50 µL PBS IT.

3.2.7.3 Radiotherapy with the Small Animal Irradiator

Radiation was delivered to the mice flank tumors in an IGRT fashion using the Xstrahl SARRP and Muriplan/Murislice software (Xstrahl Medical & Life Sciences, Camberley,

UK) located in the Cross Cancer Institute animal vivarium. The animals was maintained under anesthesia with continuous flow inhaled isoflurane gas at a concentration 1-2.5% and a flow rate of 0.5 L per minute. The animals were positioned on the contralateral flank (decubitus) from the tumor to facilitate tangential targeting to maximally spare normal tissue irradiation (**Figure 3.6**).

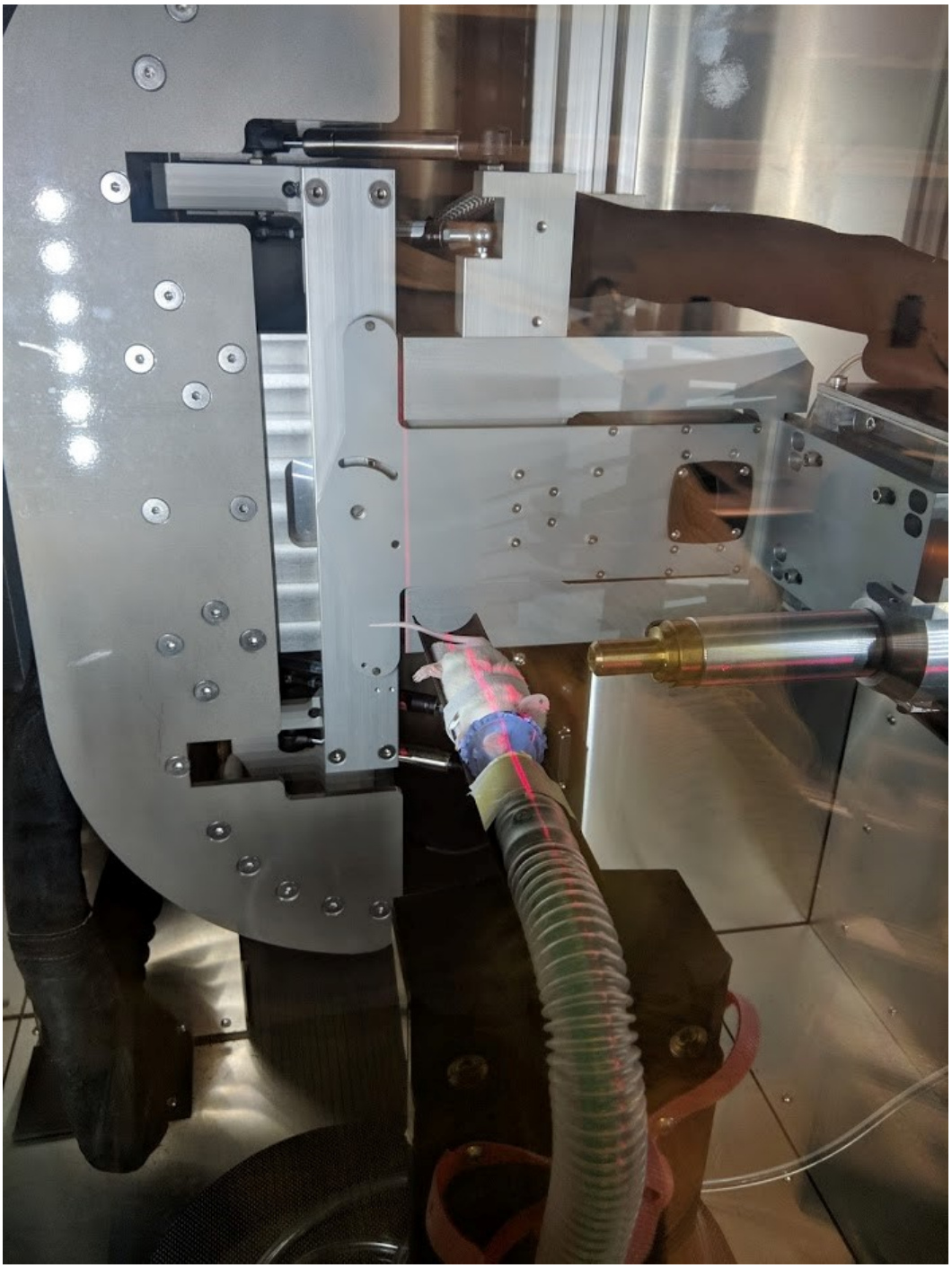

Figure 3.6: Setup of animal on SARRP system for irradiation. The mouse was positioned on the flank contralateral to the tumor thereby raising the tumor above the plane of most of the animal's body allowing targeting with tangential beams.

The animals were imaged using the SARRP's onboard Cone Beam Computed CT (CBCT) that was used to plan the tumor radiotherapy. The radiation volume was contoured to include the tumor using the Xstrahl Muriplan software. Treatment was delivered using a 1-2 isocenter forward planning multi-beam unmodulated technique. In general, a three-field technique parallel-opposed tangent beams with single orthogonal beam balanced at a beam weight at 40%, 40% and 20%, respectively was used. Muriplan was used to generate isodose curves and dose-volume histogram (DVH) for the prescription dose. Care was taken to ensure the 100% isodose line covered the whole target of tumor volume and at least 95% of the tumor volume was covered with the prescribed dose. Hotspot was limited to 110%. Maximum dose as evaluated by isodose distribution curves was limited to <2 Gy to all normal structures, and <1 Gy to the bowels and kidneys as these are the most radiosensitive organs within the radiation field.

A calibration pilot experiment was done to arrive at a dose of 6 Gy single fraction that would significantly reduce tumor volume to about half of the starting volume within 10 days, but still allow the tumor to regrow and progress. This was done to ensure the radiotherapy delivered significantly delayed tumor progression but did not ablate or cure the tumor. This allowed any additional treatment effect of adding radioPDT NP to be realized and measurable. It also allowed non-traditional radiobiological effects, such as significant acute vascular injury, sphingomyelinase-mediated ceramide production, cell membrane disruption, and increases in TGF-β; mitogen-activating protein kinase (MAPK); EGFR; and other cell signalling factors to be minimized in order to assess the radioPDT effect without confounding effects of ablative dose radiotherapy (319-325).

3.2.7.4 Assessment of radioPDT Effect *in vivo*

A four-arm comparative study was done consisting of: control (Arm I), radiotherapy only (Arm II), radioPDT NP only (Arm III) and radiotherapy and radioPDT NP combined (Arm IV) (**Figure 3.7**). PC3 xenografted NSG mice were treated with NP or control as described in **Section 3.2.7.2**. The animals in Arm II and IV were treated the next day 6 Gy in a single fraction treatment as described in **Section 3.2.7.3**. The animals were then monitored over the next 60 days with tumor measurements taken every 2-3 days and the animal's weight, behaviour, and skin monitored for signs of distress, toxicity, and ulceration/infection, respectively. The animals were euthanized if they displayed any signs of significant morbidity or the tumor reached a size of 1200 mm^3. Primary endpoint for the experiment was tumor response as measured by tumor volume changes over time, and secondary endpoints were for OS, evidence of metastatic disease, and signs of significant toxicity. If the animals were alive at the end of the 60-day monitoring period, a post-treatment PET scan was performed, and the animals were euthanized for post-mortem analysis.

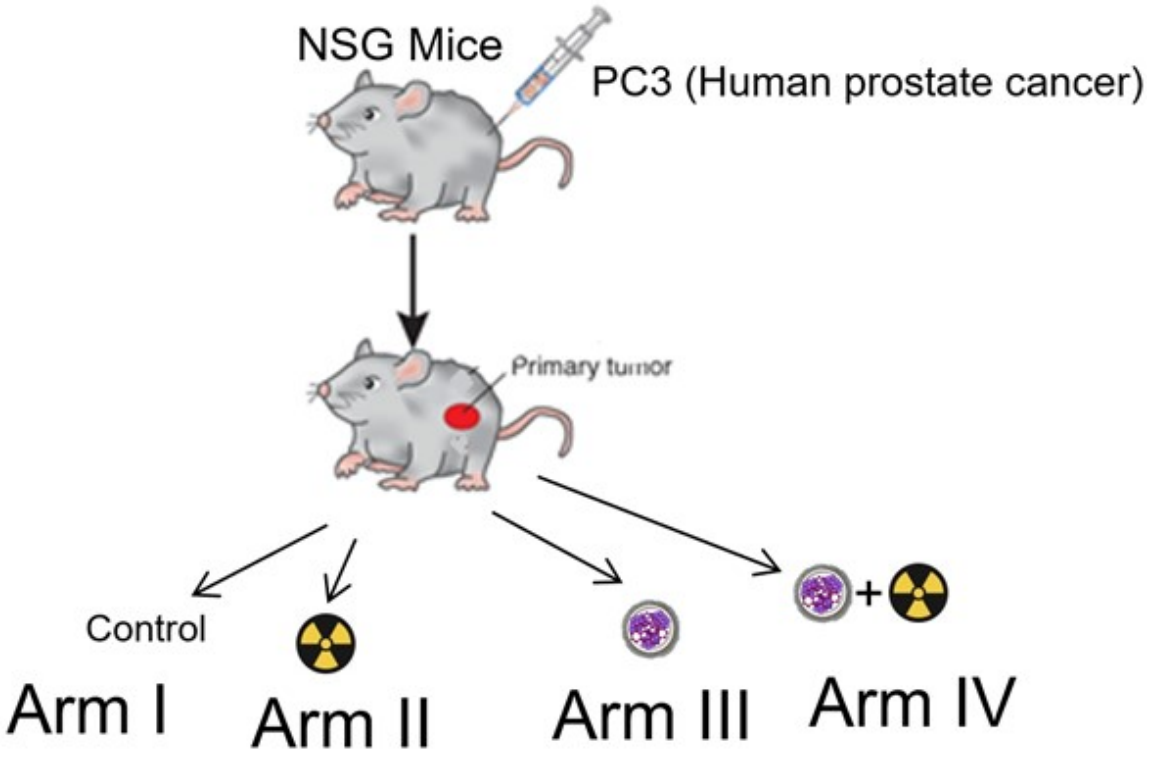

Figure 3.7: Study design of the *in vivo* radioPDT treatment study on PC3 flank tumor xenograft mice (N=4 per treatment group). The mice were littermates obtained from the same breeding colony. All mice were injected in the flank with standardized amount of PC3 cells and allowed to grow to the same tumor volume before experiments were started.

3.2.7.5 Acute Response to Treatment by [^{18}F]FLT-PET Scan

As an indicator of early response to radiotherapy, there have been preclinical and clinical studies using radiolabelled fluorothymidine (FLT) with ^{18}F in a positron emission tomography (PET) scan to assess for FLT avidity pre and post treatment (326). This is theorized to be a marker of DNA synthesis in highly proliferative cells, as the FLT is phosphorylated by upregulated thymidine kinase 1 (TK1) activity after passively entering the cell and remains trapped intracellularly, limiting its clearance from the body (327-330). The use of [^{18}F]FLT-PET scan is thought to be an early marker of tumor response and correlate with eventual tumor regression or progression.

[^{18}F]FLT radiotracer was produced by the Cross Cancer Institute cyclotron by the technicians of Dr Frank Wuest's lab (University of Alberta). Animals were anesthetized with 1-4% isoflurane gas and IV injected in the tail-vein with 5 Megabecquerel (MBq) of radiotracer. The mice were allowed to recover 1 hour before being reanesthetized and maintained under anesthesia for PET scanning on a Siemens Inveon pre-clinical PET and microCT scanner (Siemens, Germany). A 15 minute static whole animal scan protocol was used to image the mice. After PET scanning, the animals were awoken and allowed to recover. Images were analyzed using a Region of interest Visualization, Evaluation, and Image Registration (ROVER) software package (ABX GmbH, Radeberg, Germany) assessing for standardized uptake value (SUV) mean.

3.2.7.6 End of Study Assessment of Residual Disease with [^{18}F]FDG-PET/CT scan

To assess for evidence of residual disease at the end of the follow-up period, a ^{18}F tagged fluorodeoxyglucose ([^{18}F]FDG) PET scan was used to assess for evidence of residual

tumor activity and look for evidence of metastatic disease. [^{18}F]FDG-PET/CT scans are routinely used in clinical and preclinical settings to look for evidence of increase glucose metabolic activity. In cancer cells, this is mediated through the Warburg effect, which leads to preferential uptake of glucose and glucose analogs (331). [^{18}F]FDG that enters the cell is phosphorylated by hexokinase and is sequestered in the cell, slowing its rate of clearance from cancerous tissue (332). A PET scanner was then be used to observe regions of increased FDG avidity that correlates with cancerous tissue.

Mice that were still alive after the 60 day follow-up period were anesthetized and injected with 5 MBq of [^{18}F]FDG similar to **Section 3.2.7.5**. The animals were also CT scanned in the same session using the micro-CT component of the Siemens Inveon pre-clinical scanner. The mice were then sacrificed and areas of disease were assessed on necropsy.

3.2.8 Statistics

All calculations and statistical analysis were performed using Microsoft Excel 2016 (Microsoft, U.S) and GraphPad Prism 6 (USA). The graphs were plotted using GraphPad Prism 6 (USA) and FlowJo (USA). Significance for singlet oxygen yield, cytotoxic yield, and tumor response was done with analysis of variance (ANOVA) comparing multiple groups and Tukey's multiple comparison test. Dose-response relationship of oxygenation to cytotoxic yield with radioPDT was analyzed using a sigmoidal curve fit and assessing for IC50 value. Survival analysis was done by Mantel-Cox long-rank test comparing different arms to each other. All analyses use an $p=0.05$ as the threshold for significance.

3.3 Results and Discussion

3.3.1 Validation with Traditional Light PDT

To assess baseline PDT performance of the radioPDT NP, the cytotoxic effect was measured against a positive control of the commonly used PS PPIX at 50 μM, and NSC as control to assess for confounding toxicity effects of the scintillator. Viability of the cells was assessed by Alamar blue 72 hours post-irradiation with the 403 nm light source. Cells were maintained in dark conditions other than during PDT treatment with the light source. The experiment was done over different concentrations of drug to assess for dose-response effects, and in normoxic (20% oxygen) and hypoxic (1% oxygen) conditions to assess for dependence on availability of environmental oxygen.

The radioPDT NP were capable of significant PDT effect under traditional light irradiation. Cells demonstrated comparable PDT effect to PPIX alone (**Figure 3.8b-c)**. Under 10 J/cm^2 irradiation with UV light (403 nm), which is within range of the absorbance maxima of the PPIX PS, the cell viability dropped to 15-20% compared to control conditions, with much of the dose-effect seen at 2.5x10^{11} NP/mL. The PPIX content of the radioPDT NP was much higher than with aqueously dissolved PPIX used as the positive control in this experiment. There was no effect seen by illuminating the NSC impacting cell viability in treated versus untreated conditions (**Figure 3.8a-c**). The effect of hypoxia appeared to decrease the cytotoxicity of the radioPDT NP, particularly at lower concentrations of 1.25x10^{11} NP/mL (**Figure 3.8c**). Similar effects were not produced in PPIX, although this may reflect limitations in sensitivity of the assay and the magnitude of decrease in cell viability was quite a bit lower with PPIX alone than with radioPDT NP. A comparison of

the effect of 20% versus 1% oxygen concentration on PDT effect with PPIX and radioPDT is showin in **Figure 3.8d**).

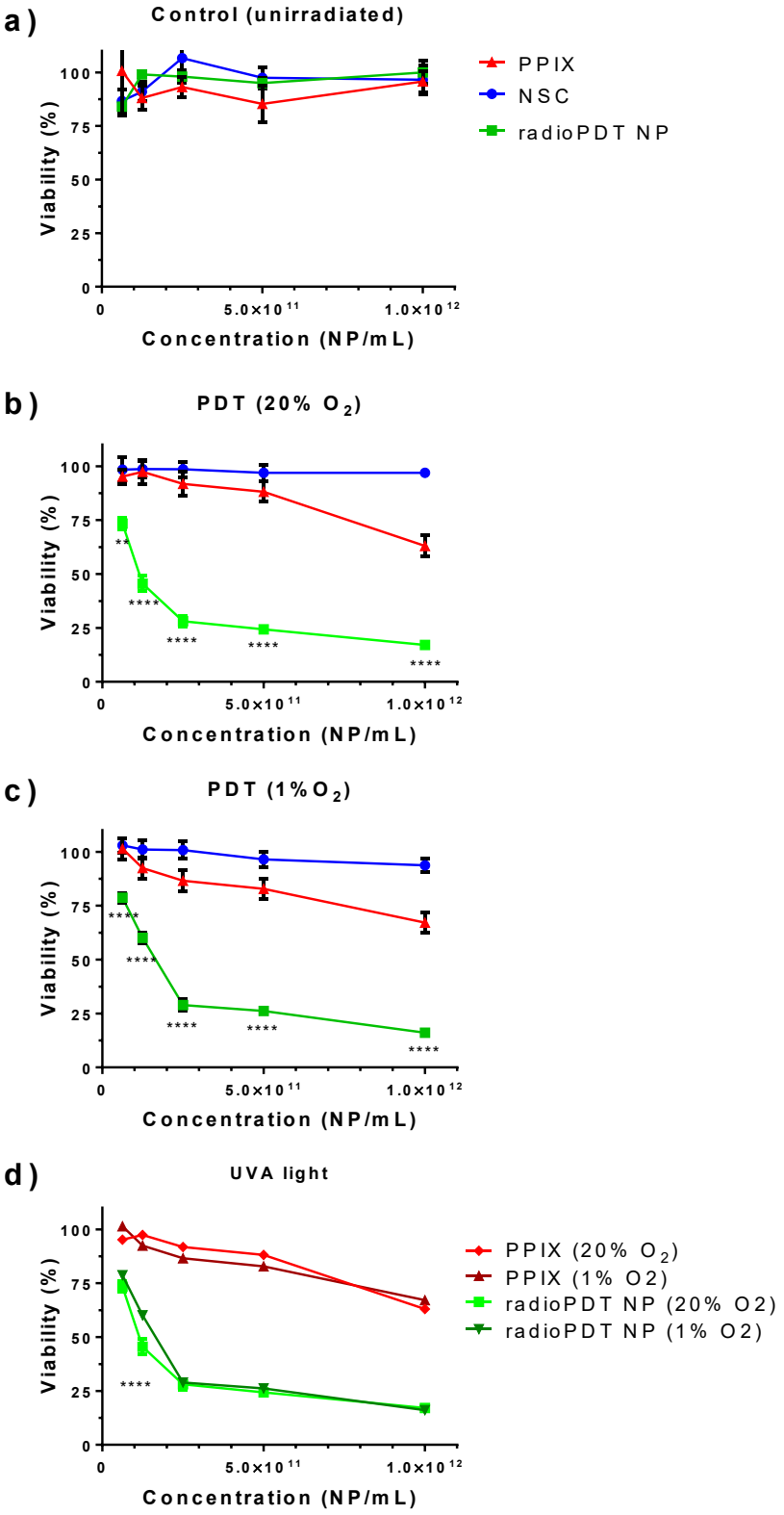

Figure 3.8: PDT effect of radioPDT NP compared to 50 μM PPIX and NSC alone in

control (unilluminated), (**a**) 10 J/cm^2 in normoxia, (**b**) and 10 J/cm^2 in hypoxia (**c**) conditions. Comparison of the PPIX and radioPDT NP in normoxic and hypoxic conditions shows significantly less cytotoxicity in hypoxic condition at lower concentrations of radioPDT NP (**d**).

3.3.2 Singlet Oxygen Yield of radioPDT in Normoxic and Hypoxic Conditions

To determine the mechanism of enhanced cell-kill, a correlative singlet oxygen yield study was performed to investigate the activity of PDT effect, since singlet oxygen is main cytotoxic effector of photosensitizers such as PPIX (333). The impact of radiation dose and hypoxia on singlet oxygen yield from the radioPDT effect was measured using the commercially available singlet oxygen sensor SOSG kit (Thermofisher, Waltham, USA). This is a green fluorescent probe that undergoes endoperoxidation when exposed to singlet oxygen, which greatly increases its fluorescence signal (334). The probe is considered highly specific for singlet oxygen over other ROS species, and its use in radioPDT has been validated in other studies (195).

To choose the appropriate concentration of SOSG for use in our radioPDT system, a calibration experiment was performed using dilutions of SOSG from 15 μM to 2.5 μM. The SOSG fluorescence was measured at baseline and after 1, 2, and 3 minutes of exposure to a 690 nm diode laser source (**Figure 3.9**). The time points were used to generate a linear regression line and the slope was used to evaluate the SOSG probe's performance at each given concentration. The 10 μM SOSG concentration was found to have the highest slope and therefore best gain in signal for a given increase in singlet oxygen. Therefore, 10 μM was the concentration used in further experiments.

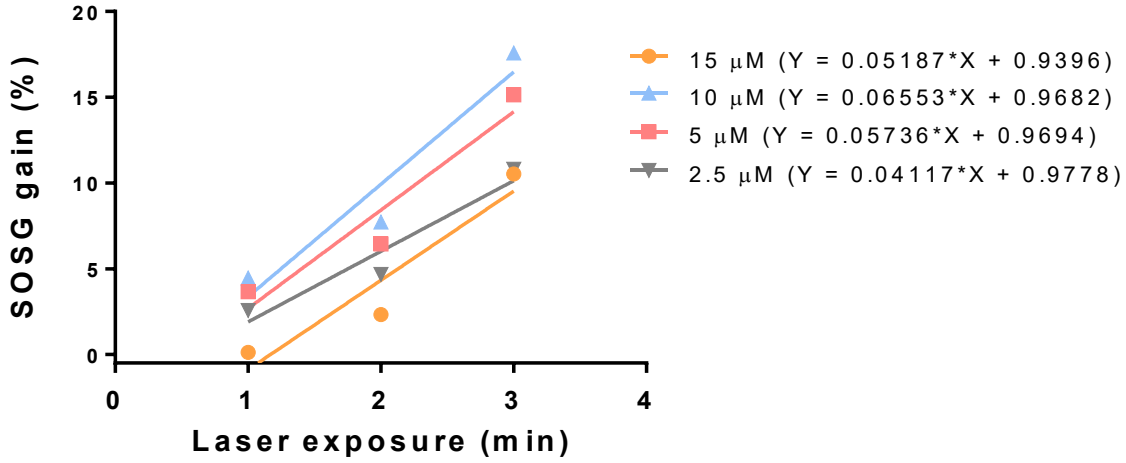

Figure 3.9: Measurement of SOSG increase after exposure to a 630 nm laser source in a solution of 5 µM PPIX. Different concentrations of SOSG were assessed over 3 laser exposure times to generate a linear regression line. The equation for the linear regression line is shown in the legend.

Further singlet oxygen yield studies were done with radiotherapy as the activation source, ranging in dose from 2 Gy to 8 Gy. Oxygen availability was controlled using the hypoxia chamber with oxygen concentrations ranging from 20% (room air) to 1%. The oxygen level was controlled to within ±0.5% with the aid of the O_2 gas probe and adjusting gas mixing ratios. The PEG-PLGA NP, NSC NP, PPIX NP, and radioPDT NP were loaded in a concentration of $5x10^{11}$ NP/mL with their payloads standardized using UV-Vis spectroscopy. **Figure 3.10** shows the resulting radiation dose-response curve per NP in gradients of hypoxia. There is a statistically significant difference in general dose response seen only in the radioPDT NP, indicating relationship between radiation energy and transfer to singlet oxygen yield. The radioPDT NP also had a significantly greater therapeutic yield ($p<0.05$) across all oxygen conditions at radiation doses of 6 Gy and 8 Gy. The other NP conditions do not show evidence of yielding singlet oxygen in response to radiotherapy, and no statistically significant difference was observed. Only the radioPDT NP is capable of using FRET to transfer radiation energy to the PS in order to undergo a Type II reaction and produce singlet oxygen.

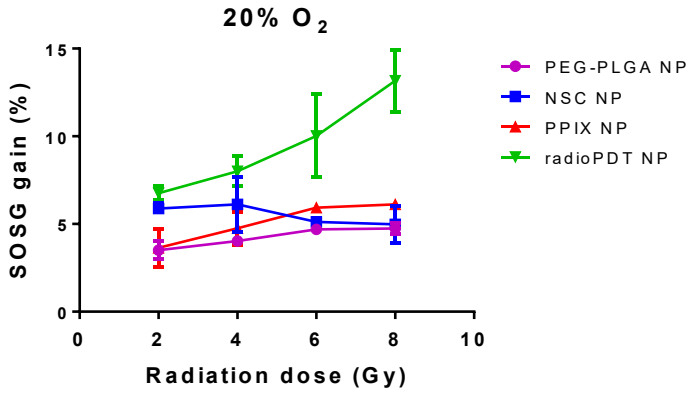
20% O2
SOSG gain (%)
Radiation dose (Gy)
PEG-PLGA NP
NSC NP
PPIX NP
radioPDT NP

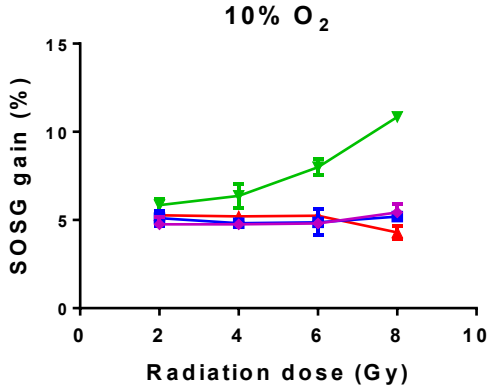
10% O2
SOSG gain (%)
Radiation dose (Gy)

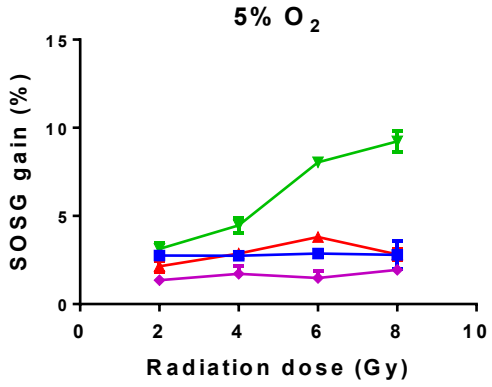
5% O2
SOSG gain (%)
Radiation dose (Gy)

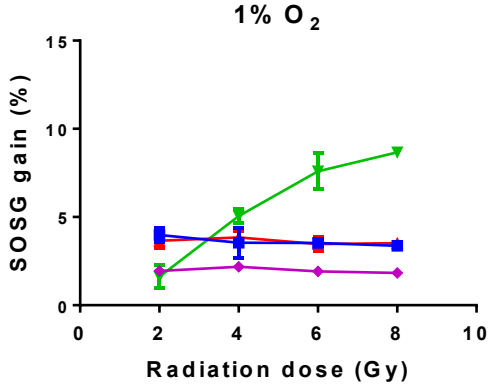
1% O2
SOSG gain (%)
Radiation dose (Gy)

Figure 3.10: Singlet oxygen yield in response to radiation for the PEG-PLGA NP, NSC NP, PPIX NP, and radioPDT NP in varying hypoxic conditions. The NP were standardized to a concentration of $5x10^{11}$ NP/mL with the NSC and PS loaded content standardized via UV-Vis absorbance measurements. Singlet oxygen yield is expressed as a ratio of SOSG probe signal pre-treatment and post-treatment. SOSG gain was significantly higher ($p<0.05$) in radioPDT NP treatment across all oxygen conditions at radiation doses greater than 4 Gy.

When the radioPDT NP's singlet oxygen yield was compared across different oxygen condition, all showed a similar dose-response curve to radiotherapy (**Figure 3.11**). No statistical difference between the SOSG yield in different oxygen conditions was seen, although the 20% and 10% oxygen groups were systematically higher than the 1% and 5% conditions. This may represent potential competition between oxyradical formation due to ionizing radiation and Type I reaction of the PS occurring simultaneously. Generally, the impact of hypoxia as low as 5% decreases the effectiveness of the PDT effect by 50% (196). This is seen in the singlet oxygen yield curve in **Figure 3.11**, where the singlet oxygen yield is about half in 5% oxygen condition as it is at 10% oxygenation. Beyond this 5% to 10% region, further oxygen concentration changes at highly hypoxic 1% and oxygen abundant 20% conditions did not manifest in large changes in SOSG signal (**Figure 3.11**).

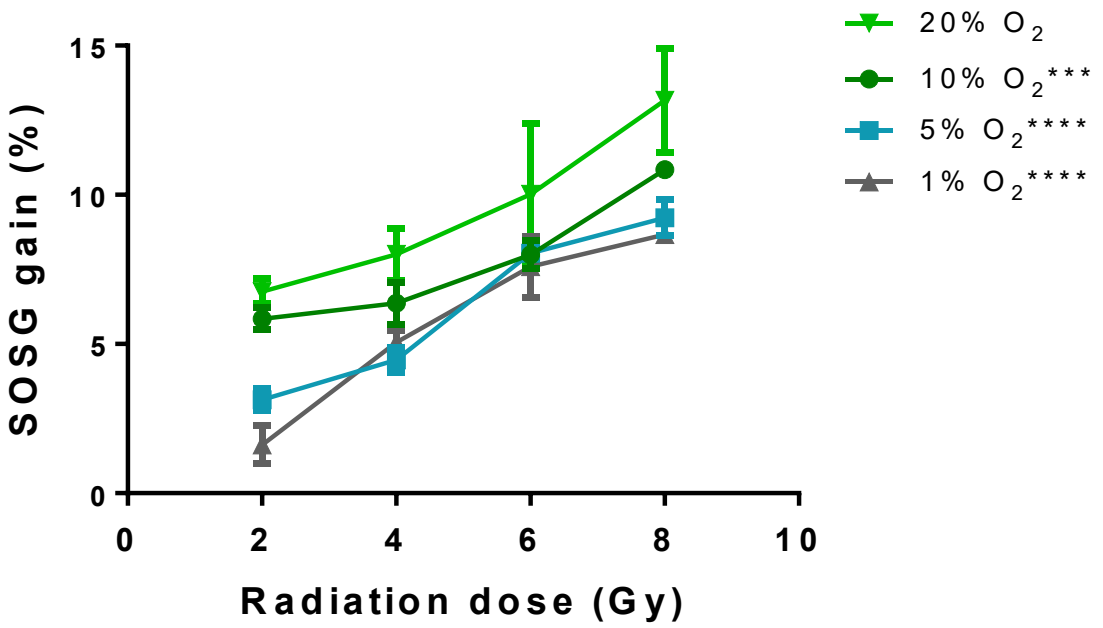

Figure 3.11: Comparison of singlet oxygen yield as measured by gain in signal of SOSG probe (expressed as a ratio from pre-treatment fluorescent intensity) in radioPDT NP irradiated with 2 Gy, 4 Gy, 6 Gy and 8 Gy under different oxygen concentrations. When compared to the highest oxygen concentration (20%), the oxygen limited conditions generated significantly lower singlet oxygen yield. ***$p<0.01$, ****$p<0.0001$

3.3.3 *In vitro* Cytotoxicity of radioPDT at Varying Radiotherapy Doses in Gradients of Hypoxic Conditions

To understand the performance of the radioPDT NP system in treating cancer under oxygen-limited conditions, a hypoxia chamber was used to control and induce hypoxic environments while the PC3 prostate cancer cells were treated with the NP and radiated. The NP used in each condition was standardized for concentration and for NP and drug concentration loaded.

3.3.3.1 Colorimetric Viability Assay with Alamar Blue

To assess for cell viability as a function of cell metabolic activity and consequent reducing potential, Alamar Blue was used. The cells were plated in 96 well plates and treated with either NSC NP, PPIX NP, or radioPDT NP in concentrations ranging from $1x10^{12}$ NP/mL to $1.25x10^{10}$ NP/mL. PEG-PLGA NP was omitted as it appears to perform the same as control PBS and NSC NP. The cells were then subjected to radiotherapy (2 Gy to 8 Gy) under different levels of oxygen using the hypoxia chamber (20% to 1% O_2).

There was a significant decrease in cell viability detected in the radioPDT treatment groups, particularly at higher doses of NP and radiation (**Figure 3.12**). NSC NP and PPIX NP performed the same as control in all conditions, where no significant difference in viability was noted over control conditions regardless of NP dose. At 2 Gy, no significant difference in viability was also noted for radioPDT NP, although there appeared to be a trend towards decreased cell viability at the highest NP dose (**Figure 3.12a-b**). Progressively lower cell viability was noted as radiation dose was increased for the radioPDT NP group, where at NP doses above $5x10^{11}$ NP/mL cell viability decreased by

approximately 25% at 4 Gy, 50% at 6 Gy, and 75% at 8 Gy. Note these decreases in cell viability are relative to the cells under the same radiation condition and represent an additive loss in cell survival over the impact of radiation alone. Hypoxic conditions of 1% appeared to manifest in a smaller change in cell viability over baseline in the lower NP concentrations, although this effect was only significant in the 6 Gy group with NP concentrations between $6x10^{10}$ NP/mL and $2x10^{11}$ NP/mL ($p<0.01$). At NP concentrations above $5x10^{11}$ NP/mL, the effect of hypoxia did not significantly diminish the radioPDT's effect in decreasing cell viability. This appears to indicate that the radioPDT NP are capable of enhancing radiation's effect on treating PC3 cells *in vitro*, have more activity with increasing doses of radiotherapy and with higher concentrations of NP, and are able to significantly decrease cell viability.

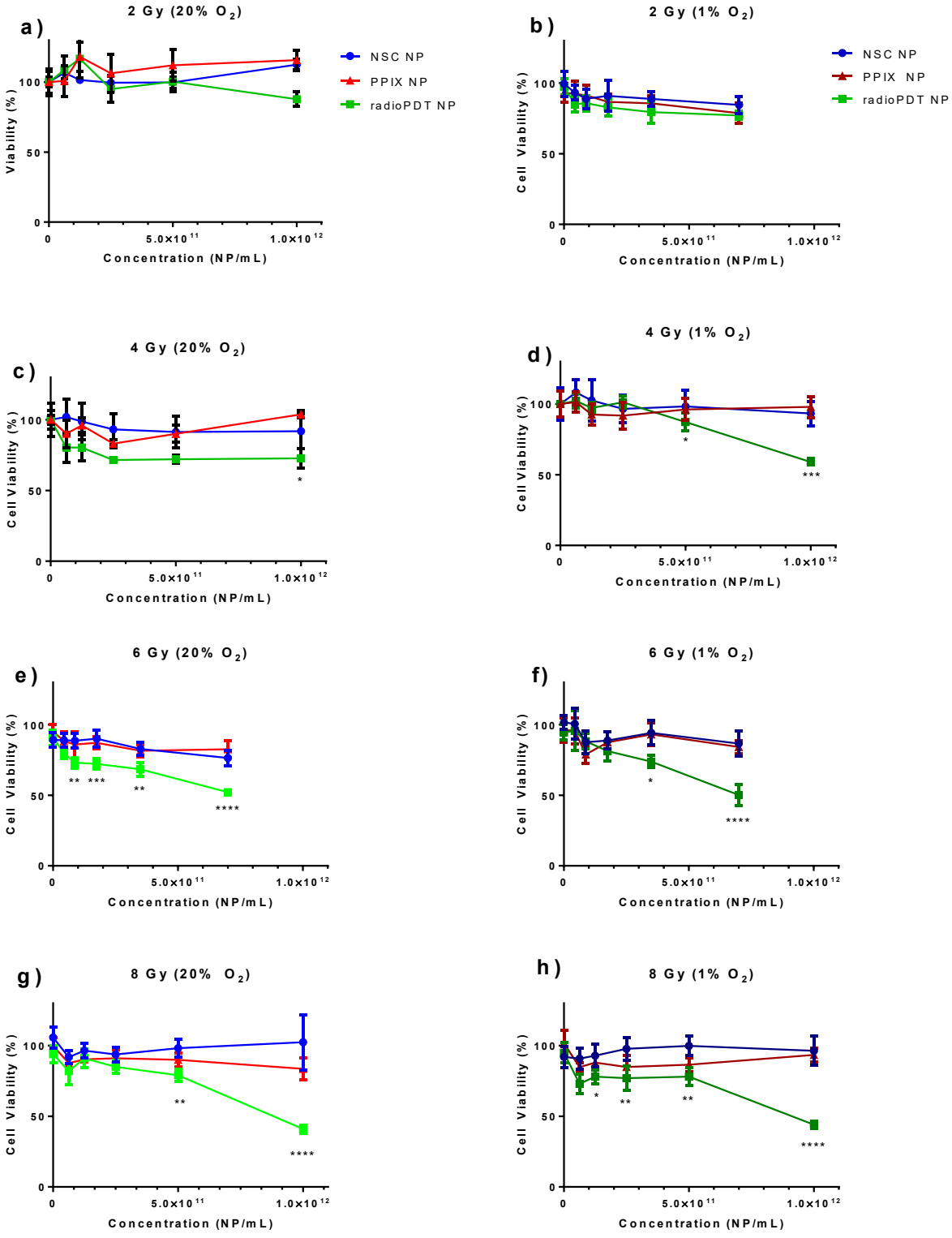

Figure 3.12: PC3 cell viability study using Alamar blue assay on cells treated with varying

concentrations of NSC NP, PPIX NP, or radioPDT NP. 2 Gy to 8 Gy of radiation was delivered under normoxic condition (**a,c,e** and **g**) and acute hypoxic condition of 1% O_2 (**b,d,f** and **h**). Cell viability was standardized to the effect of the hypoxia and radiation dose alone. *p<0.05, **p<0.01, ***p<0.001, ****p<0.0001.

The lower relative yield in cytotoxic response under radiotherapy compared to light is likely due to the much higher amount of energy deposited with UV light irradiation (**Figure 3.8**) compared to X-ray irradiation (**Figure 3.12**), where a significant amount of energy is absorbed by the media and cells. The single-step direct activation of PPIX under UV-irradiation and lack of energy loss in FRET also contribute to a higher magnitude of response in traditional PDT versus radioPDT. Despite this, radioPDT holds a potential advantage over traditional PDT in clinical scenarios since its' use of X-rays to activate the PS can easily effect cytotoxicity on much deeper structures, and radioPDT is able to produce a 50% improvement in cytotoxicity even at low palliative radiation doses and fractionation. Hence, the addition of radioPDT to radiotherapy may be very useful for cancer treatment.

3.3.3.2 Clonogenic Assay Demonstrating Impact on Cell Survival with the radioPDT Effect

The cells from **Section 3.3.3.1** were subjected to cell survival via clonogenic assay from the same cohort of treatment for correlative analysis. Cells were lifted from the 96 well plate in which they received the NP and radiotherapy treatment and transferred to a 24 well plate and grown for colony forming units (CFU). The CFUs were counted and along with the plating density a surviving fraction analysis was calculated.

The clonogenic assay in this setting was difficult to perform, however, due to the limited number of cells available to plate, the small well sizes of the 24 well plate, and the wide disparity in cell survival between radiation doses and especially between radioPDT versus control conditions (**Figure 3.13**). However, the clonogenic assays appeared to qualitatively support the findings of the viability assay. CFUs were significantly diminished even with

lower radiation doses of 4 Gy with increasing concentration of radioPDT NP. This effect was not seen with increasing concentrations of the other NP (**Figure 3.13**).

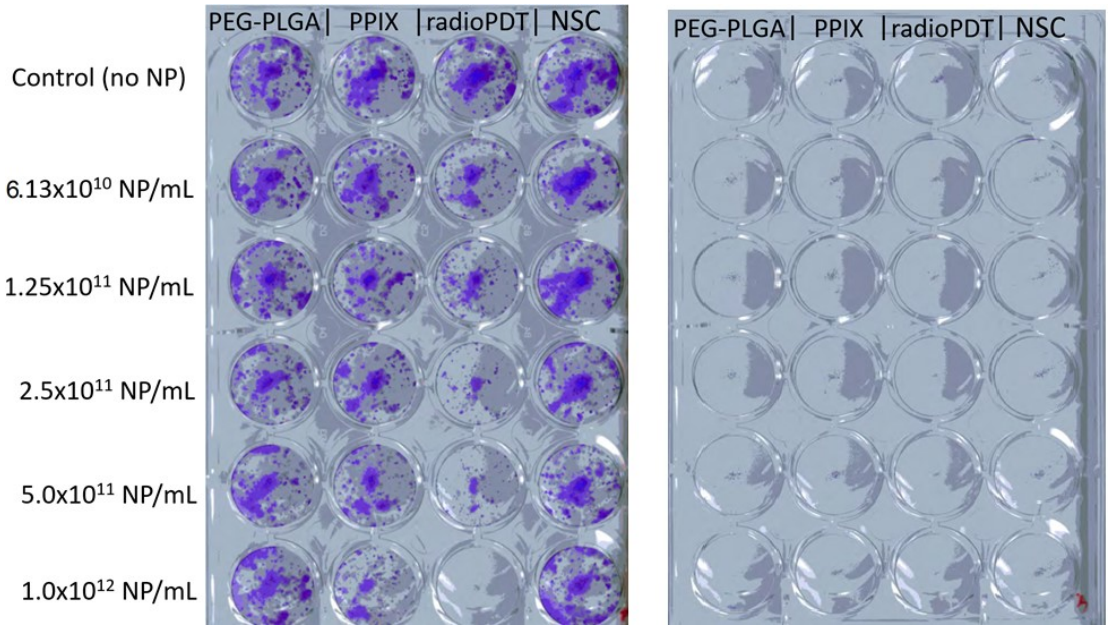

Figure 3.13: CFUs of cells treated with 4 Gy (**left plate**) and 8 Gy (**right plate**) radiotherapy with different concentrations of PEG-PLGA NP, NSC NP, PPIX NP, and radioPDT NP. Only the radioPDT NP group displayed diminished colony formation with increasing concentration of NP. The 8 Gy plate (**right**) did not demonstrate any CFUs in any condition due to insufficient cell plating density. This was due to challenges in finding the appropriate cell density for control (0 Gy) to the highest radiation dose (8 Gy) while also accommodating for the added toxicity from the radioPDT NP.

3.3.3.3 Live/dead Flow Cytometry to Demonstrate Acute Cell Death from radioPDT

For a potential better assessment of cell death to confirm cytotoxicity, a live/dead flow cytometry assay was performed with radioPDT NP and radiation on PC3 cells. Assessing the cell clonogenicity indicates a cancer cell's ability to continue to proliferate, and cells that are alive but senescent in particular are not considered viable. Newer evidence suggests senescent cells still play a role in promoting growth through cytokine signaling, and also may provide a mechanism to resist genotoxic cell damage and promote survival (335, 336). The live/dead assay was done through flow cytometry acquisition to allow for high throughput assessment. Cell death was assessed at 72 hours since in the presence of PDT effect early cell death by this time point is expected.

Initial studies were focused on comparing PI against DAPI for sensitivity in detecting radiation-induced cell death. Cells were radiated at 0 Gy, 4 Gy and 8 Gy and assessed after 72 hours. **Figure 3.14** demonstrates that DAPI was more linear and reproducible in detecting early radiation-induced cell death than PI. Additionally, PI was more troublesome to work with since it is a cytotoxic dye that starts inducing cell death within 20 minutes of addition. DAPI did not induce cell death for several hours, which made it easier to work with when sampling multiple wells and plates. Therefore, DAPI was used for additional live/dead assays studies with radioPDT NP.

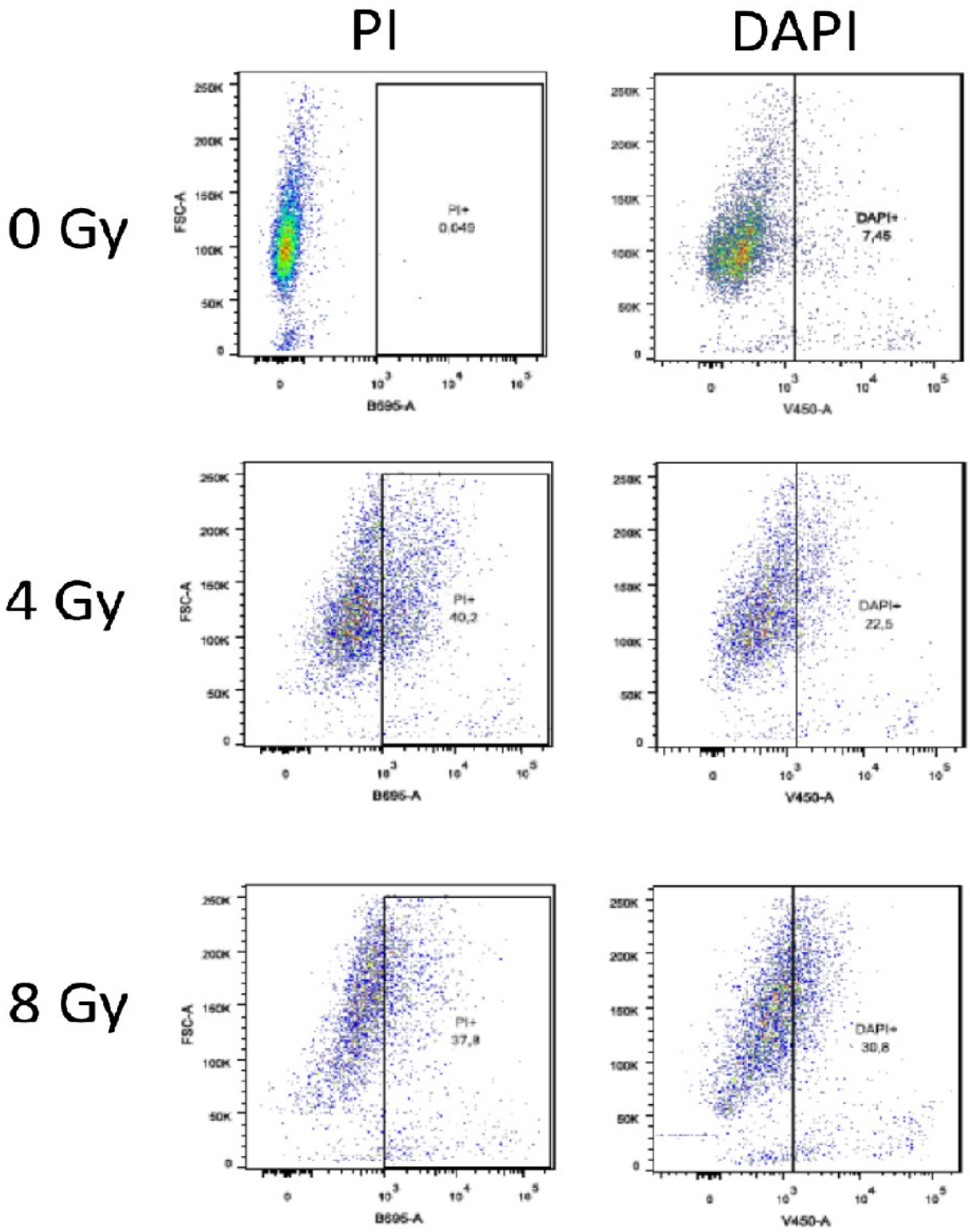
PI
DAPI
0 Gy
4 Gy
8 Gy
FSC-A
B695-A
V450-A
PI+
0,049
DAPI+
7,45
PI+
40,2
DAPI+
22,5
PI+
37,8
DAPI+
30,8

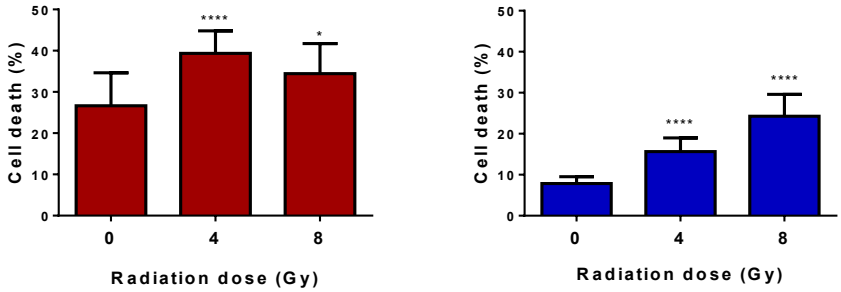

Figure 3.14: Live/dead assay comparison between PI and DAPI after control (0 Gy), 4 Gy and 8 Gy of radiation (n=10 per group). The cell distribution and gating for live vs dead cells is shown in the top 3 rows for 0, 4, and 8 Gy, respectively. Both assays were able to detect significantly increased dead cell population compared to control. PI was less consistent at detecting cell death and was confounded by time it took to for a plate to be read by the flow cytometer. Typical times to read one plate was 30 to 40 minutes, and it was noted that in 20 minutes PI would detect increased cytotoxicity regardless of the treatment condition. No such effect was noted with DAPI. *$p<0.05$, **$p<0.01$, ***$p<0.001$, ****$p<0.0001$.

Using DAPI as the fluorescent marker of dead cells, the cytotoxicity study for radioPDT NP effect was repeated as described in **Section 3.3.3**. Gating was set per oxygen condition to account for differences in cell distribution seen on flow cytometry (**Figure 3.15**). Under these conditions, radioPDT effect appeared to generate significantly higher cytotoxicity ($p<0.001$) (**Figure 3.16**). The cytotoxicity appeared to be NP dose-dependent, particularly at radiation doses between 2 to 6 Gy. Beyond 6 Gy is when nontraditional radiobiological effects such as cell membrane injury, sphingomyelinase activity, cytokine signaling, and ceramide production are known to be more active, which may contribute additionally to the cytotoxicity of radiation alone and the predominantly genotoxic cell-kill at doses below 6 Gy per fraction (319-325). This may decrease the advantage in cytotoxicity of radioPDT at higher dose per fractions, but the therapeutic yield of radioPDT is still quite high even at 8 Gy dose per fraction (**Figure 3.16**).

20% O_2

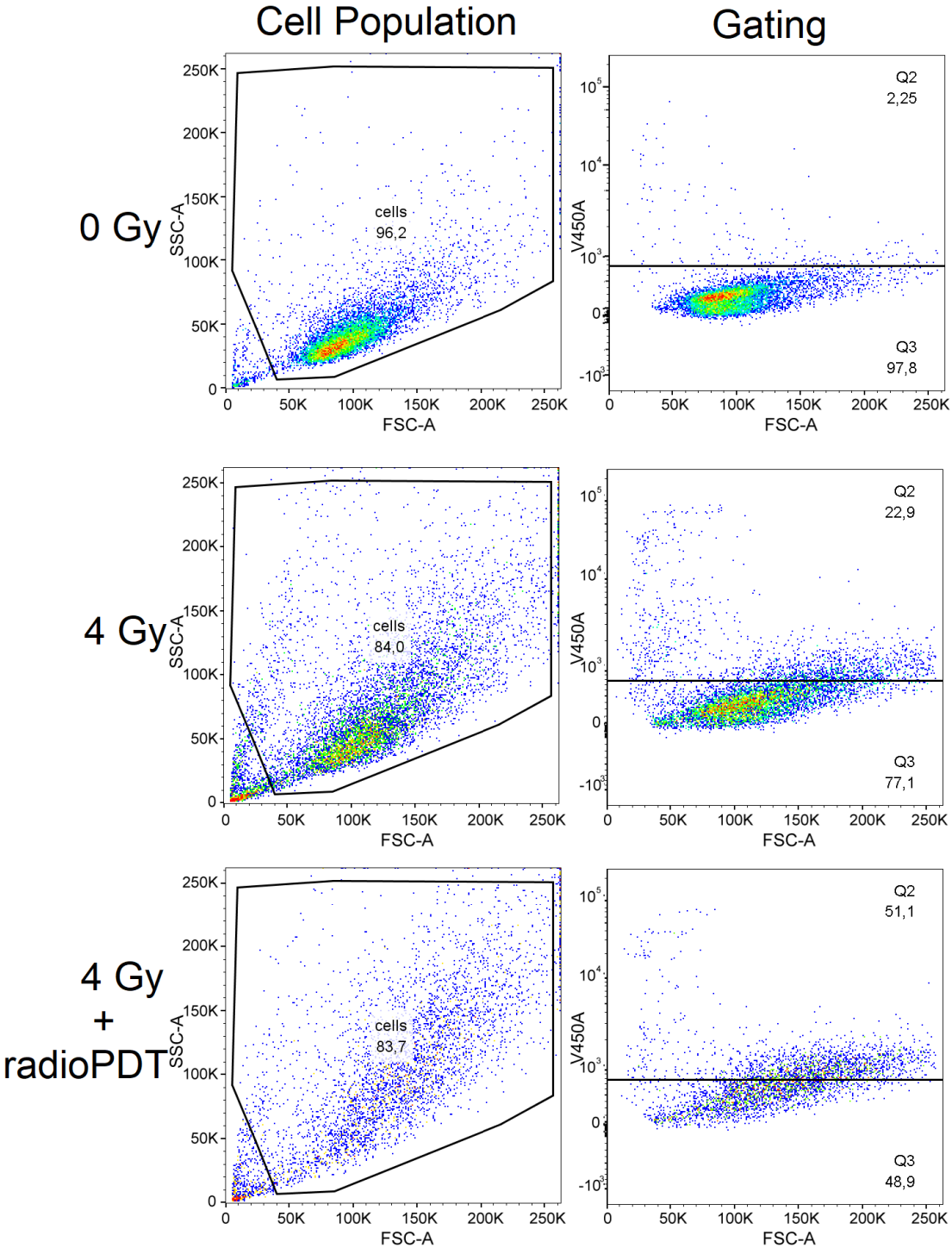
Cell Population
Gating
0 Gy
4 Gy
4 Gy
+
radioPDT
SSC-A
FSC-A
V450A
cells
96,2
cells
84,0
cells
83,7
Q2
2,25
Q3
97,8
Q2
22,9
Q3
77,1
Q2
51,1
Q3
48,9

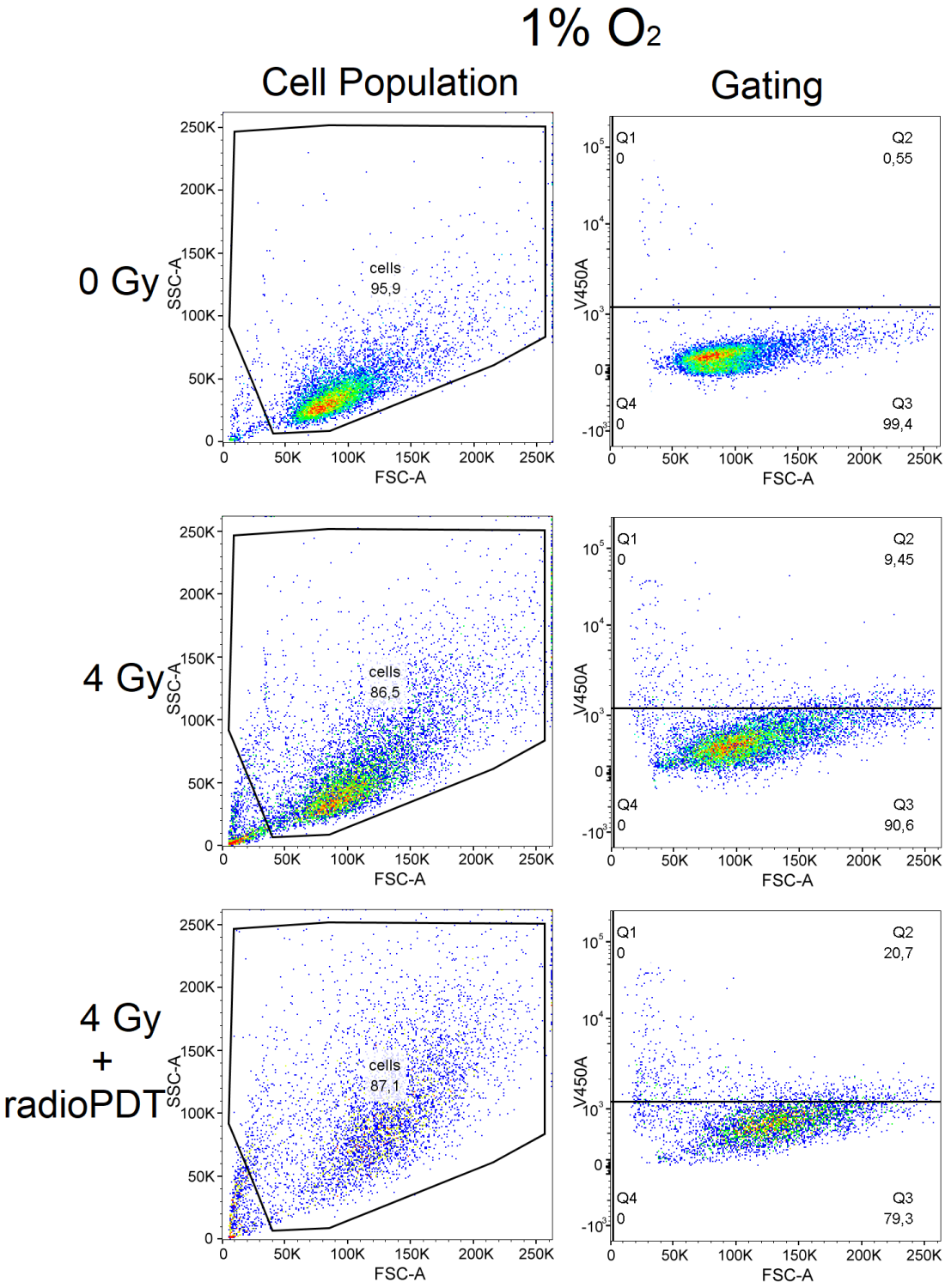

Figure 3.15: Flow cytometry acquisitions of PC3 cells treated in normoxia (20% O_2) and hypoxia (1% O_2). The cell population was selected to include the PC3 cells and the products of dead cells to include for analysis. The gates for DAPI signal were set per oxygen

concentration for the entire analysis to account for cell permeability changes with hypoxia, and the time difference between analysis of successive batches of plates.

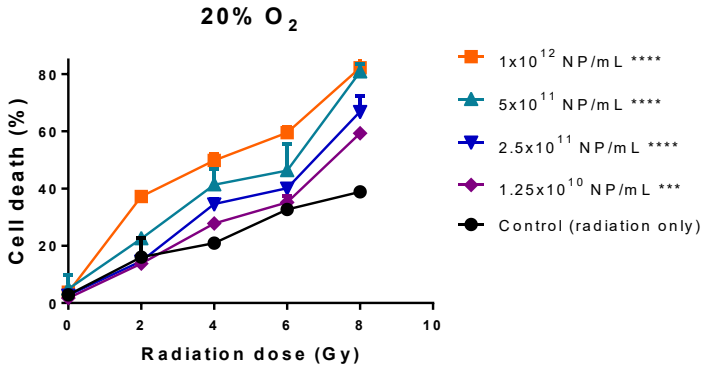
20% O2
Cell death (%)
Radiation dose (Gy)
1x10^12 NP/mL ****
5x10^11 NP/mL ****
2.5x10^11 NP/mL ****
1.25x10^10 NP/mL ***
Control (radiation only)

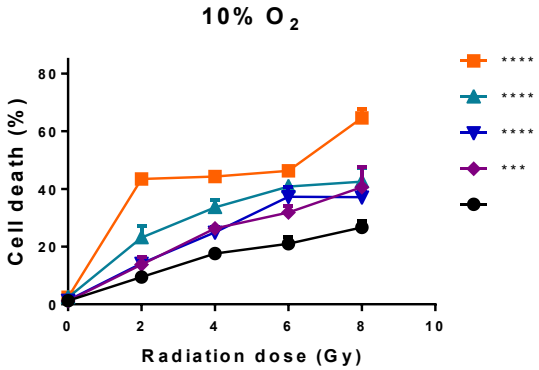
10% O2
Cell death (%)
Radiation dose (Gy)
****
****
****
***

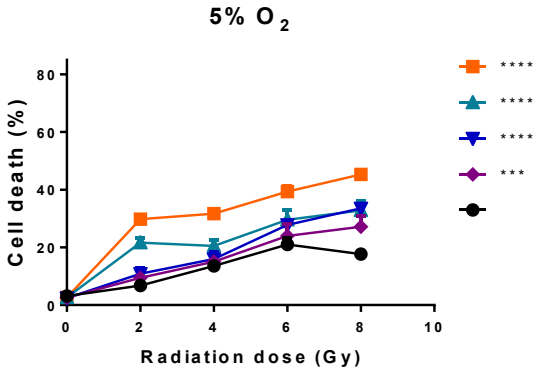
5% O2
Cell death (%)
Radiation dose (Gy)
****
****
****
***

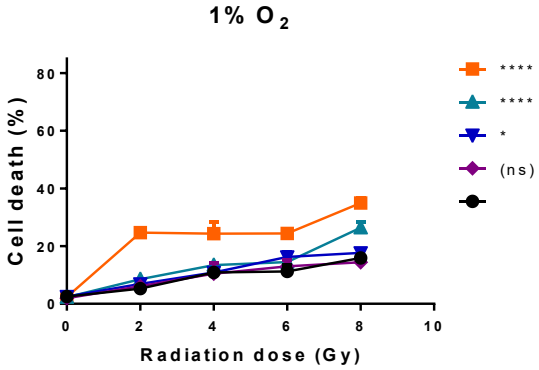
1% O2
Cell death (%)
Radiation dose (Gy)
****
****
*
(ns)

Figure 3.16: Dose response relationship of cell death to radiation dose at varying concentrations of radioPDT NP and in a gradient of hypoxic conditions, as measured by DAPI-based live/dead flow cytometry. The main effect comparison of radioPDT NP to radiation alone was significant at all radiation dose and NP concentrations except for in 1% hypoxia with NP concentrations of $1.25x10^{10}$ NP/mL. When analyzed for therapeutic effect per NP concentration and radiation dose, oxygen levels of 5% and less failed to produce significant therapeutic benefit for NP concentrations of $1.25x10^{10}$NP/mL in radiation doses below 8 Gy. At 1% hypoxia, NP concentration of $1.25x10^{10}$ NP/mL failed to produce significant additional therapeutic effect over radiation at all doses, and of $2.5x10^{10}$ NP/mL concentration only produced additional therapeutic effect above 6 Gy. All other treatment conditions produced significant differences in treatment effect in favour of radioPDT. *$p<0.05$, **$p<0.01$, ***$p<0.001$, ****$p<0.0001$.

In normoxia (20% O_2) the cytotoxicity of radiation alone was 39%, whereas at the highest dose of radioPDT NP the cytotoxicity of radiation with radioPDT was 82% ($p<0.0001$). However, the same NP and radiation dose did decrease in cytotoxic yield under hypoxic conditions, with 1% hypoxia demonstrating a cytotoxic yield of 16% for radiation alone and 35% with radioPDT ($p<0.0001$). At lower radiation doses, the radioPDT advantage is diminished with 2 Gy showing a cytotoxic yield of 37% for radioPDT and 16% for radiation alone in normoxia (20% O_2) and decreasing to 25% for radioPDT and 5% for radiation alone in 1% oxygen ($p<0.0001$). Though the magnitude of cytotoxicity drops with radioPDT as it does for radiation alone and in hypoxic conditions, radioPDT still manages to produce a strongly significant improvement in therapeutic effect dependent on NP dose, radiation dose, and oxygen conditions. In 1% oxygen the lowest concentrations of NP ($1.25x10^{10}$ NP/mL) failed to produce a significant therapeutic improvement, but NP doses higher than this continued to produce superior therapeutic effect to radiation alone.

The dose-response relationship to radioPDT NP concentration seems to be greatest at a dose of 4 Gy. **Figure 3.18** shows the relationship between radioPDT effect against oxygen concentration. There appears to be a threshold amount of oxygen of 5% needed before the PDT effect becomes more dependent on the concentration of oxygen. Additionally, there is a saturation seen around 10 to 20% oxygen, beyond which additional oxygen does not seem to confer more cytotoxicity. The saturation cytotoxicity level appears to shift up as the NP concentration is increased. This seems to suggest that in highly hypoxic environments the radioPDT effect is limited by the substrate of oxygen, but as the oxygen level is increased the NP concentration may become the limiting factor. In addition, even when in an oxygen-limited environment there is still cell killing seen, which most likely

represents the toxicity of predominantly radiotherapy in this condition (**Figure 3.16, 1% condition**). At 8 Gy the curve's minima shifts up, which may be a sign that additional cytotoxic processes beyond purely genotoxic mechanisms are becoming prevalent.

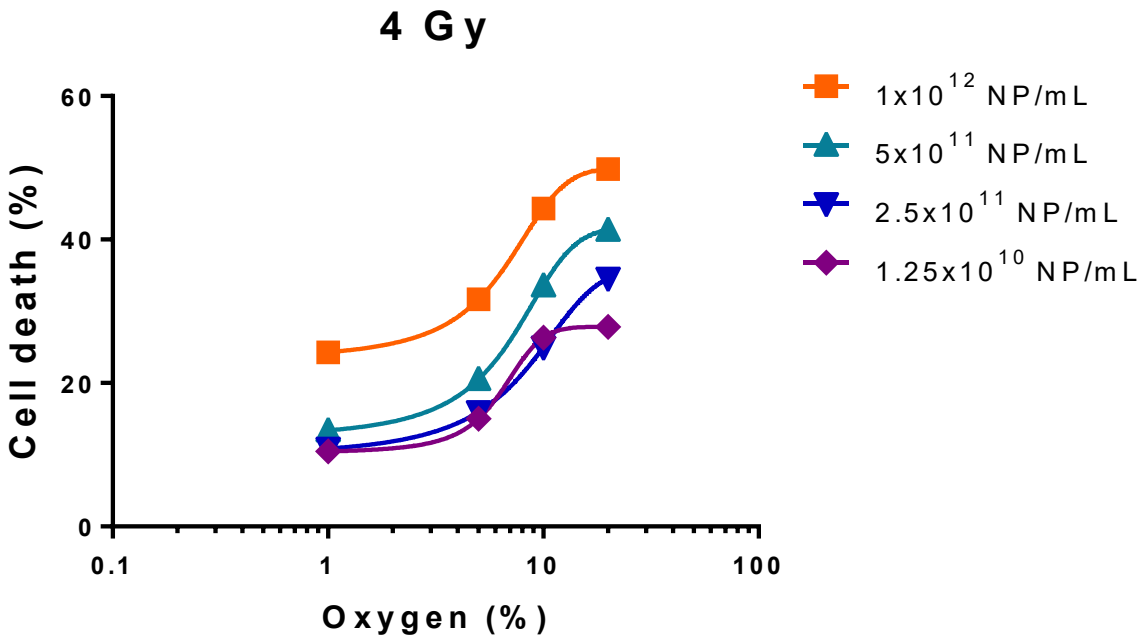

Figure 3.18: Cell-kill at 4 Gy of radiotherapy as a function of oxygen concentration for varying doses of radioPDT NP. The data was fit with a sinusoidal curve to assess for dependence on oxygen level for therapeutic effect. Cytotoxicity appearing to be rate-limited by oxygen in highly hypoxic conditions but becoming more NP concentration limited in oxygen conditions beyond 10%.

3.3.4 *In vivo* assessment on anti-tumor therapy of radioPDT

To further assess the radioPDT effect in physiologic tumor conditions, a xenograft mice model of human prostate tumor (PC3) was used. PC3 was selected because it is representative of high risk prostate cancer, which currently represents a challenge to treat with radiotherapy without undue toxicity (292-294). The tumor was grown as a flank model as opposed to an orthotopic prostate tumor model to make delivery of high-quality radiotherapy more feasible, and to also allow regular tracking of tumor size by calipers. A 4-arm study was designed to assess the effect of radioPDT against the NP alone, radiation alone, and untreated control. The experiment was done as a single drug dose and single radiation fraction to reduce complexity and possibility for error and confounders.

The NP dose was selected based on similar NP designs that show a time to preferential distribution to the tumor by about 24 hours in similar mouse flank model tumors (337, 338). Further in-house studies using CT imaging also showed accumulation within the tumor occurred by 24 hours, after which point the NP started to distribute into other organs (**see Chapter 4**).

The radiation dose was selected based on the need to deliver sufficient radiation dose to induce a detectable tumor response and delay its growth, but not as high as to induce permanently arrested tumor growth or introduce nongenotoxic mechanisms of cell injury seen with higher radiation dose-fractionations. The starting tumor size was 500 mm^3. This can be roughly estimated to contain $5x10^8$ PC3 cells. The surviving fraction of PC3 at 6 Gy radiotherapy *in vitro* is about 10% (339). This could be used to make an estimate of about 500 clonogens remaining in the tumor that could still proliferate, which would be sufficient for the tumor to regrow (after initially showing response) and progress after the

single fraction radiotherapy was completed. A pilot experiment was conducted with this radiation dose and appeared to show significant tumor response, but the tumor was able to regrow and progress within 2 weeks (**Figure 3.19**). Note, the tumors were initially over-treated to about 7.4 Gy over a sizeable region due to hotspots that developed on the periphery of the tumor from the two-field tangents-only approach. The radiotherapy treatment setup was modified to a three-field technique to mitigate the build up of a hotspot.

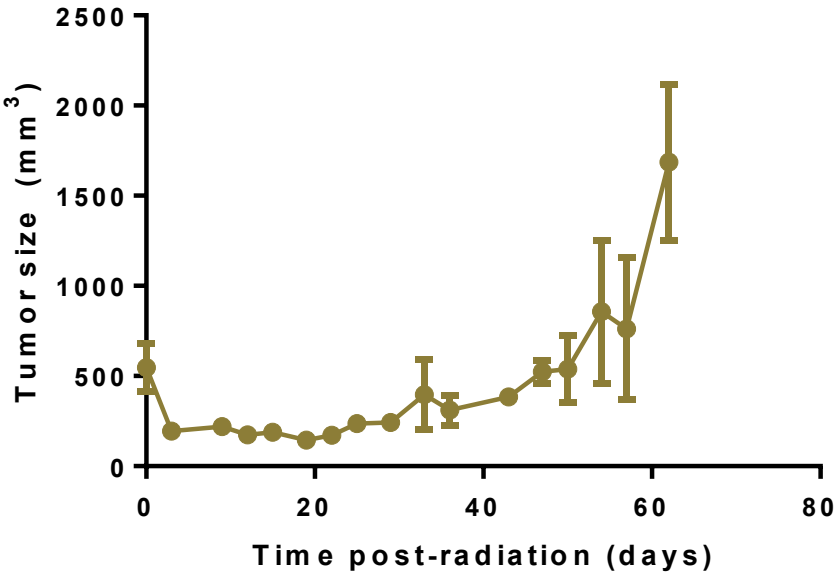

Figure 3.19: Pilot radiotherapy experiment with PC3 flank tumor-implanted NSG mice treated with single fraction 6 Gy radiotherapy via SARRP. Actual delivered dose was as high as 7.4 Gy due to large isodose hotspots that developed by using a 2 field tangent technique. The tumor showed good response for a two week period before starting to show signs of regrowth. (n=2)

3.3.4.1 Radiotherapy Delivery

Radiation was delivered to the flank model tumor using the SARRP system. All animals to be treated were maintained under anesthesia and the tumor positioned above the plane of the animal. A CBCT was acquired and used for radiation planning. Compared to the control-treated mice, the mice treated with radioPDT NP were noted to have CT detected enhancement within the tumor (**Figure 3.20**). This is likely due to the high Z lanthanides contained in the NSC of the radioPDT NP, which act as a CT contrast agent. The high Z atoms interact to a much greater extent with the incident low KV energy (60KVp in the SARRP) photons than the hydrocarbon-based tissues found in the visceral organs and tumor. This translates to increased attenuation noted by the X-ray detector, and becomes reconstructed as a high Hounsfield Unit (HU) region of the animal (340-344). The presence of this enhancement was noted to aid in image-guided planning and helped deliver higher quality radiation.

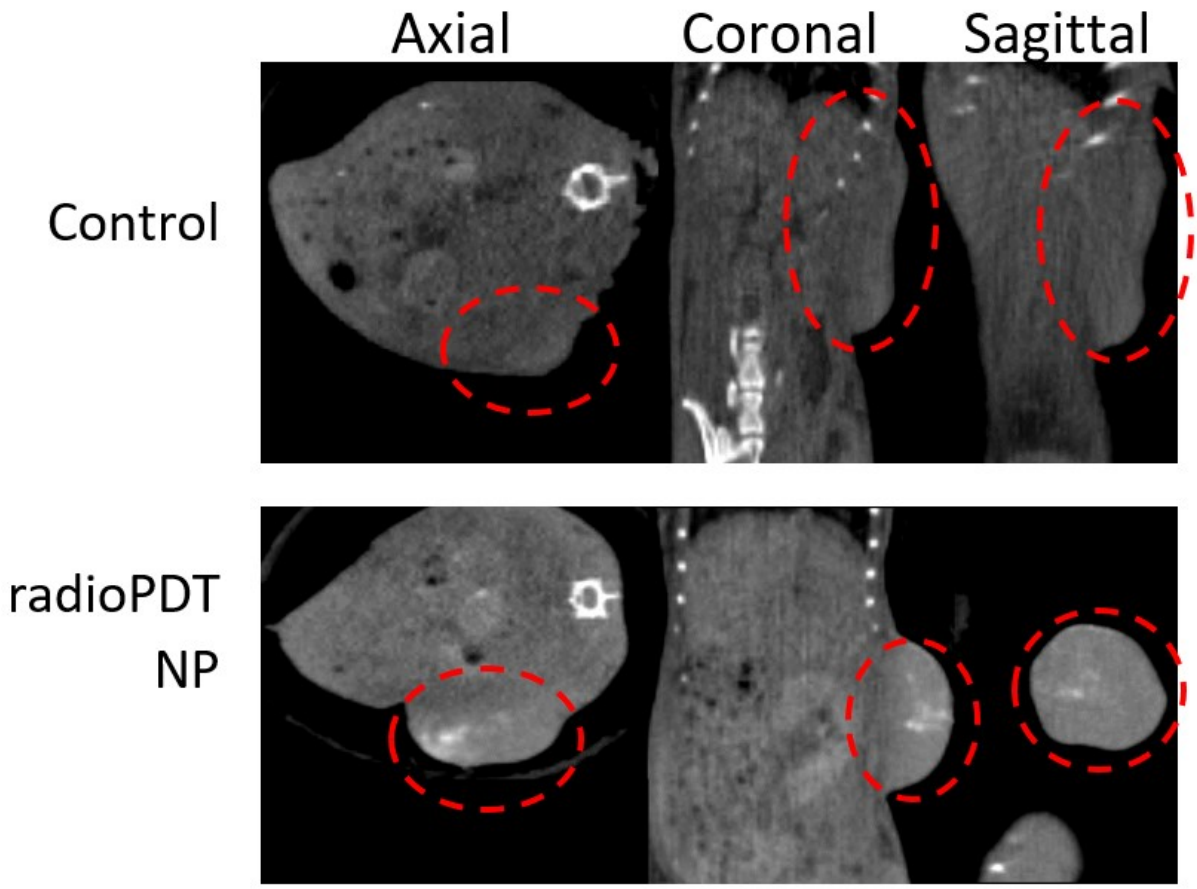

Figure 3.20: CBCT image acquisition of mice 24 hours after IT injected radioPDT NP demonstrating tumoral contrast enhancement compared to control (PBS). The region of tumor is highlighted by the dashed red line. Enhancement is evidenced by the increased attenuation (white signal) seen in the tumor of the radioPDT targeted tumor (bottom) than the control animal. Some minor enhancement is also seen in other visceral organs in the radioPDT NP, which suggests NP distribution systemically as well.

Treatment planning as carried out using Muriplan® (Xstrahl, Camberley, Surrey, UK). The clinical target volume (CTV) was defined as the tumor volume that was contoured from the CBCT images. The animal remained anesthetized in treatment position from the CBCT, during the treatment planning phase, and for radiation dose delivery. No PTV was added consequently, but a 5 mm margin to field edge was added. The dosimetry of the treatment was calculated on Muriplan with isodoses produced and a DVH graph. The dose to adjacent normal tissue was under 2 Gy and care was taken to limit dose to internal organs and small bowel to <1 Gy. The beams were positioned to limit dose to the spinal cord, which received <1 Gy. Treatment was delivered via a 3 field technique per isocenter, with the isocenter placed at the tumor center and 2 tangent beams used along with an orthogonal beam (**Figure 3.21**). In elongated tumors, a two isocenter technique was used to adequately target the entire tumor (**Figure 3.22**). The field edges were overlapped at the 50% isodose region and Muriplan was used to calculate total dose delivered. 6 Gy radiotherapy was delivered to at least 90% of the CTV with hotspots limited to <110% of prescription dose (**Figure 3.19-3.20**).

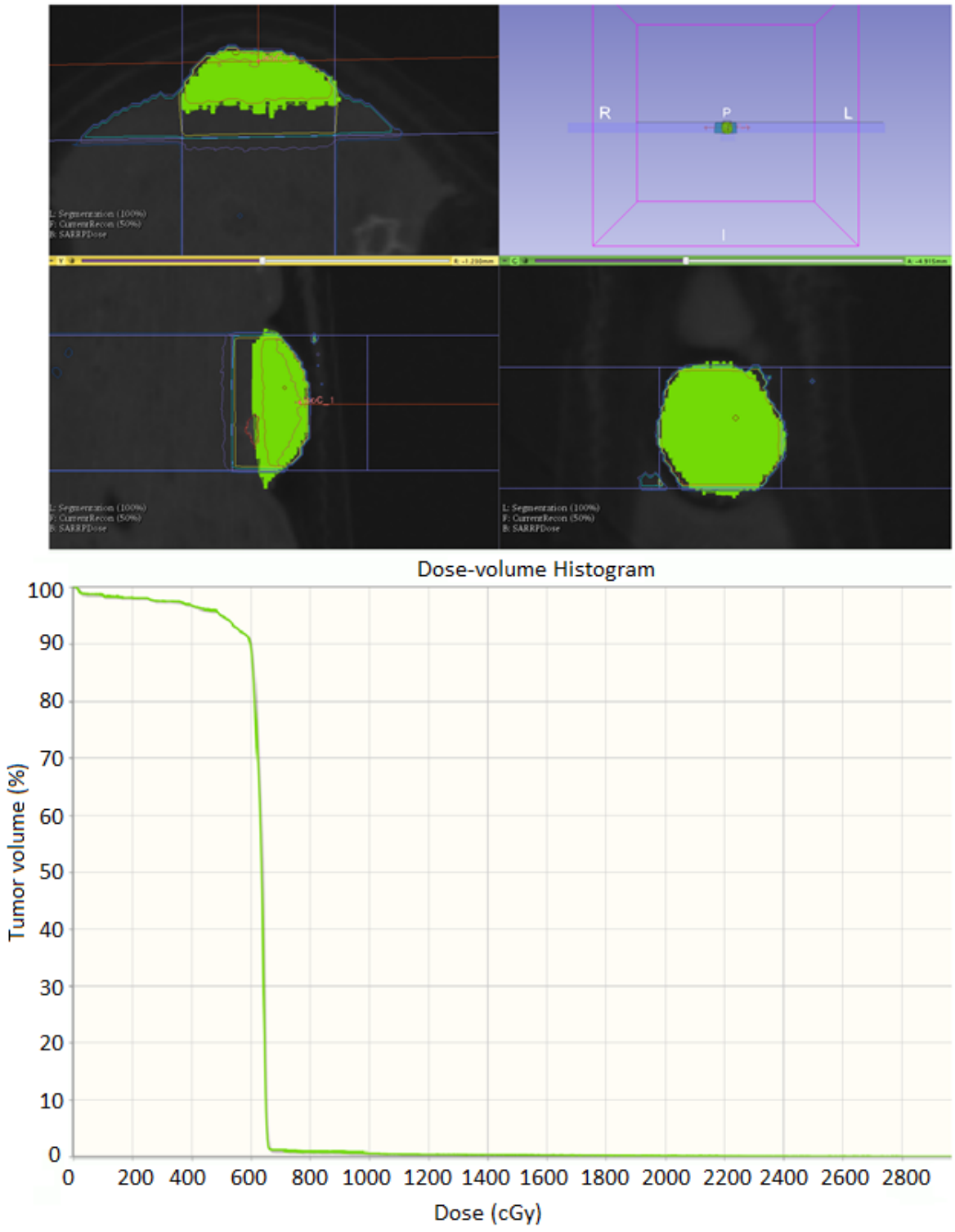

Figure 3.21: Isodose curves and DVH of a 3-field single isocenter planning technique on SARRP. The DVH graph (**bottom panel**) shows dose characteristics delivered to the

contoured tumor volume. The isodoses are shown in the top panel with axial (**top left**), coronal (**bottom left**) and sagittal (**bottom right**) views. For the isodose curves, **dark red** = 100%, **red** = 95%, **green** = 80%, **aqua** = 60% and **blue** = 20%.

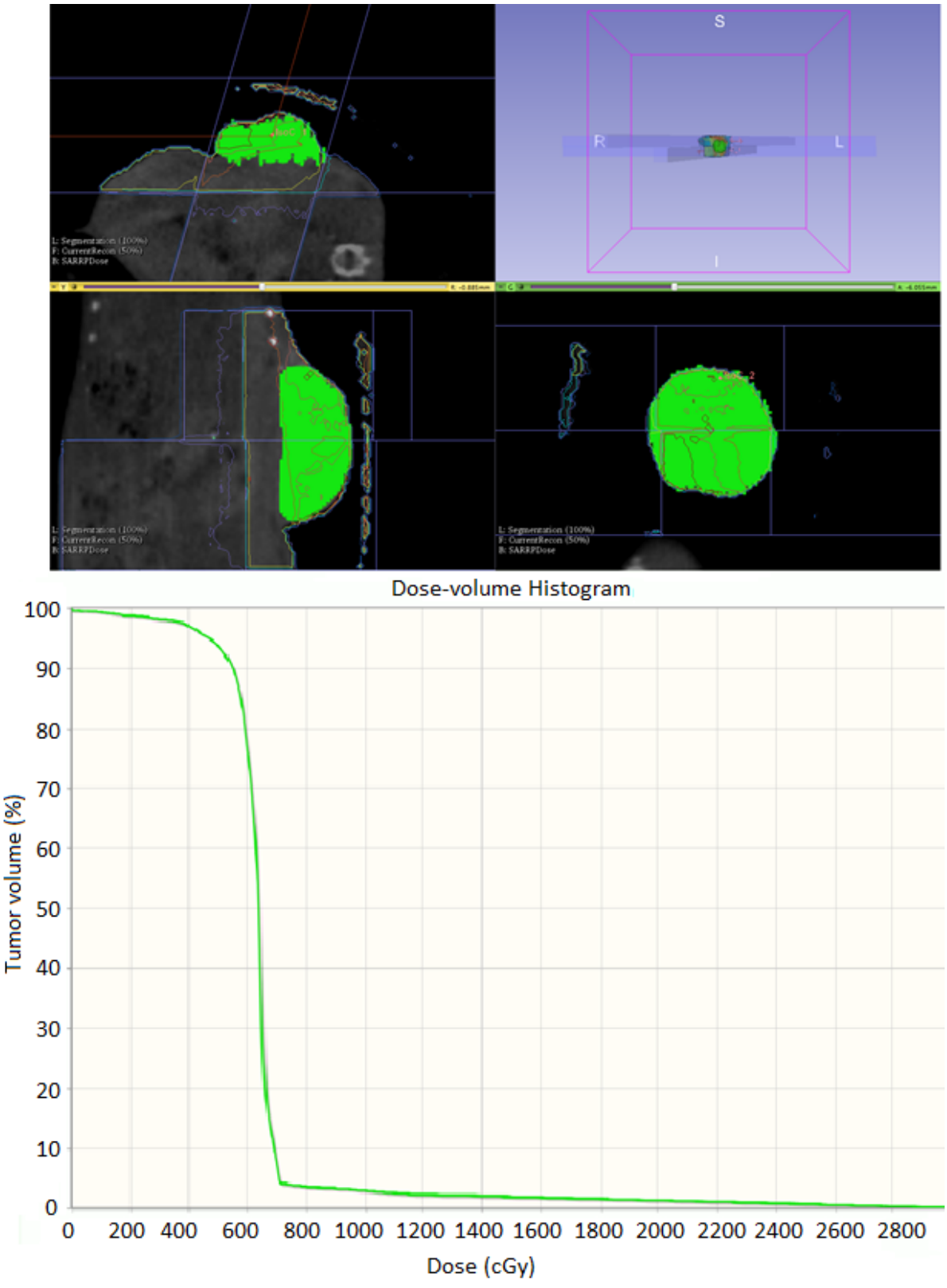

Figure 3.22: Isodose curves and DVH of a 6-field two isocenter planning technique on

SARRP. The DVH graph (**bottom panel**) shows dose characteristics delivered to the contoured tumor volume. Refer to **Figure 3.20**, bottom panel for a full scale view of the animal. The isodoses are shown in the top panel with axial (**top left**), coronal (**bottom left**) and sagittal (**bottom right**) views. For the isodose curves, **dark red** = 100%, **red** = 95%, **green** = 80%, **aqua** = 60% and **blue** = 20%.

Potential for confounding dose delivery was theorized to exist due to the high Z NSC being present in the radioPDT NP, and the use of 220 KVp irradiation energy. To further assess for this, the theoretical dose enhancement from the lanthanum and fluorine content (Z=57 and Z=9, respectively) was calculated. Cerium content was assumed as lanthanum and calculated as such since the difference in Z value (Z=58 and Z=57 for cerium and lanthanum, respectively) made a negligible difference in dose enhancement. To assess for this, standardized concentrations of NSC were CBCT-scanned on the SARRP, in order to obtain a HU to NSC concentration curve (**Figure 3.23**). This allowed quantifying the volume concentration of NSCs from the enhancement seen on CBCT (**Figure 3.21**) for the mice treated with NP by straight line fit to the experimentally derived relationship:

$$LaF(conc.) = \frac{(\#HU + 1960HU)}{786.6\frac{HU}{LaF(conc.)}} \cdot 100\%$$

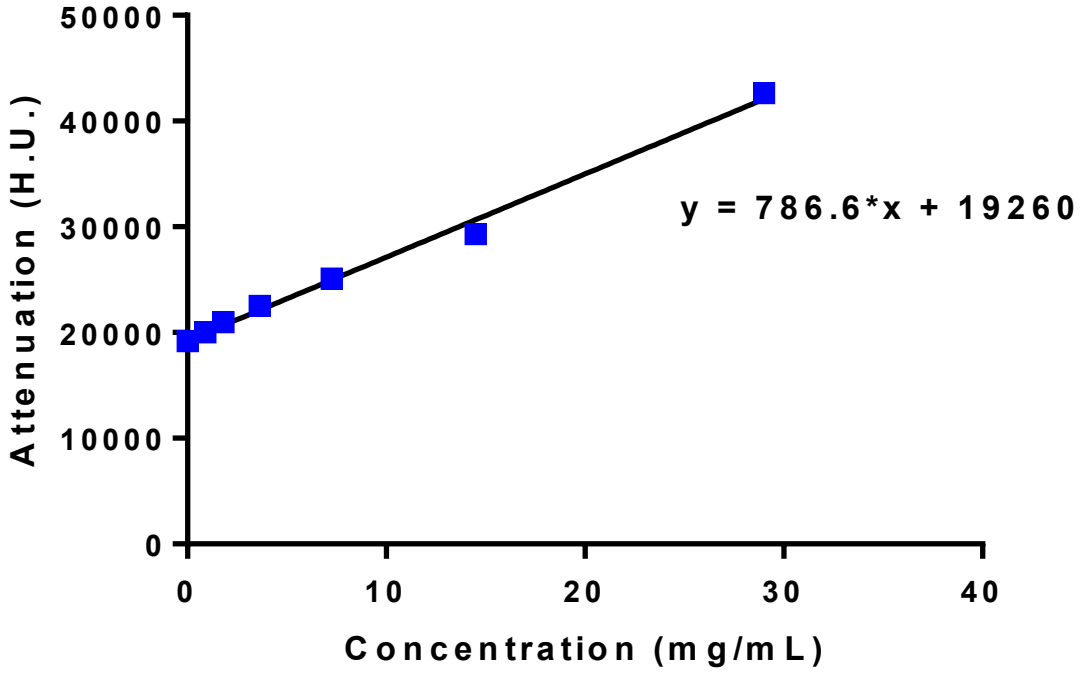

Figure 3.23: HU to $LaF_3:Ce^{3+}$ NSC concentration as measured by CBCT scan on the SARRP system. The concentration was acquired by standardized concentrations via inductive coupled plasma mass spectrometry (ICP-MS). The NSC was dispersed in water, which was used to standardize the measurements across concentrations.

With the assistance of Dr. Jans and Dr. Warkentin (Medical Physics, Cross Cancer Institute) the radiation dose enhancement factor was calculated using previously established methods (345-350). Briefly, the now-known NSC concentration was used to calculate mass-energy absorption coefficients, $\left.\frac{\mu_{en}}{\rho}\right|_{enh}$, for the enhanced tissue regions, assuming that the remainder of a given volume consisted of tumor tissue, well-approximated by the density of water:

$$\left.\frac{\mu_{en}}{\rho}\right|_{enh} = w_{water}\left(\sum_i w_i \left.\frac{\mu_{en}}{\rho}\right|_i\right)_{water} + w_{LaF}\left(\sum_i w_i \left.\frac{\mu_{en}}{\rho}\right|_i\right)_{LaF}$$

Where the w_{water} and w_{NSC} are the weight-fractions of water and the NSC in a given voxel as derived from the %-age concentration of LaF and the sums extend over the atomic constituents of each compound by weight, w_i, multiplied by that constituent's tabulated mass energy absorption coefficient $\left.\frac{\mu_{en}}{\rho}\right|_i$.

At any given voxel the dose enhancement factorf_{enh} relative to water is then given by the ratio of enhanced mass energy absorption coefficients to that of water:

$$f_{enh} = \frac{\left.\frac{\mu_{en}}{\rho}\right|_{enh}}{\left.\frac{\mu_{en}}{\rho}\right|_{water}}$$

Since this calculation is photon-energy dependent, care was taken to account for the energy spectrum of SARRP irradiator at the energy used in these experiments (keV). The value of the dose enhancement factor f_{enh} depends linearly on the observed enhancement (LaF

mass content) and can be graphed as a cumulative histogram derived from the voxels in a given enhancement region.

Regions of Interest (ROI) drawn around the enhanced portions of tumors were evaluated for the 4 mice irradiations in the NP + radiotherapy group, which are shown, together with their dose enhancement DVH, in **Figure 3.24**. The average dose enhancement across the whole tumor was calculated to be 10% (6.6 Gy) with the fraction of tumor receiving more than 15% dose enhancement (6.9 Gy) being less than 1% of the tumor volume. The D95 (dose to 95% of the volume) was still 6 Gy in all four mice. In comparison to other NP systems designed for dose enhancement, such as gold NP, our radioPDT NP has a comparatively low Z value (79 versus 57 to 58, respectively) and the molar fraction of high Z atoms in our NP is much lower due to our NP system being loaded by 10-15% NSC (351). The size of 100 nm for our NP is also not optimal for radiation dose-enhancement effect, since this impacts NP clustering and lowers the dose distributed to surrounding water and body tissue (349, 351). This suggests that the dose enhancement effect is not a significant factor with our radioPDT NP system.

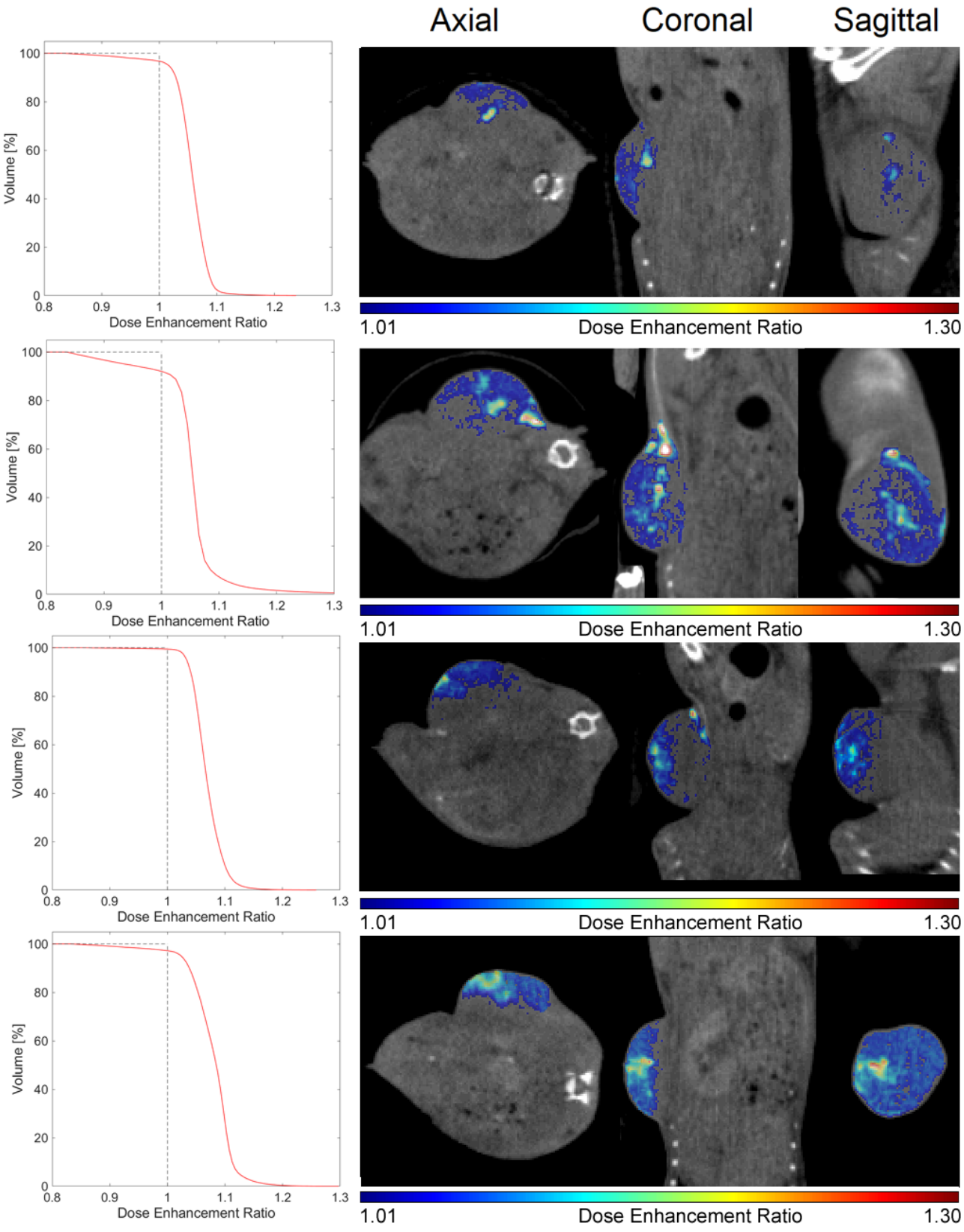
Axial
Coronal
Sagittal
Volume [%]
Dose Enhancement Ratio
1.01
Dose Enhancement Ratio
1.30

Figure 3.24: Dose enhancement factor of high Z NP elements (lanthanum cerium and fluoride) in radioPDT NP + radiation treated mice (n=4). The average dose enhancement was 10% over normal dose deposition in the tumoral tissue. The volume of tumor receiving over 15% dose enhancement was less than 1% in all mice.

3.3.4.2 Early Assessment of Tumor Response to radioPDT via [^{18}F]FLT-PET Scan

As an indicator of early response to treatment, the animals were scanned with [^{18}F]FLT-PET scan 4 days after completing treatment with radiotherapy and/or radioPDT NP. [^{18}F]FLT uptake is considered analogous to ki67 as a proliferation marker. There is some preclinical evidence to suggest [^{18}F]FLT uptake can also be used to predict for response based on the level of uptake (326).

The mice from all 4 arms of the study were scanned on day 4 post-treatment. A static whole-body scan was done for 15 minutes. The SUV value was standardized to whole body levels using ROI Visualization, Evaluationg and Image Registration (ROVER™) software (ABX GmbH, Germany). **Figure 3.25** shows the distribution uptake of [^{18}F]FLT tracer expressed as a heat map of SUV_{mean} value, and quantitative SUV_{mean} value in the flank tumor. A significant drop in SUV value was noted in the tumors from the radiated mice compared to the non-radiated mice. No significant difference was seen with the addition of NP in the radiated mice, and neither was there a difference in tumor uptake in non-irradiated mice. The NP treated mice also trended to a higher SUV_{mean} tumor value than the control mice, but this was not significantly different.

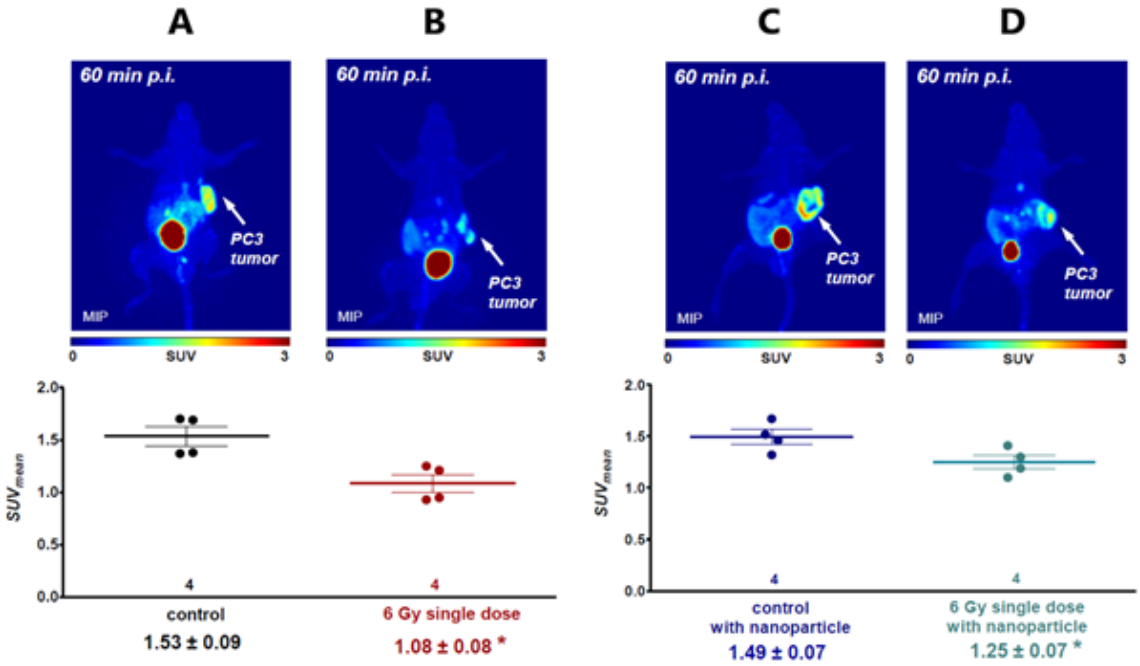

Figure 3.25: Treatment response to control (**A**), NP injection only (**B**), radiotherapy only (**C**), and radiotherapy with radioPDT NP are shown via [^{18}F]FLT-PET scans 4 days post-treatment. 5 MBq of [^{18}F]FLT was injected and a static whole-body scan was taken 60 minutes post-injection (p.i.). N=4 per group. A significant difference with the addition of radiotherapy is seen in the control injected group (**A** vs **B**) and the NP injected group (**C** vs **D**) in terms of SUV_{mean} value (p=0.029 and p=0.03). No significant difference was seen between **A** vs **C** and **B** vs **D** (p=0.5092 and p=0.0696).

The lack of response as assessed by [^{18}F]FLT in mice from Arm IV was surprising as this was not concordant with long-term tumor response and survival analysis. This may be because [^{18}F]FLT has shown mixed results as a good predictive marker in preclinical and clinical studies (352, 353). Other issues with [^{18}F]FLT may stem from the correct analysis technique to interpret the results (354). The sensitivity of measuring thymidine uptake may also not be a sensitive enough marker to provide good resolution of response (355). Therefore, the results from the [^{18}F]FLT-PET scan in this study was not considered as strongly indicative of the tumor's true response to radioPDT. The higher [^{18}F]FLT uptake in both irradiated and unirradiated NP groups may indicate confounding processes that may also be thymidine consuming, such as a reactive inflammation and clonal expansion of monocytes and neutrophils as part of the innate immune response. This was not able to be further assessed as the animals and tumors needed to be kept alive in order to investigate the other primary endpoints.

3.3.4.3 Tumor Response and Survival Analysis for radioPDT Treated Mice

The tumors were tracked after treatment via serial measurements by calipers every 2 to 3 days. The animals were also assessed for tumor size, evidence of metastatic disease, and signs of distress that would require euthanization. None of the animals needed additional treatments for infection, skin ulceration, or other symptoms related to treatment or disease. Mice that were still alive after 60 days were euthanized. Post-mortem analysis by necropsy was performed on all animals.

The mice tumors treated with NP only did not significantly differ in growth rate or survival compared to untreated control mice (**Figure 3.26a-b**). The radiation-only group had a

tumor response peaking at day 10 post-radiotherapy with a 18% reduction in tumor size, before it started to progress ($p=0.39$). Survival was improved to a median overall survival (mOS) of 36 days versus 15 days for the control group. The NP and radiation treated group (inducing a radioPDT effect) showed a significantly quicker response by day 4 compared to radiotherapy, with a tumor reduction of 54% compared to pre-treatment size ($p=0.0375$). The radioPDT treated tumors were also significantly smaller than the radiation only treated tumors, measuring 46% smaller ($p=0.0084$). The radioPDT treated tumors also showed a pattern of durable response with no trend towards regrowth over the follow-up period. Two mice euthanized at day 55 due to infected and necrotic tumors, and another mouse was euthanized at day 56 due to a symptomatic ipsilateral axillary lymph node metastasis.

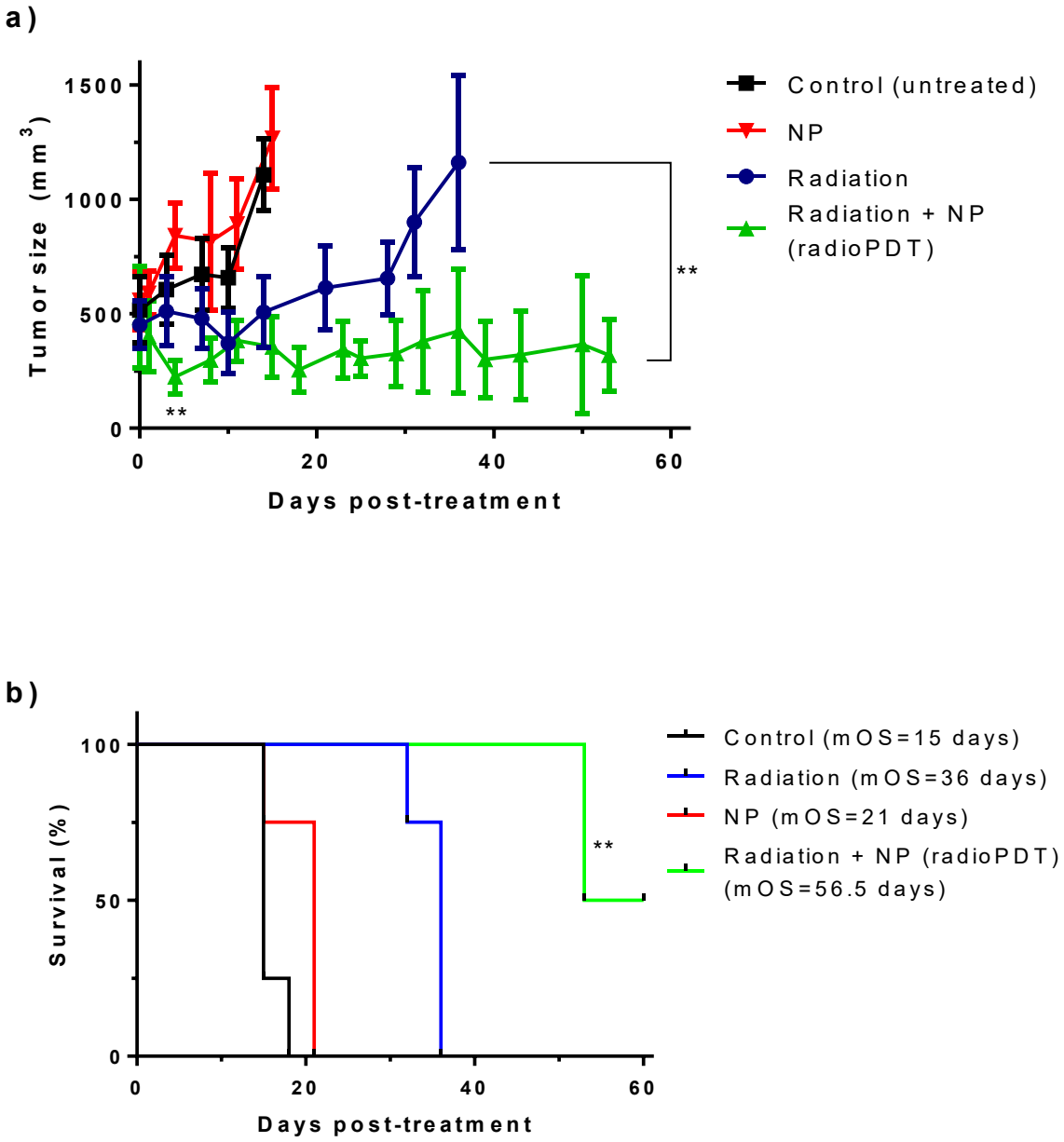

Figure 3.26: PC3 flank tumor xenograft mice were treated with NP injection, radiotherapy, or NP and radiotherapy and followed for tumor response (**a**) and overall survival (**b**) compared to control. The unirradiated mice had tumors progress at a similar rate and did not survive longer than 21 days (p=ns). The radiotherapy group induced a delay in growth compared to control ($p<0.0001$) and median survival was extended to 36 days from 15 days

($p<0.0001$). In comparison radioPDT showed a highly significant improvement in tumor response ($p=0.0084$) with increased overall survival to 56.5 days from 36 days ($p=0.010$).

Fifty percent (n=2) of the animals in the radioPDT NP + radiotherapy group were still alive at the end of the 60 day follow-up period. The mice were analyzed by [^{18}F]FDG-PET/CT on day 61 to assess for evidence of tumor metabolic activity and to assess for evidence of metastatic disease. **Figure 3.27** demonstrates minimal to no residual activity and residual flank tumors on the two remaining animals. One mouse did demonstrate evidence of axillary and lymph node metastasis, which was confirmed on post-mortem analysis (**Figure 3.27a**). The other mouse demonstrated FDG avidity in the humerus and spine, which was suspicious for potentially metastatic disease not appreciable on the CT component (**Figure 3.27b**). Histopathologic analysis, however, revealed no evidence of metastatic tumor cells were visible in these regions of abnormal FDG avidity (**Figure 3.28**). These sites of FDG avidity may alternatively correspond to an increase in glucose uptake by muscle activation (twitching/shivering) of the biceps/triceps muscles in adjacent to the humerus, and paraspinal muscles adjacent to the spine.

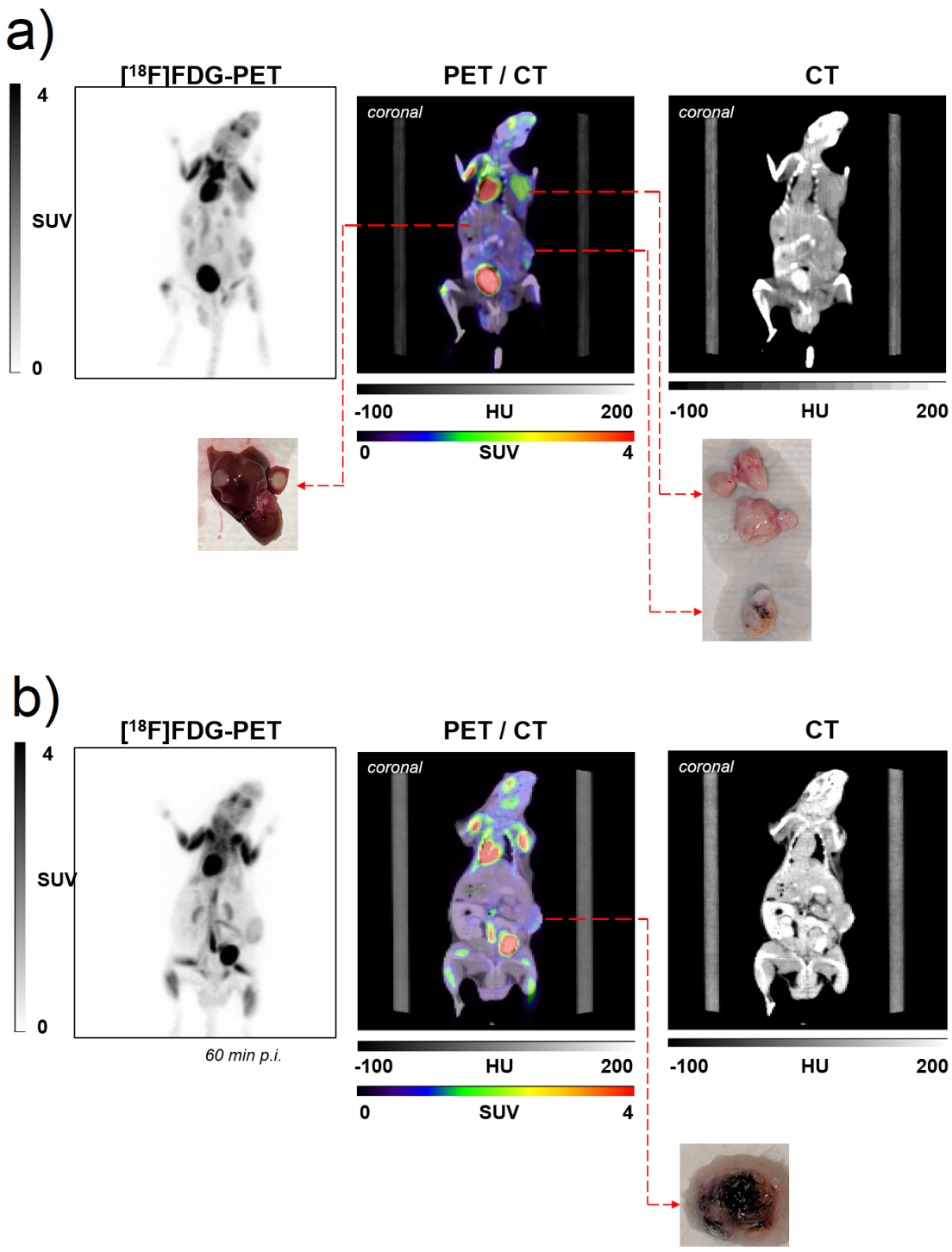

Figure 3.27: [^{18}F]FDG-PET/CT of animals treated with radioPDT after 60 days post-treatment. Minimal to no FDG avidity (a: SUV_{max}=1.25, b: SUV_{max}=0.93) remains in the tumor of the animals, which appear atrophic and scarred with granulation tissue on post-

mortem analysis (**a-b, bottom right insets**). **a)** demonstrates FDG avid lesions in the liver (SUV_{max} 1.05) and ipsilateral axillary lymph node region (SUV_{max} 1.65), which on post-mortem analysis revealed macrometastatic disease (**top left and right inset**). Regions of increased FDG avidity in the humerus and spine were seen in (**b**), but no disease was found on post-mortem analysis. Two of four mice demonstrated evidence of axillary or more distant metastatic disease. One mouse demonstrated FDG avidity. No other regions of metastatic disease were identified.

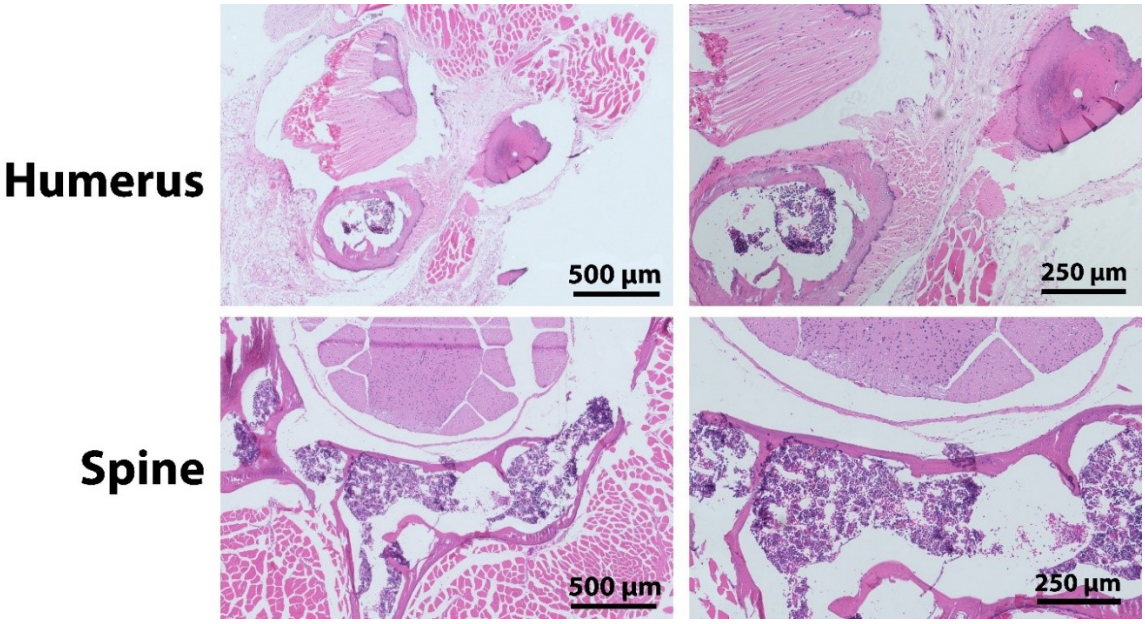

Figure 3.28: Post-mortem analysis of FDG avid areas suspected to be metastatic disease. The cortex, osseous body of the bone tissue and surrounding soft tissue in these areas did not show any evidence of metastatic tumor deposits..

The two mice euthanized prior to the study end period did not receive PET scans. Their post-mortem analysis demonstrates a necrotic and infected tumor in one animal, and a scarred down tumor similar to the other two animals shown in **Figure 3.29**. Macroscopic and microscopic comparison of the tumors from all 4 arms show a highly cellular tumor with diffusely infiltrative and proliferative PC3 cells in the control group, with many regions of mitosis evident (**Figure 3.29a, first row**). The NP treated tumors show similar high cellularity and diffusely infiltrative PC3 pattern, with some cells near the periphery of the tumor showing some pigmentation from PPIX-encapsulated NP (**Figure 3.29a, second row**). This likely represents areas of original tumor tissue at the time of injection, which have now migrated out to the periphery as the tumor grew. The radiation group demonstrated increased fibrosis with collagen fiber formation and scar tissue architecture (**Figure 3.29a, third row**). There is still however active PC3 cells visible. The radiotherapy and NP treated group shows decreased cellularity, mainly quiescent cells with mainly condensed nuclei (**Figure 3.29c, fourth row**). Large areas of cells that have taken up PPIX dye remain in the interior of the tumor, which indicates they have not been pushed to the periphery by new tumor growth. A macroscopic comparison of the tumors from the 4 arms are shown for reference (**Figure 3.29a, fifth row**). The lack of highly FDG avid lesions on the two remaining living animals along side the lack of active disease on macroscopic and microscopic post-mortem analysis of the tumors in all the radioPDT treated mice suggests these tumors were treated to the point of durable disease control.

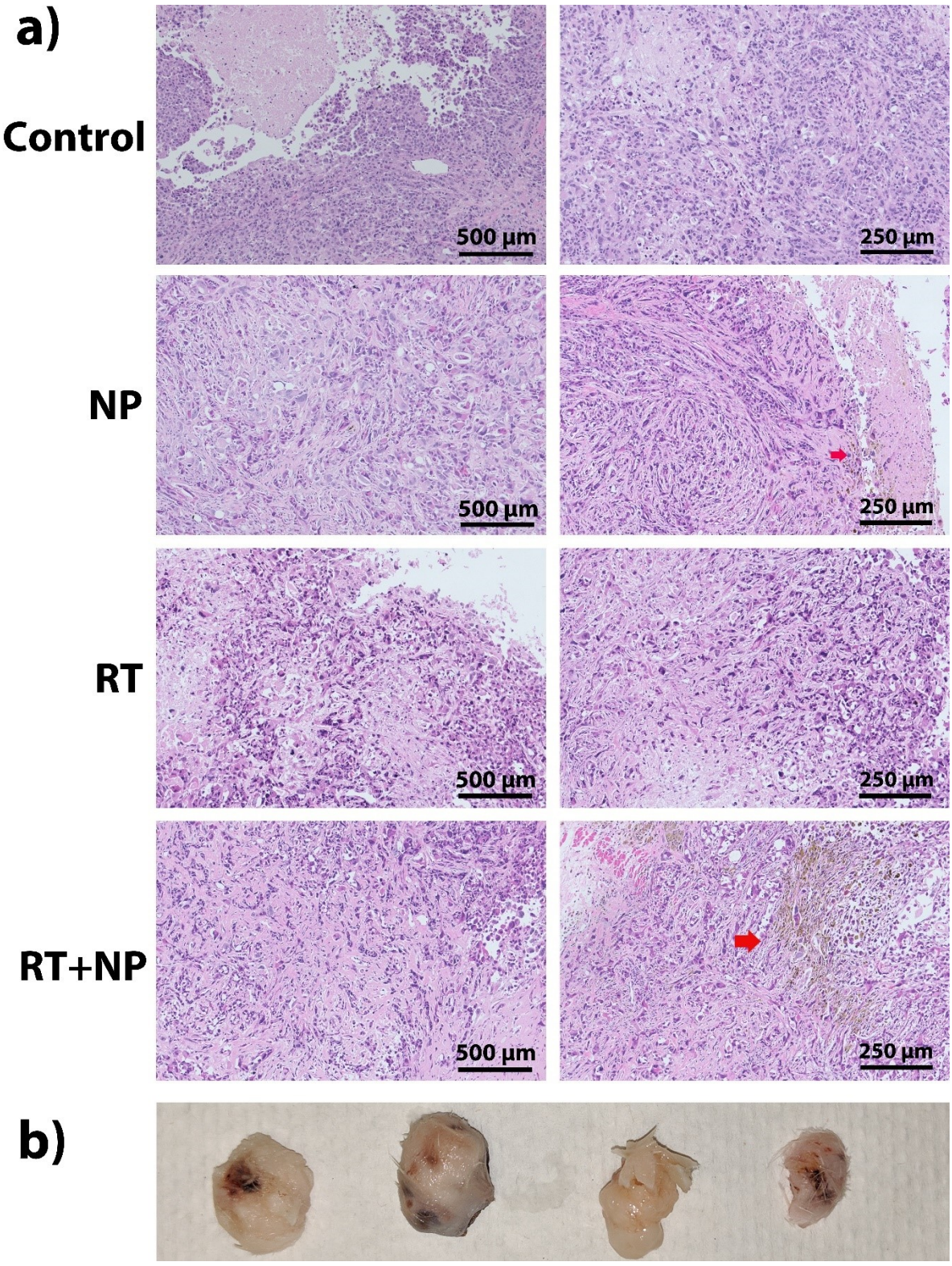

Figure 3.29: Post-mortem analysis of macroscopic and histopathologic tumor specimens from all arms of *in vivo* study. **a**): Control group shows highly cellular and proliferative

PC3 cells, with central necrosis also seen (**left image**). NP injected group shows similar high cellularity and active PC3 cells, with some cells showing some staining with PPIX dye from the radioPDT NP at the periphery of the tumor (**red arrow**). Radiotherapy (RT) group shows more abundant collagen fibers and scar tissue formation along side active PC3 cells. Radiotherapy with NP (RT+NP) shows reduced cellularity and some cells they may appear to be PC3 cells but have condensed nuclei and reduced nuclear to cytoplasmic ratio, less mitotic activity, and pigmentation likely representing PPIX-encapsulated NP taken up by quiescent cells (red arrow). **b)**: comparison of post-mortem tumors of control (**far left**), NP (**middle left**), RT (**middle right**) and RT+NP (**far right**). Some central necrosis is seen on the control tumor. The NP-injected tumor shows remnant of PPIX dye on the periphery of the tumor. The RT-treated tumor shows decreased vascularity and was adherent to the skin on excision (see superior border of tumor). The RT+NP-treated tumor was harder in texture, flat, and adherent to the skin (covering the tumor surface) with some central granulation tissue (crusting) noted.

3.4 Summary of *in vitro* and *in vivo* Therapeutic Efficacy Studies of radioPDT

The potential for radioPDT effect from the novel NP system was seen in the studies presented in this chapter. The NP design provided an effective way to augment radiotherapy with minimal added normal tissue toxicity. The additional effect of radioPDT was partially oxygen dependent but was still able to add significant anti-cancer therapeutic effect in hypoxic conditions as low as 1%. *In vivo* studies validated the radioPDT's ability to add significant therapeutic effect to low doses of radiation.

Singlet oxygen yield was assessed with SOSG probe, as a demonstration of radioPDT effect occurring. Singlet oxygen yield was found to be dose-dependent on radiotherapy dose and NP dose used. Hypoxic conditions did limit ultimate yield of singlet oxygen, and higher doses of radiotherapy were required to yield significant quantities.

In vitro cytotoxicity was demonstrated via colorimetric viability assay and live/dead flow cytometry. Viability assay showed the additional cytotoxicity on PC3 cells was once again dependent on radiation dose and NP dose. Gradients of hypoxia also limited the additional effect from radioPDT. Live/dead assay yielded significant cytotoxicity ranging from 80% in normoxia to 25% in 1% hypoxia at a high NP and radiation dose. Lower NP and radiation doses also yielded significant cytotoxicity, but the magnitude of effect could be diminished by introducing hypoxic conditions. The $1/2K_{max}$ of oxygen's effect on radioPDT was estimated to be about 5%. At low oxygen concentrations, the radioPDT effect appeared to be oxygen-limited, with different NP doses not yielding a dose-response. At higher oxygen concentrations, the radioPDT effect appears to switch to a NP-limited effect and increasing NP dose produced proportionally higher cytotoxic effect.

In vivo assessment of radioPDT NP demonstrated superior therapeutic effect to radiotherapy alone. The effect of the NP alone was no different than control, indicating the NP design with PPIX and $LaF_3:Ce^{3+}$ is not an active agent without stimulating energy. With low doses of radiotherapy, the NP was able to yield significant cytotoxic effect of the PC3 tumor and induced a strong and durable tumor response. The tumor appeared inactive for up to 60 days. This resulted in significantly longer survival for mice treated with radioPDT. The post-study analysis showed 2 of 4 mice developed metastatic disease despite superior local control. One mouse succumbed to post-treatment infection of the tumor. One mouse appeared to have an inactive tumor with no evidence of metastatic disease confirmed.

The oxygen-dependent effect in hypoxic conditions indicates molecular oxygen is the rate-limiting mechanism for the Type I reaction and singlet oxygen generation. The radioPDT effect still yields a lower, but significant, additional in cytotoxicity even in hypoxic conditions. This may be due to a greater proportion of Type II reaction occurring, which mainly uses water as a substrate. In physiologic hypoxia conditions with the *in vivo* PC3 flank tumor model, radioPDT yielded a robust anti-tumor response with minimal additional toxicity. This is likely due to the PDT effects on vasculature also contributing to direct tumor cell cytotoxicity. The evidence of metastatic disease indicates the radioPDT effect was able to control disease locally but the third component of the PDT mechanism, the immune priming effect, was not present in the immune-deficient NSG mice model used. Regardless, a potential cure was obtained on one of four mice treated, with no evidence of active disease found.

Taken together, these results show the therapeutic benefit of our novel radioPDT NP system. Even with a palliative dose of 6 Gy single fraction radiotherapy, which is even lower than the commonly-used 8 Gy single fraction regime clinically (356-358), durable long-term local control was obtained with minimal additional toxicity. This shows the potential of our radioPDT NP as a candidate for concurrent administration with radiotherapy, which could lead to greater therapeutic effect at lower radiation doses and resultant long-term radiation side effects.

CHAPTER – 4

INVESTIGATING DIAGNOSTIC UTILITY OF RADIOPDT NANOPARTICLES WITH CT IMAGING AND BIODISTRIBUTION STUDIES

.

CONTRIBUTIONS

This research required a multidisciplinary team with diverse skill sets to conduct theexperiments. I conceived the nanoparticle and theranostic paradigm, designed and performed all of the experiments, unless otherwise stated, and prepared the manuscript for publication as described in the **Preface**. Dr. Hans-Sonke Jans participated in the analysis of CT studies. Dr. Melinda Wuest and Dr. Hans-Sonke Jans performed the *in vivo* CT imaging studies. Inductive coupled plasma mass spectrometry (ICP-MS) analysis was performed by Guangcheng Chen (Department of Earth and Environmental Sciences, University of Alberta). Dr. Hua Chen assisted in data collection. Dr. John D. Lewis assisted in experimental design and analysis. Dr. David Murray, Dr. Ravin Narain, Dr. Frank Wuest, Dr. John D. Lewis, and Dr. Ronald Moore provided guidance in experimental design, data interpretation, and manuscript preparation.

4.1 Introduction

The use of theranostic agents in treatment of cancer can lead to superior treatment options for patients. Multiple clinically used theranostic agents have greatly contributed to precise treatment delivery and monitoring. The most commonly used agents in clinical cancer management are a radionuclide-based systems such as iodine-131 treatment for thyroid cancer and lutetium-177 and yttrium-90 based peptide analogues for neuroendocrine tumors (359, 360). These radionuclide systems allow imaging prior to treatment to predict efficacy and during treatment to monitor for successful delivery. Radionuclide-based agents continue to represent the majority of clinical trials in cancer care that investigate theranostic approaches (361).

Other lesser-known forms of theranostic agents have also been used in clinical treatment of cancer. PDT falls into this category as well, since the fluorescent properties of the PS can provide some diagnostic utility. The use of PS-based agents can be used as a cancer-specific fluorescent imaging dye to guide surgical resection of brain tumors, detection of colonic dysplastic and cancerous lesions, diagnose clinically invisible mucosal lesions in head-and-neck cancers, and see and treat lung and early bladder neoplasia (362-365). There are also preclinical studies that use the PS's diagnostic and therapeutic capabilities simultaneously and demonstrate the superiority of using PDT agents in a theranostic approach (366, 367).

Another class of theranostic agents in development are nanotheranostics, which use nanoparticle-based systems that can act therapeutically and diagnostically. The use of nanotheranostics is appealing in cancer care because it can build on a large body of

preclinical work within nanomedicine that has shown the safety, pharmacokinetics, and efficacy of multiple nanoparticle platforms (368). In general, they use a nanoparticle system loaded with a therapeutic agent and a diagnostic agent that can simultaneously provide both functions in managing the cancer. The ability to "watch" the drug and its therapeutic action in the body can allow for real-time adjustment in drug dosing, predictive capabilities of treatment effect, monitoring for off-target effects and potential toxicities, and personalizing the cancer therapy to the individual's body and disease. Several nanotheranostic agents have been proposed in the use of cancer treatment and are undergoing development in preclinical studies (369-371).

Contemporary radiotherapy treatment also heavily integrates diagnostics into the radiation treatment delivery system, in a process called Image-Guided Radiotherapy (IGRT). The use of IGRT leads to improved accuracy, decreased treatment volumes, decreased toxicity to surrounding normal organs, and higher quality radiotherapy (372-374). IGRT is also crucial to delivering modern RT techniques such as SRS and SBRT. Many recent innovations in radiotherapy involve improvements in the image-guided component of IGRT. As newer modalities of IGRT emerge, such as LINACs with onboard MRI scanners (MR-LINAC), we are approaching the new frontier of real-time image-guided delivery of radiotherapy (375). The ability to "see what you are treating" is becoming an integral part of modern radiotherapy and has contributed to its evolution into a higher precision modality.

Further contributions to IGRT can come in the form of nanotheranostic agents that can simultaneously augment the real-time imaging during radiotherapy as well as the efficacy of treatment. Development of such agents for IGRT have mainly been with heavy-metal

radiation dose enhancers that are also contrast enhancers on CT or MRI (376, 377). Herein, I report the use of a novel radioPDT NP and its diagnostic characteristics that could contribute towards a new theranostic approach in IGRT.

4.2 Materials and Methods

4.2.1 Calibration of CT contrast enhancement

The use of heavy metals in the scintillators lends itself to high attenuation of kilovolt range x-rays, due to the dominant x-ray attenuation modality being photoelectric effect (378). Attenuation from photoelectric effect is proportional to the cube of the atomic number. Lanthanum and cerium's atomic numbers are 57 and 58, respectively, which would predict that it would perform slightly better than iodine (atomic number: 53); a commonly used clinical contrast agent (341).

To test this, a mouse analog (phantom) was fashioned out of a 50 mL falcon tube (Millipore, US) filled with 30 mL of Agarose gel (ThermoFisher, US) and solidified at 37 °C. The male needle attachment tip of a 1mL insulin syringe (ThermoFisher, US) was pushed through the end of the falcon tube prior to adding the agarose gel. The syringe tip was then used to draw the NSC suspension into the syringe of the solution to be analysed. CT scans were acquired on a Siemens Inveon pre-clinical microCT scanner (Siemens, Germany) at 60 KVp energy, and 400 mAs exposure. Image analysis was done using ImageJ software (NIH, US).

4.2.2 *In vivo* Chorioallantoic Model (CAM) X-ray Imaging

The NSC's ability to perform as a contrast agent in an *in vivo* system was assessed in a pilot study on Chorioallanotic Membrane (CAM) chicken embryo model. A tumor was implanted into the CAM using HT1080 human fibrosarcoma tumor cells as previously described (379-381). Once the tumor reached 1 cm diameter, the CAM was X-ray imaged using a Bruker Biospin In vivo Xtreme Imaging System (Bruker Biospin, Ettlingen, Germany) at 45 KVp and 300 μA. Images were obtained serially at baseline and every 2 minutes post-injection IV. The tumor was monitored for evidence of enhancement on the X-ray image. The images were qualitatively compared for evidence of tumoral enhancement.

4.2.3 RadioPDT NP Distribution Studies in PC3 Flank-tumor Mice Models by Serial CT Imaging

More detailed assessment of the radioPDT NP system was assessed using a PC3 flank tumor-bearing NSG mouse model. The tumors were grown to a size of 500 mm^3 prior to experimentation. The animals were anesthetized with an induction 3-4% inhaled isoflurane followed by maintenance on 1-3% inhaled isoflurane. A Siemens Inveon pre-clinical microCT scanner (Siemens, Erlangen, Germany) was used to acquire CT images at 60 KVp energy, 400 mA exposure, and 260 axial slices (slice thickness of 0.4 mm, and X and Y resolution of 0.411 mm) per mouse. The mice were serially scanned across multiple timepoints and were recovered from anesthesia between scans. Images were reconstructed on the Siemens imaging platform and exported as DICOM files to ARIA Eclipse Planning System version 13.6 (Varian Medical Systems, Palo Alto, USA).

NSC NPs were synthesized as described previously in **Section 2.2.1**, using the long hexagonal NSC formulation and a single dose injection at a concentration of 500 mg/kg IV was done via tail vein (n=4) and IT (n=2). The IV injected mice were imaged at baseline pre-injection, 4 hours, 24 hours, and 48 hours post-injection. The IT injected mice additionally had timepoints of 10 minutes and 1 hour post injection. The tumor and liver were contoured using ARIA Eclipse radiation planning software (Varian, Palo Alto, USA) and the average HU value was obtained from the whole volume. After the 48 hour scan, a post-mortem analysis was performed and the liver and tumor were excised and analysed by inductive coupled plasma mass spectrometry (ICP-MS) using previously described techniques (382, 383). The tissue was immersed in an equal weight of 50% HNO_3 and sonicated with a probe sonicator (Fisherbrand™ Model 505, Thermo Fisher Scientific, Waltham, USA) for 15 minutes. The sample was left to dissolve fully over a one-week period. Analysis was carried out using a Perkin Elmer ELAN 6000 ICP-MS (Waltham, MA, USA).

The study was repeated with radioPDT NP synthesized as described in **Section 2.2.1** with short-hexagonal NSC crystal structure formulation. The mice were injected IV via tail-vein with 500 mg/kg of NP and serially imaged as described above. The left lung, left kidney, liver, tumor, spleen, and left quadricep were contoured on ARIA Eclipse software and average HU value ascertained from the whole volume. After the 48 hour scan a post-mortem analysis was performed on the left lung, left kidney, left quadricep, liver, spleen, tumor and these organs were excised for ICP-MS analysis.

4.2.4 Statistics

All calculations and statistical analysis were performed using Microsoft Excel 2016 (Microsoft, Redmond, USA) and GraphPad Prism 6 (San Diego, USA). A linear regression line was fit to the data values of the NSC calibration curve in order to obtain a HU/mg/mL value. Tumor uptake of NP and enhancement assessment was done with analysis of variance (ANOVA) comparing multiple groups and Tukey's multiple comparison test. All analyses used p=0.05 as the threshold for significance.

4.3 Results and Discussion

4.3.1 Comparison of NSC CT Contrast Enhancement and Efficiency with a Clinically used Contrast Agent (Omnipaque 300®, GE Healthcare)

The diagnostic capability of the drug was tested using small-animal phantom model from body-tissue equivalent agarose gel around a 1 mL syringe, which is analogous to the size and blood content of a mouse model. The preferred imaging modality for radiation targeting and dosimetry is CT, as this is the most commonly used on-board image-targeting system in modern radiation delivery machines (384). The phantom was loaded with samples of control (water), NSC NPs, or clinical standard iodine-based CT contrast agent of Omnipaque 300® (GE Healthcare, Chicago, USA). CT scans were acquired with an animal model microCT scanner (Siemens Inveon, Erlangen, Germany).

Initial studies compared the performance of the different crystal structures of $LaF_3:Ce^{3+}$.

Figure 4.1 (bottom right) shows an axial slide of the mouse phantom loaded with water, NSC, and Omnipaque 300®. Using the scanning software's built in HU region-of-interest measurement tool, the average HU over a standardized slice in the scan frame was attained

for each condition. The experiment was repeated in dilutions of positive control (omnipaque), NSC concentrations, and negative control (water). The resultant values are plotted for HU vs concentration to demonstrate the efficiency of the agent in acting as a contrast agent. The contrast efficiency was quantified using the slope of the linear regression of plotted data points.

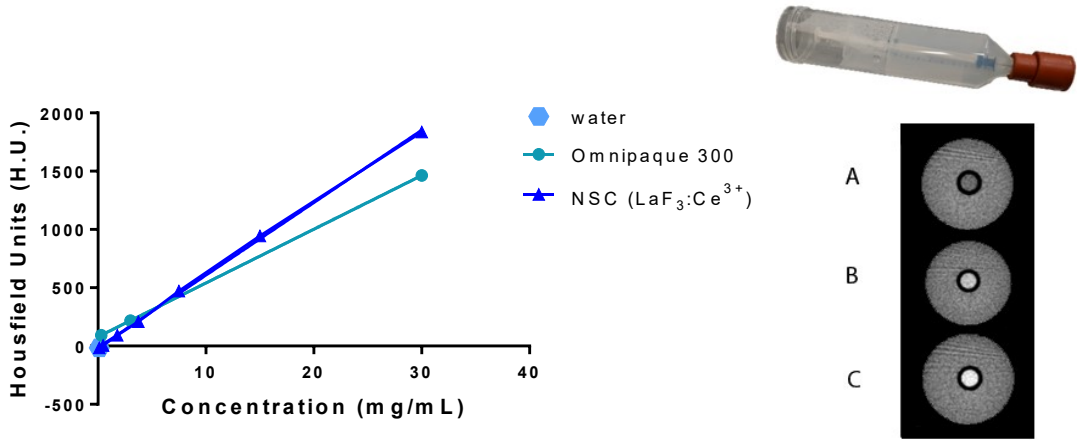

Figure 4.1: On the left, the graph shows contrast efficiency of NSC (short hexagonal structure) compared to clinical CT constrast agent of Omnipaque 300®. Scans were acquired at 60 KVp energy on a flat-panel based preclinical micro CT scanner. From the slope, the contrast efficiency of Omnipaque 300® is 46 HU/mg/ml versus contrast efficiency of NSC which is 62 HU/mg/mL. On the right, the mouse CT phantom is shown (**top**), and an axial cross-section of the CT phantom is shown when filled with water (**A**), omnipaque (**B**), and NSC (**C**) at a concentration of 5 mg/mL.

The NSC showed appreciable CT contrast efficiency and was close to the clinical standard of Omnipaque with a value of 62 HU/mg/mL vs 46 HU/mg/mL, respectively (**Figure 4.1, left**). This contrast efficiency compares favourably against other reported iodine-based PEGylated micelles that function only as contrast agents (385). The contrast efficiency of NSC appears even slightly higher than Omnipaque. The use of heavy metals as scintillators lends itself to high attenuation of kilovolt range x-rays, due to the dominant x-ray attenuation modality being photoelectric effect (378). Attenuation from photoelectric effect is proportional to the cube of the atomic number. Lanthanum and cerium's atomic numbers are 57 and 58, respectively, which would predict that it would perform slightly better than iodine (atomic number: 53); a commonly used clinical contrast agent (341).

The short and long hexagonal formulations were shown to have different fluorescent characteristics (**Section 2.3.1**). They were also observed to have similar density but different volume per crystal, which would predict for a higher weight per crystal (**Table 2.1**). This would suggest a given concentration of NP would have a higher amount of NSC atoms and therefore, higher Z atoms to interact and undergo photoelectric effect. To investigate this, the attenuation efficient of the two NSC crystal structures were compared. **Figure 4.2** demonstrates their contrast enhancement efficiency of the two NSC crystal structures. The contrast efficency of the long hexagonal crystal structure is about 10 times lower, with a value of 6.2 HU/mg/mL compared with 62 HU/mg/mL for the short hexagonal structure. From **Table 2.1**, the short hexagonal crystal structure has about three times the volume for the same density as the long hexagonal structure, which translates to about 3 times more mass and atoms. This would greatly increase the photon stopping power of incident low KV X-rays. However, the effect is not linear, as NP use as an X-ray

attenuator is susceptible to NP clustering effects in tissue and solution (349, 351, 386-388). Factors affecting X-ray absorption include the NSC size, clustering, cross-sectional area, and concentration. With gold NP, clustering of the NP into 90 or more cluster units tend to decrease the X-ray attenuation. Due to the PEG-PLGA encapsulation, the NSC in our radioPDT NP system do not tend to cluster closely, with no more than about 3 to 5 NSC per NP (**Figure 2.11**). This increases the cross-sectional area of the NSC to incident X-rays and may non-linearly raise the attenuation to a much greater extent that predicted by the just the increase in atoms alone.

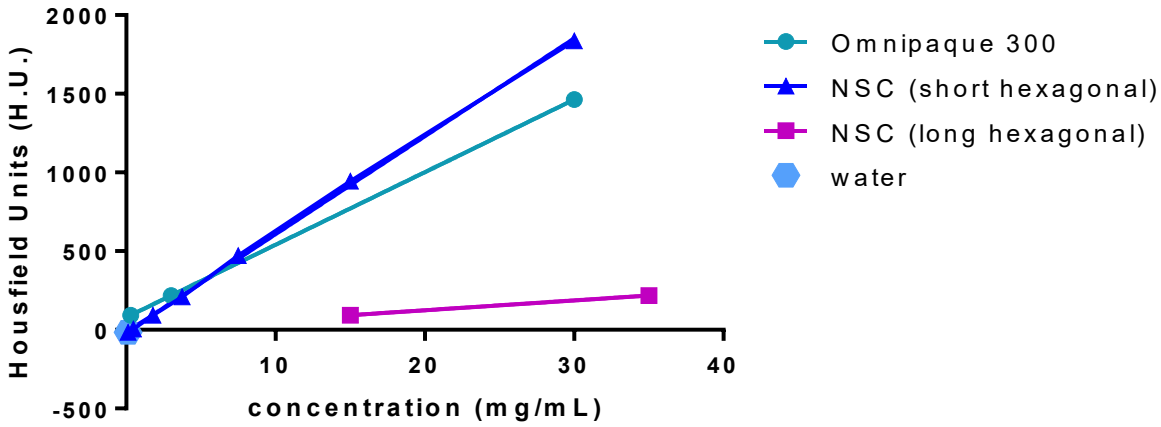

Figure 4.2: Comparison of X-ray attenuation efficiency of short hexagonal and long hexagonal crystal latter structures of NSC. The attenuation efficiency of short hexagonal NSC was found to be 62 HU/mg/mL upon fitting a linear regression curve to the data points. The attenuation efficiency of long hexagonal NSC was 6.2 HU/mg/mL in comparison.

4.3.2 Proof-of-Concept X-ray Diagnostic Imaging Studies in Chorioallontoic Membrane (CAM) Models Implanted with HT1080 Tumors

To assess if the NSC could provide meaningful contrast-enhancement under x-ray imaging in an *in vivo* system, a CAM model implanted with a HT1080 fibrosarcoma tumor was employed. These are known to be highly vascular tumors that recruit vasculature from the CAM (389). The tumors were grown for 5 days to reach a 1 cm diameter before pursuing imaging studies with a baseline and follow-up X-ray of the CAM tumor. Baseline X-ray image did not demonstrate any appreciable contrast enhancement of the tumor. The CAM was then injected IV with 100 µL of contrast agent. After injection with the positive control of 1% Omnipaque 300® (GE Healthcare) or NSC, the CAM was imaged 10 minutes later to assess for signs of contrast enhancement.

The CAM model was able to successfully demonstrate accumulation of Omnipaque® in the tumor and in peri-tumoral neoangiogenesis (**Figure 4.3a**). When injected with 3mg/mL NSC a similar enhancement pattern into the tumor and peri-tumoral neoangiogenesis was also seen. This indicated the NSC could have potential as a diagnostic agent under *in vivo* conditions.

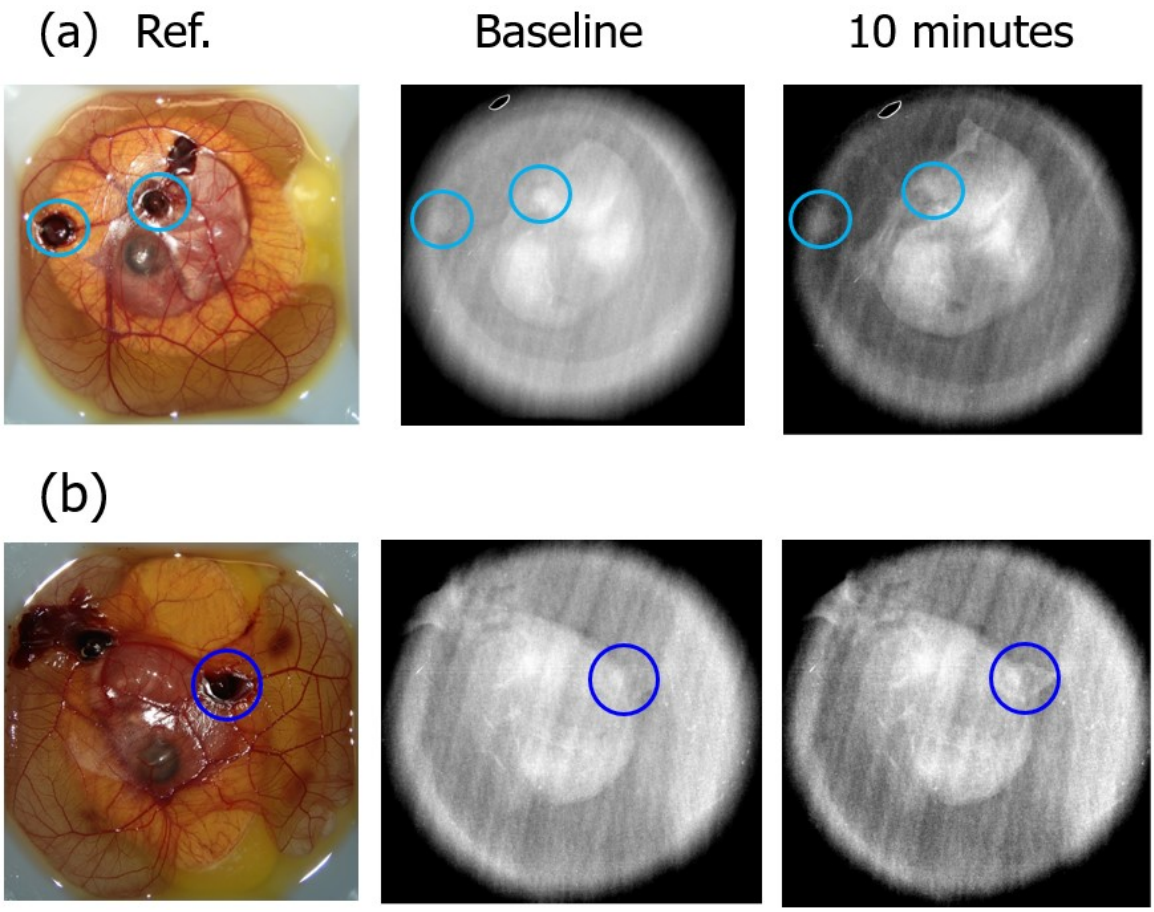

Figure 4.3: Comparison of Omnipaque ® (GE Healthcare) and NSC (long hexagonal structure) in producing contrast enhancement in a CAM tumor model. The CAM models were implanted with HT1080 cell line tumors that were grown to a diameter of about 1 cm before being imaged (**see Ref. images**). **a**) The CAM was implanted with two tumors (**light blue circles**) at baseline (preinjection), with the right tumor showing evidence of peritumoral neoangiogenesis. X-ray imaging did not clearly visualize the tumor or hemorrhage. 10 minutes post-IV injection of Omnipaque® produced contrast enhancement and clearly distinguishable tumors as well as highlighting the area of neoangiogenesis. **b**) Similar findings were also seen in with CAM tumor models with IV injection of NSC.

4.3.3 *In vivo* CT Detection and Biodistribution Studies of radioPDT NP in Flank Tumor-bearing Mice

Further assessment of the NSC's ability to act as a CT contrast agent was carried out using PC3 prostate cancer flank tumor models grown in NSG mice. The tumors were grown to a size of 500 mm^3 before commencing experiments. The animals were imaged with a microCT scanner (Siemens, Germany) prior to injection of NP and then serially imaged at 4 hours, 24 hours, and 48 hours. Based on similar NP *in vivo* biodistribution studies, the NP was expected to start accumulating first in the liver and other large organs at 4 hours, then peak in accumulation in the tumor around 24 hours, followed by clearing from the tumor at 48 hours (390, 391). The first set of experiments were conducted injecting mice with long hexagonal-based NSC NP IV and IT (**Figure 4.4**). When tracking the changes in HU in the liver and tumor, there was a significant rise in liver enhancement by about 30 HU seen ($p=0.0189$) but no difference was seen in the tumor's HU levels post-injection. The IT treated group showed a rise in the tumor and liver HU, but no significant difference was detected, although this may be limited by the sample size ($n=2$). This indicates the NSC NP can act as a contrast agent, but the long hexagonal crystal structure may not have the contrast efficiency to demonstrate uptake into the tumor.

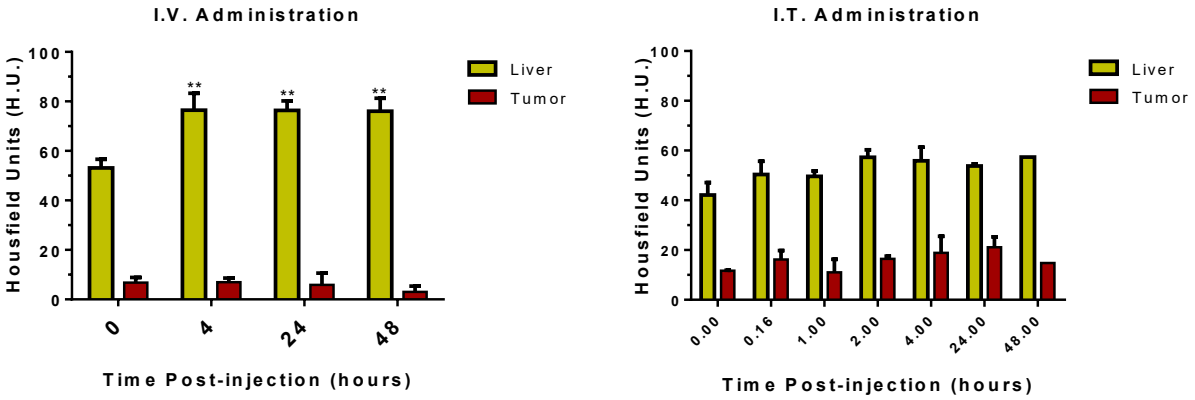

Figure 4.4: Comparison of IV and IT administered long hexagonal NSC NP in PC3 flank tumor-bearing mice. IV injected mice (n=4) showed a significant increase in liver HU from 53.1 HU pre-injection to 76.4 HU, 76.4 HU, and 76.0 HU at 4 hours, 24 hours, and 48 hours post-injection (p=0.0158), which indicates uptake of the NP. The tumor did not show any statistically significant difference. The IT treated mice showed a rise in the liver and tumor but no statistically significant difference (n=2).

Upon viewing the images of the IT treated mice, it is clear that there is a region of strong contrast enhancement where the NP were injected into the tumor (**Figure 4.5, bottom row**). This region also showed redistribution through the tumor over time as well. Some of the mice in the IV administered group also showed evidence of enhancement in the tumor (**Figure 4.5, top row**). However, this effect was not consistently replicated across the other IV injected mice. This seems to suggest the contrast efficiency of the long ***hexagonal NSC*** was not high enough to act as an effective method of tracking NP distribution into the tumor.

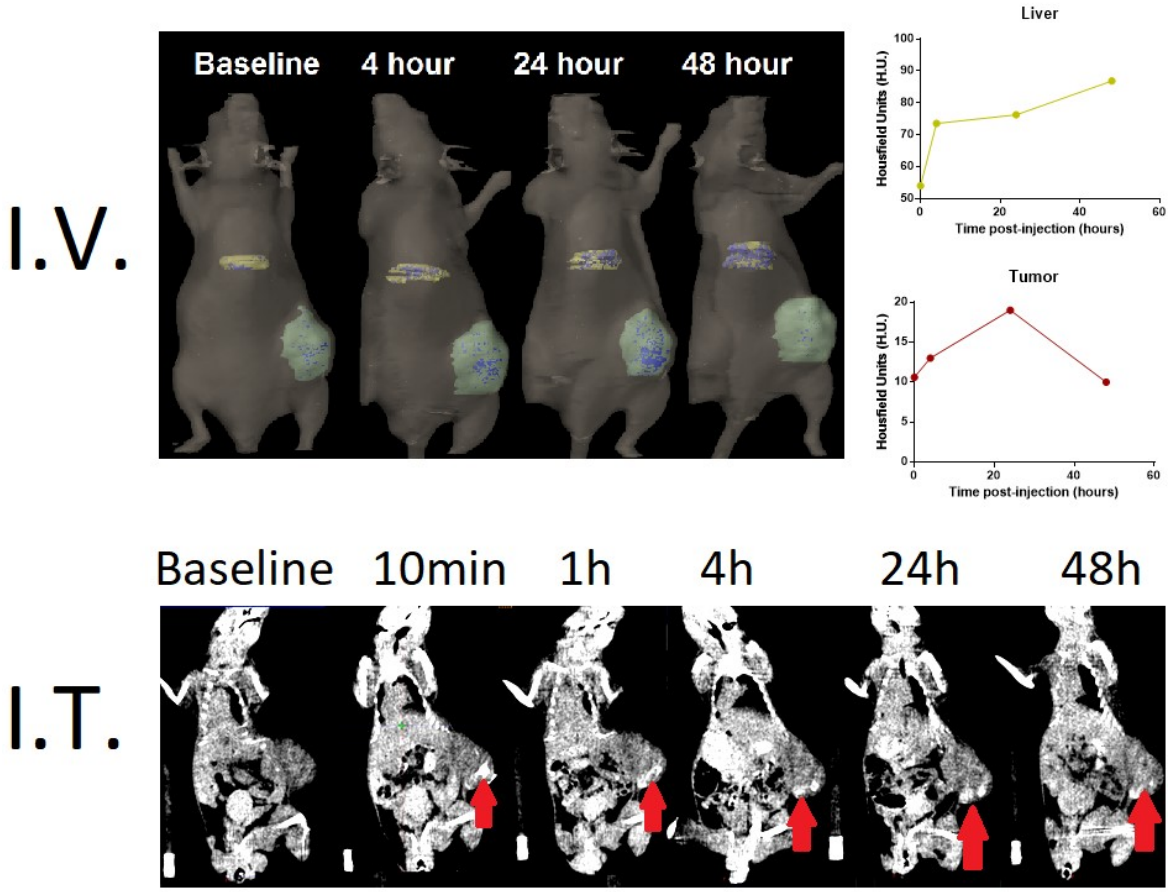

Figure 4.5: Serial CT images showing distribution of enhancement through the mice treated with long hexagonal NSC NP IV or IT. **Top row:** Maximum Intensity Projection (MIP) image of an IV injected mouse showing enhancement (**blue**) of HU > 70 in the flank tumor (green) and liver (**yellow**) over time, with corresponding whole tumor and whole liver HU quantification shown to the right. **Bottom row:** A bright spot of enhancement (**red arrow**) is seen in the IT treated mice in the tumor 10 minutes post injection, which seems to distribute through the tumor with time and disperse.

To improve on these results, ***short hexagonal NSC*** were used to synthesize radioPDT NP to treat the next group of mice with and assess enhancement response on serial CT scans. A similar experimental design to above was followed. All mice were injected with radioPDT NP IV prior to imaging with CT. Strongly significant rise in the liver HU measurements were seen from baseline (51.9 HU) to a 26.0 HU increase at 4 hours (77.9 HU, p=0.0006), 27.9 HU increase at 24 hours (79.8 HU, p=0.0001) and 30.8 HU increase at 48 hours (82.8 HU, p=0.0002). In comparison to the long hexagonal NSC in **Figure 4.4**, the IV injected mice reached a value of 36.9 HU at 24 hours, representing a statistically significant rise of 6.9 HU from baseline (p=0.0462), which indicates more contrast enhancement was occurring with the short hexagonal crystal lattice. Significant increases were also seen in the kidney and spleen as well (**Figure 4.6**). The increased CT attenuation performance of the short hexagonal NSC was once again likely not due to intrinsic properties of the crystal lattice but more of a function of increased number of atoms per NSC due to a larger internal volume, leading to higher contrast efficiency per NSC.

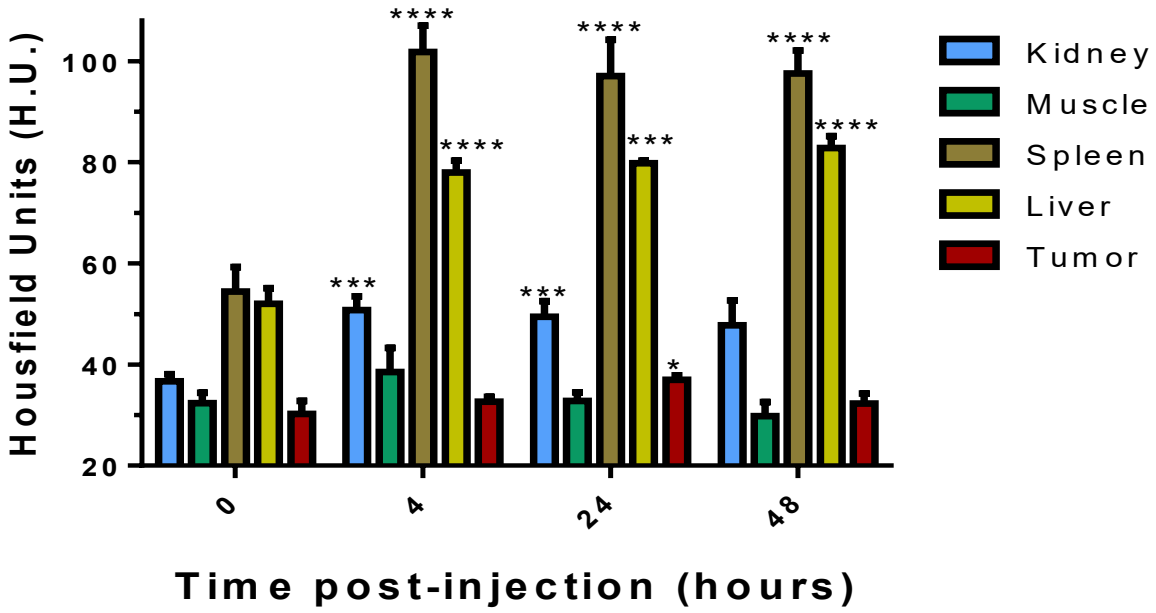

Figure 4.6: Measurement of CT enhancement in flank-tumor bearing mice after IV administration of radioPDT NP using ***short hexagonal NSC*** formulation. Serial CT scans were taken pre-injection of NP and 4 hours, 24 hours, and 48 hours post-injection. The average HU intensity of select organs were measured and compared pre and post-injection. The liver had an increase in CT enhancement from 51.9 HU pre-injection to 77.9 HU (p=0.0006), 79.8 HU (p=0.0001) and 82.8 HU (p=0.0002) at 4 hours, 24 hours, and 48 hours post-injection. The spleen had an increase in CT enhancement from 54.4 HU pre-injection to 101.8 HU (p=0.0005), 97.0 HU (p=0.0027) and 97.5 HU (p=0.0006) at 4 hours, 24 hours, and 48 hours post-injection. The kidney had an increase in CT enhancement from 36.6 HU pre-injection to 50.8 HU (p=0.0005), 49.4 HU (p=0.0027) and 47.8 HU (p=0.0737) at 4 hours, 24 hours, and 48 hours post-injection. The tumor had an increase in CT enhancement from 30.2 HU pre-injection to 32.6 HU (p=0.4072), 36.9 HU (p=0.0462) and 32.3 HU (p=0.5411) at 4 hours, 24 hours, and 48 hours post-injection. No significant changes in HU were seen for the quadricep muscle or lung (not shown).

Assessment of the spleen also showed a strongly significant increase in HU post-injection (**Figure 4.6**). The magnitude of CT enhancement was by about 45 HU, which indicates the majority of the NP was sequestered in the spleen and liver. This would be in keeping with clearance of the polymeric NPs through the MPS system, which is seen with similar polymeric NPs (390, 392, 393). The use of a PEGylated coating our NP system helps decrease the rate of clearance by MPS and allow more time in circulation and distribution to the target tumor, but MPS still remains the dominant mechanism for NP clearance from the body. The kidney also showed a significantly increased uptake at the earlier time points (approximately 15 HU increase over baseline, **Figure 4.6**), which may be an indication of its highly vascular nature and blood flow carrying the NP through the kidney. Previous assessment with fluorescent microscopy did not demonstrate appreciable uptake into the kidney interstitium (**Figure 2.21**).

The muscle and lung tissue did not demonstrate significant increase in HU with injection of radioPDT NP, with average HU values remaining at 32.3 ± 2.0 HU and -347 ± 28 HU, respectively. The relative HU values of these organs at the 48-hour time point also corresponds to post-mortem ICP-MS analysis for the La content from the NSC (**Table 4.1**). Of note, detectable levels of NSC were seen in the lungs as well even though contrast enhancement was not seen. Lung vasculature is a well-known organ system in the MPS clearance of NP, but the heterogeneity in the lung tissue along with respiratory motion during CT acquisition causes too much variability in lung HU measurement to detect increase in HU signal from enhancement. Analysis of the HU changes over time showed a significant HU increase at the 48 hour time point for liver, spleen, and kidney. When the NSC content in these organs was measured by ICP-MS it appears to show the ppm values

do not linearly scale with the additional HU measured by CT. This is again likely a demonstration of non-linear x-ray attenuation characteristics of NP content-to-enhancement in body tissues, due to dependence on additional characteristics such as NP clustering and cross-section to incoming X-ray in these different-sized organs.

Table 4.1 Comparison of crystal structure physical characteristics between aqueous and organic phase synthesized $LaF_3:Ce^{3+}$ NSC.

	Kidney	Lung	Muscle	Spleen	Tumor	Liver
La concentration (ppm)	0.46 ± 0.16	1.31 ± 1.70	0.04 ± 0.03	82.2 ± 35.0	0.13 ± 0.05	72.5 ± 14.0

The quantitative enhancement was also correlated with enhancement seen qualitatively on ARIA Eclipse CT viewing software (**Figure 4.7**). At 4 hours post injection, there is marked enhancement seen in the liver and some small regions of increase in enhancement in the tumor. At the 24 hour mark the liver is homogenously enhanced, and the tumor shows heterogenous enhancement throughout. By 48 hours the liver continues to have increase CT enhancement, and the tumor appears to start losing enhancement at some of the periphery. The superior aspect of the tumor (**Figure 4.7, red arrow**) appears to show a relatively greater extent of contrast increase and decrease over time, potentially indicating the NP is able to extravasate into interstitium and leave from this portion of the tumor at a faster pharmacokinetic rate than others. This highlights the aberrant vasculature within the tumor and the inhomogeneous uptake and clearance of therapeutic agents from tumors.

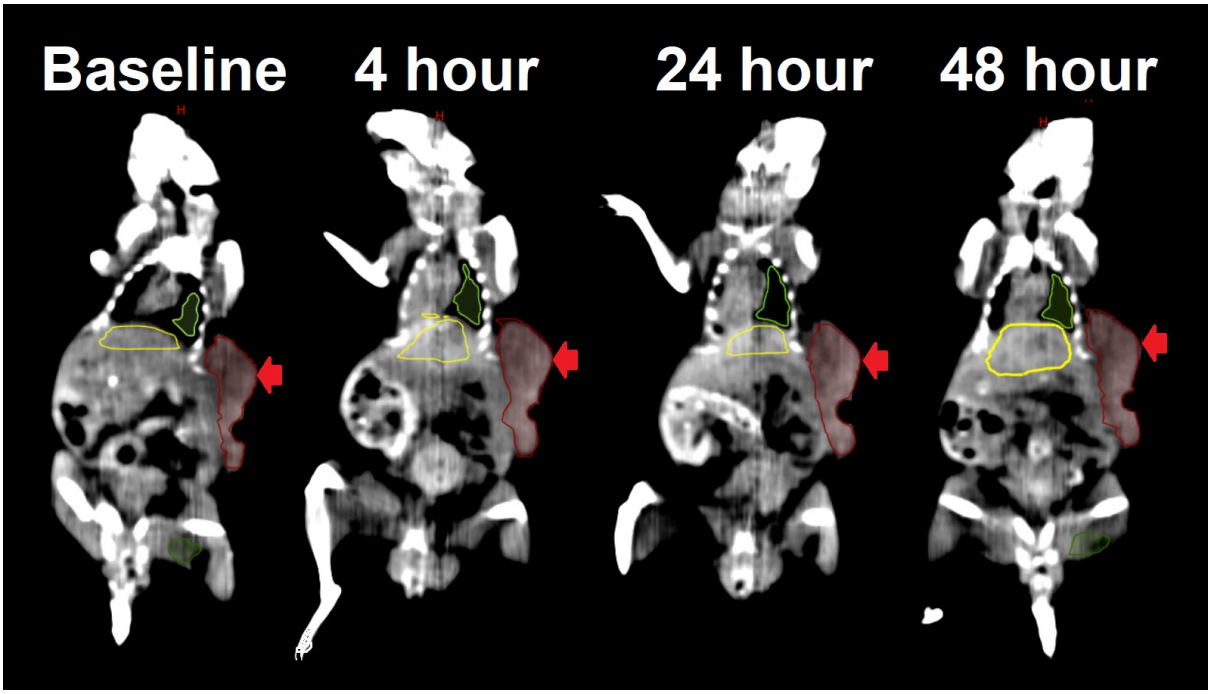

Figure 4.7: Coronal section of a mouse demonstrating CT contrast enhancement at serial scans post-injection with radioPDT NP with short hexagonal NSC structure. The Baseline image shows no enhancement in the liver (**yellow outline**) and tumor (**red outline**). At the 4-hour timepoint, marked increase in contrast is seen in the liver and tumor, particularly in the superior portion of the tumor compared to baseline (**red arrow**). At 24 hours, the liver appears homogenously enhanced, and more CT contrast is seen in the tumor again. By 48 hours, the superior portion of the tumor starts to lose contrast enhancement (**red arrow**).

4.4 Summary of Diagnostic Capability *in vivo*

This study demonstrates feasibility in using our novel therapeutic NP designed for radioPDT to be detected on diagnostic imaging, which allows it to act as a potential nanotheranostic in combination with IGRT. The benefits of nanotheranostics have been theorized and studied in the preclinical setting for more than a decade. Theranostic NPs allow monitoring of treatment efficacy, detection of potential off-target effects, and better standardization of treatments. Modern radiotherapy's high dependence on IGRT to provide diagnostic information and guide therapy is one of the most common examples of using diagnostic imaging to improve cancer treatment. The utility of our radioPDT NP in improving therapeutic effect has been demonstrated in Chapter 3. Its utility in combination with CT imaging as well to provide contrast enhancement, allowing detection of tumor and normal structures can add to its therapeutic potential.

The NP has demonstrated a high contrast efficiency, which can exceed standard clinically used contrast agents under ideal conditions. The diagnostic properties can be tuned using the nanocrystal lattice structure, in order to improve contrast efficiency. Imaging studies in a CAM model as well as in PC3 flank tumor-bearing mice model have demonstrated its ability to act as an *in vivo* CT contrast agent. With optimization of the NSC, the radioPDT NP was able to generate significant contrast enhancement in the tumor and normal structures. This can be used even as a surrogate marker of biodistribution and correlated with NP quantification by mass spectrometry. The tissue enhancement generated by the NP was sufficient to aid in defining target and organs-at-risk with a clinical radiation planning system.

The contrast enhancement capability of the radioPDT NP was ultimately significant but a small magnitude of increase in enhancement at the tumor. Other diagnostic agents have achieved better results in providing diagnostic quality information (394). However, the aim of our radioPDT NP is not to provide high quality diagnostic information, but to be detectable by onboard imagers in radiation machines. Improvements can be made with further refinements in NSC used, and possibly co-loading with high efficiency imaging contrast agents such as iohexol. The advantages of these types of modifications must be balanced with potential detrimental effects on the radioPDT NP's main goal of therapeutic effect.

Due to its contrast enhancement capabilities, the NP may be able to be detected by onboard CBCT imagers on modern LINACs. This can allow direct visualization of the NP distribution to correct for pharmacokinetic variances, which is an important issue in cancer therapeutics (395-398). The CT enhancement effect can also aid in identifying targets and organs-at-risk to match with the planned radiotherapy treatment for each fraction. It can also aid in adaptive planning and tumor-tracking algorithms by providing the contrast needed for machine-learning algorithms to precisely guide radiotherapy delivery (399-401). The use of nanotheranostics such as our radioPDT agent that can synergize with traditional radiotherapy with better tumor-targeting and tumor-treatment may lead to significant advances in this commonly used modality of cancer care.

CHAPTER – 5

DISCUSSION AND FUTURE DIRECTIONS

5.1 Summary of key findings

This thesis presents a novel biodegradable polymeric NP developed with the intent to address unmet needs within radiotherapy and cancer care today. The novel NP was developed by combining a $LaF_3:Ce^{3+}$ NSC possessing x-ray scintillating and attenuating properties with the most widely used clinical PS, PPIX, and encapsulating it into a biodegradable FDA-approved PEG-PLGA polymeric nanocarrier with a proven safety record in Phase II clinical trials (271, 402). The goal was to use radioPDT in a NP system that has an excellent safety profile and provided superior therapeutic efficacy than radiotherapy alone. This would produce a high TI treatment strategy and create a new paradigm within radiation oncology to treat cancers.

The unique method of NSC preparation using drop-wise synthesis in aqueous and anhydrous conditions have produced two variants of NSC with characteristics that are suitable for use in a theranostic setting. Co-encapsulating the NSC with PPIX into a PEG-PLGA nanosphere was accomplished with a modified nanoprecipitation technique. ***The synthesis procedure produces NP of favourable size and physical characteristics, high stability in physiologic environments, and negligible toxicity of the NP and its constituent parts in-vitro and in-vivo.*** The NP also exhibited no burst-release characteristics, high encapsulation efficiency, and allowed the radioPDT system to stay intact *in vivo* for up to 24 hours before releasing the encapsulants and breaking down.

The radioPDT NP also demonstrated superior therapeutic efficacy to radiation alone in-vitro and in-vivo. The NP construct was able to demonstrate FRET as a method of transferring energy from a radiation beam to a PS to activate PDT. This decouples the PDT process from the need for direct visible light, which is often difficult or impossible to

deliver to a deep-seated tumor. radioPDT's use of x-ray as the activating energy, combined with modern radiotherapy's ability to target cancer anywhere in the body, allows PDT to be effectively used to treat deep-seated tumors. ***The radioPDT NP showed the ability to generate singlet oxygen even in hypoxic conditions, which is often present in deep-seated tumors*** (403, 404). This manifested in the radioPDT NP's ability to generate significant cytotoxicity with PC3 human prostate cancer cells through multiple cytotoxic assays, including colorimetric viability, clonogenic, and live/dead flow cytometry assays in hypoxia levels as low as 1%. Although transient and chronic hypoxic states of 1% and lower can exist *in vivo*¸ many deep-seated tumors measured in patients are within the range of 0.5% to 10% (198, 404-407). ***The cytotoxic yield of radioPDT NP was found to be oxygen-limited in hypoxic conditions of 5% and lower. Even in hypoxia levels of 1%, however, significant therapeutic yield could still be maintained with enough radiation and NP dose.*** This suggests that radioPDT can act in oxygen-independent pathways as well, such as the Type II PDT reaction. The therapeutic yield was maintained with *in vivo* investigations of PC3 flank tumor-bearing NSG mice, where mice treated with a sub-curative radiation dose of 6 Gy in a single fraction were able to achieve durable long-term control, which rendered 50% of the mice with no identifiable cancerous lesions, and led to almost doubling mOS compared to radiotherapy alone.

The NSC's x-ray attenuation properties were also investigated for potential use in diagnostic imaging, in order to endow the radioPDT NP with theranostic capabilities. ***Depending on the crystal lattice structure, the $LaF_3:Ce^{3+}$ NSC was able to exhibit appreciable to excellent x-ray attenuation characteristics, which allowed it to generate significant enhancement under CT imaging.*** Its performance as an enhancing agent was

tested *in vivo* with a CAM tumor model and a PC3 tumor-bearing mouse model. With the short hexagonal crystal lattice structure, $LaF_3:Ce^{3+}$ NSC encapsulated into radioPDT NP was able to generate significant CT contrast of normal tissues and the tumor. The enhancement was also able to be used as a surrogate marker for NP biodistribution, which can allow personalized therapy via NP dose and scheduling adjustments to account for variances in pharmacokinetics. It can also aid in increasing the precision of radiotherapy by acting as a liquid fiducial marker for IGRT-targeting.

The report in this thesis of the development and validation of a novel radioPDT NP, as well as the number of significant findings in radioPDT's effectiveness in hypoxia and potential therapeutic benefit in a well designed system, may serve as the starting point for future preclinical and clinical studies to significantly advance the field of radiotherapy. By leveraging the benefits of PDT and radiotherapy together, while simultaneously addressing each modality's weaknesses, radioPDT may open up a new class of therapy within radiation oncology***. It differs from traditional radiosensitizers in that it does not augment the ionizing and genotoxic effects of radiotherapy, but instead adds the additional and potentially synergistic mechanism of PDT***. RadioPDT also adds a new mechanism of tumor selectivity beyond just the spatial and radiobiological selection of traditional radiotherapy, by also taking advantage of nanotheranostics to selectively deliver the NP to the target and reduce off-target effects. These findings significantly advance the field of radioPDT with a new standard of safety and efficacy set, as well as contributed a novel radioPDT NP that can potentially be taken forward into clinical trials to introduce this new therapeutic paradigm into cancer care.

5.2 Optimization of radioPDT Effect through Dose and Fractionation

This thesis reports encouraging results with the use of radioPDT in a single dose and fraction scheme for the administration of NP and radiotherapy. However, to be clinically applicable it would be first important to understand the impact of fractionated radiotherapy and NP administration. Radiotherapy is typically fractionated treatment with generally 2 Gy per fraction over multiple sessions. The main reason for this is to induce a biological advantage to healthy normal tissues over cancerous tissues, thereby limiting the damage done by radiotherapy to normal tissue in the pursuit of clearing cancerous tissue from the radiation field. This would be an important limitation to address with further research.

Hence, future studies in combining radioPDT into the radiotherapy treatment approach will need to investigate the optimal dosing scheme for the NP to maintain high tumoral levels of NP and low normal tissue levels during radiation sessions. The effect of low doses per fractionation, in the 2 Gy to 4 Gy range, also diminishes the activity of radioPDT, particularly in hypoxia. This loss of radioPDT effect can be mitigated, however, if treatment is to occur over multiple fractions. The early responding nature of PDT-treated tumors combined with the IGRT and adaptive planning to shrinking tumors may actually decrease the normal tissue impact while maintaining high therapeutic efficacy to the tumor. The oxygenation of the tumor is also expected to dynamically change in response to radioPDT, even over a timescale of 3 days. This is due to the induction of vascular infarction by the PDT effect and subsequent creation of a potentially hypoxic condition. The distribution of NP through the tumor can also be affected by the vascular collapse, which can further complicate the radioPDT effect in a fractionated scheme. These effects

need to be investigated with further preclinical studies to understand the tumor's response to fractionated radioPDT treatments.

Conversely, radioPDT may synergize well with modern hypofractionated radiotherapy techniques. The use of hypofractionated and ultra-hypofractionated regimens in the form of stereotactic radiotherapy are on the rise and are bringing some of the most important new advances to the field of radiotherapy (408-411). With the advent of SBRT and SRS, radiotherapy's role and impact on traditionally radioresistant and minimal burden metastatic disease are being dramatically revised (412-418). The success in using high dose per fraction radiotherapy has necessitated new fundamental research into radiobiology that can more accurately model the effects of stereotactic radiation, since the linear quadratic model has proven inadequate at such high doses (244, 419-421). Investigations presented in **Chapter 3** show that as radiation dose per fraction transitions between 6 to 8 Gy, which is generally considered the boundary between ultra-hypofractionation and non-traditional radiobiological effects, the additive effect of radioPDT tends to be unproportionally augmented, even in hypoxic conditions. There exists a possibility that large dose per fractions, such as what is increasingly being used in modern radiotherapy, may be advantageous for radioPDT. Further investigations alongside hypofractionated radiotherapy may open new directions of optimizing therapeutic effect.

5.3 The effect of the Immune System on radioPDT

PDT's induction of ICD through mechanisms reviewed in **Chapter 1** are one of the three main mechanisms through which it induces and maintains durable oncologic control. Although the individual effects of radiotherapy and PDT individually on the immune

system is understood, their effect in combination has not been explored. Some of the immune-priming mechanism is shared with radiotherapy and PDT, but key differences do exist.

Radiotherapy and PDT both have the potential of generating abscopal effects in isolation via systemic spread of T cells and B cells sensitized to tumor neoantigens. Both rely on DAMP-mediated APC activity leading to recruitment and activation of effector T cells ($T_{eff,}$) and both cause chemokine and chemotaxic release to promote T cell infiltration and inflammation (63, 89, 104). One of the key differences with PDT is it has a much larger component of innate immune response causing high degree of tumor inflammation, which tips the balance of immune-priming and immune-dampening more towards the former. ROS damage to tumor cells favours necrosis and a high load of DAMPs from the cytosol being directly spilled into the environment. This induces strong cytokine/chemokine activation for the innate immune response and produces many neoantigens for the adaptive immune response. Radiotherapy's cytotoxicity is primarily genotoxic damage and cell death from this, along with DAMP presentation and cGAS-STING activation, does not produce as profound an innate immune response and inflammation (90, 422). This is evident in inflammation/necrosis seen in clinical PDT versus radiotherapy (105). Hence, the immune response to radioPDT may take advantage of PDT's strong immune-activating abilities, and both radiotherapy and PDT effects may also synergistically promote ICD through their shared immune system effects. This may hold the answer for a multimodal therapy that can reliably prime a strong immune response in combination with immunotherapy agents, without significantly raising toxicity.

In the *in vivo* studies presented in **Chapter 3** of this thesis, radioPDT treated mice appeared to have very good local control even in immune-deficient mice. Fifty percent of the mice did progress with disease, but these progressions were mainly at the site of metastatic disease rather than local disease. The effects of the immune system were intentionally omitted in this thesis in order to understand the radioPDT NP's performance and the effect of hypoxia with minimal confounders, but the importance of the immune response in radiation and PDT does mean this is an important limitation of our current findings. ***Therefore, the next evolution of in-vivo studies into radioPDT should involve immune-competent tumor models for the investigation of the immune system's contribution to the radioPDT effect.*** Radiotherapy's use in converting tumors unresponsive to conventional immunotherapy into responsive tumors have thus far met with mixed response (423-425). Thus, radioPDT's use in augmenting the effectiveness of immunotherapy may be an important direction of investigation to explore.

5.4 Next Generation radioPDT Agents

Another potential evolution for radioPDT is the incorporation of newer scintillator and PS technology, as well as more advanced nanocarrier systems. Several advances in PS generations have led to newer contrast agents with higher quantum yields than PPIX (426). Agents such as hypocrellins and pthalocyanine-based PS have significantly improved cytotoxic effects through more efficient PDT processes (427). A key factor appears to be the optimization of the triplet-state PS system and enhancing its transfer of energy to molecular oxygen in the Type II reaction. Newer generation PS are also influenced to a

lesser extent by hypoxic condition than porphyrin derivatives, which can help improve radioPDT's efficacy in hypoxic conditions.

Several new scintillators may also augment the FRET efficiency in a radioPDT system. Advances in NSC are mainly driven by the X-ray detector industry where high efficiency scintillators are important in developing more sensitive radiation detectors (428). Perskovite-based NSC technology, which share similarities with high efficiency solar cells, can generate up to 21,000 photons/MeV, or nearly 100 times more luminescence for the same X-ray energy input as $LaF_3:Ce^{3+}$. Many of these newer NSC and PS agents do have issues of toxicity that need to be considered, since they often consist of toxic heavy metal or organic components. Further development in this area though may yield newer agents with similar safety to $LaF_3:Ce^{3+}$ and PPIX but with greater efficacy. ***Another evolution would be agents that are able to combine the NSC and PS function into one and directly transfer X-ray energy into producing singlet oxygen, which reduces FRET inefficiencies and increases singlet oxygen yield for a given amount of radiation energy absorbed*** (429, 430). For example, quantum dot (QD) conjugated porphyrin structures can exhibit a FRET efficiency nearing 100% for radioPDT (431). Challenges with biocompatibility, pharmacokinetics, clearance, and toxicity in using these agents *in vivo* will be one of the major challenges to overcome to reduce these novel radioPDT agents into a clinically applicable system.

Alternatively, more traditional PS systems could be modified for higher effect by targeting more critical structures of the cell, such as the nucleus, where much lower singlet oxygen yield is needed to cause cell death (432). With the lower levels of incident light energy needed to inflict cell death, these PS may even be able to take advantage of

the Chervenkov light from high energy radiation beams as the activating source for PDT effect (432, 433). This is a fairly new approach to radioPDT, however, and more research needs to be done on its feasibility and ultimate efficacy.

The other area of development is in the nanocarrier that can be used to target the cancerous tissue. The current strategy employed by our radioPDT NP is a passive targeting system using the EPR effect. For NP in the size range of 100 nm, EPR effect alone appears to be just as effective as active targeting with aptamers designed to recognize cancer-specific markers (434). A move to smaller NP size may increase its ability to perfuse into cancerous tissue and more thoroughly treat areas of disease but would also increase its extravasation into normal tissue and cause off-target effects. A smaller NP with active targeting via aptamers may help mitigate this. Additionally, a NP designed for radioPDT actually requires different characteristics than traditional nanomedicines, which typically aim to deliver chemotherapeutics in a controlled and sustained release preferentially at the site of tumor. For radioPDT, release of the NSC and PS would be disadvantageous as it would increase the distance between these two agents and decrease the ability to transfer energy via FRET due to luminescence intensity decreasing by the inverse-square of distance. Thus, further development of nanocarrier systems will have to be specifically tailored towards radioPDT agents in order to optimize past our polymeric design.

5.5 RadioPDT in Clinical Translation

Once fully optimized, the next major challenge for radioPDT is successful translation into clinical practice. Cancer drugs have notoriously been difficult to successfully translate to standard of care therapies, with about 95% of drugs failing to pass all stages of clinical

trials (435). In particular, one of the challenges with a radioPDT agent is this is a relatively new class of radiotherapy-drug combination, with about 10 years of develop since the first publication. The mechanism and best approach for preclinical and clinical application is still being discovered, with some debate that exists in the field. Feasibility of radioPDT process in terms of X-ray energy absorption at clinically used X-ray energy levels (typically MV range radiation energy), fluorescence efficiency of the NSC and FRET efficiency are all highly debated (436). Before clinical translation can be attempted, further preclinical studies will need to be done to further understand its mechanism of therapeutic effect and limitations in terms of minimum drug needed for radioPDT effect and minimum X-ray absorption required for activation.

Beyond challenges in preclinical development, an equally important factor is identifying the correct area of cancer care to integrate a radioPDT therapeutic strategy. Once the TI of the radioPDT system is optimized, its best chance of clinical translation will come from addressing an unmet need within radiotherapy. This will likely be one of two scenarios: a cancer type that is difficult to treat successfully with radiotherapy, such as primary radiotherapy for locally advanced lung cancer, or a cancer type that is difficult to treat successfully without undue toxicity, such as prostate cancer. Other situations where radioPDT can be quite beneficial is in recurrent radioresistant cancers, where reirradiation at full dose risks morbid normal tissue toxicity with a lower likely hood of achieving tumor control.

Another area of radiotherapy use that can greatly benefit from PDT is in emergency radiotherapy treatments of spinal cord compressions. Up to 5% of cancer patients experience a spinal cord compression, where a tumor invades in the spinal canal and

compresses the spinal cord, cuts off blood supply and causes ischemia and neuronal death within the cord (437-439). This results in a transverse myelitis at the level of cord compression and loss of sensory/motor function and bowel/bladder function, which can be quite debilitating and predicts for early mortality (439). Surgical decompressions are often not feasible due to the morbidity of surgery and patient comorbidities, which leaves steroids and emergency radiotherapy to shrink the tumor as rapidly as possible to take the pressure off the spinal cord, and hopefully reverse the symptoms. It can take many weeks for radiotherapy to have its peak decompressive effects on the compressing tumor, and has an overall return-of-function rate of 30-60% (440). Furthermore, about 40% of patients recur with a cord compression within a previously treated radiation field, which makes it difficult to deliver more radiation dose to this site without morbid normal tissue toxicity (440). As demonstrated in **Chapter 3**, radioPDT can have a faster time to tumor cytotoxicity and response by decrease in size than radiation alone. Perhaps in the scenario of a cord compression, using radioPDT could lead to faster decompression of the spinal cord and potentially higher success rates, while also using a lower dose of radiotherapy for the same therapeutic effect and thus allowing retreatments with less concern about normal tissue toxicity.

The theranostic capability within the radioPDT NP discussed in this thesis also contributes towards better integration into a clinical treatment context. Modern radiotherapy is heavily dependent on IGRT, which provides a convenient way of imaging the NP prior to treatment with radiotherapy. This potentially allows for the monitoring of the NP delivery and accumulation in the target, which can help standardize the NP dose and therapeutic effect between each fraction of radiotherapy. It can also allow for a more standardized therapeutic

delivery from one patient to another, which eliminates issues of differences in pharmacokinetics and tumor uptake characteristics. Furthermore, if the amount of NP could be quantified for each treatment using onboard imaging during IGRT, then the therapeutic yield from radioPDT can be calculated if the scintillation and FRET efficiency is known.

The design, characterization and therapeutic and diagnostic studies presented in this thesis were done in a manner that focuses on addressing some of the challenges in clinical translation. This has led to the development of a novel radioPDT NP that is capable of addressing the major questions of biocompatibility, *in vivo* distribution and tumor-targeting, diagnostic capability, and therapeutic potential in various radiation doses and in hypoxic conditions. By leveraging clinical experience and knowledge in radiotherapy, a forward planned approach can be adopted to further preclinical studies in radioPDT and may help pre-empt crucial issues that need to be answered for successful clinical translation in the future.

REFERENCES

1. Statistics CC. Canadian Cancer Society. 2016.

2. Arruebo M, Vilaboa N, Sáez-Gutierrez B, Lambea J, Tres A, Valladares M, et al. Assessment of the Evolution of Cancer Treatment Therapies. Cancers. 2011;3(3):3279-330.

3. Gianfaldoni S, Gianfaldoni R, Wollina U, Lotti J, Tchernev G, Lotti T. An Overview on Radiotherapy: From Its History to Its Current Applications in Dermatology. Open Access Macedonian Journal of Medical Science. 2017;5(4):521-5.

4. Lawrence EO, Livingston MS. The Production of High Speed Light Ions Without the Use of High Voltages. Physical Review. 1932;40(1):19-35.

5. Coutard H. PRINCIPLES OF X RAY THERAPY OF MALIGNANT DISEASES. The Lancet. 1934;224(5784):1-8.

6. International Atomic Energy Agency V. Radiation oncology physics: A handbook for teachers and students. International Atomic Energy Agency (IAEA): IAEA; 2005.

7. Pawlik TM, Keyomarsi K. Role of cell cycle in mediating sensitivity to radiotherapy. International journal of radiation oncology, biology, physics. 2004;59(4):928-42.

8. Lomax ME, Folkes LK, O'Neill P. Biological Consequences of Radiation-induced DNA Damage: Relevance to Radiotherapy. Clinical Oncology. 2013;25(10):578-85.

9. Beitler JJ, Zhang Q, Fu KK, Trotti A, Spencer SA, Jones CU, et al. Final results of local-regional control and late toxicity of RTOG 9003: a randomized trial of altered fractionation radiation for locally advanced head and neck cancer. International Journal of Radiation Oncology • Biology • Physics. 2014;89(1):13-20.

10. Choppin GR, Liljenzin J-O, Rydberg JAN. CHAPTER 6 - Absorption of Nuclear Radiation. In: Choppin GR, Liljenzin J-O, Rydberg JAN, editors. Radiochemistry and Nuclear Chemistry (Third Edition). Woburn: Butterworth-Heinemann; 2002. p. 123-65.

11. Hall EJ, Cox JD. Chapter 1 - Physical and Biologic Basis of Radiation Therapy. In: Cox JD, Ang KK, editors. Radiation Oncology (Ninth Edition). Philadelphia: Content Repository Only!; 2010. p. 3-49.

12. Public Health Agency of C, Statistics C, Canadian Cancer S, provincial/territorial cancer r. Release notice - Canadian Cancer Statistics 2019. Health Promotion and Chronic Disease Prevention in Canada. 2019;39(8-9):255-.

13. Garibaldi C, Jereczek-Fossa BA, Marvaso G, Dicuonzo S, Rojas DP, Cattani F, et al. Recent Advances in Radiation Oncology. 2017;11:785-.

14. Bulski W, Rostkowska J, Gwiazdowska B. History of dosimetry comparisons and audits for radiotherapy centres in Poland in 1936-2009. International Atomic Energy Agency (IAEA): 2010 1011-2669 Contract No.: INIS-XA--11I0984.

15. Jennings W. Evolution over the past century of quantities and units in radiation dosimetry. Journal of Radiological Protection. 2007;27(1):5-16.

16. Paliwal B, Tewatia D. Advances in radiation therapy dosimetry. Journal of Medical Physics. 2009;34(3):108-16.

17. van der Veen J, Nuyts S. Can Intensity-Modulated-Radiotherapy Reduce Toxicity in Head and Neck Squamous Cell Carcinoma? Cancers. 2017;9(10):135.

18. Jin L, Wang R, Jiang S, Yue J, Liu T, Dou X, et al. Dosimetric and clinical toxicity comparison of critical organ preservation with three-dimensional conformal radiotherapy, intensity-modulated radiotherapy, and RapidArc for the treatment of locally advanced cancer of the pancreatic head. Current Oncology. 2015;23(1):8.

19. Palacios-Eito A, García-Cabezas S. Oligometastatic disease, the curative challenge in radiation oncology. World Journal of Clinical Oncology. 2015;6(4):30-4.

20. Pitroda SP, Khodarev NN, Huang L, Uppal A, Wightman SC, Ganai S, et al. Integrated molecular subtyping defines a curable oligometastatic state in colorectal liver metastasis. Nature Communications. 2018;9(1):1793.

21. Palma DA, Salama JK, Lo SS, Senan S, Treasure T, Govindan R, et al. The oligometastatic state - separating truth from wishful thinking. Nature Reviews Clinical Oncology. 2014;11(9):549-57.

22. Boyle T, McPadden E. The contemporary use of radiation therapy in the management of lymphoma. Surgical Oncology Clinics of North America. 2000;9(3):621-37, xi.

23. Jairam V, Roberts KB, Yu JB. Historical trends in the use of radiation therapy for pediatric cancers: 1973-2008. International Journal of Radiation Oncology • Biology • Physics. 2013;85(3):e151-e5.

24. Ohri N, Dicker AP, Showalter TN. Late toxicity rates following definitive radiotherapy for prostate cancer. Canadian Journal of Urology. 2012;19(4):6373-80.

25. Mori Y, Kaneda N, Hagiwara M, Ishiguchi T. Dosimetric Study of Automatic Brain Metastases Planning in Comparison with Conventional Multi-Isocenter Dynamic Conformal Arc Therapy and Gamma Knife Radiosurgery for Multiple Brain Metastases. Cureus. 2016;8(11):e882-e.

26. Navarria P, Clerici E, Carta G, Attuati L, Picozzi P, Franzese C, et al. Randomized Phase III Trial Comparing Gamma Knife and Linac Based (EDGE) Approaches for Brain Metastases Radiosurgery: Results from the Gadget Trial. International Journal of Radiation Oncology • Biology • Physics. 2018;102(3):S143-S4.

27. Fowler JF, Adams GE, Denekamp J. Radiosensitizers of hypoxic cells in solid tumors. Cancer Treatment Reviews. 1976;3(4):227-56.

28. Wang H, Mu X, He H, Zhang X-D. Cancer Radiosensitizers. Trends in Pharmacological Sciences. 2018;39(1):24-48.

29. Seiwert TY, Salama JK, Vokes EE. The concurrent chemoradiation paradigm—general principles. Nature Clinical Practice Oncology. 2007;4(2):86-100.

30. Verma V, Simone CB, 2nd, Werner-Wasik M. Acute and Late Toxicities of Concurrent Chemoradiotherapy for Locally-Advanced Non-Small Cell Lung Cancer. Cancers. 2017;9(9):120.

31. Morris ZM, P.; Kruser T.J. Combined Chemoradiation Therapy in the Treatment of Squamous Cell Carcinoma of the Head and Neck—An Evolving Paradigm Oncology & Hematology Review. 2013;9(2):115-21.

32. Warenius HM, White R, Peacock JH, Hanson J, Britten RA, Murray D. The Influence of Hypoxia on the Relative Sensitivity of Human Tumor Cells to 62.5 MeV (p→Be) Fast Neutrons and 4 MeV Photons. Radiation Research. 2000;154(1):54-63.

33. Murray D, Mirzayans R, Scott A, Allalunis-Turner M. Influence of Oxygen on the Radiosensitivity of Human Glioma Cell Lines. American Journal of Clinical Oncology. 2003;26:e169-77.

34. Koh W-J, Rasey JS, Evans ML, Grierson JR, Lewellen TK, Graham MM, et al. Imaging of hypoxia in human tumors with [F-18]fluoromisonidazole. International Journal of Radiation Oncology • Biology • Physics. 1992;22(1):199-212.

35. Rockwell S, Dobrucki IT, Kim EY, Marrison ST, Vu VT. Hypoxia and radiation therapy: past history, ongoing research, and future promise. Current Molecular Medicine. 2009;9(4):442-58.

36. Hong B-J, Kim J, Jeong H, Bok S, Kim Y-E, Ahn GO. Tumor hypoxia and reoxygenation: the yin and yang for radiotherapy. Radiation Oncology Journal. 2016;34(4):239-49.

37. Yoshimura M, Itasaka S, Harada H, Hiraoka M. Microenvironment and radiation therapy. BioMed Research International. 2013;2013:685308.

38. Harada H. How can we overcome tumor hypoxia in radiation therapy? Journal of Radiation Research. 2011;52(5):545-56.

39. Shin KH, Diaz-Gonzalez JA, Russell J, Chen Q, Burgman P, Li XF, et al. Detecting changes in tumor hypoxia with carbonic anhydrase IX and pimonidazole. Cancer Biology & Therapy. 2007;6(1):70-5.

40. Urtasun RC, Parliament MB, McEwan AJ, Mercer JR, Mannan RH, Wiebe LI, et al. Measurement of hypoxia in human tumours by non-invasive spect imaging of iodoazomycin arabinoside. The British Journal of Cancer Supplement. 1996;27:S209-12.

41. Moore RB, Chapman JD, Mercer JR, Mannan RH, Wiebe LI, McEwan AJ, et al. Measurement of PDT-induced hypoxia in Dunning prostate tumors by iodine-123-iodoazomycin arabinoside. Journal of Nuclear Medicine. 1993;34(3):405-11.

42. Gérard M, Corroyer-Dulmont A, Lesueur P, Collet S, Chérel M, Bourgeois M, et al. Hypoxia Imaging and Adaptive Radiotherapy: A State-of-the-Art Approach in the Management of Glioma. Frontiers in Medicine. 2019;6(117).

43. Marcu L, Olver I. Tirapazamine: from bench to clinical trials. Current Clinical Pharmacology. 2006;1(1):71-9.

44. Hirsch BD, Walz NC, Meeker BE, Arnfield MR, Tulip J, McPhee MS, et al. Photodynamic Therapy-Induced Hypoxia in Rat Tumors and Normal Tissues. Photochemistry and Photobiology. 1987;46(5):847-52.

45. Baas P, Oppelaar H, Stavenuiter M, van Zandwijk N, Stewart FA. Interaction of the bioreductive drug SR 4233 and photodynamic therapy using photofrin in a mouse tumor model. International Journal of Radiation Oncology • Biology • Physics. 1993;27(3):665-70.

46. Rischin D, Peters LJ, O'Sullivan B, Giralt J, Fisher R, Yuen K, et al. Tirapazamine, cisplatin, and radiation versus cisplatin and radiation for advanced squamous cell carcinoma of the head and neck (TROG 02.02, HeadSTART): a phase III trial of the Trans-Tasman Radiation Oncology Group. Journal of Clinical Oncology. 2010;28(18):2989-95.

47. Overgaard J. Hypoxic radiosensitization: adored and ignored. Journal of Clinical Oncology. 2007;25(26):4066-74.

48. Overgaard J, Horsman MR. Modification of Hypoxia-Induced Radioresistance in Tumors by the Use of Oxygen and Sensitizers. Seminars in Radiation Oncology. 1996;6(1):10-21.

49. Baudino TA. Targeted Cancer Therapy: The Next Generation of Cancer Treatment. Current Drug Discovery Technologies. 2015;12(1):3-20.

50. Mallarkey G, Coombes RC. Targeted Therapies in Medical Oncology: Successes, Failures and Next Steps. Therapeutic Advances in Medical Oncology. 2013;5(1):5-16.

51. Maeda H, Khatami M. Analyses of Repeated Failures in Cancer Therapy for Solid Tumors: Poor Tumor-selective Drug Delivery, Low Therapeutic Efficacy and Unsustainable Costs. Journal of Translational Medicine. 2018;7(1):11-.

52. Sabnis AJ, Bivona TG. Principles of Resistance to Targeted Cancer Therapy: Lessons from Basic and Translational Cancer Biology. Trends in Molecular Medicine. 2019;25(3):185-97.

53. Wong CH, Siah KW, Lo AW. Estimation of Clinical Trial Success Rates and Related Parameters. Biostatistics. 2019;20(2):273-86.

54. Weichselbaum RR, Hellman S. Oligometastases Revisited. Nature reviews Clinical Oncology. 2011;8(6):378-82.

55. Onderdonk BE, Chmura SJ. The Yin and Yang of Cytoreductive SBRT in Oligometastases and Beyond. Fronties in Oncology. 2019;9:706-.

56. Abufaraj M, Dalbagni G, Daneshmand S, Horenblas S, Kamat AM, Kanzaki R, et al. The Role of Surgery in Metastatic Bladder Cancer: A Systematic Review. European Urology. 2018;73(4):543-57.

57. Cheung FP, Alam NZ, Wright GM. The Past, Present and Future of Pulmonary Metastasectomy: A Review Article. Annals of Thoracic and Cardiovascular Surgery. 2019;25(3):129-41.

58. Buscarini M, Josephson DY, Stein JP. Lymphadenectomy in bladder cancer: a review. Urologia Internationalis. 2007;79(3):191-9.

59. Zhou J, Shan G, Chen Y. The effect of lymphadenectomy on survival and recurrence in patients with ovarian cancer: a systematic review and meta-analysis. Japanese Journal of Clinical Oncology. 2016;46(8):718-26.

60. Palma DA, Olson R, Harrow S, Gaede S, Louie AV, Haasbeek C, et al. Stereotactic Ablative Radiotherapy versus Standard of Care Palliative Treatment in Patients with Oligometastatic Cancers (SABR-COMET): A Randomised, Phase 2, Open-Label Trial. The Lancet. 2019;393(10185):2051-8.

61. Iyengar P, Wardak Z, Gerber DE, Tumati V, Ahn C, Hughes RS, et al. Consolidative Radiotherapy for Limited Metastatic Non-Small-Cell Lung Cancer: A Phase 2 Randomized Clinical Trial. JAMA Oncology. 2018;4(1):e173501.

62. Gomez DR, Tang C, Zhang J, Blumenschein GR, Jr., Hernandez M, Lee JJ, et al. Local Consolidative Therapy Vs. Maintenance Therapy or Observation for Patients With

Oligometastatic Non-Small-Cell Lung Cancer: Long-Term Results of a Multi-Institutional, Phase II, Randomized Study. Journal of Clinical Oncology. 2019;37(18):1558-65.

63. Weichselbaum RR, Liang H, Deng L, Fu YX. Radiotherapy and Immunotherapy: A Beneficial Liaison? Nature reviews Clinical Oncology. 2017;14(6):365-79.

64. Demaria S, Coleman CN, Formenti SC. Radiotherapy: Changing the Game in Immunotherapy. Trends in Cancer. 2016;2(6):286-94.

65. Chang J, Rattner DW. History of Minimally Invasive Surgical Oncology. Surgical oncology clinics of North America. 2019;28(1):1-9.

66. Lee M-TG, Chiu C-C, Wang C-C, Chang C-N, Lee S-H, Lee M, et al. Trends and Outcomes of Surgical Treatment for Colorectal Cancer between 2004 and 2012- an Analysis using National Inpatient Database. Scientific Reports. 2017;7(1):2006.

67. Yu HY, Friedlander DF, Patel S, Hu JC. The current status of robotic oncologic surgery. CA: A Cancer Journal for Clinicians. 2013;63(1):45-56.

68. Seigne JD, Cass I, Wong SL. Requiem for Robotic Cancer Surgery? Not So Fast. Annals of Surgical Oncology. 2019;26(11):3425-7.

69. Chang JY, Senan S, Paul MA, Mehran RJ, Louie AV, Balter P, et al. Stereotactic Ablative Radiotherapy versus Lobectomy for Operable Stage I Non-Small-Cell Lung Cancer: A Pooled Analysis of Two Randomised Trials. Lancet Oncology. 2015;16(6):630-7.

70. Bourhis J, Montay-Gruel P, Gonçalves Jorge P, Bailat C, Petit B, Ollivier J, et al. Clinical Translation of FLASH Tadiotherapy: Why and How? Radiotherapy and Oncology. 2019;139:11-7.

71. Nishikawa H, Osaki Y. Comparison of High-Intensity Focused Ultrasound Therapy and Radiofrequency Ablation for Recurrent Hepatocellular Carcinoma. Hepatobiliary Surgery and Nutrition. 2013;2(3):168-70.

72. Goode JA, Matson MB. Embolisation of Cancer: What is the Evidence? Cancer Imaging. 2004;4(2):133-41.

73. Glazer ES, Curley SA. The Ongoing History of Thermal Therapy for Cancer. Surgical oncology clinics of North America. 2011;20(2):229-vii.

74. van Straten D, Mashayekhi V, de Bruijn HS, Oliveira S, Robinson DJ. Oncologic Photodynamic Therapy: Basic Principles, Current Clinical Status and Future Directions. Cancers. 2017;9(2).

75. Dolmans DEJGJ, Fukumura D, Jain RK. Photodynamic Therapy for Cancer. Nature Review Cancer. 2003;3(5):380-7.

76. Huang Z. A review of progress in clinical photodynamic therapy. Technology in Cancer Research & Treatment. 2005;4(3):283-93.

77. Hatogai K, Yano T, Kojima T, Onozawa M, Daiko H, Nomura S, et al. Salvage Photodynamic Therapy for Local Failure after Chemoradiotherapy for Esophageal Squamous Cell Carcinoma. Gastrointestinal Endoscopy. 2016;83(6):1130-9.e3.

78. Siegel RL, Miller KD. Cancer Statistics, 2019. 2019;69(1):7-34.

79. Debele TA, Peng S, Tsai HC. Drug Carrier for Photodynamic Cancer Therapy. International Journal of Molecular Sciences. 2015;16(9):22094-136.

80. Castano AP, Demidova TN, Hamblin MR. Mechanisms in Photodynamic Therapy: Part One-photosensitizers, Photochemistry and Cellular Localization. Photodiagnosis and Photodynamic Therapy. 2004;1(4):279-93.

81. Besur S, Hou W, Schmeltzer P, Bonkovsky HL. Clinically important features of porphyrin and heme metabolism and the porphyrias. Metabolites. 2014;4(4):977-1006.

82. Brancaleon L, Moseley H. Laser and Non-laser Light sources for Photodynamic Therapy. Lasers in Medical Science. 2002;17(3):173-86.

83. Bolze F, Jenni S, Sour A, Heitz V. Molecular Photosensitisers for Two-photon Photodynamic Therapy. Chemical Communications. 2017;53(96):12857-77.

84. Wan G-Y, Liu Y, Chen B-W, Liu Y-Y, Wang Y-S, Zhang N. Recent Advances of Sonodynamic Therapy in Cancer Treatment. Cancer Biology & Medicine. 2016;13(3):325-38.

85. Kennedy JC, Pottier RH, Pross DC. Photodynamic therapy with endogenous protoporphyrin IX: basic principles and present clinical experience. Journal of Photochemistry and Photobiology B. 1990;6(1-2):143-8.

86. Castano AP, Demidova TN, Hamblin MR. Mechanisms in Photodynamic Therapy: Part Two-cellular Signaling, Cell Metabolism and Modes of Cell Death. Photodiagnosis and Photodynamic Therapy. 2005;2(1):1-23.

87. Castano AP, Demidova TN, Hamblin MR. Mechanisms in Photodynamic Therapy: Part Three-Photosensitizer Pharmacokinetics, Biodistribution, Tumor Localization and Modes of Tumor Destruction. Photodiagnosis and Photodynamic Therapy. 2005;2(2):91-106.

88. Korbelik M, Krosl G, Krosl J, Dougherty GJ. The Role of Host Lymphoid Populations in the Response of Mouse EMT6 Tumor to Photodynamic Therapy. Cancer research. 1996;56(24):5647-52.

89. Panzarini E, Inguscio V, Dini L. Immunogenic Cell Death: Can it be Exploited in PhotoDynamic Therapy for Cancer? BioMed Research International. 2013;2013:482160.

90. Chen K, Liu J, Cao X. cGAS-STING Pathway in Senescence-Related Inflammation. National Scientific Review. 2017:nwx146-nwx.

91. Retif P, Pinel S, Toussaint M, Frochot C, Chouikrat R, Bastogne T, et al. Nanoparticles for Radiation Therapy Enhancement: the Key Parameters. Theranostics. 2015;5(9):1030-44.

92. Takahashi J, Misawa M. Analysis of Potential Radiosensitizing Materials for X-Ray-Induced Photodynamic Therapy. Journal of Nanobiotechnology. 2007;3(2):116-26.

93. Zou X, Yao M, Ma L, Hossu M, Han X, Juzenas P, et al. X-Ray-Induced Nanoparticle-Based Photodynamic Therapy of Cancer. Nanomedicine. 2014;9(15):2339-51.

94. Chen W, Zhang J. Using Nanoparticles to Enable Simultaneous Radiation and Photodynamic Therapies for Cancer Treatment. Journal of Nanoscience and Nanotechnology. 2006;6(4):1159-66.

95. Liu Y, Chen W, Wang S, Joly AG. Investigation of Water-Soluble X-ray Luminescence Nanoparticles for Photodynamic Activation. Applied Physics Letters. 2008;92(4):043901.

96. Maleki Vareki S. High and low mutational burden tumors versus immunologically hot and cold tumors and response to immune checkpoint inhibitors. Journal for ImmunoTherapy of Cancer. 2018;6(1):157.

97. Sevenich L. Turning "Cold" Into "Hot" Tumors-Opportunities and Challenges for Radio-Immunotherapy Against Primary and Metastatic Brain Cancers. Frontiers in Oncology. 2019;9:163-.

98. Gollnick SO, Brackett CM. Enhancement of anti-tumor immunity by photodynamic therapy. Immunologic Research. 2010;46(1-3):216-26.

99. Rodríguez ME, Cogno IS, Milla Sanabria LS, Morán YS, Rivarola VA. Heat shock proteins in the context of photodynamic therapy: autophagy, apoptosis and immunogenic cell death. Photochemical & Photobiological Sciences. 2016;15(9):1090-102.

100. Vanpouille-Box C, Alard A, Aryankalayil MJ, Sarfraz Y, Diamond JM, Schneider RJ, et al. DNA Exonuclease Trex1 Regulates Radiotherapy-Induced Tumour Immunogenicity. Nature Communications. 2017;8:15618-.

101. Kwon ED, Drake CG, Scher HI, Fizazi K, Bossi A, van den Eertwegh AJ, et al. Ipilimumab versus Placebo after Radiotherapy in Patients with Metastatic Castration-Resistant Prostate Cancer that had Progressed after Docetaxel Chemotherapy (CA184-043): A Multicentre, Randomised, Double-Blind, Phase 3 Trial. The Lancet Oncology. 2014;15(7):700-12.

102. Kaur P, Asea A. Radiation-induced effects and the immune system in cancer. Frontiers in Oncology. 2012;2:191-.

103. Asna N, Livoff A, Batash R, Debbi R, Schaffer P, Rivkind T, et al. Radiation Therapy and Immunotherapy—A Potential Combination in Cancer Treatment. Current Oncology. 2018;25(5).

104. Thong PS, Ong KW, Goh NS, Kho KW, Manivasager V, Bhuvaneswari R, et al. Photodynamic-therapy-activated immune response against distant untreated tumours in recurrent angiosarcoma. Lancet Oncology. 2007;8(10):950-2.

105. Lee JE, Park HS, Jung SS, Kim SY, Kim JO. A Case of Small Cell Lung Cancer Treated with Chemoradiotherapy Followed by Photodynamic Therapy. Thorax. 2009;64(7):637.

106. Billena C, Khan AJ. A Current Review of Spatial Fractionation: Back to the Future? International Journal of Radiation Oncology • Biology • Physics. 2019;104(1):177-87.

107. Agostinis P, Berg K, Cengel KA, Foster TH, Girotti AW, Gollnick SO, et al. Photodynamic therapy of cancer: an update. CA: A Cancer Journal for Clinicians. 2011;61(4):250-81.

108. Dougherty TJ, Gomer CJ, Henderson BW, Jori G, Kessel D, Korbelik M, et al. Photodynamic therapy. Journal of the National Cancer Institute. 1998;90(12):889-905.

109. Santos Al, Almeida D, Terra L, Baptista M, Labriola L. Photodynamic Therapy in Cancer Treatment - An Update Review. Journal of Cancer Metastasis and Treatment. 2019;2019(5):25.

110. Moore RB, Xiao Z, Owen RJ, Ashforth R, Dickey D, Helps C, et al. Photodynamic therapy of the canine prostate: intra-arterial drug delivery. CardioVascular and Interventional Radiology. 2008;31(1):164-76.

111. Huang YY, Sharma SK, Dai T, Chung H, Yaroslavsky A, Garcia-Diaz M, et al. Can Nanotechnology Potentiate Photodynamic Therapy? Nanotechnology Reviews. 2012;1(2):111-46.

112. Shafirstein G, Bellnier D, Oakley E, Hamilton S, Potasek M, Beeson K, et al. Interstitial Photodynamic Therapy-A Focused Review. Cancers. 2017;9(2):12.

113. Morton CA, Braathen LR. Daylight Photodynamic Therapy for Actinic Keratoses. American Journal of Clinical Dermatology. 2018;19(5):647-56.

114. Lui H, Hobbs L, Tope WD, Lee PK, Elmets C, Provost N, et al. Photodynamic Therapy of Multiple Nonmelanoma Skin Cancers With Verteporfinand Red Light–Emitting Diodes: Two-Year Results Evaluating Tumor Response and Cosmetic Outcomes. Archives of Dermatology. 2004;140(1):26-32.

115. Yano T, Muto M, Yoshimura K, Niimi M, Ezoe Y, Yoda Y, et al. Phase I Study of Photodynamic Therapy Using Talaporfin Sodium and Diode Laser for Local Failure after Chemoradiotherapy for Esophageal Cancer. Radiation Oncology. 2012;7:113.

116. Yano T, Muto M, Minashi K, Iwasaki J, Kojima T, Fuse N, et al. Photodynamic therapy as salvage treatment for local failure after chemoradiotherapy in patients with esophageal squamous cell carcinoma: A phase II study. International Journal of Cancer. 2012;131(5):1228-34.

117. Vander Poorten V, Meulemans J, Nuyts S, Clement P, Hermans R, Hauben E, et al. Postoperative Photodynamic Therapy As a New Adjuvant Treatment After Robot-Assisted Salvage Surgery of Recurrent Squamous Cell Carcinoma of the Base of Tongue. World Journal of Surgical Oncology. 2015;13:214.

118. de Visscher SA, Melchers LJ, Dijkstra PU, Karakullukcu B, Tan IB, Hopper C, et al. mTHPC-Mediated Photodynamic Therapy of Early Stage Oral Squamous Cell Carcinoma: A Comparison to Surgical Treatment. Annals of Surgical Oncology. 2013;20(9):3076-82.

119. Usuda J, Ichinose S, Ishizumi T, Hayashi H, Ohtani K, Maehara S, et al. Outcome of Photodynamic Therapy using NPe6 for Bronchogenic Carcinomas in Central Airways >1.0 cm in Diameter. Clinical Cancer Research. 2010;16(7):2198-204.

120. Kahaleh M, Mishra R, Shami VM, Northup PG, Berg CL, Bashlor P, et al. Unresectable Cholangiocarcinoma: Comparison of Survival in Biliary Stenting Alone versus Stenting with Photodynamic Therapy. Clinical Gastroenterology and Hepatology. 2008;6(3):290-7.

121. Network NCC. Basal Cell Skin Cancer (Version 1.2020) [December 21, 2019]. Available from: https://www.nccn.org/professionals/physician_gls/pdf/nmsc.pdf.

122. Network NCC. Squamous Cell Skin Cancer (Version 1.2020) [December 21, 2019]. Available from: https://www.nccn.org/professionals/physician_gls/pdf/squamous.pdf.

123. Network NCC. Malignant Pleural Mesothelioma (Version 1.2020) [December 21, 2019]. Available from: https://www.nccn.org/professionals/physician_gls/pdf/mpm.pdf.

124. Friedman M, Mikityansky I, Kam A, Libutti SK, Walther MM, Neeman Z, et al. Radiofrequency Ablation of Cancer. Journal of Vascular and Interventional Radiology: JVIR. 2004;27(5):427-34.

125. Basset-Seguin N, Ibbotson SH, Emtestam L, Tarstedt M, Morton C, Maroti M, et al. Topical Methyl Aminolaevulinate Photodynamic Therapy versus Cryotherapy for Superficial Basal Cell Carcinoma: a 5 Year Randomized Trial. European Journal of Dermatology : EJD. 2008;18(5):547-53.

126. Morton C, Horn M, Leman J, Tack B, Bedane C, Tjioe M, et al. Comparison of Topical Methyl Aminolevulinate Photodynamic Therapy with Cryotherapy or Fluorouracil for Treatment of Squamous Cell Carcinoma in situ: Results of a Multicenter Randomized Trial. Archives of Dermatology. 2006;142(6):729-35.

127. Burger M, Grossman HB, Droller M, Schmidbauer J, Hermann G, Dragoescu O, et al. Photodynamic Diagnosis of Non-muscle-invasive Bladder Cancer with Hexaminolevulinate Cystoscopy: A Meta-analysis of Detection and Recurrence Based on Raw Data. European Urology. 2013;64(5):846-54.

128. Simone CB, 2nd, Cengel KA. Photodynamic Therapy for Lung Cancer and Malignant Pleural Mesothelioma. Seminars in Oncology. 2014;41(6):820-30.

129. Du KL, Both S, Friedberg JS, Rengan R, Hahn SM, Cengel KA. Extrapleural Pneumonectomy, Photodynamic Therapy and Intensity Modulated Radiation Therapy for the Treatment of Malignant Pleural Mesothelioma. Cancer Biology & Therapy. 2010;10(5):425-9.

130. Stummer W, Pichlmeier U, Meinel T, Wiestler OD, Zanella F, Reulen HJ. Fluorescence-Guided Surgery with 5-Aminolevulinic Acid for Resection of Malignant Glioma: A Randomised Controlled Multicentre Phase III Trial. Lancet Oncology. 2006;7(5):392-401.

131. Friedberg JS, Mick R, Stevenson JP, Zhu T, Busch TM, Shin D, et al. Phase II Trial of Pleural Photodynamic Therapy and Surgery for Patients with Non-Small-Cell Lung Cancer with Pleural Spread. Journal of Clinical Oncology. 2004;22(11):2192-201.

132. Azzouzi AR, Vincendeau S, Barret E, Cicco A, Kleinclauss F, van der Poel HG, et al. Padeliporfin Vascular-targeted Photodynamic Therapy versus Active Surveillance

in Men with Low-risk Prostate Cancer (CLIN1001 PCM301): an Open-label, Phase 3, Randomised Controlled Trial. Lancet Oncology. 2017;18(2):181-91.

133. Daneshmand S, Bazargani ST, Bivalacqua TJ, Holzbeierlein JM, Willard B, Taylor JM, et al. Blue Light Cystoscopy for the Diagnosis of Bladder Cancer: Results from the US Prospective Multicenter Registry. Urologic Oncology. 2018;36(8):361.e1-.e6.

134. Dickey DJ, Moore RB, Rayner DC, Tulip J. Physics in Medicine and Biology. 2001;46(9):2359-70.

135. Dickey DJ, Partridge K, Moore RB, Tulip J. Light Dosimetry for Multiple Cylindrical Diffusing Sources for Use in Photodynamic Therapy. Physics in Medicine and Biology. 2004;49(14):3197-208.

136. Xiao Z, Halls S, Dickey D, Tulip J, Moore RB. Fractionated versus Standard Continuous Light Delivery in Interstitial Photodynamic Therapy of Dunning Prostate Carcinomas. Clinical Cancer Research. 2007;13(24):7496-505.

137. Busch TM, Hahn SM, Evans SM, Koch CJ. Depletion of Tumor Oxygenation during Photodynamic Therapy: Detection by the Hypoxia Marker EF3 [2-(2-Nitroimidazol-1[H]-yl)-N-(3,3,3-trifluoropropyl)acetamide]. Cancer Research. 2000;60(10):2636-42.

138. Tong X, Srivatsan A, Jacobson O, Wang Y, Wang Z, Yang X, et al. Monitoring Tumor Hypoxia Using 18F-FMISO PET and Pharmacokinetics Modeling after Photodynamic Therapy. Scientific Reports. 2016;6(1):31551.

139. James NS, Cheruku RR, Missert JR, Sunar U, Pandey RK. Measurement of Cyanine Dye Photobleaching in Photosensitizer Cyanine Dye Conjugates Could Help in Optimizing Light Dosimetry for Improved Photodynamic Therapy of Cancer. Molecules. 2018;23(8):1842.

140. Jacques S, Joseph R, Gofstein G. How photobleaching affects dosimetry and fluorescence monitoring of PDT in turbid media: SPIE; 1993.

141. Shafirstein G, Bellnier D, Oakley E, Hamilton S, Potasek M, Beeson K, et al. Interstitial Photodynamic Therapy-A Focused Review. Cancers. 2017;9(2).

142. Klotz L. Active surveillance for low-risk prostate cancer. Current Urology Reports. 2015;16(4):24.

143. Hayes JH, Ollendorf DA, Pearson SD, Barry MJ, Kantoff PW, Stewart ST, et al. Active Surveillance Compared With Initial Treatment for Men With Low-Risk Prostate Cancer: A Decision Analysis. JAMA. 2010;304(21):2373-80.

144. Moschini M, Carroll PR, Eggener SE, Epstein JI, Graefen M, Montironi R, et al. Low-risk Prostate Cancer: Identification, Management, and Outcomes. European Urology. 2017;72(2):238-49.

145. Hamdy FC, Donovan JL, Lane JA, Mason M, Metcalfe C, Holding P, et al. 10-Year Outcomes after Monitoring, Surgery, or Radiotherapy for Localized Prostate Cancer. The New England Journal of Medicine. 2016;375(15):1415-24.

146. Lou PJ, Jager HR, Jones L, Theodossy T, Bown SG, Hopper C. Interstitial Photodynamic Therapy as Salvage Treatment for Recurrent Head and Neck Cancer. British Journal of Cancer. 2004;91(3):441-6.

147. Huggett MT, Jermyn M, Gillams A, Illing R, Mosse S, Novelli M, et al. Phase I/II Study of Verteporfin Photodynamic Therapy in Locally Advanced Pancreatic Cancer. British Journal of Cancer. 2014;110(7):1698-704.

148. Fisher C, Ali Z, Detsky J, Sahgal A. Photodynamic Therapy for the Treatment of Vertebral Metastases: A Phase I Clinical Trial. Clinical Cancer Research. 2019;25(19):5766-76.

149. Wilson BC, Patterson MS. The physics, biophysics and technology of photodynamic therapy. Physics in Medicine and Biology. 2008;53(9):R61-R109.

150. Johansson A, Axelsson J, Andersson-Engels S, Swartling J. Realtime light dosimetry software tools for interstitial photodynamic therapy of the human prostate. Medical Physics. 2007;34(11):4309-21.

151. Wilson BC, Patterson MS. The physics, biophysics and technology of photodynamic therapy. Physics in Medicine and Biology. 2008;53(9):R61-109.

152. Blanco KC, Moriyama LT, Inada NM, Sálvio AG, Menezes PFC, Leite EJS, et al. Fluorescence guided PDT for optimization of the outcome of skin cancer treatment. Frontiers in Physics. 2015;3(30).

153. Azzouzi A-R, Lebdai S, Benzaghou F, Stief C. Vascular-targeted Photodynamic Therapy with TOOKAD® Soluble in Localized Prostate Cancer: Standardization of the Procedure. World Journal of Urology. 2015;33(7):937-44.

154. Yoon I, Li JZ, Shim YK. Advance in Photosensitizers and Light Delivery for Photodynamic Therapy. Clinical Endoscopy. 2013;46(1):7-23.

155. Fernandez JM, Bilgin MD, Grossweiner LI. Singlet oxygen generation by photodynamic agents. Journal of Photochemistry and Photobiology B. 1997;37(1):131-40.

156. Abrahamse H, Hamblin MR. New Photosensitizers for Photodynamic Therapy. Biochemical Journal. 2016;473(4):347-64.

157. Menter JM, Hollins TD, Sayre RM, Etemadi AA, Willis I, Hughes SN. Protection Against Photodynamic Therapy (PDT)-Induced Photosensitivity by Fabric Materials. Photodermatology, Photoimmunology & Photomedicine. 1998;14(5-6):154-9.

158. Dougherty TJ, Cooper MT, Mang TS. Cutaneous Phototoxic Occurrences in Patients Receiving Photofrin®. Laser Medicine & Surgery. 1990;10(5):485-8.

159. Steinbauer J, Schreml S, Karrer S, Ackermann G, Babilas P, Landthaler M, et al. Phototoxic reactions in healthy volunteers following photodynamic therapy with methylaminolevulinate cream or with cream containing 5-aminolevulinic acid: a phase II, randomized study. Photodermatology, Photoimmunology & Photomedicine. 2009;25(5):270-5.

160. Chen B, Pogue BW, Hoopes PJ, Hasan T. Vascular and Cellular Targeting for Photodynamic Therapy. Critical Reviews in Eukaryotic Gene Expression. 2006;16(4):279-305.

161. Master A, Livingston M, Sen Gupta A. Photodynamic nanomedicine in the treatment of solid tumors: perspectives and challenges. Journal of Controlled Release. 2013;168(1):88-102.

162. Li WT. Nanotechology-based strategies to enhance the efficacy of photodynamic therapy for cancers. Current Drug Metabolism. 2009;10(8):851-60.

163. Ash C, Dubec M, Donne K, Bashford T. Effect of Wavelength and Beam Width on Penetration in Light-tissue Interaction using Computational Methods. Lasers in Medical Science. 2017;32(8):1909-18.

164. Yuan Z, Yu S, Cao F, Mao Z, Gao C, Ling J. Near-infrared light triggered photothermal and photodynamic therapy with an oxygen-shuttle endoperoxide of anthracene against tumor hypoxia. Polymer Chemistry. 2018;9(16):2124-33.

165. Maruyama T, Akutsu Y, Suganami A, Tamura Y, Fujito H, Ouchi T, et al. Treatment of Near-Infrared Photodynamic Therapy Using a Liposomally Formulated Indocyanine Green Derivative for Squamous Cell Carcinoma. PLOS ONE. 2015;10(4):e0122849.

166. Kim HS, Lee DY. Near-Infrared-Responsive Cancer Photothermal and Photodynamic Therapy Using Gold Nanoparticles. Polymers. 2018;10(9):961.

167. Deng K, Li C, Huang S, Xing B, Jin D, Zeng Q, et al. Recent Progress in Near Infrared Light Triggered Photodynamic Therapy. Small. 2017;13(44):1702299.

168. Yang Z, Sun Z, Ren Y, Chen X, Zhang W, Zhu X, et al. Advances in nanomaterials for use in photothermal and photodynamic therapeutics (Review). Molecular Medicine Reports. 2019;20(1):5-15.

169. Cho S, Shin MH, Kim YK, Seo J-E, Lee YM, Park C-H, et al. Effects of Infrared Radiation and Heat on Human Skin Aging in vivo. Journal of Investigative Dermatology Symposium Proceedings. 2009;14(1):15-9.

170. Veeranarayanan S, Mohamed MS, Poulose AC, Rinya M, Sakamoto Y, Maekawa T, et al. Photodynamic Therapy at Ultra-Low NIR Laser Power and X-Ray Imaging Using Cu(3)BiS(3) Nanocrystals. Theranostics. 2018;8(19):5231-45.

171. Bhawalkar JD, Kumar ND, Zhao CF, Prasad PN. Two-photon photodynamic therapy. Journal of clinical laser medicine & surgery. 1997;15(5):201-4.

172. Qiu H, Tan M, Ohulchanskyy TY, Lovell JF, Chen G. Recent Progress in Upconversion Photodynamic Therapy. Nanomaterials. 2018;8(5):344.

173. Liu P, Yang W, Shi L, Zhang H, Xu Y, Wang P, et al. Concurrent photothermal therapy and photodynamic therapy for cutaneous squamous cell carcinoma by gold nanoclusters under a single NIR laser irradiation. Journal of Materials Chemistry B. 2019;7(44):6924-33.

174. Pinto A, Pocard M. Photodynamic therapy and photothermal therapy for the treatment of peritoneal metastasis: a systematic review. Pleura and Peritoneum, 2018.

175. Weber M. New Developments in Photodynamic and Sonodynamic Cancer Therapy. Journal of Global Oncology. 2018;4(Supplement 2):222s-s.

176. Pfeiffer D, Berger J, Gross A. Single Application of High-Intensity Focused Ultrasound as Primary Therapy of Localized Prostate Cancer: Treatment-Related Predictors of Biochemical Outcomes. Asian Journal of Urology. 2015;2(1):46-52.

177. Hahn SM, Fraker DL, Mick R, Metz J, Busch TM, Smith D, et al. A Phase II Trial of Intraperitoneal Photodynamic Therapy for Patients with Peritoneal Carcinomatosis and Sarcomatosis. Clinical Cancer Research. 2006;12(8):2517-25.

178. Casey S, Best L, Vujovic O, Jordan K, Fisher B, Carey D, et al. Use of Protoporphyrin Fluorescence to Determine Clinical Target Volume for Non-melanotic Skin Cancers Treated with Primary Radiotherapy. Cureus. 2016;8(9):e767-e.

179. Edward Y. Photodynamic Therapy: The Light Treatment for Cutaneous Non-Melanoma Malignancies. Current Cancer Therapy Reviews. 2016;12(2):124-37.

180. Stewart F, Baas P, Star W. What does photodynamic therapy have to offer radiation oncologists (or their cancer patients)? Radiotherapy and Oncology. 1998;48(3):233-48.

181. Chen B, Pogue BW, Hoopes PJ, Hasan T. Combining vascular and cellular targeting regimens enhances the efficacy of photodynamic therapy. International Journal of Radiation Oncology • Biology • Physics. 2005;61(4):1216-26.

182. Baskar R, Dai J, Wenlong N, Yeo R, Yeoh K-W. Biological Response of Cancer Cells to Radiation Treatment. Frontiers in Molecular Biosciences. 2014;1:24-.

183. Luksiene Z, Kalvelyte A, Supino R. On the combination of photodynamic therapy with ionizing radiation. Journal of Photochemistry and Photobiology B. 1999;52(1):35-42.

184. Allman R, Cowburn P, Mason M. Effect of Photodynamic Therapy in Combination with Ionizing Radiation on Human Squamous Cell Carcinoma Cell Lines of the Head and Neck. British Journal of Cancer. 2000;83(5):655-61.

185. Bulin A-L, Broekgaarden M, Simeone D, Hasan T. Low Dose Photodynamic Therapy Harmonizes with Radiation Therapy to Induce Beneficial Effects on Pancreatic Heterocellular Spheroids. Oncotarget. 2019;10(27):2625-43.

186. Montazerabadi AR, Sazgarnia A, Bahreyni-Toosi MH, Ahmadi A, Aledavood A. The effects of combined treatment with ionizing radiation and indocyanine green-mediated photodynamic therapy on breast cancer cells. Journal of Photochemistry and Photobiology B. 2012;109:42-9.

187. Sazgarnia A, Montazerabadi AR, Bahreyni-Toosi MH, Ahmadi A, Aledavood A. In vitro survival of MCF-7 breast cancer cells following combined treatment with ionizing radiation and mitoxantrone-mediated photodynamic therapy. Photodiagnosis and Photodynamic Therapy. 2013;10(1):72-8.

188. Ghoodarzi R, Changizi V, Montazerabadi AR, Eyvazzadaeh N. Assessing of integration of ionizing radiation with Radachlorin-PDT on MCF-7 breast cancer cell treatment. Lasers in Medical Science. 2016;31(2):213-9.

189. Nakano A, Watanabe D, Akita Y, Kawamura T, Tamada Y, Matsumoto Y. Treatment Efficiency of Combining Photodynamic Therapy and Ionizing Radiation for Bowen's Disease. Journal of the European Academy of Dermatology and Venereology. 2011;25(4):475-8.

190. Freitag L, Ernst A, Thomas M, Prenzel R, Wahlers B, Macha H-N. Sequential Photodynamic Therapy (PDT) and High Dose Brachytherapy for Endobronchial Tumour Control in Patients with Limited Bronchogenic Carcinoma. Thorax. 2004;59(9):790-3.

191. Sanfilippo NJ, Hsi A, DeNittis AS, Ginsberg GG, Kochman ML, Friedberg JS, et al. Toxicity of Photodynamic Therapy after Combined External Beam Radiotherapy and Intraluminal Brachytherapy for Carcinoma of the Upper Aerodigestive Tract. Laser Medicine & Surgery. 2001;28(3):278-81.

192. Kusuzaki K, Murata H, Matsubara T, Miyazaki S, Okamura A, Seto M, et al. Clinical Trial of Photodynamic Therapy Using Acridine Orange with/without Low Dose Radiation as New Limb Salvage Modality in Musculoskeletal Sarcomas. Anticancer Research. 2005;25(2b):1225-35.

193. Clement S, Deng W, Camilleri E, Wilson BC, Goldys EM. X-ray induced singlet oxygen generation by nanoparticle-photosensitizer conjugates for photodynamic therapy: determination of singlet oxygen quantum yield. Scientific Reports. 2016;6:19954.

194. Elmenoufy AH, Tang Y, Hu J, Xu H, Yang X. A novel deep photodynamic therapy modality combined with CT imaging established via X-ray stimulated silica-modified lanthanide scintillating nanoparticles. Chemical Communications. 2015;51(61):12247-50.

195. Clement S, Deng W, Camilleri E, Wilson BC, Goldys EM. X-ray induced singlet oxygen generation by nanoparticle-photosensitizer conjugates for photodynamic therapy: determination of singlet oxygen quantum yield. Scientific Reports. 2016;6(1):19954.

196. Moore RB, Xiao Z, Tulip J, Chapman JD. A Comparison of Susceptibility to Photodynamic Treatment between Endothelial and Tumor Cells in vitro and in vivo. Photodiagnosis and Photodynamic Therapy. 2007;4(3):160-9.

197. Grimes DR, Warren DR, Warren S. Hypoxia Imaging and Radiotherapy: Bridging the Resolution Gap. British Journal of Radiology. 2017;90(1076):20160939-.

198. Milosevic M, Warde P, Menard C, Chung P, Toi A, Ishkanian A, et al. Tumor hypoxia predicts biochemical failure following radiotherapy for clinically localized prostate cancer. Clinical Cancer Research. 2012;18(7):2108-14.

199. Rockwell S, Dobrucki IT, Kim EY, Marrison ST, Vu VT. Hypoxia and radiation therapy: past history, ongoing research, and future promise. Current molecular medicine. 2009;9(4):442-58.

200. Zhang C, Zhao K, Bu W, Ni D, Liu Y, Feng J, et al. Marriage of Scintillator and Semiconductor for Synchronous Radiotherapy and Deep Photodynamic Therapy with Diminished Oxygen Dependence. Angewandte Chemie. 2015;54(6):1770-4.

201. Dinakaran D, Chen H, Wuest M, Sonke-Jans H, Wuest F, Murray D, et al. Novel X-ray Activated Photodynamic (radioPDT) Nanoparticles for Deep-Seated Tumors. International Journal of Radiation Oncology • Biology • Physics. 2019;105(1):E676.

202. Wang GD, Nguyen HT, Chen H, Cox PB, Wang L, Nagata K, et al. X-Ray Induced Photodynamic Therapy: A Combination of Radiotherapy and Photodynamic Therapy. Theranostics. 2016;6(13):2295-305.

203. Shrestha S, Wu J, Sah B, Vanasse A, Cooper LN, Ma L, et al. X-ray induced photodynamic therapy with copper-cysteamine nanoparticles in mice tumors. Proceedings of the National Academy of Sciences. 2019;116(34):16823-8.

204. Turner JH. Recent Advances in Theranostics and Challenges for the Future. British Journal of Radiology. 2018;91(1091):20170893.

205. Dinakaran D, Chen H, Warkentin B, Kumar P, Usmani NH, Narain R, et al. Novel Radiation-Activated Photodynamic (radioPDT) Nanoparticles for Treating Deep-Seated Tumors. International Journal of Radiation Oncology • Biology • Physics. 2018;102(3):e181-e2.

206. Chen H, Sun X, Wang GD, Nagata K, Hao Z, Wang A, et al. LiGa5O8:Cr-Based Theranostic Nanoparticles for Imaging-Guided X-ray Induced photodynamic Therapy of Deep-Seated Tumors. Materials Horizons. 2017;4(6):1092-101.

207. Rajkumar S, Prabaharan* M. Theranostics Based on Iron Oxide and Gold Nanoparticles for Imaging- Guided Photothermal and Photodynamic Therapy of Cancer. Current Topics in Medicinal Chemistry. 2017;17(16):1858-71.

208. Xu H, Ohulchanskyy TY, Yakovliev A, Zinyuk R, Song J, Liu L, et al. Nanoliposomes Co-Encapsulating CT Imaging Contrast Agent and Photosensitizer for Enhanced, Imaging Guided Photodynamic Therapy of Cancer. Theranostics. 2019;9(5):1323-35.

209. Ostroverkhov P, Semkina A, Naumenko V, Plotnikova E, Yakubovskaya R, Vodopyanov S, et al. HSA—Coated Magnetic Nanoparticles for MRI-Guided Photodynamic Cancer Therapy. Pharmaceutics. 2018;10(4):284.

210. Jenni S, Sour A. Molecular Theranostic Agents for Photodynamic Therapy (PDT) and Magnetic Resonance Imaging (MRI). Inorganics. 2019;7:10.

211. Wicki A, Witzigmann D, Balasubramanian V, Huwyler J. Nanomedicine in cancer therapy: challenges, opportunities, and clinical applications. Journal of Controlled Release. 2015;200:138-57.

212. Tran S, DeGiovanni P-J, Piel B, Rai P. Cancer nanomedicine: a review of recent success in drug delivery. Clinical and Translational Medicine. 2017;6(1):44-.

213. Kaur P, Aliru ML, Chadha AS, Asea A, Krishnan S. Hyperthermia using nanoparticles--Promises and pitfalls. International Journal of Hyperthermia. 2016;32(1):76-88.

214. Chen H, Zhen Z, Todd T, Chu PK, Xie J. Nanoparticles for Improving Cancer Diagnosis. Materials Science & Engineering R: Reports. 2013;74(3):35-69.

215. Muthu MS, Leong DT, Mei L, Feng SS. Nanotheranostics - application and further development of nanomedicine strategies for advanced theranostics. Theranostics. 2014;4(6):660-77.

216. Lammers T, Kiessling F, Hennink WE, Storm G. Nanotheranostics and image-guided drug delivery: current concepts and future directions. Molecular Pharmaceutics. 2010;7(6):1899-912.

217. Puri A, Loomis K, Smith B, Lee J-H, Yavlovich A, Heldman E, et al. Lipid-based nanoparticles as pharmaceutical drug carriers: from concepts to clinic. Critical Reviews in Therapeutic Drug Carrier Systems. 2009;26(6):523-80.

218. Rezigue M. Lipid and Polymeric Nanoparticles: Drug Delivery Applications. In: Krishnan A, Chuturgoon A, editors. Integrative Nanomedicine for New Therapies. Cham: Springer International Publishing; 2020. p. 167-230.

219. Suhail M, Rosenholm JM, Minhas MU, Badshah SF, Naeem A, Khan KU, et al. Nanogels as drug-delivery systems: a comprehensive overview. Therapeutic Delivery. 2019;10(11):697-717.

220. Ferguson CTJ, Huber N, Landfester K, Zhang KAI. Dual-Responsive Photocatalytic Polymer Nanogels. Angewandte Chemie International Edition. 2019;58(31):10567-71.

221. Wicki A, Witzigmann D, Balasubramanian V, Huwyler J. Nanomedicine in cancer therapy: Challenges, opportunities, and clinical applications. Journal of Controlled Release. 2015;200:138-57.

222. Vile R, Ando D, Kirn D. The oncolytic virotherapy treatment platform for cancer: Unique biological and biosafety points to consider. Cancer Gene Therapy. 2002;9(12):1062-7.

223. Steinmetz NF. Viral nanoparticles as platforms for next-generation therapeutics and imaging devices. Nanomedicine. 2010;6(5):634-41.

224. Sivasubramanian M, Chuang YC, Lo L-W. Evolution of Nanoparticle-Mediated Photodynamic Therapy: From Superficial to Deep-Seated Cancers. Molecules. 2019;24(3):520.

225. Cho C-F, Yu L, Nsiama TK, Kadam AN, Raturi A, Shukla S, et al. Viral nanoparticles decorated with novel EGFL7 ligands enable intravital imaging of tumor neovasculature. Nanoscale. 2017;9(33):12096-109.

226. Fenaroli F, Repnik U, Xu Y, Johann K, Van Herck S, Dey P. Enhanced Permeability and Retention-like Extravasation of Nanoparticles from the Vasculature into Tuberculosis Granulomas in Zebrafish and Mouse Models. ACS Nano. 2018;12(8):8646-61.

227. Hanahan D, Weinberg Robert A. Hallmarks of Cancer: The Next Generation. Cell. 2011;144(5):646-74.

228. Albanese A, Tang PS, Chan WCW. The Effect of Nanoparticle Size, Shape, and Surface Chemistry on Biological Systems. Annual Review of Biomedical Engineering. 2012;14(1):1-16.

229. Wittrup KD, Thurber GM, Schmidt MM, Rhoden JJ. Practical theoretic guidance for the design of tumor-targeting agents. Methods Enzymology. 2012;503:255-68.

230. Qie Y, Yuan H, von Roemeling CA, Chen Y, Liu X, Shih KD, et al. Surface modification of nanoparticles enables selective evasion of phagocytic clearance by distinct macrophage phenotypes. Scientific Reports. 2016;6:26269.

231. Klibanov AL, Maruyama K, Torchilin VP, Huang L. Amphipathic polyethyleneglycols effectively prolong the circulation time of liposomes. FEBS letters. 1990;268(1):235-7.

232. Gelderblom H, Verweij J, Nooter K, Sparreboom A. Cremophor EL: the drawbacks and advantages of vehicle selection for drug formulation. European Journal of Cancer. 2001;37(13):1590-8.

233. Gradishar WJ. Albumin-bound paclitaxel: a next-generation taxane. Expert Opinion on Pharmacotherapy. 2006;7(8):1041-53.

234. Miele E, Spinelli GP, Miele E, Tomao F, Tomao S. Albumin-bound formulation of paclitaxel (Abraxane ABI-007) in the treatment of breast cancer. International Journal of Nanomedicine. 2009;4:99-105.

235. Bonvalot S, Rutkowski PL, Thariat J, Carrere S, Ducassou A, Sunyach MP, et al. NBTXR3, a first-in-class radioenhancer hafnium oxide nanoparticle, plus radiotherapy versus radiotherapy alone in patients with locally advanced soft-tissue sarcoma (Act.In.Sarc): a multicentre, phase 2-3, randomised, controlled trial. Lancet Oncology. 2019;20(8):1148-59.

236. Abele JT, Moore R, Tymchak W, Owen RJ. Prostate perfusion mapped by technetium-99m macroaggregated albumin after selective arterial injection. Journal of Vascular and Interventional Radiology. 2015;26(3):418-25.

237. Gonzalez S, Arnfield MR, Meeker BE, Tulip J, Lakey WH, Chapman JD, et al. Treatment of Dunning R3327-AT rat prostate tumors with photodynamic therapy in combination with misonidazole. Cancer Research. 1986;46(6):2858-62.

238. Bremner JC, Bradley JK, Adams GE, Naylor MA, Sansom JM, Stratford IJ. Comparing the anti-tumor effect of several bioreductive drugs when used in combination with photodynamic therapy (PDT). International Journal of Radiation Oncology • Biology • Physics. 1994;29(2):329-32.

239. Conger AD, Luippold HJ. Studies on the Mechanism of Acquired Radioresistance in Cancer. Cancer Research. 1957;17(9):897-903.

240. Chaiswing L, Weiss HL, Jayswal RD, Clair DKS, Kyprianou N. Profiles of Radioresistance Mechanisms in Prostate Cancer. Critical Reviews in Oncogenesis. 2018;23(1-2):39-67.

241. Tang L, Wei F, Wu Y, He Y, Shi L, Xiong F, et al. Role of metabolism in cancer cell radioresistance and radiosensitization methods. Journal of Experimental & Clinical Cancer Research. 2018;37(1):87.

242. Weichselbaum RR, Beckett MA, Vokes EE, Brachman DG, Haraf D, Hallahan D, et al. Cellular and molecular mechanisms of radioresistance. In: Hong WK, Weber RS, editors. Head and Neck Cancer: Basic and Clinical Aspects.1995:131-40.

243. Wardman P. Chemical radiosensitizers for use in radiotherapy. Clinical Oncology. 2007;19(6):397-417.

244. Brown JM, Carlson DJ, Brenner DJ. The tumor radiobiology of SRS and SBRT: are more than the 5 Rs involved? International Journal of Radiation Oncology • Biology • Physics. 2014;88(2):254-62.

245. He H, Liu L, Morin EE, Liu M, Schwendeman A. Survey of Clinical Translation of Cancer Nanomedicines-Lessons Learned from Successes and Failures. Accounts of Chemical Research. 2019;52(9):2445-61.

246. Shi J, Kantoff PW, Wooster R, Farokhzad OC. Cancer nanomedicine: progress, challenges and opportunities. Nature Reviews Cancer. 2017;17(1):20-37.

247. Michalski JM, Bae K, Roach M, Markoe AM, Sandler HM, Ryu J, et al. Long-term toxicity following 3D conformal radiation therapy for prostate cancer from the RTOG 9406 phase I/II dose escalation study. International Journal of Radiation Oncology • Biology • Physics. 2010;76(1):14-22.

248. Moses WW, Derenzo SE. The scintillation properties of cerium-doped lanthanum fluoride. Nuclear Instruments and Methods in Physics Research. 1990;299(1):51-6.

249. Farokhzad OC, Langer R. Nanomedicine: developing smarter therapeutic and diagnostic modalities. Advanced Drug Delivery Reviews. 2006;58(14):1456-9.

250. Saager RB, Cuccia DJ, Saggese S, Kelly KM, Durkin AJ. Quantitative fluorescence imaging of protoporphyrin IX through determination of tissue optical properties in the spatial frequency domain. Journal of Biomedical Optics. 2011;16(12):126013.

251. Srinivasan TK, Panigrahi BS, Arora AK, Venkatraman B, Ponraju D. Gamma irradiation effect on photoluminescence from functionalized LaF3:Ce nanoparticles. Radiation Physics and Chemistry. 2014;99:92-6.

252. Vargas JM, Blostein JJ, Sidelnik I, Brito DR, Palomino LAR, Mayer RE. Luminescent and scintillating properties of lanthanum fluoride nanocrystals in response to gamma/neutron irradiation: codoping with Ce activator, Yb wavelength shifter, and Gd neutron captor. Journal of Instrumentation. 2016;11(09):P09007-P.

253. Sankar K, Plumley JB, Akins BA, Memon TA, Withers NJ, Smolyakov GA, et al. Synthesis and characterization of scintillating cerium-doped lanthanum fluoride nanocrystals: SPIE; 2009.

254. Rollakanti KR, Kanick SC, Davis SC, Pogue BW, Maytin EV. Techniques for fluorescence detection of protoporphyrin IX in skin cancers associated with photodynamic therapy. Photonics & Lasers in Medicine. 2013;2(4):287-303.

255. Sankar K, B. Plumley J, Akins B, Memon T, Withers N, A. Smolyakov G, et al. Synthesis and characterization of scintillating cerium-doped lanthanum fluoride nanocrystals. SPIE; 2009.

256. Kim J, Lee J-H, An H, Lee J, Park S-H, Seo Y-S, et al. Luminescence properties of LaF3:Ce nanoparticles encapsulated by oleic acid. Materials Research Bulletin. 2014;57:110-5.

257. Klier DT, Kumke MU. Analysing the effect of the crystal structure on upconversion luminescence in Yb3+,Er3+-co-doped NaYF4 nanomaterials. Journal of Materials Chemistry C. 2015;3(42):11228-38.

258. Anderson DF. Properties of the high-density scintillator cerium fluoride. IEEE Transactions on Nuclear Science. 1989;36(1):137-40.

259. Jacobsohn LG, Sprinkle KB, Kucera CJ, James TL, Roberts SA, Qian H, et al. Synthesis, luminescence and scintillation of rare earth doped lanthanum fluoride nanoparticles. Optical Materials. 2010;33(2):136-40.

260. Martinez Rivas CJ, Tarhini M, Badri W, Miladi K, Greige-Gerges H, Nazari QA, et al. Nanoprecipitation process: From encapsulation to drug delivery. International Journal of Pharmaceutics. 2017;532(1):66-81.

261. Honary S, Zahir F. Effect of Zeta Potential on the Properties of Nano-Drug Delivery Systems - A Review (Part 2). Tropical Journal of Pharmaceutical Research. 2013. 12(2).

262. Dalwadi G, Benson HAE, Chen Y. Comparison of Diafiltration and Tangential Flow Filtration for Purification of Nanoparticle Suspensions. Pharmaceutical Research. 2005;22(12):2152-62.

263. Dalwadi G, Sunderland VB. Purification of PEGylated nanoparticles using tangential flow filtration (TFF). Drug Development and Industrial Pharmacy. 2007;33(9):1030-9.

264. Shirane D, Tanaka H, Nakai Y, Yoshioka H, Akita H. Development of an Alcohol Dilution–Lyophilization Method for Preparing Lipid Nanoparticles Containing Encapsulated siRNA. Biological and Pharmaceutical Bulletin. 2018;41(8):1291-4.

265. Hanahan D, Weinberg RA. Hallmarks of cancer: the next generation. Cell. 2011;144(5):646-74.

266. Atukorale PU, Covarrubias G, Bauer L, Karathanasis E. Vascular targeting of nanoparticles for molecular imaging of diseased endothelium. Advanced Drug Delivery Reviews. 2017;113:141-56.

267. Greish K. Enhanced permeability and retention (EPR) effect for anticancer nanomedicine drug targeting. Methods in Molecular Biology. 2010;624:25-37.

268. Fortuni B, Inose T, Ricci M, Fujita Y, Van Zundert I, Masuhara A, et al. Polymeric Engineering of Nanoparticles for Highly Efficient Multifunctional Drug Delivery Systems. Scientific Reports. 2019;9(1):2666.

269. Larue L, Ben Mihoub A, Youssef Z, Colombeau L, Acherar S, Andre JC, et al. Using X-rays in photodynamic therapy: an overview. Photochemical & Photobiological Sciences. 2018;17(11):1612-50.

270. Wang J, Li S, Han Y, Guan J, Chung S, Wang C, et al. Poly(Ethylene Glycol)-Polylactide Micelles for Cancer Therapy. Frontiers in Pharmacology. 2018;9:202-.

271. Autio KA, Dreicer R, Anderson J, Garcia JA, Alva A, Hart LL, et al. Safety and Efficacy of BIND-014, a Docetaxel Nanoparticle Targeting Prostate-Specific Membrane Antigen for Patients With Metastatic Castration-Resistant Prostate Cancer: A Phase 2 Clinical Trial. JAMA Oncology. 2018;4(10):1344-51.

272. Liu D, Mori A, Huang L. Role of liposome size and RES blockade in controlling biodistribution and tumor uptake of GM1-containing liposomes. Biochimica et Biophysica Acta. 1992;1104(1):95-101.

273. Perry JL, Reuter KG, Luft JC, Pecot CV, Zamboni W, DeSimone JM. Mediating Passive Tumor Accumulation through Particle Size, Tumor Type, and Location. Nano Letters. 2017;17(5):2879-86.

274. Aggarwal P, Hall JB, McLeland CB, Dobrovolskaia MA, McNeil SE. Nanoparticle interaction with plasma proteins as it relates to particle biodistribution, biocompatibility and therapeutic efficacy. Advanced Drug Delivery Reviews. 2009;61(6):428-37.

275. Li SD, Huang L. Pharmacokinetics and biodistribution of nanoparticles. Molecular Pharmaceutics. 2008;5(4):496-504.

276. Eliasof S, Lazarus D, Peters CG, Case RI, Cole RO, Hwang J, et al. Correlating preclinical animal studies and human clinical trials of a multifunctional, polymeric nanoparticle. Proceedings of the National Academy of Sciences of the United States of America. 2013;110(37):15127-32.

277. Chen H-T, Neerman MF, Parrish AR, Simanek EE. Cytotoxicity, Hemolysis, and Acute in Vivo Toxicity of Dendrimers Based on Melamine, Candidate Vehicles for Drug Delivery. Journal of the American Chemical Society. 2004;126(32):10044-8.

278. Clement S, Chen W, Deng W, Goldys EM. X-ray radiation-induced and targeted photodynamic therapy with folic acid-conjugated biodegradable nanoconstructs. International Journal of Nanomedicine. 2018;13:3553-70.

279. Larue L, Ben Mihoub A, Youssef Z, Colombeau L, Acherar S, André JC, et al. Using X-rays in photodynamic therapy: an overview. Photochemical & Photobiological Sciences. 2018;17(11):1612-50.

280. Society CC. Canadian Cancer Statistics. 2017.

281. Morris KA, Haboubi NY. Pelvic radiation therapy: Between delight and disaster. World Journal of Gastrointestinal Surgery. 2015;7(11):279-88.

282. Baskar R, Lee KA, Yeo R, Yeoh KW. Cancer and radiation therapy: current advances and future directions. International Journal of Medical Sciences. 2012;9(3):193-9.

283. Mirzayans R, Andrais B, Scott A, Wang YW, Murray D. Ionizing radiation-induced responses in human cells with differing TP53 status. International Journal of Medical Sciences. 2013;14(11):22409-35.

284. Lo SS, Fakiris AJ, Chang EL, Mayr NA, Wang JZ, Papiez L, et al. Stereotactic body radiation therapy: a novel treatment modality. Nature reviews Clinical oncology. 2010;7(1):44-54.

285. Do NL, Nagle D, Poylin VY. Radiation proctitis: current strategies in management. Gastroenterology Research and Practice. 2011;2011:917941.

286. Browne C, Davis NF, Mac Craith E, Lennon GM, Mulvin DW, Quinlan DM, et al. A Narrative Review on the Pathophysiology and Management for Radiation Cystitis. Advances in Urology. 2015;2015:346812.

287. Pasalic D, Kuban DA, Allen PK, Tang C, Mesko SM, Grant SR, et al. Dose Escalation for Prostate Adenocarcinoma: A Long-Term Update on the Outcomes of a Phase 3, Single Institution Randomized Clinical Trial. International Journal of Radiation Oncology • Biology • Physics. 2019;104(4):790-7.

288. Zaorsky NG, Palmer JD, Hurwitz MD, Keith SW, Dicker AP, Den RB. What is the ideal radiotherapy dose to treat prostate cancer? A meta-analysis of biologically equivalent dose escalation. Radiotherapy and Oncology. 2015;115(3):295-300.

289. Zietman AL, DeSilvio ML, Slater JD, Rossi CJ, Jr., Miller DW, Adams JA, et al. Comparison of conventional-dose vs high-dose conformal radiation therapy in clinically localized adenocarcinoma of the prostate: a randomized controlled trial. JAMA. 2005;294(10):1233-9.

290. Zelefsky MJ, Kattan MW, Fearn P, Fearon BL, Stasi JP, Shippy AM, et al. Pretreatment nomogram predicting ten-year biochemical outcome of three-dimensional conformal radiotherapy and intensity-modulated radiotherapy for prostate cancer. Urology. 2007;70(2):283-7.

291. Cheung MR, Tucker SL, Dong L, de Crevoisier R, Lee AK, Frank S, et al. Investigation of bladder dose and volume factors influencing late urinary toxicity after external beam radiotherapy for prostate cancer. International Journal of Radiation Oncology • Biology • Physics. 2007;67(4):1059-65.

292. Rodda S, Tyldesley S, Morris WJ, Keyes M, Halperin R, Pai H, et al. ASCENDE-RT: An Analysis of Treatment-Related Morbidity for a Randomized Trial Comparing a Low-Dose-Rate Brachytherapy Boost with a Dose-Escalated External Beam Boost for High- and Intermediate-Risk Prostate Cancer. International Journal of Radiation Oncology • Biology • Physics. 2017;98(2):286-95.

293. Morris WJ, Pickles T, Keyes M. Using a surgical prostate-specific antigen threshold of >0.2 ng/mL to define biochemical failure for intermediate- and high-risk prostate cancer patients treated with definitive radiation therapy in the ASCENDE-RT randomized control trial. Brachytherapy. 2018;17(6):837-44.

294. Morris WJ, Tyldesley S, Rodda S, Halperin R, Pai H, McKenzie M, et al. Androgen Suppression Combined with Elective Nodal and Dose Escalated Radiation Therapy (the ASCENDE-RT Trial): An Analysis of Survival Endpoints for a Randomized Trial Comparing a Low-Dose-Rate Brachytherapy Boost to a Dose-Escalated External Beam Boost for High- and Intermediate-risk Prostate Cancer. International Journal of Radiation Oncology • Biology • Physics. 2017;98(2):275-85.

295. Zelefsky MJ, Kollmeier M, McBride S, Varghese M, Mychalczak B, Gewanter R, et al. Five-Year Outcomes of a Phase 1 Dose-Escalation Study Using Stereotactic Body Radiosurgery for Patients With Low-Risk and Intermediate-Risk Prostate Cancer. International Journal of Radiation Oncology • Biology • Physics. 2019;104(1):42-9.

296. Wegner RE, Abel S, Horne ZD, Hasan S, Verma V, Ranjan T, et al. National trends in radiation dose escalation for glioblastoma. Radiation Oncology Journal. 2019;37(1):13-21.

297. Bradley JD, Paulus R, Komaki R, Masters G, Blumenschein G, Schild S, et al. Standard-dose versus high-dose conformal radiotherapy with concurrent and consolidation carboplatin plus paclitaxel with or without cetuximab for patients with stage IIIA or IIIB non-small-cell lung cancer (RTOG 0617): a randomised, two-by-two factorial phase 3 study. Lancet Oncology. 2015;16(2):187-99.

298. Turrisi AT, Kim K, Blum R, Sause WT, Livingston RB, Komaki R, et al. Twice-Daily Compared with Once-Daily Thoracic Radiotherapy in Limited Small-Cell Lung Cancer Treated Concurrently with Cisplatin and Etoposide. New England Journal of Medicine. 1999;340(4):265-71.

299. Skinner HD, Strom EA, Motwani SB, Woodward WA, Green MC, Babiera G, et al. Radiation dose escalation for loco-regional recurrence of breast cancer after mastectomy. Radiation Oncology. 2013;8:13.

300. Brower JV, Chen S, Bassetti MF, Yu M, Harari PM, Ritter MA, et al. Radiation Dose Escalation in Esophageal Cancer Revisited: A Contemporary Analysis of the National Cancer Data Base, 2004 to 2012. International Journal of Radiation Oncology • Biology • Physics. 2016;96(5):985-93.

301. Gerard JP, Conroy T, Bonnetain F, Bouche O, Chapet O, Closon-Dejardin MT, et al. Preoperative radiotherapy with or without concurrent fluorouracil and leucovorin in T3-4 rectal cancers: results of FFCD 9203. Journal of Clinical Oncology. 2006;24(28):4620-5.

302. Ceelen WP, Van Nieuwenhove Y, Fierens K. Preoperative chemoradiation versus radiation alone for stage II and III resectable rectal cancer. The Cochrane Database of Systematic Reviews. 2009(1):Cd006041.

303. VanderWalde NA, Meyer AM, Deal AM, Layton JB, Liu H, Carpenter WR, et al. Effectiveness of chemoradiation for head and neck cancer in an older patient population. International Journal of Radiation Oncology • Biology • Physics. 2014;89(1):30-7.

304. Cooper JS, Guo MD, Herskovic A, Macdonald JS, Martenson J, James A., Al-Sarraf M, et al. Chemoradiotherapy of Locally Advanced Esophageal CancerLong-term Follow-up of a Prospective Randomized Trial (RTOG 85-01). JAMA. 1999;281(17):1623-7.

305. Sause W, Kolesar P, Taylor SIV, Johnson D, Livingston R, Komaki R, et al. Final Results of Phase III Trial in Regionally Advanced Unresectable Non-Small Cell Lung Cancer: Radiation Therapy Oncology Group, Eastern Cooperative Oncology Group, and Southwest Oncology Group. CHEST. 2000;117(2):358-64.

306. Gillison ML, Trotti AM, Harris J, Eisbruch A, Harari PM, Adelstein DJ, et al. Radiotherapy plus cetuximab or cisplatin in human papillomavirus-positive oropharyngeal cancer (NRG Oncology RTOG 1016): a randomised, multicentre, non-inferiority trial. The Lancet. 2019;393(10166):40-50.

307. DiSilvestro PA, Ali S, Craighead PS, Lucci JA, Lee Y-C, Cohn DE, et al. Phase III Randomized Trial of Weekly Cisplatin and Irradiation Versus Cisplatin and Tirapazamine and Irradiation in Stages IB2, IIA, IIB, IIIB, and IVA Cervical Carcinoma Limited to the Pelvis: A Gynecologic Oncology Group Study. Journal of Clinical Oncology. 2014;32(5):458-64.

308. Cui L, Her S, Borst GR, Bristow RG, Jaffray DA, Allen C. Radiosensitization by gold nanoparticles: Will they ever make it to the clinic? Radiotherapy and Oncology. 2017;124(3):344-56.

309. Vilotte F, Jumeau R, Bourhis J. High Z nanoparticles and radiotherapy: a critical view. Lancet Oncology. 2019;20(10):e557.

310. Al Tameemi W, Dale TP, Al-Jumaily RMK, Forsyth NR. Hypoxia-Modified Cancer Cell Metabolism. Frontiers in Cell and Developmental Biology. 2019;7(4).

311. Saxena K, Jolly MK. Acute vs. Chronic vs. Cyclic Hypoxia: Their Differential Dynamics, Molecular Mechanisms, and Effects on Tumor Progression. Biomolecules. 2019;9(8):339.

312. Eales KL, Hollinshead KER, Tennant DA. Hypoxia and metabolic adaptation of cancer cells. Oncogenesis. 2016;5(1):e190-e.

313. Kummrow A, Frankowski M, Bock N, Werner C, Dziekan T, Neukammer J. Quantitative assessment of cell viability based on flow cytometry and microscopy. International Society for Advancement of Cytometry. 2013;83(2):197-204.

314. Crowley LC, Scott AP, Marfell BJ, Boughaba JA, Chojnowski G, Waterhouse NJ. Measuring Cell Death by Propidium Iodide Uptake and Flow Cytometry. Cold Spring Harbor protocols. 2016;2016(7).

315. Al-Rubeai M, Welzenbach K, Lloyd DR, Emery AN. A rapid method for evaluation of cell number and viability by flow cytometry. Cytotechnology. 1997;24(2):161-8.

316. Sauvat A, Wang Y, Segura F, Spaggiari S, Müller K, Zhou H, et al. Quantification of cellular viability by automated microscopy and flow cytometry. Oncotarget. 2015;6(11):9467-75.

317. Wallberg F, Tenev T, Meier P. Analysis of Apoptosis and Necroptosis by Fluorescence-Activated Cell Sorting. Cold Spring Harbor protocols. 2016;2016(4):pdb.prot087387.

318. Banerjee A, Majumder P, Sanyal S, Singh J, Jana K, Das C, et al. The DNA intercalators ethidium bromide and propidium iodide also bind to core histones. FEBS Open Bio. 2014;4:251-9.

319. Kolesnick R, Fuks Z. Radiation and ceramide-induced apoptosis. Oncogene. 2003;22(37):5897-906.

320. Schroder S, Broese S, Baake J, Juerss D, Kriesen S, Hildebrandt G, et al. Effect of Ionizing Radiation on Human EA.hy926 Endothelial Cells under Inflammatory Conditions and Their Interactions with A549 Tumour Cells. Journal of Immunology Research. 2019:9645481.

321. Fuks Z, Kolesnick R. Engaging the vascular component of the tumor response. Cancer Cell. 2005;8(2):89-91.

322. Truman J-P, García-Barros M, Kaag M, Hambardzumyan D, Stancevic B, Chan M, et al. Endothelial membrane remodeling is obligate for anti-angiogenic radiosensitization during tumor radiosurgery. PloS one. 2010;5(8):e12310-e.

323. Murakami N, Kühnel A, Schmid TE, Ilicic K, Stangl S, Braun IS, et al. Role of membrane Hsp70 in radiation sensitivity of tumor cells. Radiation Oncology. 2015;10(1):149.

324. Dent P, Reardon DB, Park JS, Bowers G, Logsdon C, Valerie K, et al. Radiation-induced release of transforming growth factor alpha activates the epidermal growth factor receptor and mitogen-activated protein kinase pathway in carcinoma cells, leading to increased proliferation and protection from radiation-induced cell death. Molecular Biology of the Cell. 1999;10(8):2493-506.

325. Paul-Gilloteaux P, Potiron V, Delpon G, Supiot S, Chiavassa S, Paris F, et al. Optimizing radiotherapy protocols using computer automata to model tumour cell death as a function of oxygen diffusion processes. Scientific Reports. 2017;7(1):2280.

326. Lee WC, Chang CH, Ho CL, Chen LC, Wu YH, Chen JT, et al. Early detection of tumor response by FLT/microPET Imaging in a C26 murine colon carcinoma solid tumor animal model. Journal of Biomedicine & Biotechnology. 2011;2011:535902.

327. Sanghera B, Wong WL, Sonoda LI, Beynon G, Makris A, Woolf D, et al. FLT PET-CT in evaluation of treatment response. Indian Journal of Nuclear Medicine. 2014;29(2):65-73.

328. Schelhaas S, Heinzmann K, Bollineni VR, Kramer GM, Liu Y, Waterton JC, et al. Preclinical Applications of 3'-Deoxy-3'-[(18)F]Fluorothymidine in Oncology - A Systematic Review. Theranostics. 2017;7(1):40-50.

329. Bollineni VR, Kramer GM, Jansma EP, Liu Y, Oyen WJ. A systematic review on [(18)F]FLT-PET uptake as a measure of treatment response in cancer patients. European journal of cancer. 2016;55:81-97.

330. Been LB, Suurmeijer AJ, Cobben DC, Jager PL, Hoekstra HJ, Elsinga PH. [18F]FLT-PET in oncology: current status and opportunities. European Journal of Nuclear Medicine and Molecular Imaging. 2004;31(12):1659-72.

331. Liberti MV, Locasale JW. The Warburg Effect: How Does it Benefit Cancer Cells? Trends in Biochemical Sciences. 2016;41(3):211-8.

332. Griffeth LK. Use of PET/CT scanning in cancer patients: technical and practical considerations. Proceedings / Baylor University Medical Center. 2005;18(4):321-30.

333. Jarvi MT, Patterson MS, Wilson BC. Insights into photodynamic therapy dosimetry: simultaneous singlet oxygen luminescence and photosensitizer photobleaching measurements. Biophysical Journal. 2012;102(3):661-71.

334. Kim S, Fujitsuka M, Majima T. Photochemistry of singlet oxygen sensor green. The journal of physical chemistry B. 2013;117(45):13985-92.

335. Saleh T, Tyutyunyk-Massey L, Gewirtz DA. Tumor Cell Escape from Therapy-Induced Senescence as a Model of Disease Recurrence after Dormancy. Cancer research. 2019;79(6):1044-6.

336. Sabin RJ, Anderson RM. Cellular Senescence - its role in cancer and the response to ionizing radiation. Genome Integrity. 2011;2(1):7.

337. Stapleton S, Milosevic M, Allen C, Zheng J, Dunne M, Yeung I, et al. A mathematical model of the enhanced permeability and retention effect for liposome transport in solid tumors. PLoS One. 2013;8(12):e81157.

338. Hrkach J, Von Hoff D, Ali MM, Andrianova E, Auer J, Campbell T, et al. Preclinical Development and Clinical Translation of a PSMA-Targeted Docetaxel Nanoparticle with a Differentiated Pharmacological Profile. Science Translational Medicine. 2012;4(128):128ra39-ra39.

339. van Oorschot B, Hovingh SE, Rodermond H, Guclu A, Losekoot N, Geldof AA, et al. Decay of gamma-H2AX foci correlates with potentially lethal damage repair in prostate cancer cells. Oncology Reports. 2013;29(6):2175-80.

340. Seibert JA. X-ray imaging physics for nuclear medicine technologists. Part 1: Basic principles of x-ray production. Journal of Nuclear Medicine Technology. 2004;32(3):139-47.

341. Lusic H, Grinstaff MW. X-ray-computed tomography contrast agents. Chemical Reviews. 2013;113(3):1641-66.

342. Yeh BM, FitzGerald PF, Edic PM, Lambert JW, Colborn RE, Marino ME, et al. Opportunities for new CT contrast agents to maximize the diagnostic potential of emerging spectral CT technologies. Advanced Drug Delivery Reviews. 2017;113:201-22.

343. Cormode DP, Naha PC, Fayad ZA. Nanoparticle contrast agents for computed tomography: a focus on micelles. Contrast Media and Molecular Imaging. 2014;9(1):37-52.

344. Shilo M, Reuveni T, Motiei M, Popovtzer R. Nanoparticles as computed tomography contrast agents: current status and future perspectives. Nanomedicine. 2012;7(2):257-69.

345. Leung MKK, Chow JCL, Chithrani BD, Lee MJG, Oms B, Jaffray DA. Irradiation of gold nanoparticles by x-rays: Monte Carlo simulation of dose enhancements and the spatial properties of the secondary electrons production. Medical Physics. 2011;38(2):624-31.

346. Nikjoo H, Lindborg L. RBE of low energy electrons and photons. Physics in Medicine & Biology. 2010;55(10):R65-109.

347. Lechtman E, Chattopadhyay N, Cai Z, Mashouf S, Reilly R, Pignol JP. Implications on clinical scenario of gold nanoparticle radiosensitization in regards to photon energy, nanoparticle size, concentration and location. Physics in Medicine & Biology. 2011;56(15):4631-47.

348. Kuncic Z, Lacombe S. Nanoparticle radio-enhancement: principles, progress and application to cancer treatment. Physics in Medicine & Biology. 2018;63(2):02tr1.

349. Byrne H, McNamara A, Kuncic Z. Impact of Nanoparticle Clustering on Dose Radio-enhancement. Radiation Protection Dosimetry. 2019;183(1-2):50-4.

350. Attix F. Introduction to Radiological Physics and Radiation Dosimetry. 2007:154-92.

351. Zhang XD, Wu D, Shen X, Chen J, Sun YM, Liu PX, et al. Size-dependent radiosensitization of PEG-coated gold nanoparticles for cancer radiation therapy. Biomaterials. 2012;33(27):6408-19.

352. Surov A, Meyer HJ, Wienke A. Associations Between PET Parameters and Expression of Ki-67 in Breast Cancer. Translational Oncology. 2019;12(2):375-80.

353. Woolf DK, Beresford M, Li SP, Dowsett M, Sanghera B, Wong WL, et al. Evaluation of FLT-PET-CT as an imaging biomarker of proliferation in primary breast cancer. British Journal of Cancer. 2014;110(12):2847-54.

354. Chalkidou A, Landau DB, Odell EW, Cornelius VR, O'Doherty MJ, Marsden PK. Correlation between Ki-67 immunohistochemistry and 18F-fluorothymidine uptake in patients with cancer: A systematic review and meta-analysis. European Journal of Cancer. 2012;48(18):3499-513.

355. Zhang CC, Yan Z, Li W, Kuszpit K, Painter CL, Zhang Q, et al. [¹⁸F]FLT–PET Imaging Does Not Always “Light Up” Proliferating Tumor Cells. Clinical Cancer Research. 2012;18(5):1303-12.

356. 8 Gy single fraction radiotherapy for the treatment of metastatic skeletal pain: randomised comparison with a multifraction schedule over 12 months of patient follow-up. Bone Pain Trial Working Party. Radiotherapy and Oncology. 1999;52(2):111-21.

357. Shuja M, Elghazaly AA, Iqbal A, Mohamed R, Marie A, Tunio MA, et al. Efficacy of 8 Gy Single Fraction Palliative Radiation Therapy in Painful Bone Metastases: A Single Institution Experience. Cureus. 2018;10(1):e2036-e.

358. Kachnic L, Berk L. Palliative Single-Fraction Radiation Therapy: How Much More Evidence Is Needed? JNCI: Journal of the National Cancer Institute. 2005;97(11):786-8.

359. Navalkissoor S, Flux G, Bomanji J. Molecular radiotheranostics for neuroendocrine tumours. Clinical Medicine. 2017;17(5):462-8.

360. Silberstein EB. Radioiodine: the classic theranostic agent. Seminars in Nuclear Medicine. 2012;42(3):164-70.

361. Chen Y-P, Lv J-W, Liu X, Zhang Y, Guo Y, Lin A-H, et al. The Landscape of Clinical Trials Evaluating the Theranostic Role of PET Imaging in Oncology: Insights from an Analysis of ClinicalTrials.gov Database. Theranostics. 2017;7(2):390-9.

362. Hadjipanayis CG, Widhalm G, Stummer W. What is the Surgical Benefit of Utilizing 5-Aminolevulinic Acid for Fluorescence-Guided Surgery of Malignant Gliomas? Neurosurgery. 2015;77(5):663-73.

363. Messmann H, Endlicher E, Freunek G, Rümmele P, Schölmerich J, Knüchel R. Fluorescence endoscopy for the detection of low and high grade dysplasia in ulcerative colitis using systemic or local 5-aminolaevulinic acid sensitisation. Gut. 2003;52(7):1003-7.

364. Baik FM, Hansen S, Knoblaugh SE, Sahetya D, Mitchell RM, Xu C, et al. Fluorescence Identification of Head and Neck Squamous Cell Carcinoma and High-Risk Oral Dysplasia With BLZ-100, a Chlorotoxin-Indocyanine Green Conjugate. JAMA Otolaryngology and Head & Neck Surgery. 2016;142(4):330-8.

365. Al'-Shukri S, Danil'chenko DI, Kenig F, Shnorr D. [ALA fluorescent diagnosis of bladder cancer]. Urologiia. 2000(5):48-50.

366. Lashkari SM, Kariminezhad H, Amani H, Mataji P, Rahimnejad M. Introduction of 5-aminolevulinic acid as a theranostics agent in dentistry. Photodiagnosis and Photodynamic Therapy. 2019;25:336-43.

367. Lin T-Y, Li Y, Liu Q, Chen J-L, Zhang H, Lac D, et al. Novel theranostic nanoporphyrins for photodynamic diagnosis and trimodal therapy for bladder cancer. Biomaterials. 2016;104:339-51.

368. Lammers T, Aime S, Hennink WE, Storm G, Kiessling F. Theranostic Nanomedicine. Accounts of Chemical Research. 2011;44(10):1029-38.

369. Wang L-S, Chuang M-C, Ho J-AA. Nanotheranostics--a review of recent publications. International Journal of Nanomedicine. 2012;7:4679-95.

370. Reis C, Pinho J, Lopes J, Almeida A, Gaspar M. Current Trends in Cancer Nanotheranostics: Metallic, Polymeric, and Lipid-Based Systems. Pharmaceutics. 2019;11:1-40.

371. Thakur V, Kutty RV. Recent advances in nanotheranostics for triple negative breast cancer treatment. Journal of Experimental & Clinical Cancer Research. 2019;38(1):430.

372. Sterzing F, Engenhart-Cabillic R, Flentje M, Debus J. Image-guided radiotherapy: a new dimension in radiation oncology. Deutsches Ärzteblatt International. 2011;108(16):274-80.

373. Greco C, Clifton Ling C. Broadening the scope of image-guided radiotherapy (IGRT). Acta Oncology. 2008;47(7):1193-200.

374. Schwarz M, Giske K, Stoll A, Nill S, Huber PE, Debus J, et al. IGRT versus non-IGRT for postoperative head-and-neck IMRT patients: dosimetric consequences arising from a PTV margin reduction. Radiation Oncology. 2012;7(1):133.

375. Keall PJ, Nguyen DT, O'Brien R, Zhang P, Happersett L, Bertholet J, et al. Review of Real-Time 3-Dimensional Image Guided Radiation Therapy on Standard-Equipped Cancer Radiation Therapy Systems: Are We at the Tipping Point for the Era of Real-Time Radiation Therapy? International Journal of Radiation Oncology • Biology • Physics. 2018;102(4):922-31.

376. Liu Y, Zhang P, Li F, Jin X, Li J, Chen W, et al. Metal-based NanoEnhancers for Future Radiotherapy: Radiosensitizing and Synergistic Effects on Tumor Cells. Theranostics. 2018;8(7):1824-49.

377. Joh DY, Kao GD, Murty S, Stangl M, Sun L, Zaki AA, et al. Theranostic Gold Nanoparticles Modified for Durable Systemic Circulation Effectively and Safely Enhance the Radiation Therapy of Human Sarcoma Cells and Tumors. Translational Oncology. 2013;6(6):722-IN32.

378. Bushberg JT. The AAPM/RSNA physics tutorial for residents. X-ray interactions. Radiographics. 1998;18(2):457-68.

379. Palmer TD, Lewis J, Zijlstra A. Quantitative analysis of cancer metastasis using an avian embryo model. Journal of Visualized Experiments. 2011(51):2815.

380. Paproski RJ, Jovel J, Wong GK-S, Lewis JD, Zemp RJ. Enhanced Detection of Cancer Biomarkers in Blood-Borne Extracellular Vesicles Using Nanodroplets and Focused Ultrasound. Cancer Research. 2017;77(1):3-13.

381. Stoletov K, Willetts L, Paproski RJ, Bond DJ, Raha S, Jovel J, et al. Quantitative in vivo whole genome motility screen reveals novel therapeutic targets to block cancer metastasis. Nature Communications. 2018;9(1):2343.

382. Razzak R, Zhou J, Yang X, Pervez N, Bédard E, Moore R, et al. The biodistribution and pharmacokinetic evaluation of choline-bound gold nanoparticles in a human prostate tumor xenograft model. Clinical and investigative medicine Médecine Clinique et Experimentale. 2013;36:E133.

383. Roa W, Xiong Y, Chen J, Yang X, Song K, Yang X, et al. Pharmacokinetic and toxicological evaluation of multi-functional thiol-6-fluoro-6-deoxy-d-glucose gold nanoparticlesin vivo. Nanotechnology. 2012;23(37):375101.

384. Srinivasan K, Mohammadi M, Shepherd J. Applications of linac-mounted kilovoltage Cone-beam Computed Tomography in modern radiation therapy: A review. Polish Journal of Radiology. 2014;79:181-93.

385. Ding J, Wang Y, Ma M, Zhang Y, Lu S, Jiang Y, et al. CT/fluorescence dual-modal nanoemulsion platform for investigating atherosclerotic plaques. Biomaterials. 2013;34(1):209-16.

386. Kirkby C, Koger B, Suchowerska N, McKenzie DR. Dosimetric consequences of gold nanoparticle clustering during photon irradiation. Medical Physics. 2017;44(12):6560-9.

387. Jayarathna S, Manohar N, Ahmed MF, Krishnan S, Cho SH. Evaluation of dose point kernel rescaling methods for nanoscale dose estimation around gold nanoparticles using Geant4 Monte Carlo simulations. Scientific Reports. 2019;9(1):3583.

388. Ahn SH, Chung K, Shin JW, Cheon W, Han Y, Park HC, et al. Study on dependence of dose enhancement on cluster morphology of gold nanoparticles in radiation therapy using a body-centred cubic model. Physics in Medicine & Biology. 2017;62(19):7729-40.

389. Lewis JD, Destito G, Zijlstra A, Gonzalez MJ, Quigley JP, Manchester M, et al. Viral nanoparticles as tools for intravital vascular imaging. Nature Medicine. 2006;12(3):354-60.

390. Cheng J, Teply BA, Sherifi I, Sung J, Luther G, Gu FX, et al. Formulation of functionalized PLGA-PEG nanoparticles for in vivo targeted drug delivery. Biomaterials. 2007;28(5):869-76.

391. Hoshyar N, Gray S, Han H, Bao G. The effect of nanoparticle size on in vivo pharmacokinetics and cellular interaction. Nanomedicine. 2016;11(6):673-92.

392. Qie Y, Yuan H, von Roemeling CA, Chen Y, Liu X, Shih KD, et al. Surface modification of nanoparticles enables selective evasion of phagocytic clearance by distinct macrophage phenotypes. Scientific Reports. 2016;6(1):26269.

393. Storm G, Belliot SO, Daemen T, Lasic DD. Surface modification of nanoparticles to oppose uptake by the mononuclear phagocyte system. Advanced drug delivery reviews. 1995;17(1):31-48.

394. Park S-M, Aalipour A, Vermesh O, Yu JH, Gambhir SS. Towards clinically translatable in vivo nanodiagnostics. Nature Reviews Materials. 2017;2(5):17014.

395. White-Koning M, Osborne C, Paci A, Boddy AV, Chatelut E, Veal GJ. Investigating the potential impact of dose banding for systemic anti-cancer therapy in the

paediatric setting based on pharmacokinetic evidence. European Journal of Cancer. 2018;91:56-67.

396. Lucas CJ, Martin JH. Pharmacokinetic-Guided Dosing of New Oral Cancer Agents. The Journal of Clinical Pharmacology. 2017;57(S10):S78-S98.

397. Ratain MJ. Body-surface area as a basis for dosing of anticancer agents: science, myth, or habit? Journal of Clinical Oncology. 1998;16(7):2297-8.

398. Gao B, Yeap S, Clements A, Balakrishnar B, Wong M, Gurney H. Evidence for therapeutic drug monitoring of targeted anticancer therapies. Journal of Clinical Oncology. 2012;30(32):4017-25.

399. Yun J, Yip E, Gabos Z, Wachowicz K, Rathee S, Fallone BG. Neural-network based autocontouring algorithm for intrafractional lung-tumor tracking using Linac-MR. Medical physics. 2015;42(5):2296-310.

400. Yun J, Yip E, Wachowicz K, Rathee S, Mackenzie M, Robinson D, et al. Evaluation of a lung tumor autocontouring algorithm for intrafractional tumor tracking using low-field MRI: a phantom study. Medical physics. 2012;39(3):1481-94.

401. Yun J, Wachowicz K, Mackenzie M, Rathee S, Robinson D, Fallone B. First demonstration of intrafractional tumor-tracked irradiation using 2D phantom MR images on a prototype linac-MR. Medical physics. 2013;40:051718.

402. Von Hoff DD, Mita MM, Ramanathan RK, Weiss GJ, Mita AC, LoRusso PM, et al. Phase I Study of PSMA-Targeted Docetaxel-Containing Nanoparticle BIND-014 in Patients with Advanced Solid Tumors. Clinical Cancer Research. 2016;22(13):3157-63.

403. Deep G, Panigrahi GK. Hypoxia-Induced Signaling Promotes Prostate Cancer Progression: Exosomes Role as Messenger of Hypoxic Response in Tumor Microenvironment. 2015;20(5-6):419-34.

404. Höckel M, Vaupel P. Tumor Hypoxia: Definitions and Current Clinical, Biologic, and Molecular Aspects. JNCI: Journal of the National Cancer Institute. 2001;93(4):266-76.

405. Evans SM, Judy KD, Dunphy I, Jenkins WT, Nelson PT, Collins R, et al. Comparative Measurements of Hypoxia in Human Brain Tumors Using Needle Electrodes and EF5 Binding. Cancer Research. 2004;64(5):1886-92.

406. Carreau A, El Hafny-Rahbi B, Matejuk A, Grillon C, Kieda C. Why is the partial oxygen pressure of human tissues a crucial parameter? Small molecules and hypoxia. Journal of Cellular and molecular Medicine. 2011;15(6):1239-53.

407. Graham K, Unger E. Overcoming tumor hypoxia as a barrier to radiotherapy, chemotherapy and immunotherapy in cancer treatment. International Journal of Nanomedicine. 2018;13:6049-58.

408. Halasz LM, Rockhill JK. Stereotactic radiosurgery and stereotactic radiotherapy for brain metastases. Surgical Neurology International. 2013;4(Suppl 4):S185-S91.

409. Arabpour A, Shahbazi-Gahrouei D. Effect of Hypofractionation on Prostate Cancer Radiotherapy. International Journal of Cancer Management. 2017;10(10):e12204.

410. Thompson MK, Poortmans P, Chalmers AJ, Faivre-Finn C, Hall E, Huddart RA, et al. Practice-changing radiation therapy trials for the treatment of cancer: where are we 150 years after the birth of Marie Curie? British Journal of Cancer. 2018;119(4):389-407.

411. Spencer KL, van der Velden JM, Wong E, Seravalli E, Sahgal A, Chow E, et al. Systematic Review of the Role of Stereotactic Radiotherapy for Bone Metastases. JNCI: Journal of the National Cancer Institute. 2019;111(10):1023-32.

412. Alongi F, Arcangeli S, Filippi AR, Ricardi U, Scorsetti M. Review and uses of stereotactic body radiation therapy for oligometastases. The Oncologist. 2012;17(8):1100-7.

413. Franceschini D, Bianciardi F, Mazzola R, De Rose F, Gentile P, Alongi F, et al. Can thoracic nodes oligometastases be safely treated with image guided hypofractionated radiation therapy? British Journal of Radiology. 2019;92(1103):20181026.

414. Matsushita H, Jingu K. Stereotactic Radiotherapy for Oligometastases in Lymph Nodes-A Review. Technology in Cancer Research & Treatment. 2018;17:1533033818803597.

415. Nguyen PL. Using Stereotactic Body Radiotherapy to Overcome the Radioresistant Reputation of Renal Cell Carcinoma. European Urology Oncology. 2019;2(5):524-5.

416. Lesueur P, Lequesne J, Barraux V, Kao W, Geffrelot J, Grellard J-M, et al. Radiosurgery or hypofractionated stereotactic radiotherapy for brain metastases from radioresistant primaries (melanoma and renal cancer). Radiation Oncology. 2018;13(1):138.

417. Ogawa Y, Shibamoto Y, Hashizume C, Kondo T, Iwata H, Tomita N, et al. Repeat stereotactic body radiotherapy (SBRT) for local recurrence of non-small cell lung cancer and lung metastasis after first SBRT. Radiation Oncology. 2018;13(1):136.

418. Rühle A, Andratschke N, Siva S, Guckenberger M. Is there a role for stereotactic radiotherapy in the treatment of renal cell carcinoma? Clinical and Translational Radiation Oncology. 2019;18:104-12.

419. Castle KD, Kirsch DG. Establishing the Impact of Vascular Damage on Tumor Response to High-Dose Radiation Therapy. Cancer Research. 2019;79(22):5685-92.

420. Wennberg B, Lax I. The impact of fractionation in SBRT: analysis with the linear quadratic model and the universal survival curve model. Acta Oncology. 2013;52(5):902-9.

421. Nahum AE. The radiobiology of hypofractionation. Clinical Oncology. 2015;27(5):260-9.

422. Ng KW, Marshall EA, Bell JC, Lam WL. cGAS–STING and Cancer: Dichotomous Roles in Tumor Immunity and Development. Trends in Immunology.39(1):44-54.

423. Wang Y, Deng W, Li N, Neri S, Sharma A, Jiang W, et al. Combining Immunotherapy and Radiotherapy for Cancer Treatment: Current Challenges and Future Directions. Frontiers in Pharmacology. 2018;9:185.

424. Slovin SF, Beer TM, Higano CS, Tejwani S, Hamid O, Picus J, et al. Initial phase II experience of ipilimumab (IPI) alone and in combination with radiotherapy (XRT) in patients with metastatic castration-resistant prostate cancer (mCRPC). Journal of Clinical Oncology. 2009;27(15_suppl):5138.

425. Kwon ED, Drake CG, Scher HI, Fizazi K, Bossi A, van den Eertwegh AJM, et al. Ipilimumab versus placebo after radiotherapy in patients with metastatic castration-resistant prostate cancer that had progressed after docetaxel chemotherapy (CA184-043): a multicentre, randomised, double-blind, phase 3 trial. Lancet Oncology. 2014;15(7):700-12.

426. Kataoka H, Nishie H, Hayashi N, Tanaka M, Nomoto A, Yano S, et al. New photodynamic therapy with next-generation photosensitizers. Annals of Translational Medicine. 2017;5(8):183-.

427. Zhang J, Jiang C, Figueiró Longo JP, Azevedo RB, Zhang H, Muehlmann LA. An updated overview on the development of new photosensitizers for anticancer photodynamic therapy. Acta Pharmaceutica Sinica B. 2018;8(2):137-46.

428. Chen Q, Wu J, Ou X, Huang B, Almutlaq J, Zhumekenov AA, et al. All-inorganic perovskite nanocrystal scintillators. Nature. 2018;561(7721):88-93.

429. Ouyang Z, Liu B, Yasmin-Karim S, Sajo E, Ngwa W. Nanoparticle-aided external beam radiotherapy leveraging the Čerenkov effect. Physica Medica. 2016;32(7):944-7.

430. Pogue BW, Wilson BC. Optical and x-ray technology synergies enabling diagnostic and therapeutic applications in medicine. Journal of Biomedical Optics. 2018;23(12):121610.

431. Yang W, Read PW, Mi J, Baisden JM, Reardon KA, Larner JM, et al. Semiconductor nanoparticles as energy mediators for photosensitizer-enhanced radiotherapy. International Journal of Radiation Oncology • Biology • Physics. 2008;72(3):633-5.

432. Clement S, Anwer A, Deng W, Wilson B, Allen C, Goldys E. Nuclear targeted x-ray activated photodynamic therapy: a solution to treat pancreatic cancer (Conference Presentation): SPIE; 2019.

433. Tendler II, Hartford A, Jermyn M, LaRochelle E, Cao X, Borza V, et al. Experimentally Observed Cherenkov Light Generation in the Eye During Radiation Therapy. International Journal of Radiation Oncology • Biology • Physics. 2020;106(2):422-9.

434. Jiang T, Jin K, Liu X, Pang Z. 8 - Nanoparticles for tumor targeting. In: Jana S, Maiti S, Jana S, editors. Biopolymer-Based Composites: Woodhead Publishing. 2017; 221-67.

435. Seyhan AA. Lost in translation: the valley of death across preclinical and clinical divide – identification of problems and overcoming obstacles. Translational Medicine Communications. 2019;4(1):18.

436. Sun W, Zhou Z, Pratx G, Chen X, Chen H. Nanoscintillator-Mediated X-Ray Induced Photodynamic Therapy for Deep-Seated Tumors: From Concept to Biomedical Applications. Theranostics. 2020;10(3):1296-318.

437. Ribas ESC, Schiff D. Spinal Cord Compression. Current Treatment Options in Neurology. 2012;14(4):391-401.

438. Robson P. Metastatic spinal cord compression: a rare but important complication of cancer. Clinical Medicine. 2014;14(5):542-5.

439. Guddati AK, Kumar G, Shapira I. Early intervention results in lower mortality in patients with cancer hospitalized for metastatic spinal cord compression. Journal of investigative medicine. 2017;65(4):787-93.

440. Prewett S, Venkitaraman R. Metastatic Spinal Cord Compression: Review of the Evidence for a Radiotherapy Dose Fractionation Schedule. Clinical Oncology. 2010;22(3):222-30.

441. Bednarkiewicz A, Nyk M, Samoc M, Strek W. Up-conversion FRET from Er3+/Yb3+:NaYF4 Nanophosphor to CdSe Quantum Dots. The Journal of Physical Chemistry C. 2010;114(41):17535-41.

442. Klier DT, Kumke MU. Upconversion Luminescence Properties of NaYF4:Yb:Er Nanoparticles Codoped with Gd3+. The Journal of Physical Chemistry C. 2015;119(6):3363-73.

443. Xiao YD, Paudel R, Liu J, Ma C, Zhang ZS, Zhou SK. MRI contrast agents: Classification and application (Review). International Journal of Molecular Medicine. 2016;38(5):1319-26.

444. Campbell DR, Flemming BK, Mason WF, Jackson SA, Hirsch DJ, MacDonald KJ. A comparative study of the nephrotoxicity of iohexol, iopamidol and ioxaglate in peripheral angiography. Canadian Association of Radiologists journal = Journal l'Association Canadienne des Radiologistes. 1990;41(3):133-7.

445. Moos SI, van Vemde DN, Stoker J, Bipat S. Contrast induced nephropathy in patients undergoing intravenous (IV) contrast enhanced computed tomography (CECT) and the relationship with risk factors: a meta-analysis. European Journal of Radiology. 2013;82(9):e387-99.

APPENDIX

7.1 Synthesis and Characterization of PEG-PLGA Encapsulated CoreNaFGdY$_4$ and ShellGd-CoreNaFGdY$_4$ Upconverting Nanoparticles

Contributions

Dr. Michael Kumke (University of Potsdam, Potsdam, Germany) contributed NaFGdY$_4$-based up-converting nanoparticles for use in this project. Ahasanur Rahman (undergraduate summer student whom I supervised) presented this project in Department of Biochemistry's summer student day as part of the fulfillment towards his summer studentship in the lab. Dr. Keith Wahowicz (Medical Physics, Cross Cancer Institute) performed the MRI scans with a Philips 3T MRI/MRS scanner (Philips Healthcare, Andover, USA).

The use of Up-Converting Nanoparticles (UCNP) in diagnosis via localization of fluorescence signal has been previously reported in preclinical applications (257, 441, 442). $NaFY_4$ based UCNPs have the ability to be co-doped with many other metallic elements to achieve particular luminescent properties. One such element that is commonly used is gadolinium (Gd), which is also a commonly used element in MRI contrast agents. This is due to Gd's high magnetic moment (443). The large magnetic moment has led to the development of clinical MRI contrast agents such as gadobutrol, or Gadovist 1.0 (Bayer AG, Leverkusin, Germany). The use of Gd in a NP construct such as in UCNPs may confer similar MRI contrast enhancing properties. The large magnetic moment of the UCNP can cause local disturbances in magnetic field lines in an MRI magnet. The disturbances can result in perturbation of relaxivity in adjacent protons when subjected to an electromagnetic pulse. The change in relaxivity can be acquired by the MRI detectors and interpreted as contrast enhancement.

Incorporating a magnetic moment in NP may allow dual-modality imaging with upconverting luminescence and MRI imaging. The challenge with UCNPs such as $NaYF_4$ based agents is biocompatibility. Here, we report an attempt at encapsulating two $NaYF_4$ constructs, $CoreNaFGdY_4$ and $ShellGd\text{-}CoreNaFGdY_4$, into a PEG-PLGA nanosphere for the purpose of increasing biocompatibility.

The UNCP NP agents were synthesized similar to the synthesis of NSC NP described in **Chapter 2**. The synthesized NP (called core NP for $CoreNaFGdY_4$ and core-shell NP for $ShellGd\text{-}CoreNaFGdY_4$) appeared to be successfully encapsulated by UV-Vis spectroscopy and TEM, and demonstrated fair stability by size and zeta potential for core NP, but sub-ideal stability for core-shell NP (**Figure A1.1, A1.2 and A1.3**). The size

distribution of by Nanosight NTA appeared to be more homogenous for core NP than core-shell NP.

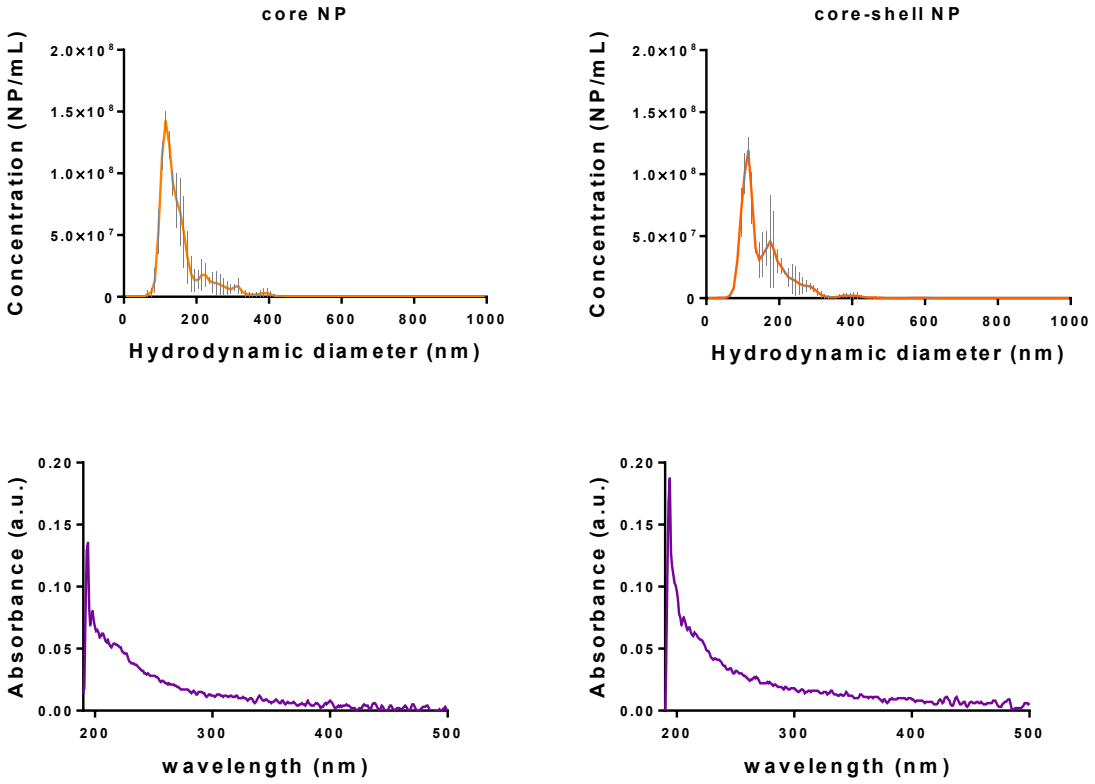

Figure A1.1: Characterization of core NP and core-shell NP by Nanosight NTA and UV-Vis spectroscopy. The core NP appeared to have a lower polydispersity with a mean hydrodynamic diameter of 147±4nm while the core-shell had two peaks of NP size with a mean hydrodynamic diameter of 151±7 nm. The UV-Vis spectra appeared similar between the two NP with a peak at 195nm, which likely represents the PEG-PLGA content, and a broad region of absorbance between 200 to 300nm.

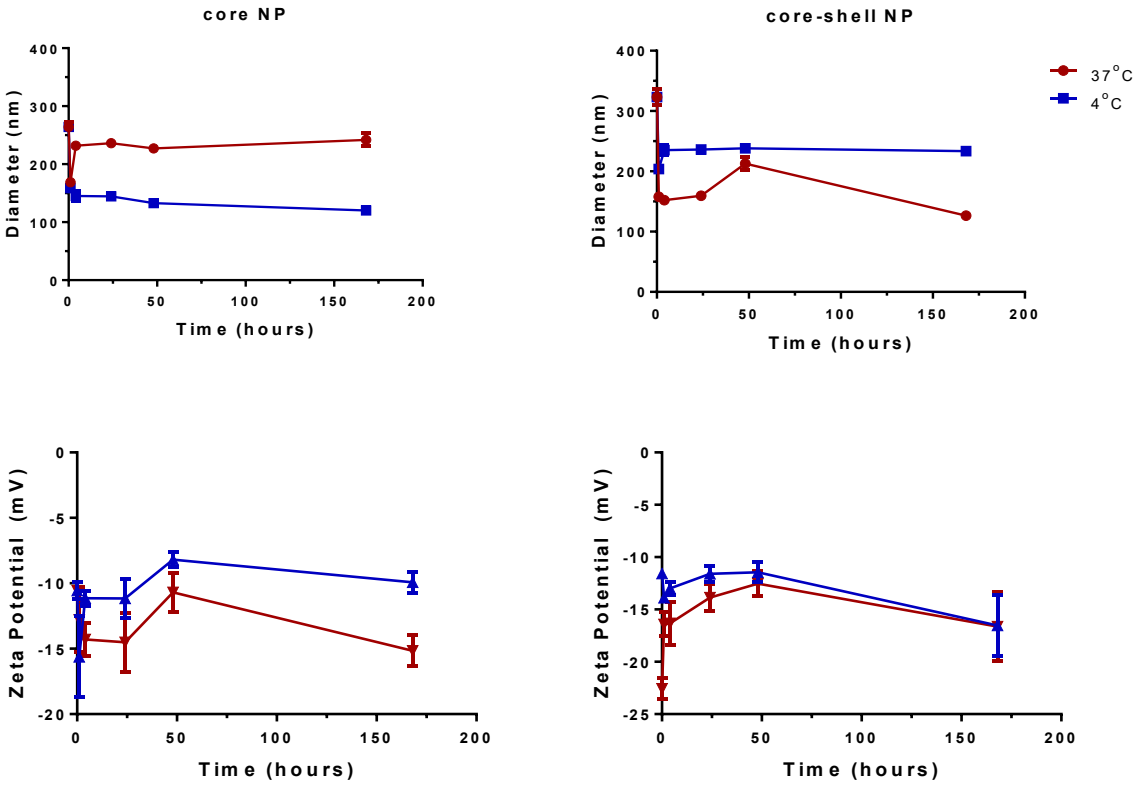

Figure A1.2: core NP and core-shell NP size and zeta potential over time as an assessment of stability. Size was measured at serial timepoints by DLS. The NP appeared stable for about 48 hours in 4ºC and 37ºC before experiencing changes in size and zeta potential.

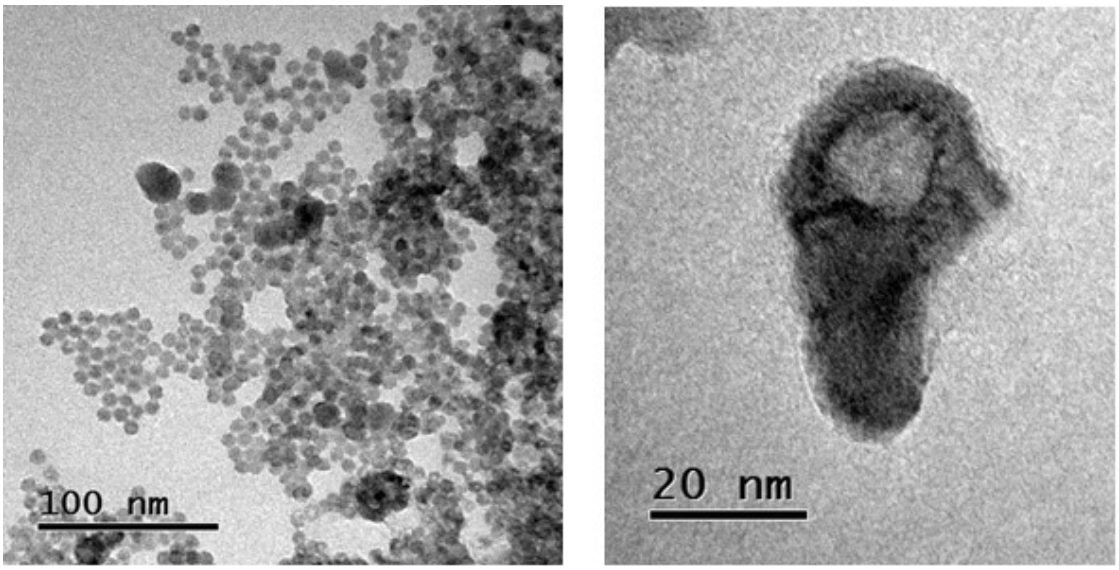

Figure A1.3: CoreNaFGdY$_4$ shown on the left and PEG-PLGA encapsulated CoreNaFGdY$_4$ NP shown on the right.

Cytotoxicity assays revealed these NP were still relatively cytotoxic to NKC normal kidney cell line and PC3 prostate cancer cell line, despite the use of a PEG-PLGA coating (**Figure A1.4**). Assessment of their MRI performance did show appreciable contrast particularly in T1 sequence compared to Gadovist (**Figure A1.5**).

The toxicity assessment was done via MTT assay similar to as described in **Chapter 2**. NKC normal kidney cancer cell line was used as an analogue to toxic effects towards normal tissue, and PC3 prostate cancer cell line was used to represent toxicity towards a highly proliferative human cell line. The results were compared against Gadovist and doxorubicin. **Figure A1.4** demonstrates the toxicity of the core NP and core-shell NP was still significantly higher than Gadovist ($p<0.01$) and not statistically different than doxorubicin for both cell lines. This indicates that the encapsulation with PEG-PLGA was not enough to mitigate the toxicity risk of these NP. The highest concentration of the NPs and Gadovist was sent for ICP-MS to quantify the Gd content. Despite Gadovist having the highest Gd content by about 35 times, its still had a lower toxicity profile than the UCNPs. This indicates the toxicity of these NP stem from a source other than the Gd content.

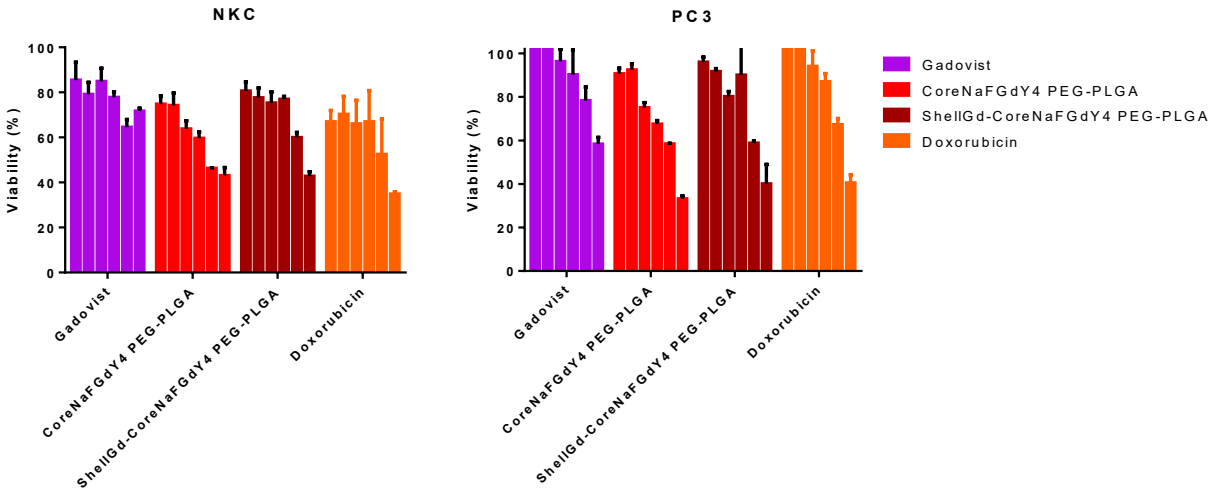

Gadovist (mM)	core NP (NP/mL)	core-shell NP (NP/mL)	Doxorubicin (uM)
1 (174ppm Gd)	$1x10^{12}$ (6.61ppm Gd)	$1x10^{12}$ (4.10ppm Gd)	40
0.5	$5x10^{11}$	$5x10^{11}$	20
0.25	$2.5x10^{11}$	$2.5x10^{11}$	10
0.125	$1.25x10^{11}$	$1.25x10^{11}$	5
0.0625	$6.25x10^{10}$	$6.25x10^{10}$	2.5
0.03125	$3.13x10^{10}$	$3.13x10^{10}$	1.25

Figure A1.4: MTT toxicity assay of core NP and core-shell NP compared with Gadovist and Doxorubicin. The bar graph depicts the concentrations of each agent shown in the table, with increasing concentration going from left to right on the bar graph.

In comparing the relaxivity of the core and core-shell NP against Gadovist in a Philips 3T MRI, no appreciable relaxivity was seen on T1 (**Figure A1.5**). On T2, there was a change in relaxivity seen for core NP, but this was not statistically significant compared to water.

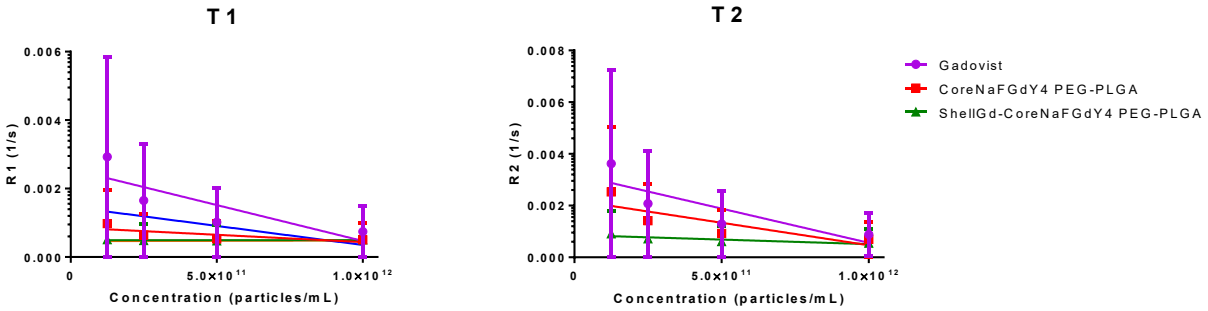

Figure A1.5: Relaxivity of core NP and core-shell NP compared to Gadovist in T1 and T2 sequences. No statistically significant difference was seen between the core and core-shell NP from baseline of no relaxivity (equivalent to water).

Taken together, these results suggest CoreNaFGdY$_4$ and ShellGd-CoreNaFGdY$_4$ can be successfully encapsulated in a PEG-PLGA polymer, but this did not successfully mitigate the toxicity of the UCNPs, which still had a toxicity profile comparable to doxorubicin. Furthermore, the relaxivity profile did not suggest any appreciable contrast existed in T1, and T2 there was a slight amount of relaxivity difference seen with the core NP variant, this was not statistically significant. The lack of relaxivity likely comes from the aggregate magnetic moment of the UCNP may not be very large, despite the atoms of Gd individually having large magnetic moments. The toxicity profile suggests other methods of nanoparticle encapsulation may be more successful in making the UCNPs more biologically compatible.

7.2 Synthesis and Assessment of Iohexol Encapsulated PEG-PLGA NP for *in vivo* Diagnostic Performance

To assess the capability of the PEG-PLGA NP platform to support further diagnostic capabilities than seen in **Chapter 4**, a variant of the NP was created in an attempt to encapsulate iohexol. A commonly used CT contrast agent, iohexol (Omnipaque®, GE Healthcare, USA) is considered a standard-of-care contrast agent used in diagnostic scans. While iohexol is usually well-tolerated, the incidence rate of iohexol-related nephrotoxicity is well known (444, 445). In an attempt to reduce the toxicity risk of iohexol, modify its biodistribution profile to preferentially target tumors via EPR effect, and tag the PEG-PLGA NP system for imaging-based biodistribution studies, a iohexol encapsulated NP (iohexol NP) was created. An encapsulation procedure similar to NSC NP in **Chapter 2** was followed. 10mg of iohexol dry powder was dissolved in 10mL

acetonitrile along with 100mg of PEG-PLGA. Nanoprecipitation was done as described previously. Considerable difficulty was encountered due to aggregation during the nanoprecipitation process. The majority of the drug appeared to be lost during the encapsulation attempt in the washing of the media after synthesis (see **Figure A2.1 a and b**). Nanosight NTA also showed multiple sizes and populations of NPs created, with the dominant population being about 105nm (**Figure A2.1c**).

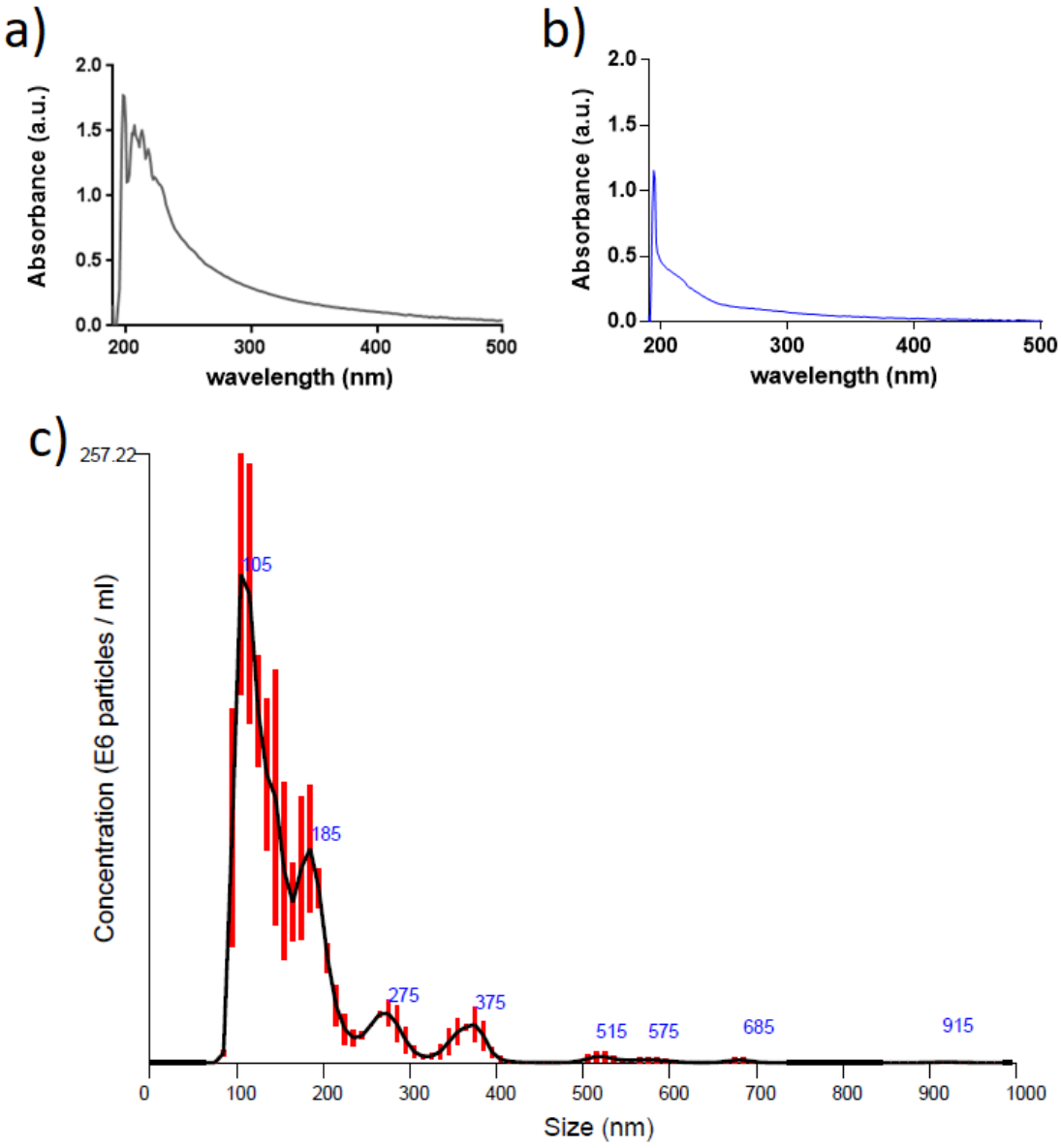

Figure A2.1: Characterization of iohexol encapsulated PEG-PLGA NP by UV-Vis absorbance spectra and Nanosight NTA. The reagent solution (a) appeared to have a high content of iohexol and PEG-PLGA, but by the end of the synthesis and washing steps, a significant amount of product was lost as evidenced by the drop in absorbance signal (b). The NPs also exhibited poor uniformity with multiple sub populations created during synthesis (c).

The NP were concentrated and administered IV to PC3 flank tumor-bearing NSG mice, similar to as described in **Chapter 4**. No signs of significant contrast enhancement were seen in the mice tested (**Figure A2.2a**). There was, however, a statistically non-significant rise seen in the liver and tumor across the cohort of mice imaged (N=3). Attempts at visualizing the enhancement within the tumor were unsuccessful (**Figure A2.2c**).

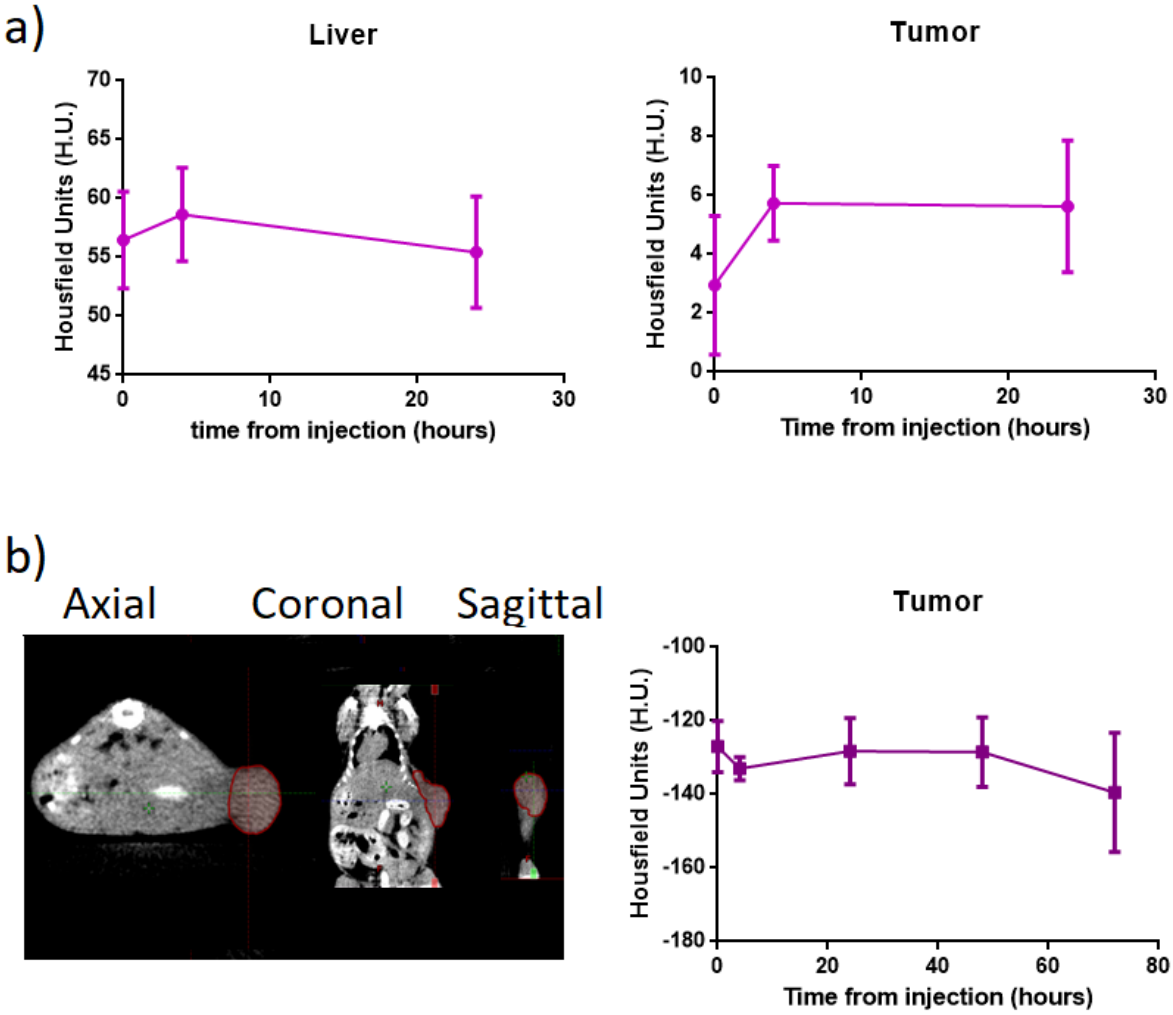

Figure A2.2: CT assessment of PC3 flank tumor-bearing NSG mice injected with iohexol NP. No significant difference in enhancement, quantified as a significant rise in HU in the tumor and liver, was seen over time (a). Visual and quantitative analysis of a mouse imaged by CT also failed to show any signs of enhancement in the tumor (b). Note, b) was imaged on a different CT protocol in an attempt to boost sensitivity.

The lack of enhancement on CT with the iohexol NP further confirms that successful encapsulation of a significant amount of the iohexol was not achieved. This may be because the previously described nanoprecipitation technique may not be ideal for iohexol, as it is a strongly hydrophilic molecule. Given the core of the PEG-PLGA is a hydrophobic environment, this may not be suitable for ideal encapsulation conditions. A switch to a single or double emulsion technique would likely be needed to increase encapsulation efficiency.

The other factor that impacts CT contrast enhancement performance is iohexol is usually a freely dissolved compound that is injected into the body tissue and diffusely distributes through tissues. This leads to the compound having a high cross-section to incident X-ray beams used for imaging. Sequestering iohexol in NPs can lower its cross-section to the imaging X-ray beams, and decrease its ability to attenuate the beam.